

UC San Diego

UC San Diego Electronic Theses and Dissertations

Title

Polymeric Nanoparticle and Bioconjugate MRI Contrast Agents for In Vivo Imaging

Permalink

<https://escholarship.org/uc/item/6419g2x1>

Author

Le Guyader, Clare Lee Matilda

Publication Date

2017

Peer reviewed|Thesis/dissertation

UNIVERSITY OF CALIFORNIA, SAN DIEGO

**POLYMERIC NANOPARTICLE AND BIOCONJUGATE MRI CONTRAST
AGENTS FOR IN VIVO IMAGING**

A thesis submitted in partial satisfaction of the requirements for the degree Doctor of
Philosophy

in

Chemistry

by

Clare Lee Matilda Le Guyader

Committee in Charge:

Professor Nathan C. Gianneschi, Chair

Professor Thomas Hermann

Professor Robert F. Mattrey

Professor F. Akif Tezcan

Professor Emmanuel Theodorakis

2017

Copyright

Clare Lee Matilda Le Guyader, 2017

All rights reserved.

The dissertation of Clare Lee Matilda Le Guyader is approved, and it is acceptable in quality and form for publication on microfilm and electronically:

Chair

University of California, San Diego

2017

DEDICATION

I dedicate this thesis to my grandmothers, the two kindest and strongest women I have known; who have encouraged me to work hard, and to learn as much as I can.

EPIGRAPH

"We adore chaos because we love to produce order."

M.C. Escher

TABLE OF CONTENTS

SIGNATURE PAGE	iii
DEDICATION	iv
EPIGRAPH	v
TABLE OF CONTENTS.....	vi
LIST OF ABBREVIATIONS	x
LIST OF FIGURES	xiv
LIST OF TABLES	xx
ACKNOWLEDGEMENTS	xxii
VITA.....	xxv
ABSTRACT OF THE DISSERTATION	xxvi
Chapter 1	1
Introduction to Polymeric Nanoparticles and Bioconjugates for Nanomedicine Applications	1
1.1 Nanoparticle and Protein-Based Drug Delivery	1
1.2 Considerations for Nanomedicines	3
1.2.1 The EPR Effect	3
1.2.2 Nanoparticle Physicochemical Properties	6
Size Effects	6
Shape Effects	8
Surface Functionalization and Charge	9
1.2.3 Active Targeting	10
1.2.4 Challenges to Studying Nanoparticles in the Lab	12
1.3 Polymer Amphiphile Self-Assembled Nanoparticles	12
1.3.1 Theories on Self-Assembly	13
1.3.2 Experimental Investigations of Polymer Self-Assembly	14
1.3.3 Kinetic and Thermodynamic Equilibria in Polymer Self-Assembly	16
1.3.4 Polymer Architecture for Self-Assembly.....	17
1.4 Nanoparticles for In Vivo Imaging Using MRI	20
1.4.1 Molecular Basis for Gadolinium-based T ₁ contrast agents	20
1.5 Albumin as a Drug Carrier.....	25
1.6 Conclusions for Introduction and Dissertation Overview.....	31

1.7	References.....	32
Chapter 2.....		41
Accessing Diverse Nanoparticle Morphologies via Ring Opening Metathesis Polymerization		
.....		41
2.1	Introduction.....	41
2.2	Selection of Monomers and Preparation of Polymers.....	44
2.3	Nanoparticle Formulation	46
2.4	Fluorinated Monomer, Polymers, and Nanoparticles	50
2.5	Conclusions and Outlook.....	55
2.6	Acknowledgments.....	57
2.7	Methods	57
2.7.1	Monomer Synthesis	58
2.7.2	Polymer Synthesis and Characterization.....	59
2.7.3	Formulation of Nanoparticles	63
2.8	References.....	67
Chapter 3.....		69
MRI Contrast Agent Labeled Polymeric Nanomaterials for In Vivo Imaging		69
3.1	Introduction.....	69
3.2	Graft-Through Polymerization of a Gd-DOTA Moiety.....	73
3.2.1	Synthesis of Gd-DOTA Norbornyl Monomers.....	74
3.2.2	Preparation and Characterization of Polymers with Gd-DOTA as Hydrophilic Entity	75
3.2.3	Nanoparticle Formulation and Characterization	75
3.2.4	In Vitro Relaxivity	80
3.3	In Vivo Analysis of Gadolinium-Containing SMN and FMN.....	82
3.3.1	Ex Vivo Analysis	88
3.4	Incorporation of Gd-DOTA as a Chain Transfer Agent	89
3.4.1	End-labeling of Polymers.....	91
3.4.2	Nanoparticle Formulation	92
3.4.3	Application of End Termination of Polymers with Gd-Based Agent	93
3.5	Applications of Peptide Polymeric Materials with a MRI Contrast Agent.....	94
3.6	Conclusions and Outlook.....	97
3.7	Acknowledgements.....	99
3.8	Methods	99
3.8.1	Monomer Synthesis	100
3.8.2	Symmetric Chain Transfer Agent Synthesis	101

3.8.3	Polymer Synthesis and Characterization.....	103
3.8.4	Formulation of Polymeric Nanoparticles.....	106
3.8.5	Characterization of Nanomaterials.....	106
3.8.6	¹ H NMRD Profiles, Fitting Parameters, and Description	111
3.8.7	In Vitro and In Vivo MRI	114
3.8.8	Analysis of T ₁ Data.....	115
3.8.9	Ex vivo ICP-MS Analysis of Organs.....	116
3.8.10	Concentration Determination of Gadolinium in Aqueous Nanoparticles ..	119
3.8.11	Relaxivity Measurements for CTA Polymer Nanoparticles	120
3.9	References.....	121
Chapter 4.....		124
Fatty Acid Conjugates for Hitchhiking on Albumin: Diagnostic and Therapeutic Applications		
.....		124
4.1	Introduction.....	124
4.2	Fatty Acid Conjugates as Diagnostic Agents.....	126
4.2.1	Synthesis and Formulation Strategy	127
4.2.2	Relaxivity Measurements.....	129
4.2.3	In Vivo Evaluation	130
4.3	Fatty Acid-Taxol Conjugates for Therapeutic Applications	134
4.3.1	Stability of PTX-FA.....	134
4.3.2	Formulation of PTX-FA with Albumin	135
4.3.3	In Vitro Toxicity	136
4.3.4	In Vivo Efficacy.....	140
4.4	Exploring the Scope of the Fatty Acid Platform.....	140
4.4.1	Other Paclitaxel-Derivatives	141
4.4.2	Other Categories of Therapeutic Agents.....	144
4.4.3	Peptide Conjugates.....	145
4.5	Cellular Internalization of Fatty Acid Conjugates	147
4.5.1	Cell Uptake Evaluated by Flow Cytometry	148
4.5.2	Evaluation of Mechanism of Action	151
4.6	Conclusions and Outlook.....	153
4.7	Acknowledgments.....	157
4.8	Methods	158
4.8.1	General Synthetic Methods.....	158
4.8.2	Critical Micelle Concentration Determination.....	160
4.8.3	Relaxivity Measurements.....	161
4.8.4	General In Vivo Imaging Methods	163
4.8.5	Blood Half -Life Studies and Protocols	167
4.8.6	General Ex Vivo Analysis Methods.....	169

4.8.7	General Cell Culture Methods	171
4.8.8	Cytotoxicity.....	171
4.8.9	Cell Uptake Experiments	182
4.8.10	Cell Uptake Mechanistic Experiments.....	182
4.8.11	Flow Cytometry Analysis	183
4.9	References.....	194
Chapter 5.....		196
Conclusions and Perspectives		196
5.1	Conclusions on Polymeric Nanoparticle and Bioconjugate MRI Contrast Agents for In Vivo Imaging	196
5.2	On-Going and Future Work.....	197
5.3	Perspective: The Future of Translatable Nanoparticle Drug Delivery Systems ..	198
5.4	References.....	200

LIST OF ABBREVIATIONS

ABX	abraxane
Au	gold
AFM	atomic force microscopy
Ar	aryl
ATRP	atom transfer radical polymerization
- <i>b</i> -	block, in block copolymer
BCPs	block copolymers
°C	degrees Celsius
¹³ C	carbon
CA	contrast agent
CDCl ₃	deuterated chloroform
CHCl ₃	chloroform
CPP	cell penetrating peptide
CT	computed tomography
CTA	chain transfer agent
δ	chemical shift
d	doublet, days, deuterated
dd	doublet of doublet
DCM	dichloromethane
DIPEA	N,N-Diisopropylethylamine
DLS	dynamic light scattering
DMEM	Dulbecco's minimum essential medium
DMF	dimethylformamide
DMSO	dimethylsulfoxide
dn/dc	change in refractive index with respect to change in concentration
DNA	deoxyribonucleic acid
DOTA	1,4,7,10-tetraazacyclododecane-1,4,7,10-tetraacetic acid
DP	degree of polymerization
DPBS	Dulbecco's phosphate buffered saline
DTPA	diethylenetriaminepentaacetic acid
EDAPT	enzyme-directed assembly of nanoparticles at tumor
ESI-MS	electrospray ionization mass spectrometry
EPR	enhanced permeation and retention effect
equiv	equivalents
EtOAc	ethyl acetate
EVE	ethyl vinyl ether
¹⁹ F	fluorine
FA	fatty acid
FACS	fluorescence-activated cell sorting
FDA	food and drug administration
FMN	fibrillar micellar nanoparticles
FMOC	fluorenylmethyloxycarbonyl chloride
FRET	fluorescence-resonance imaging transfer
FSC	forward scatter
g	grams
GBCAs	gadolinium based contrast agents
Gd	gadolinium

gp18, 60, 30	glycoprotein 18, 60 and 30
h	hours
^1H	proton
HATU	(1-[Bis(dimethylamino)methylene]-1H-1,2,3-triazolo[4,5-b]pyridinium 3-oxid hexafluorophosphate)
HCl	hydrochloric acid
HNO_3	nitric acid
H_2O	water
HOPO	hydroxypyridinonate
HPLC	high performance liquid chromatography
HSA	human serum albumin
h ν	light
Hz	Hertz (s^{-1})
ICP-OES	inductively coupled plasma optical emission spectrometry
ICP-MS	inductively coupled plasma mass spectrometry
IP	intraperitoneal
IS	inner sphere
IV	intravenous
J	NMR coupling constant
K	degrees Kelvin
kDa	kilodalton
kcal	kilocalories
k_{ex}	exchange rate
λ_{abs}	absorbance wavelength
λ_{em}	emission wavelength
λ_{ex}	excitation wavelength
L	liters, ligand
LCV	large compound vesicle
LRMS	low resolution mass spectrometry
m	meter, multiplet
M	molar
MALS	multi-angle light scattering
Me	methyl (CH_3)
MeOH	methanol (CH_3OH)
Mes	mesityl, 2,4,6-trimethylphenyl ($2,4,6\text{-Me}_3\text{C}_6\text{H}_2$)
MgSO_4	magnesium sulfate
mg	milligram
MI	myocardial infarction
min	minutes
mL	milliliters
MMP	matrix metalloproteinase
Mn	number average molecular weight
mol	moles
MRI	magnetic resonance imaging
MS	mass spectrometry
Mw	weight average molecular weight
Mn	number average molecular weight
MWCO	molecular weight cut-off
NaHCO_3	sodium bicarbonate

NaOH	sodium hydroxide
NHS	<i>N</i> -hydroxysuccinimide
nm	nanometer (10 Å)
NMR	Nuclear Magnetic Resonance
NMRD	Nuclear Magnetic Relaxation Dispersion
NPs	nanoparticles
ns	nanoseconds
OEG	oligoethylene glycol
ODDA	octadecanedioic acid
PAMAM	poly(amidoamine)
PBS	phosphate buffered saline
PD	pharmacodynamic
PEG	poly(ethylene glycol)
PEO	poly(ethylene oxide)
PET	positron emission tomography
Ph	phenyl
PK	pharmacokinetic
PPA	peptide polymer amphiphile
ppb	parts per billion
ppm	parts per million
PRINT®	particle replication in non-wetting template
PNA	peptide nucleic acid
PS	polystyrene
PTX	paclitaxel
PTX-FA	paclitaxel-fatty acid conjugate
q	hydration number
r_1	relaxivity, $1/T_1$, (L/mmol · s ⁻¹)
R	organic group, alkyl group
RAFT	reversible addition-fragmentation chain-transfer
RES	reticuloendothelial system
RF	radiofrequency
RI	refractive index
RNA	ribonucleic acid
ROP	ring-opening polymerization
ROMP	ring-opening metathesis polymerization
RP	reverse-phase
r.t.	room temperature
σ	sigma
s	singlet, seconds
SDS	sodium dodecyl sulfate
SEC	size-exclusion chromatography
S-FIL	step-flash imprint lithography
SLS	static light scattering
SMN	spherical micellar nanoparticles
SPARC	secreted protein, acidic and rich in cysteine
SPPS	solid phase peptide synthesis
SSC	side scatter
STORM	stochastic optical reconstruction microscopy
t	triplet

$t_{1/2}$	half-life
τ_D	rotational correlation time
τ_m	mean residency time of bound water molecules
τ_r	rotational correlation time
τ_{RG}	global rotational correlation time
T_1	longitudinal proton relaxation time
T_{1e}	electronic relation time
T_{1m}	T_1 relaxation time of water
T_2	transverse proton relaxation time
T	Tesla
TEM	transmission electron microscopy
Temp	temperature
TIP	template-induced printing
TFA	trifluoroacetic acid
TFE	2,2,2-trifluoroethanol
T_g	glass transition temperature
THF	tetrahydrofuran
TIPS	triisopropylsilane
TLC	thin layer chromatography
Tris	tris(hydroxymethyl)aminomethane
UV	ultraviolet
μm	micrometer
μM	micromolar
V	volts
V_{max}	maximum velocity
X	halide, peptide sequence

LIST OF FIGURES

Figure 1.1 Considerations of Nanoparticles for Nanomedicine.....	2
Figure 1.2 Small molecule and nanoparticle accumulation in healthy versus tumor tissue.....	4
Figure 1.3 Active targeting of Nanoparticles to tumor tissue.....	11
Figure 1.4 Clinically approved small molecule gadolinium based contrast agents.....	22
Figure 1.5 Molecular parameters of GBCA interreacting with water to enhance relaxation time and contrast.....	23
Figure 1.6 Effect of rotational correlation time on relaxivity at different field strengths.....	24
Figure 1.7 Depiction of albumin and albumin-bound molecules accumulating in tumor tissue.....	28
Figure 2.1 Ring opening metathesis polymerization (ROMP) scheme used to prepare all polymers....	45
Figure 2.2 NPs 1-3 , formed from P1-3 , respectively	48
Figure 2.3 TEMs of FNP1-3 , dialyzed from trifluoroethanol to water	53
Figure 2.4 TEMs of FNP2 prepared from different organic solvent conditions.	54
Figure 2.5 TEM of FNP3 prepared from different organic solvent conditions.	55
Figure 2.6 Synthetic scheme to prepare monomers 2, 3 and 4	58
Figure 2.7 SEC-MALS traces for polymers P1-P8	61
Figure 2.8 SEC-MALS traces for P9-P17	62
Figure 2.9 SEC-MALS traces for FP1-3	63
Figure 2.10 TEMs of NP2	64
Figure 2.11 TEMs of NP9, NP10 and NP11 , from polymers P9, P10 and P11 , respectively.....	65
Figure 2.12 TEMs of NP8	66
Figure 2.13 TEMs of NP4, NP5, NP6, NP7 and NP17	67
Figure 3.1 Scheme of macromolecular effects of GBCA.....	71
Figure 3.2 ROMP scheme for incorporation of a gadolinium-containing monomer or chain transfer agent.	72
Figure 3.3 Particle characterization by electron microscopy of spherical micellar nanoparticles (SMNs) and fibril-shaped micellar nanoparticles (FMNs).	76

Figure 3.4 SMN phase analysis.	77
Figure 3.5 FMN phase analysis	77
Figure 3.6 Stability of Nanomaterials in biological milieu: Cryo-TEM of SMN in Water and Blood Serum for 1 week.....	79
Figure 3.7 Stability of Nanomaterials in biological milieu: Cryo-TEM of FMN in Water and Blood Serum. a) and b) Cryo-TEM of FMN in water	80
Figure 3.8 ¹ H NMRD profiles for Gd-DOTA, SMN, and FMN.....	81
Figure 3.9 Anatomical MRI post-injection of contrast agent demonstrating successful introduction of materials IP.	84
Figure 3.10 Axial T ₁ -weighted images of the abdomen approximately 2 hours following IP injection of a) Gd-DOTA, b) SMN, and c) FMN	85
Figure 3.11 Time progression of signal enhancement, quantified as T ₁ , and corresponding axial T ₁ - weighted images of the bladder after IP-injection of a) Gd-DOTA, b) SMN, and c) FMN.	86
Figure 3.12 Time progression of contrast enhancement, reported as T ₁ , and corresponding anatomical scans of the liver after IP-injection of a) Gd-DOTA, b) SMN, and c) FMN. Any contrast enhancement in the stomach is due to food, not injected material. Red arrows indicate the stomach, white arrows indicate a vessel, and blue arrows indicate part of the liver.....	87
Figure 3.13 Accumulation of SMN and FMN in the spleen a), liver b), and bowel c), at 2, 12 or 24 hours following IP injections as detected by the presence of Gd by ICP-MS and ICP-OES.....	89
Figure 3.14 Polymer amphiphiles end-terminated with Gd-DOTA moiety.	90
Figure 3.15 TEM images and DLS of NP3-6 and dynamic light scattering, formulated from polymers P3-6, end-labeled with a gadolinium-containing CTA	93
Figure 3.16 Polymer scheme for enzyme-responsive, MRI-labeled materials.	95
Figure 3.17 Evaluation of enzyme-responsive polymeric nanoparticles. morphology.....	96
Figure 3.18 Monomer 2 characterization following purification by RP-HPLC..	101
Figure 3.19 Scheme to prepare Gd-CTA.....	102
Figure 3.20 Characterization of Gd-CTA.....	102

Figure 3.21 Alternative preparation of Gd-CTA. Described as in Ref. 42.	103
Figure 3.22 Characterization of P1, 1 ₂₁₀ -b-24.	104
Figure 3.23 Characterization of P2 1 ₄₂ -b-2 ₂	105
Figure 3.24 SEC-MALS traces for P3-6.....	105
Figure 3.25 TEM of SMN, imaged 14 months after preparation.....	108
Figure 3.26 TEM of FMN, imaged 14 months after preparation.....	109
Figure 3.27 STEM-EDS Analysis of SMN.	110
Figure 3.28 STEM-EDS Analysis of FMN.	111
Figure 3.29 NMRD Proton relaxivity as a function of temperature for SMN (left) and FMN (right) at 20 MHz and pH=7.2 and 560 ns for FMN and SMN, respectively, in full agreement with the temperature-dependence study.	113
Figure 3.30 Anatomical MRI of IP space at two hours post-injection demonstrating no signal enhancement (for Gd-DOTA) or signal enhancement (for SMN and FMN): NP formulations are retained in the IP space longer than Gd-DOTA.	115
Figure 3.31 Average and three individual mice for SMN at 2, 12 and 24 hrs.	117
Figure 3.32 Average and three individual mice for FMN at 2, 12 and 24 hrs.	118
Figure 3.33 Detection of gadolinium in mice 1 week post injection.	119
Figure 3.34 Relativity measurements using inversion recovery experiments at 300 MHz, with R- squared of the linear best fit inset	120
Figure 4.1 PTX-FA + HSA was tested head-to-head against Abraxane in a xenograft HT-1080 tumor model.	125
Figure 4.2 A cartoon of FA-Gd conjugates of a diagnostic warhead, designed to selectively interact with HSA	127
Figure 4.3 The synthetic strategy for preparing FA-Gd-DOTA	128
Figure 4.4 Representative relaxivity plots comparing FA-Gd, MultiHance (MH) formulated with HSA and FA-Gd formulated with HSA.....	130

Figure 4.5 Representative MRI scans for tumor-burdened mice receiving high dose of FA-Gd, MH or Gd-DOTA.	133
Figure 4.6 Blood Half-life. FA-Gd, MultiHance (MH), and Gd-DOTA, formulated with HSA, and injected <i>via</i> tail vein in a tumor-burdened animal (HT-1080 xenograft).	134
Figure 4.7 HPLC traces of PTX-FA under various experimental conditions.	135
Figure 4.8 Representative IC ₅₀ curves for conjugates of PTX, and formulations thereof.	138
Figure 4.9 IC ₅₀ plots of PTX-FA and formulation with HSA across 6 cell lines.	139
Figure 4.10 Various fatty acid-PTX conjugates evaluating key features of the fatty acid compounds.	142
Figure 4.11 Cytotoxicity of taxane-type conjugates in HeLa cells.	143
Figure 4.12 FA-CPT and FA-MTX: cytotoxic drugs modified with a ODDA.	144
Figure 4.13 A “KLA peptide” conjugate, FA-KLA.	145
Figure 4.14 Fluorescein conjugates formulated with HSA to evaluate cell uptake pathway.	148
Figure 4.15 Concentration dependent uptake of (a) FA-fl and (b) FA-fl + HSA in complete media or serum-free media in HeLa cells.	149
Figure 4.16 Internalization of FA-fl in other cell lines.	150
Figure 4.17 Internalization of fluorophore labeled peptides (FA-KLA(fluor)) in different cell lines.	151
Figure 4.18 FA-fl (a) or FA-fl + HSA (b) treatment of HeLa cells under various conditions, all at 4.6 μ M with respect to fluorescein.	153
Figure 4.19 Semi-preparative RP-HPLC purification of FA-Gd-DOTA, and ESI-MS, positive ion mode, low resolution.	159
Figure 4.20 HPLC trace after prep-HPLC purification of FA-CPT.	160
Figure 4.21 Critical micelle concentration using pyrene assay and DLS.	161
Figure 4.22 MRI scans of healthy animals receiving 1 μ mol FA-Gd or MH. For FA-Gd, contrast enhancement is clearly visible in the gall bladder out to 7 hours, and recovers to baseline at 24 hours, indicating clearance from the animal.	164
Figure 4.23 Representative MRI scans of tumor-burdened mouse receiving FA-Gd at low dose.	165

Figure 4.24 Representative MRI scans of tumor-burdened mouse receiving MH at low dose	166
Figure 4.25 Representative MRI scans for tumor-burdened mice receiving high doses of FA-Gd, MH or Gd-DOTA.	167
Figure 4.26 MRI scans of tumor-burdened animals receiving FA-Gd.	167
Figure 4.27 Blood half-life healthy animals.	168
Figure 4.28 Pilot study, blood half-life tumor-burdened animal, average of n=3.	168
Figure 4.29 Blood Half Life, tumor-burdened animal.	169
Figure 4.30 Biodistribution in tumor-burdened animals, Low Dose	170
Figure 4.31 Plots describing total ng of Gd detected in the animal (sum organs) and %injected dose are described; these plots correspond to the animals in Fig. 4.30, which were perfused prior to organ harvest.....	171
Figure 4.32 Representative IC ₅₀ curves for PTX-FA conjugates compared to parent PTX compound in complete versus serum-free media, with 0.1%DMSO to solubilize the organic compounds, in HeLa cells.....	173
Figure 4.33 Representative IC ₅₀ curves for PTX-FA formulations with HSA in HeLa cells.	173
Figure 4.34 Representative IC ₅₀ curves for PTX-FA and formulations with HSA in HT-1080 cells..	175
Figure 4.35 Representative IC ₅₀ curves for PTX-FA and formulations with HSA in HT-29 cells.....	175
Figure 4.36 Representative IC ₅₀ curves for PTX-FA and formulations with HSA in H522 cells.	176
Figure 4.37 Representative IC ₅₀ curves for PTX-FA and formulations with HSA in PANC-1 cells. .	177
Figure 4.38 Representative IC ₅₀ curves for PTX-FA and PTX-FA + HSA (5:1) formulations in HepG2 cells.....	178
Figure 4.39 Representative IC ₅₀ curves for C ₁₆ -PTX, C _{18unsat} -PTX, C ₂₀ -PTX and Me-C ₁₈ -C ₆ link-PTX in HeLa cells.	179
Figure 4.40 Cytotoxicity of MTX, FA-MTX and CPT, FA-CPT in HeLa.	180
Figure 4.41 Representative IC ₅₀ curves for FA-KLA and FA-KLA + HSA in HeLa cells.....	181

Figure 4.42 Dot plots showing forward scattering (FSC, x axes) versus side scattering (SSC, y axes) for representative experiment of HeLa cells treated with FA-fl or FA-fl + HSA, and gating used for healthy cell populations.	184
Figure 4.43 Representative histograms for cell uptake, showing concentration dependent uptake of FA-fl using a) complete media or b) serum-free media for HeLa cells.	185
Figure 4.44 Representative histogram for cell uptake, showing concentration dependent uptake of formulations with HSA using a) complete media or b) serum-free media.	185
Figure 4.45 Dot plots showing forward scattering versus side scattering for representative experiments investigating mechanism of uptake of FA-fl, FA-fl + HSA, FA-KLA or FA-KLA + HSA materials in HT-1080 cells, and gating used for healthy cell populations	186
Figure 4.46 Representative histograms for cell uptake of FA-fl, FA-fl + HSA, FA-KLA or FA-KLA + HSA in HT-1080 cells.	187
Figure 4.47 Dot plots showing forward scattering versus side scattering for representative experiments investigating mechanism of uptake of FA-fl, FA-fl + HSA, FA-KLA or FA-KLA + HSA materials in HT-29 cells, and gating used for healthy cell populations.	188
Figure 4.48 Representative histograms for cell uptake of FA-fl, FA-fl + HSA, FA-KLA or FA-KLA + HSA in HT-29 cells.	189
Figure 4.49 Dot plots showing forward scattering versus side scattering for representative experiments investigating mechanism of uptake of FA-fl, FA-fl + HSA, FA-KLA or FA-KLA + HSA materials in HepG2 cells, and gating used for healthy cell populations	190
Figure 4.50 Representative histograms for cell uptake of FA-fl, FA-fl + HSA, FA-KLA or FA-KLA + HSA in HepG2 cells.	191
Figure 4.51 HeLa cells treated with FA-fl formulations in complete media.	192
Figure 4.52 HeLa cells treated with FA-fl formulations in serum-free media.....	193
Figure 4.53 Representative histograms for mechanistic cell uptake studies on HeLa cells for FA-fl (a and c) and FA-fl + HSA (b and d) formulations under various conditions.....	194

LIST OF TABLES

Table 2.1 Molecular Characterizations of P1-P8.....	46
Table 2.2 Fluorinated polymer characterizations.....	51
Table 2.3 Molecular Characterizations of P9-P17.....	60
Table 3.1 Polymer Characterization.	75
Table 3.2 Measured volumes of spheres and non-spheres in FMN.	78
Table 3.3 Relaxation parameters obtained from the analysis of NMRD profiles reported in Fig. 3.8. ^a ..	82
Table 3.4 Polymers End-labeled with gadolinium-containing CTA.....	91
Table 4.1 IC ₅₀ values PTX-FA and PTX-FA + HSA (1), (2), and (5) in various cell lines.	139
Table 4.2 IC ₅₀ values PTX-FA, C ₁₆ -PTX, C _{18unsat} -PTX, C ₂₀ -PTX and C _{6link} -PTX in HeLa cells.	144
Table 4.3 Relaxivity Data.	162
Table 4.4 Relaxivity measurements FA-Gd, varying ratios with HSA.....	163
Table 4.5 Toxicity of PTX, PTX-FA, and formulations with HSA in HeLa cells. Evaluation in complete media and serum-free media (OM) are reported.	174
Table 4.6 Toxicity of PTX, PTX-FA, and formulations with HSA in HT-1080 cells. Evaluation in complete media are reported.....	175
Table 4.7 Toxicity of PTX, PTX-FA, and formulations with HSA in HT-29 cells. Evaluation in complete media are reported.....	176
Table 4.8 Toxicity of PTX-FA and formulations with HSA in H522 cells. Evaluation in complete media are reported.	177
Table 4.9 Toxicity of PTX-FA and formulations with HSA in PANC-1 cells. Evaluation in complete media are reported.	177
Table 4.10 Toxicity of PTX-FA and formulations with HSA in HepG2 cells. Evaluation in complete media are reported.	178
Table 4.11 Toxicity of C ₁₆ -PTX, C _{18unsat} -PTX, C ₂₀ -PTX and Me-C ₁₈ -C _{6link} -PTX in HeLa cells. Evaluation in complete media are reported.	179

Table 4.12 Toxicity of control (parent) compounds CPT and MTX.	180
Table 4.13 Toxicity of FA-CPT and FA-MTX in HeLa cells.....	180
Table 4.14 Toxicity of FA-KLA and FA-KLA + HSA in HeLa cells. Evaluation in complete media as and serum-free media (OM) is reported.	181

ACKNOWLEDGEMENTS

I would not be here, nor have attempted any of this research, without my advisor Nathan Gianneschi taking me on as a student in 2011. Thank you for the opportunities to pursue a scientific research journey, which in turn has allowed me to become a more independent and effective scientist. And thank you for the non-chemistry related opportunities to develop other professional skills to make me a well-rounded scientist. Through both gentle and more direct guidance, I can truly say I am a better scientist than when I joined the lab.

Thank you also, to my thesis committee members, who have patiently guided me through my graduate career. Professors Hermann, Mattrey, Tezcan and Theodorakis have provided intellectually challenging conversations over the years to help me become a better scientist, and I thank them for their time and insights.

The Chemistry Department at UCSD and the campus has provided a rich environment for me to learn about, and how, to do chemical research. There are countless professors, post-post-docs, scientists, and students I have had the pleasure of working with throughout graduate school. Each person and conversation has provided learning moments that have helped me reach the point I am at today. I cannot list every person here, but I will acknowledge those who have pointedly affected my graduate training experience.

The Gianneschi group members come from diverse backgrounds, and from them, I have learned different perspectives on solving problems with chemistry. I am grateful for the time spent working alongside them. Former members of the lab I would like to acknowledge are: Miao-Ping Chien (PhD), Angela Blum (PhD), Steven Nguyen (PhD), Jacquelin Kammeyer (PhD), Sarah Beck-Pancer, Joe Patterson (PhD), Yiwen Li (PhD), Anthony Rush (PhD), Dustin Crystal, Alfred Tam, Alex Caldwell, Ti-Hsuan Ku (PhD), Kelsey Alexander, Joo-Hee Lee, and Billy Pistel. Current lab group members I would like to acknowledge include: Chris Forman (PhD), Treff Ditre (PhD), Andrea Luthi (PhD), Lucas Parent (PhD), Gina Policastro (PhD),

Alex Roloff (PhD), Dan Wright (PhD), Andrea Carlini, Wonmin Choi, Naneki Collins-McCallum, Ziyang Hu, Yuran Huang, Kevin Luo, Miles Markmann, Swagat Sahu, Mollie Touve, Zhao Wang, Nanzhi Zang, and Rob Hennis. I'd especially like to thank the following people, who provided critical support at different points throughout graduate school: Carrie James (PhD) who provided a refreshingly realistic viewpoint on life; Lyndsay Randolph (PhD), with whom I worked closely on the hallmark project of my thesis; Dr. Micahel Hahn who is the only person I know that owns and uses a beeper, and who has extremely insightful thoughts on the imaging related projects we worked on together; and Nia Bell (PhD), for thoughtful discussions over the years, and pushing me to learn AFM.

Perhaps most importantly, I'd like to thank my colleagues and friends, who helped make San Diego and Pacific Hall a better place to live and work, and without whom I would not have made it to this point: Julia Michaelis (PhD), for her thoughtful discussions and perspectives on graduate school and life; Sarah Barnhill, one of the most interesting and authentic people I know; Lizanne Koch Nilweski, who is unbelievably supportive and optimistic and showed me around San Diego; Matt Thompson (PhD), who runs the lab and without whom me nor any other group member could achieve the success we have, and who introduced me to the hobby of camping; Maria Proetto, who shares many similar perspectives on life and work, Cassandra Callmann, with whom recent collaborations have made her a mentor to me in pursuit of a scientific career path, and with whom I spend an incredible amount of time experimenting with animals; Lisa Adamiak (PhD), who is a tremendously diligent scientist, who provided numerous consultative discussions over the years, and a particularly fun and supportive friend.

Finally, I'd like to deeply thank my friends outside of UCSD and my family for their unwavering support over the years, and continued friendship despite thousands of miles of distance. Mom, Dad, Sydney, Travis, Matt, Molly, Katie, Courtney, Devin, Kelly, Suz,

Lindsay, Hope and Stephanie helped me realize that I am capable of so much more than I think I am. Their belief in my abilities often outweighed my own, and without them I don't think I could have completed this process.

I thank the following people, who have provided tremendous technical support and training over the years: Anthony Mrse, Dr. Su, Chris Barback, Miriam Scadeng, Arnie Garcia and Rich Cochran. I also thank those who provided critical administrative support: Robyn Swanland, Jeanine Sun, Erica Twining, Jeff Rances, and many more.

Chapter 3 is adapted, in part, from material as it appears in Chemical Science 2016. Randolph, Lyndsay M.; LeGuyader, Clare L. M.; Hahn, Michael E.; Andolina, Christopher M.; Patterson, Joseph P.; Mattrey, Robert F.; Millstone, Jill E.; Botta, Mauro; Scadeng, Miriam; and Gianneschi, Nathan C. The dissertation author is a co-primary investigator and author of this paper.

Chapter 4, in part, was published as a patent: "Modified Cytotoxins and Their Therapeutic Use." Callmann, Cassandra; Thompson, Matthew P.; LeGuyader, Clare L. M.; Bertin, Paul A. and Gianneschi Nathan C. 2016. The dissertation author was a contributing author on this reference.

Chapter 4, in part, was also published as a patent entitled "Modified MRI Contrast Agents and Uses Thereof." LeGuyader, Clare L. M.; Thompson, Matthew P.; Callmann, Cassandra; Ditri, Treffly; Bertin, Paul A.; Gianneschi, Nathan C. 2017. The dissertation author is the primary investigator of this material.

Chapter 4 also contains material that is currently being prepared for submission for publication: Callmann, C.; Thompson, Matthew P.; Barback, Christopher; LeGuyader, Clare L. M.; Hennis, Robert; Henriksen, Niel; Jaremko, Matthew; Momper, Jeremiah; Burkart, Michael; Bertin, Paul A. and Gianneschi, Nathan C. The dissertation author is a contributing author of this pending manuscript.

VITA

2011	Bachelor of Science, Chemistry The College of William and Mary
2013	Master of Science, Chemistry University of California, San Diego
2017	Doctor of Philosophy, Chemistry University of California, San Diego

PUBLICATIONS

Callmann, C.; Thompson, M. P.; Barback, C.; LeGuyader, C. L. M.; Hennis, R.; Henriksen, N.; Jaremkov, M.; Momper, J.; Burkart, M.; Bertin, P. A.; Gianneschi, N. C. "ODDA-paclitaxel conjugates for targeting and treating cancer tumor." **2017**, *Manuscript in preparation*

Adamiak, L.; Touve, M.; LeGuyader, C. L. M.; Gianneschi, N. C. "Peptide Brush Polymers and Nanoparticles with Enzyme-Regulated Structure and Charge for Inducing or Evading Macrophage Cell Uptake." **2017**, *Manuscript in preparation*

LeGuyader, C. L. M.; Thompson, M.; Callmann, C.; Ditri, T.; Bertin, P.; Gianneschi, N. C. "Modified MRI Contrast Agents and Uses Thereof," **2017**, US application number 62/491,159.

Callmann, C.; Thompson, M.; LeGuyader, C. L. M.; Bertin, P.; Gianneschi, N. C. "Modified Cytotoxins and Their Therapeutic Use." **2016**, PCT/US2016/052829.

Randolph, L. M.*; LeGuyader, C. L. M.*; Hahn, M. E.*; Andolina, C. M.; Patterson, J. P.; Mattrey, R.; Millstone, J.; Botta, M.; Scadeng, M.; Gianneschi, N. C. "Polymeric Gd-DOTA Amphiphiles Form Spherical and Fibril-Shaped Nanoparticle MRI Contrast Agents," *Chem. Sci.*, **2016**, 7, 4230-4236.

Wang, Z.; Li, Y.; Huang, H.; Thompson, M. P.; LeGuyader, C. L. M.; Sahu, S.; Gianneschi, N. C. "Enzyme-Regulated Topology of a Cyclic Peptide Brush Polymer for Tuning Assembly," *Chem. Comm.* **2015**, 51, 17108-17111.

Bell, N. C.; Doyle, S. J.; Battistelli, G.; LeGuyader, C. L. M.; Thompson, M. P.; Poe, A. M.; Rheingold, A.; Moore, C.; Montalti, M.; Thayumanavan, S.; Tauber, M. J.; Gianneschi, N. C. "Dye Encapsulation in Polynorbornene Micelles," *Langmuir* **2015**, 31 (35), 9707-9717.

Childress, E.S.; Roberts, C.A.; Sherwood, D.Y.; LeGuyader, C.L.M.; Harbron, E.J. "Ratiometric Fluorescence Detection of Mercury Ions in Water by Conjugated Polymer Nanoparticles," *Anal. Chem.* **2012**, 84, 1235-1239.

(* equal contribution)

ABSTRACT OF THE DISSERTATION

**POLYMERIC NANOPARTICLE AND BIOCONJUGATE MRI CONTRAST
AGENTS FOR IN VIVO IMAGING**

by

Clare Lee Matilda Le Guyader

Doctor of Philosophy in Chemistry

University of California, San Diego 2017

Professor Nathan C. Gianneschi, Chair

Nanoparticles are the hallmark of nanomedicine, proving clinically relevant for the delivery of therapeutic and diagnostic drugs. Nanomaterials are highly versatile, with the ability for scientists to tailor composition and function to suit the desired application. Herein, two types of nanocarriers are investigated in the context of magnetic resonance imaging contrast agents: polymeric nanoparticles and protein carriers.

A key research focus in applying nanoparticles for drug delivery is in understanding physicochemical properties affecting *in vivo* fate. Shape or morphology of a particle is a vastly underutilized property in the design of nanoparticles, and is difficult to predictably control in the context of polymeric nanoparticles. Investigations of block copolymer nanoassemblies

evaluate effects of the polymer structure and the self-assembly process to form interesting and diverse structures.

In this work, ring-opening metathesis polymerization is employed to prepare and study block copolymer amphiphile self-assembly. First, a small library of amphiphiles are prepared in which the hydrophobic block functionality is varied. In varying the polymer structure and the solvent for assembly, different morphologies are produced, including small and large spheres, cylinders, y-junctions, and rods. In several cases, one polymer can take on different morphologies depending on the organic cosolvent used during micellization, highlighting the importance of assembly conditions and dynamics in forming kinetically trapped structures versus thermodynamically stable structures. These are important considerations when designing, synthesizing, and formulating polymeric nanoparticles for *in vivo* applications.

Next, direct incorporation of a gadolinium based contrast agent for magnetic resonance imaging is studied. A novel monomer and chain transfer agent of a gadolinium-chelate are used to directly incorporate the contrast agent in to a polynorbornene polymer backbone. The resulting spherical and fibrillar nanoparticles exhibited enhanced relaxivity and are studied as MRI contrast agents using live imaging in murine models.

Finally, a fatty acid ligand is conjugated to a gadolinium-based contrast agent is prepared and formulated with human serum albumin. In formulation with HSA, the agent exhibits high relaxivity and prolonged blood circulation. In addition, therapeutic conjugates formulated with HSA are evaluated for *in vitro* cytotoxicity and found to be effective in tumor growth suppression *in vivo*.

Chapter 1

Introduction to Polymeric Nanoparticles and Bioconjugates for Nanomedicine Applications

1.1 Nanoparticle and Protein-Based Drug Delivery

Nanoparticles are materials ranging in size from 1 to 1000 nm and used for a range of applications in the field of biotechnology. Nanoparticles (NPs) are the hallmark of nanomedicine, proving clinically relevant for the delivery of therapeutic and diagnostic drugs. These materials are highly versatile, with the ability for scientists to tailor composition and function to suit the desired application. The first examples of NP therapeutics involved polymer drug conjugates: polymeric materials enhance solubility, blood circulation time, stability and targeting of their small molecule counterparts, extending the therapeutic window, and thus efficacy, of therapeutics.¹ The first clinical trial of polymeric anticancers was conducted in the 1960s. The following decades of research were driven by the development of various polymer drug conjugates and micelle formulations.¹ In 1995, Doxil, a liposomal formulation of doxorubicin, was approved for cancer treatment, leading the way for rapid development and approval of nanomedicines thereafter. Nanocarriers were thus identified as “an emerging platform for cancer therapy.”^{2,3} By the end of 2016, at least 50 unique NPs are approved for cancer treatments, as well as other diseases, with hundreds of other clinical trials ongoing.^{2,4}

In nanomedicine, NPs are used in therapeutic and imaging applications. The motivation in using nanoparticles is to find a more optimized strategy for delivering the existing

pharmaceutical drugs in humans.⁵ To achieve this aim requires collaborations between many different scientific disciplines including chemistry, engineering, pharmacology and medicine. Advantages of nanoparticle formulations of existing therapeutics include strategies for delivering insoluble drugs, dosing at higher concentration, safer/less-toxic delivery and prolonged circulation time coupled with favorable biodistribution. The NP platform offers a highly modular and tailorable architecture that can incorporate targeting functional groups, multidrug loading at high doses and stimuli-responsive units, to name a few.

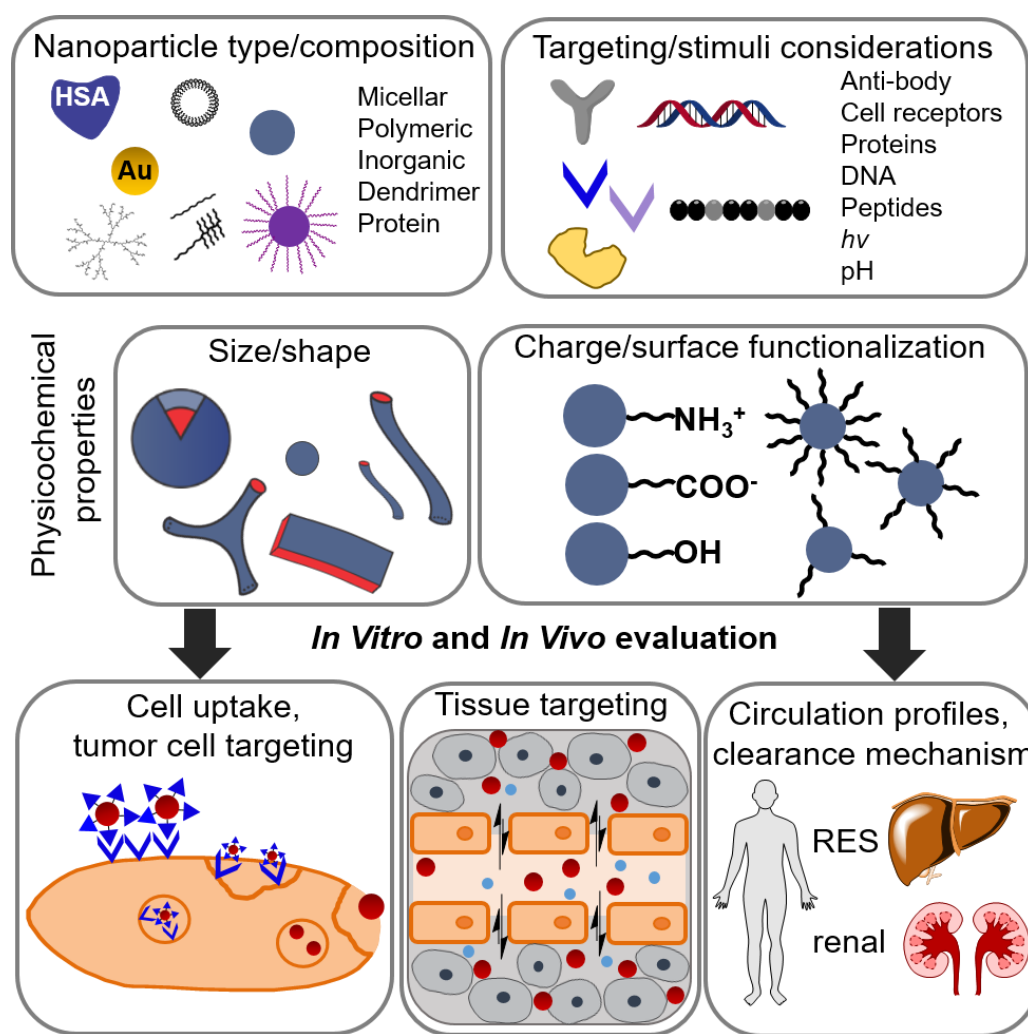


Figure 1.1 Considerations of Nanoparticles for Nanomedicine. Many of these considerations are discussed throughout this dissertation, with focus on polymeric nanoparticle shape on *in vivo* circulation profiles and tumor targeting.

Successful use of NPs for cancer therapy stems from physicochemical properties specific to the nanoscaled material. These properties target nanoparticle delivery to tumor tissue, locally delivering cytotoxins or imaging agents. The Enhanced Permeability and Retention Effect (EPR) describes the apparent accumulation of macromolecular species in tumor tissue and nanoparticles are ideally situated as objects subject to this phenomenon. However, the translation of this effect in humans has limited the large-scale use of NPs in nanomedicine applications.

The challenges to the clinical use of NPs prompts investigation of other modes of drug delivery. Using an endogenous drug delivery system that takes advantage of naturally evolved biological systems presents an intriguing and successful way to formulate small molecule and peptide medicines. Drug delivery involving human serum albumin, or HSA, has emerged as a promising platform for imparting favorable pharmacokinetic properties on drugs, and in some cases targeted delivery. Covalent or non-covalent tethering to HSA is a clever way to use a long-circulating blood protein to overcome barriers to drug delivery, including solubility, enhanced blood circulation times, and non-desired immune response.

1.2 Considerations for Nanomedicines

1.2.1 The EPR Effect

The Enhanced Permeability and retention effect (EPR), coined by Matsuma in 1985, describes the preference of macromolecular or nanoscaled species like polymers and protein conjugates to accumulate in tumor tissue compared to normal tissue.⁶⁻⁸ The macromolecular targeting effect is attributed to the abnormal vasculature of the tumor and poor lymphatic drainage. The angiogenesis of new, leaky blood vessels in tumors is described thoroughly in the literature^{7,9}; leaky tumor vessels in tumor tissue contributes to the enhanced permeability of the vasculature to macromolecular species. The compromised lymphatic drainage in tumor

contributes to the enhanced retention of large species, which are not subject to the diffusive properties that small molecules exhibit. Combined with the advantages that a high molecular weight (MW) species offers in terms of increased blood circulation times compared to small molecules, nanoparticles loaded with drugs offer many advantages in the drug delivery field.

The advantages of nanoscaled accumulation in healthy versus tumor tissue is highlighted in Fig. 1.2 on the most simplistic level *via* the EPR effect. In healthy tissue (1.2a), small molecules and even small NPs may penetrate the extracellular space; through lymphatic drainage or diffusion, the materials are readily cleared from the tissue. Accumulation of small molecules or NPs in healthy tissue is an off-target effect, and is a negative aspect of small molecule therapeutics and nanoparticle delivery systems. In tumor tissue, the endothelial layer is leaky (1.2b), and small molecules and nanoscaled objects readily cross in to the extravascular space. Small molecules can diffuse out of the tissue, while NPs are retained and accumulate in the extracellular space. Further cell-specific targeting is described in Fig. 1.3.

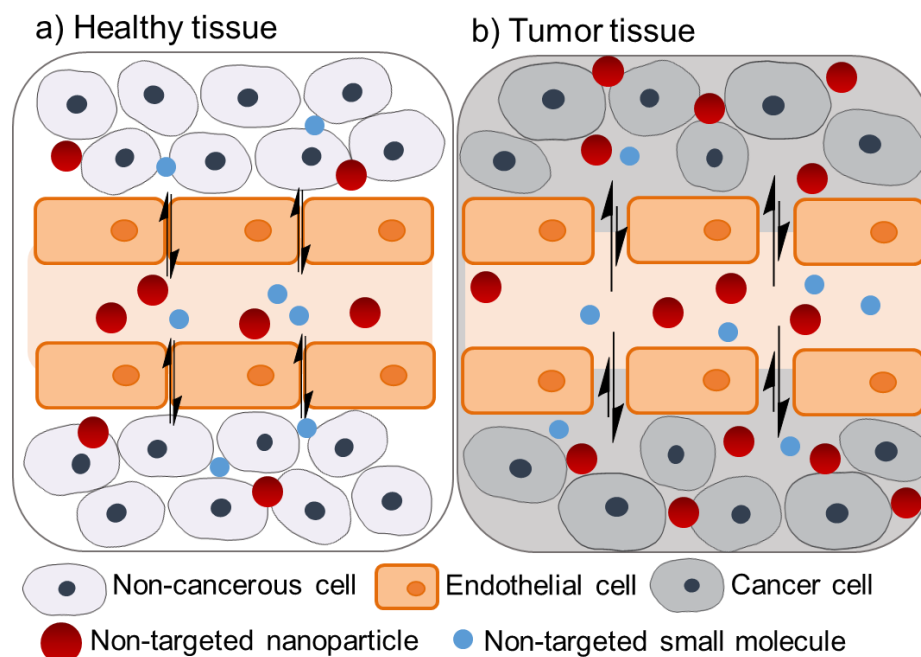


Figure 1.2 Small molecule and nanoparticle accumulation in healthy versus tumor tissue.

Though the EPR effect continues to be cited as the mechanism of accumulation of NPs and other macromolecular materials at tumor sites,^{10–14} critical reviews of nanoparticles for drug delivery argue that many claims of NP targeting are overstated and oversimplified. The attribution of targeting via the EPR effect does not translate as a targeting mechanism in humans.^{15–19} Further, the degree of leakiness in tumor endothelium and lymphatic structure is not uniform, and depends on the disease type, stage/progression, and site.^{7,9,18–20} In addition the tumor microenvironment is highly heterogeneous and varies from cancer type to cancer type affecting things like diffusivity of particle through the extravascular space (penetrating versus remaining on periphery²¹), and interactions of the NP with cellular targets.^{7,22,23} While genetic profiling of patients and tumors is paving the way for personalized medicine and tailoring of nanoparticle to a specific disease profile, tumor microenvironments can vary greatly across patient populations, even in the same disease state. It is not surprising, then, that NP therapeutics designed to accumulate based on the EPR effect have varying degrees of efficacy. A recent meta-review of nanoparticle targeted delivery reveals that a median of 0.7% of an injected NP dose reaches a solid tumor; this number accounts for particles of different sizes, shapes, charges, and compositions, employing active or passive targeting strategies.²⁴ There remains a need for a better understanding of nanoparticle interactions in the highly complex *in vivo* environment in order to better engineer materials for efficient and effective therapeutic and diagnostic delivery.

There is a tremendous interest in utilizing the capabilities researchers have for precise execution of NP design, and away from abstract, passive targeting effects (e.g. EPR) that seem to only be relevant in murine models.^{24,25} Further, it is argued that the EPR effect is not a targeting mechanism, but rather reflects the normal flow and diffusion of molecules throughout and out of the blood stream. The EPR effect should not be relied on for sufficient accumulation at tumor target sites. To reach the next generation of ubiquitous NP efficacy in targeted

delivery, a more robust understanding of the physicochemical properties of NPs leading to their accumulation in a target site must be realized.

1.2.2 Nanoparticle Physicochemical Properties

A key research focus in applying nanoparticles for drug delivery is in understanding physicochemical properties affecting *in vivo* fate and designing NPs within those constraints, tailored to the application.²⁴ Many publications studying nanoparticle targeting convey that the physicochemical properties of NPs, including size, shape, charge, and surface functionalization, can dictate the materials' pharmacokinetic (PK) and pharmacodynamic (PD) properties. Most studies of NPs for *in vivo* applications address at least one aspect of the physicochemical property that leads to its success.^{17,22–24,26–36} Though individual studies and reviews indicate trends in favorable physicochemical properties of nanoparticles, no set design principles have been established in the preparation of NPs for all applications.³¹ There is no single property that overrides all other with regards to dictating *in vivo* PK/PD, highlighting the fact that nanoparticle systems are a multi-leveled, synergistic systems, with relatively unpredictable behavior *in vivo*. Furthermore, studies sometimes show contradictory conclusions with regards to the importance of physicochemical characteristics. Opposing conclusions may depend on the strategies used to evaluate nanoparticle efficacy, or the *in vivo* model employed. Overall it is difficult to make definitive trends or claims because of multiple changing factors per iteration of material, as well as variability in material, tumor microenvironment, and animal model tested. Herein, key examples highlighting the importance of physicochemical features are described, with an emphasis on nanoparticle shape.

Size Effects

Nanoparticle size affects extravasation, targeting in tumors, blood circulation time, and clearance mechanism.^{29,30,36} The size of a nanoparticle is important when considering

extravasation in leaky tumor vasculature, which has limits on fenestration size. In compromised endothelium of tumorigenic tissues, nanoparticles up to 200 nm, and even up to 2 μm may diffuse in to the interstitium.^{7,16} Smaller particles may accumulate and penetrate the tumor more effectively, whereas larger NPs may retain in the tumor longer, an artifact of the retention part of the EPR effect, attributed to poor lymphatic drainage of tumors.¹⁶ Studies have tracked the effects that small changes in size have on tumor accumulation: smaller NPs (2-3 nm) accumulate faster, penetrate the tumor better, but diffuse out of the tissue, compared to 25 nm NPs which demonstrated greater accumulation but were limited in distribution in the tumor.²¹ In other cases, NPs of different sizes (30, 50, 70 and 100 nm) circulate in the bloodstream on the same order, and diffuse at a similar extent through hyperpermeable tumors such as murine colon adenocarcinoma. In models like human pancreatic adenocarcinoma that are less permeable, only NPs less than 70 nm penetrate and accumulate tumor tissue.³⁷ These select examples demonstrate that a range of NPs may be appropriate for *in vivo* applications, but the effects may be countered by other physicochemical parameters and the heterogenous tumor microenvironment.

Another artifact of a NP's size is the effect on the cell uptake pathway: specifically, larger NPs greater than ~500 nm to micron-scaled nanoparticles will be phagocytosed, while subtle changes in NP size can affect endocytotic uptake mechanism.^{38,39} These are important considerations when therapeutic targets are inside the cell, and when aiming to avoid macrophage uptake.

Perhaps the most important aspect of size is the inherent increased molecular weight, resulting in NPs with extended circulation time, and a shift towards clearance via the reticuloendothelial system (RES). Low molecular weight small molecules and small NPs < 5-10 nm are rapidly cleared from the blood stream via the kidney (renal clearance).^{30,36} Very large NPs (> 1 μM) are opsonized and readily taken up in the RES system (liver, spleen). NPs on the

order of 20-200 nm represent a good range of target size as these will circulate in the bloodstream for a while, and have favorable sizes for extravasating in tumor tissue.

Shape Effects

A drastically under-utilized property of nanoparticles for *in vivo* applications is the shape, geometry or morphology. It is generally accepted that cylindrical NPs, or those with higher aspect ratios than spheres, exhibit good tumor targeting while evading premature clearance. Other less common morphologies, such as rods and bicompartamental micelles, are less studied *in vivo*. Admittedly, studying shape effects of polymeric NPs is challenging due to the difficulty of predictably preparing these materials *via* self-assembly processes, and compounded by the fact that changing one variable (e.g. shape) also changes other variables (size, overall charge). This offers an aim for future studies, and a motivation for the research in this thesis.

A number of studies highlight the importance of particle shape/geometry, either on its own or in conjunction with other physicochemical parameters (size, charge), with regards to *in vivo* or *in vitro* effects (e.g. cell uptake).^{28,33,34,40–44} Some key studies highlight the advantages of high aspect ratio nanoparticles over spherical counterparts with regards to tissue targeting and cell uptake. A prominent example from the Discher group evaluates the prolonged circulation time of biodegradable filomicelles compared to stealth-like spherical nanoparticles; the filomicelles circulate up to a week post injection, accumulate in a tumor, and evade RES uptake.^{45,46} Colleagues in the Sailor Lab at UCSD have systematically evaluated advantages of dextran-coated iron oxide nanoworms for tumor targeting. The nanoworms target tumors better than spheres, with neutral peptide targeting moieties and poly(ethyleneglycol)-linkers aiding in favorable circulation times and multivalent interactions with the tumor target.^{40,47}

With regards to cell uptake effects, many studies have found a positive correlation between high aspect ratio particles and greater uptake *via* endocytosis, with some dependence on material composition. For example, mesoporous nanoscaled particles with an aspect ratio of two are internalized faster and to a greater extent than longer or shorter rods.^{48,49} Templated, rod-like NPs were taken in to HeLa cells faster and to greater values compared to micron-scaled particles, or their spherical counterparts.²⁷ The Mitragotri group showed that macrophage phagocytosis of large nano- or microparticles depends on both the shape of the particle and the contact angle; rod-like particles approaching on the short axis are more readily phagocytosed compared to approach on the long-axis.^{39,50}

Overall, cylindrical, worm-like, or NPs with aspect ratios greater than one hold promise for more efficient NP drug delivery carriers based on their prolonged circulation times, ability to evade RES uptake, and flexibility. The multivalency of less-curved surfaces allows for more favorable interactions with the NP surface, an especially important point when incorporating targeting moieties.

Surface Functionalization and Charge

As alluded to above, charge and surface chemistry are important when it comes to how an organism interacts with the NP. Surface functionality may include PEGylation, a strategy often employed for both solubility and stealth-like properties to evade protein opsonization and RES uptake.

Though incorporating positively charged moieties is a useful tool for internalizing materials in to cells,^{49,51} cationic charges can have detrimental effects on systemically introduced NP solutions. Positively charged NPs are more likely to induce an inflammatory response than negative or neutral particles,³⁸ and can have hemolytic/cytotoxic properties, in addition to high RES-uptake.⁵² Interestingly, highly negatively charged NPs also demonstrate

high levels of accumulation in the liver, though not as high cytotoxic properties.⁵² These observations indicate that charged species encourage unfavorable interactions with *in vivo* components like blood proteins and macrophages.

Examples demonstrating the importance of charge is highlighted by studies investigating the charge effects on dendrimer NP in biodistribution patterns. Small dendritic NPs (G4 and G7-PAMAM) around 8-10 nm with cationic charge show greater accumulation in the liver compared to the kidney, and compared to neutral or negatively charged counterpart, despite their small size.⁵³ In another example, cationic, PEGylated particles displayed hemolytic activity and toxicity in cultured macrophage cells.⁵² *In vivo*, the PEGylated NPs with either highly positive or highly negative charges demonstrate a high degree of liver uptake, whereas particles with a slightly negative charge evaded RES uptake and instead accumulated at the tumor.

1.2.3 Active Targeting

Strategies to incorporate targeting moieties such as antibodies or cell penetrating peptides are meant to target NPs to specific cell receptors or extracellular markers at the site of interest (Fig. 1.2). This in turn leads to greater accumulation than effects from macromolecular accumulation due to poor lymphatic drainage. However, clinical translation of active targeted NPs has been minimal.^{7,30-32} Another approach to actively targeting NPs is to incorporate stimuli-responsive units, where stimuli can be light, a change in pH or specific enzymes.³¹ The Gianneschi lab has an interest in using enzymatic stimuli, specifically enzymes that are associated with cancer, in a platform coined enzyme-directed assembly of nanoparticles at tumor (EDAPT). Matrix metalloproteinases (MMPs) are extracellular matrix proteins involved in matrix remodeling, and have long been studied as target biomarkers for drug delivery materials.⁵⁴⁻⁶² In the Gianneschi Lab, peptides designed to be recognized by MMP-2/9

enzymes, which are known to be upregulated in cancers and heart tissue post-myocardial infarction (MI), are incorporated in to a polymer backbone. Upon self-assembly in buffer, the peptides are displayed upon the corona of the NP, accessible to enzymatic processing. Fluorescence-resonance imaging transfer (FRET) dye-pairs rhodamine and fluorescein are incorporated to track NP circulation *in vivo*. When recognized by the enzyme, the sequence is cleaved, disrupting the hydrophobic-hydrophilic interactions of the assembly, resulting in a microscaled aggregate which retains in the tissue and exhibits a unique FRET signal. Accumulation of material in the tissue confirmed via *in vivo* imaging⁶³; further, super-resolution fluorescence microscopy (stochastic optical reconstruction microscopy, STORM) confirmed that the aggregates of NPs accumulate in tissue, and not an accumulation of spherical particles.⁶⁴ EDAPT's effectiveness has been demonstrated in the delivery of enzyme-responsive therapeutic compound-carrying NPs in cancer or MI animal models.^{65,66}

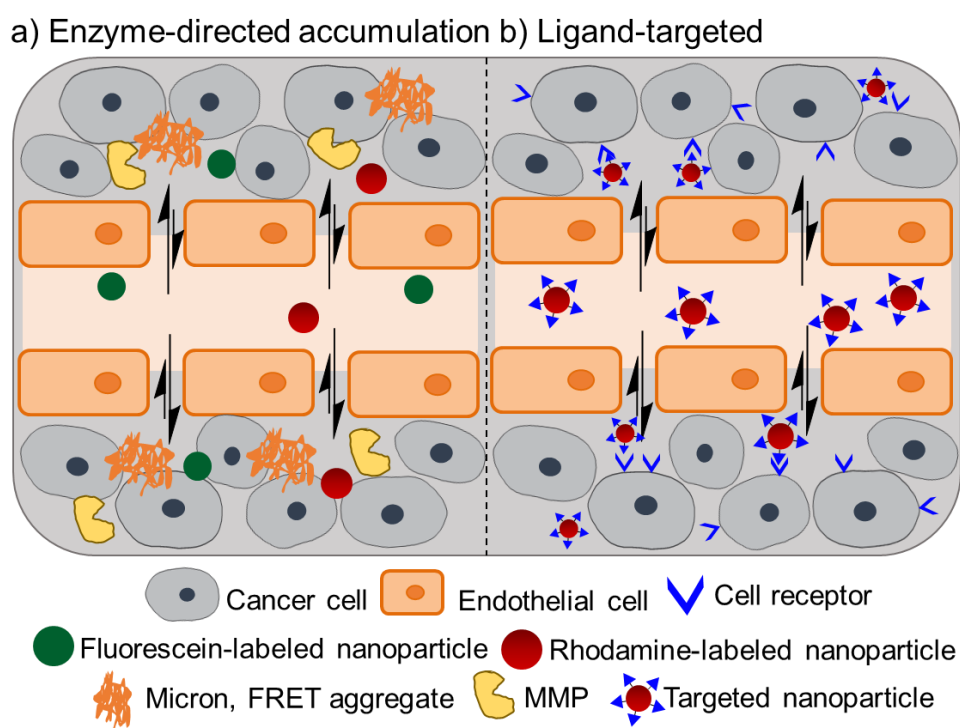


Figure 1.3 Active targeting of Nanoparticles to tumor tissue.

1.2.4 Challenges to Studying Nanoparticles in the Lab

Another aspect of clinical translation involves the process by which novel NPs are developed and tested in the lab. In the lab, toxicity and cellular targeting are evaluated *in vitro* using high through-put assays. Pharmacological parameters of absorption, deposition, metabolism and elimination are performed *in vivo* to determine toxicity and efficacy. Identifying *in vitro* and *in vivo* preclinical models that indicate potential for success of a nanotherapeutic is crucial.⁵ Cultured cells for *in vitro* screens is a reasonable and telling way to identify intracellular targets and efficacy, and is the standard used by the National Cancer Institute to evaluate toxicity of new compounds.⁵ However, these cells are typically grown in monolayers, in isolation, with optimized media and growth conditions and is thus not representative of the highly heterogeneous tumor microenvironment. *In vivo* xenograft models of human cancers are established and ubiquitous methods to evaluate efficacy across the spectrum of cancer cells, either cultured or from patient biopsies. For the most part, preclinical translation to humans reflects efficacy in xenograft models when the same cancer type is evaluated, while the response is not as strong when different cancers are evaluated.⁵ Nonetheless, cancer is a heterogeneous disease, and cells and mice grown in controlled environments are simply experimental vessels.

1.3 Polymer Amphiphile Self-Assembled Nanoparticles

Controlling a self-assembled nanoparticles' physicochemical properties offers a good starting platform for tailoring NPs to the intended target. However, as alluded to above, control over the self-assembly process in terms of predictability of a nanostructure "product" is not ubiquitous. The ability to have predictive control over NPs structure, particularly shape, motivates the next section of this introduction.

Two strategies towards preparing discrete NPs with specific physicochemical properties and functions employ either a bottom-up approach or top-down methodology. Bottom-up approaches include self-assembly of molecules, synthesis of macromolecules, or preparation of inorganic nanoparticles. The self-assembly approach is favorable in the number of parameters tailorable towards the scientist's application, encompassing atomic- and molecular-level control.⁴² Self-assembly approaches are inspired by nature, where molecular self-assembly is responsible for creating hierarchically ordered composite structures with exquisite control and function.^{43,67} In contrast, templated NP preparations or top-down approaches are also widely used in nanoparticle applications due to their ability to prepare well-defined and complex structures with excellent control. Common top-down approaches include particle replication in non-wetting template (PRINT®),^{27,68} elastic stretching of spherical particles,^{39,50} step-flash imprint lithography (S-FIL, Molecular Imprint®)⁶⁹ and template-induced printing (TIP).⁴²

The strategy of choice in this work is to use amphiphilic block copolymers in a bottom-up approach to self-assembled NPs. This approach allows for many opportunities to control the outcome of self-assembled polymeric NP, which fall in to two inherently interrelated categories: control in polymer synthesis and architecture, and control in the self-assembly process.

1.3.1 Theories on Self-Assembly

Theories of self-assembly establish that assembled nanoparticle structures are dependent on the volume ratio of the blocks and the packing parameter of unimers. The spontaneous formation of ordered macromolecular surfactants relies on favorable hydrophobic interactions in the core, interplay between corona and core, and corona solvation of core and repulsion of strands.^{70,71} The morphology a nanoparticle adopts depends on these interactions,

and can be affected by parameters such as polymer chemical structure (e.g. change in molecular weight and block ratios of polymer) and environmental factors like solvent conditions during assembly.¹³ Nanoparticle geometry is dictated by the packing parameter (p) of the polymer components, which is in turn determined by volume (v) and length (l) of hydrophobic block, and interfacial area per molecule (a) according to the equation $p = v/(al)$.^{43,70,72} For $p < 1/3$, spherical micelles are the predicted nanoassembly, $1/3 < p < 1/2$ for cylindrical micelles, and $1/2 < p < 1$ for bilayers. For the surface area a , the optimal interfacial area is not a geometric area, but a thermodynamic value determined from equilibrium.⁷² Therefore, the polymer chemical structure dictates the constraints of possible, thermodynamically stable geometries (parameters volume and length above), while the process of self-assembly can be used to modulate polymer interactions and block solubility affecting interfacial surface area. Taking advantage of the self-assembly process can lead to kinetically “trapped” structures that are locally stable, perhaps even for months, unless perturbed by outside parameters. Some block copolymers (BCPs) are thus nonergodic: the self-assembly pathway selected results in many kinetically trapped structures from one polymer, and these structures may or may not be the most thermodynamically stable species.^{73,74} Nonetheless, it is clear that polymer structure and pathway of assembly may be optimized to prepare nanoparticles of tailored morphologies for optimal performance in the desired application. Over the years, many groups have studied the assembly processes of BCP towards understanding these parameters.

1.3.2 Experimental Investigations of Polymer Self-Assembly

Understanding, predicting, and controlling the self-assembly process of organic polymers in aqueous environments is of utmost importance as polymeric NPs become more prevalent for applications in areas like drug delivery. Polymer self-assembly has been studied by many research groups of different disciplines over the last few decades.^{43,73–95} From these

studies, trends and key observations on controlling the assembly of polymers in to discrete and interesting NP architectures has been observed. Eisenberg and coworkers, for example, have studied crew-cut BCPs (in which the core block is greater than the corona block) and the many morphologies of NPs they can take, including spheres, rods, vesicular, lamellar, large compound-micelles, bicontinuous micelles, and other inter-connected or network like bilayer structures.^{78,81} These studies investigate both polymer structure effects on NP self-assembly, and modulators of the self-assembly process.⁸² A general trend is seen with varying ratios of hydrophilic-to-hydrophobic block: as the weight percent of hydrophilic portion increases, NPs trend towards higher curvature assemblies, e.g. spheres. Specifically, study of the assembly of polystyrene-*b*- poly(acrylic acid) polymers shows that as acrylic acid (hydrophilic) content is decreased, aggregate morphology goes from spheres to cylinders, bilayer morphologies (lamellar and vesicular) and compound micelles.⁷⁸ In a set of comprehensive studies by the Bates group, a phase diagram for a set of PS-*b*-PEO BCPs was established.^{84,85} By systematically varying the ratio of hydrophilic to hydrophobic blocks, and overall polymer MW, self-assembled nanostructures were surveyed. Again, the trend of higher weight ratios of hydrophilic blocks favoring formation of high curvature spheres was observed. The exact weight ratio required to form spheres versus cylindrical versus bilayer structures was dependent on the polymer chemical identity.^{84,85}

Complicating effects of polymer architecture on self-assembly structure, parameters such as solvent selection, electrolyte additives and temperature can affect the morphology of an identical polymer chain.^{74,83} For example, a polystyrene-*b*-poly(ethyleneoxide) (PS-*b*-PEO) BCPs assembles in to lamellar structures under one solvent condition, but upon adding salts, the assemblies are large compound vesicles. Assembling the polymer at sub-ambient temperatures also favors bilayer aggregates like large compound vesicle (LCV), compared to

rod-like or lamellar structures when assembly occurs at room temperatures.⁷⁴ These studies show both how polymer structure and solvent conditions can lead to various NP structures.

1.3.3 Kinetic and Thermodynamic Equilibria in Polymer Self-Assembly

Many self-assemblies of soft materials are often found as mixed-phases, evidence of the delicate balance of kinetic and thermodynamic properties in forming stable nanoscaled aggregates. For example, in the Bates study, uniformed phases consisting of cylinders only existed in a narrow window, and were often found as mixed phases with spherical structures.⁸⁵ The importance of thermodynamic or kinetic control in NP self-assembly are investigated alongside the above described studies looking at final nanostructure morphology. Eisenberg studied the thermodynamics of micelles in mixed solvent systems for various polymer architectures.⁸² In aqueous conditions, BCP assembly is a balance of entropic penalties and enthalpic- favored interactions: under experimentally investigated conditions, low weight % water solvent mixtures had negative enthalpies, overcoming negative entropically unfavorable events to form defined assemblies. Here, hydrophobic block solubility drives the micellization, whereas the hydrophilic block is not as important. As water content increases, solubilizing of the hydrophilic portion and entropy is more important for micellization. There is a critical water content value necessary for BCPs to assemble; exact values will depend on the polymer system and solubility in the solvent mixture.

Detailed studies highlight the importance of kinetic and thermodynamic equilibria in polymer self-assemblies. An advantage of using large MW amphiphiles as opposed to small molecule surfactants is the ability to kinetically trap structures that are not at the globally most stable conformation. Two kinetic processes contribute to stable macromolecular assemblies: the fast, intramicellar chain rearrangement as a solution reaches a critic water concentration for aggregation, followed by slow chain exchange kinetics of individual polymer strands towards

reaching a thermodynamically stable assembly.⁷⁶ The hydrophobic effect drives the former, fast process, wherein the insoluble block immediately aggregates to a conformation that minimizes interactions with the poor solvent. The second step, wherein unimer (polymer) exchange occurs, is very slow due to the relative stability of the already existing nanoassembly, and the high energetic penalty for exchange or global rearrangement, leading to mostly frozen structures. Though these initial assemblies may not be the most thermodynamically stable nanostructure possible based on packing parameter considerations, they can be stable up to months after formation,^{86,87} and are thus referred to as kinetically trapped structures. Researchers highlight the value of trapping complex structures by using the process of assembly to exhibit kinetic control over micelle assembly.⁷³ In a detailed study by Epps and coworkers,⁹² the kinetic formation and stability of a polymeric NP in mixed solvent environment (0-50% tetrahydrofuran in water) was evaluated. After formulating spherical NPs, the structure was allowed to equilibrate to its thermodynamically favorable state. Over several weeks the authors observed a change in morphology to larger spheres as the amphiphilic polymer unimers rearranged to a more thermodynamically stable structure. In other studies, solvent selection was used to kinetically trap non-thermodynamically equilibrated structures like complex dislike micelle, demonstrating the idea of BCP nonergodicity.^{73,87} These studies, among many others in the literature, indicate that solvent selection and processing of polymer amphiphiles, including dynamics of assembly, are important considerations towards reaching kinetically or thermodynamically stable nanoparticles.

1.3.4 Polymer Architecture for Self-Assembly

It is apparent that the polymer architecture, can play a role in polymeric self-assembly towards distinct NPs. There are numerous polymerization methods that can yield desired polymer architectures with good control. These methods including reversible addition-

fragmentation chain transfer (RAFT), ring-opening polymerization (ROP), atom transfer radical polymerization (ATRP), anionic polymerization and ring-opening metathesis polymerization (ROMP), among others.^{89,96} Studies of polymer amphiphiles obtained from ROMP are of particular interest because of the range of functional groups amenable to the technique and low dispersity of resulting polymer, stemming from living polymer growth mechanism.⁹⁷

ROMP enables preparation of functional block copolymers BCPs via graft-to, graft-through or graft-from approach. The Gianneschi lab primarily uses ROMP towards polymeric NPs in graft-to and graft-through approaches. In a graft-to approach, a conjugatable monomer unit is polymerized in to the polynorborne BCP scaffold, followed by post-polymerization reaction with a functional unit to achieve the desired BCP. In the graft-through approach, functional monomers are first prepared, then polymerized, with the resulting BCP amphiphile ready for micellization. The functional group tolerance of ROMP extends to various hydrophobic and hydrophilic moieties, conjugatable units, a range of fluorescent and quencher dye molecules, magnetic resonance imaging agents (MRI) and biomolecules, facilitating preparation of highly functional and useful polymeric materials.^{98–100} An overview of polymeric NPs from polynorbornene polymers is described elsewhere,⁸⁹ with some key examples highlighted here. Carrillo and Kane tuned NP size by controlling the composition of the BCP: as overall polymer MW increased, NP size similarly increased.⁹⁰ Another study looked at the effect of polymer architecture on self-assembly, finding that BCPs more readily formed spherical micelles in an organic solvent mixture compared to blended copolymers.⁹¹ In a systematic study of ROMP a hydrophilic-to-hydrophobic block ratio and overall polymer MW were varied to investigate micelle formations effects.⁹³ When the block ratios were fixed at an equal-block ratio and the overall MW varied, micelle size increased with polymer size. When the overall block length was kept constant, and the block ratio was varied, micelle size

was constant, while the core size decreased correlating with decrease in hydrophobic block length. A comprehensive and systematic study of polymer effects on micelle assembly was carried out in the Gianneschi lab to establish phase diagrams for polynorbornene structures of interest.⁷¹ In a similar method to Bates,⁸⁵ hydrophilic-to-hydrophobic block ratios were varied, along with polymer MW (low and high degrees polymerizations) and identity of chemical functionality used as the hydrophilic molecule. As higher weight fractions of hydrophilic portion were prepared, spherical nanoassemblies were observed. However, the phase diagram and regime of morphological distribution was highly dependent on the hydrophilic functional group, indicating that solvation of the corona and repulsive forces of charged functional groups are critical. Larger MW polymers did not see the diversity in morphologies as the lower MW polymers did. Similar to other studies investigating kinetically trapped nature of some polymer self-assemblies, some polymers assemble in to different structures depending on the process, or solvent, used during micellization. In all examples in this study, the hydrophobic group is kept constant (norbornyl-phenyl). In some cases, however, the core group may need to be changed, for example to include a hydrophobic drug moiety.⁶⁵ For example, stimuli-responsive polymeric NPs incorporating peptides or nucleic acids are restricted to architectures where the biomolecule is incorporated as the hydrophilic portion, displayed on the corona of the NP so as to promote interactions with its environment.^{63,101–105}

In this work, there is an interest in using chemical control of polymer synthesis to prepare nanoparticles of discrete and diverse morphologies. By introducing a variety of hydrophobic functionalities, and changing solvent conditions during self-assembly, control over nanoparticle structure was achieved. Building off previous work in the lab, we present new strategies for preparing polynorbornene polymers towards nanoassemblies of diverse morphologies.

1.4 Nanoparticles for *In Vivo* Imaging Using MRI

Nanoparticle (NP) based drugs have reached the clinical mainstream, with established efficacy predominantly in oncology and infectious diseases.^{106–108} There is a growing interest in NPs as carriers of diagnostic agents capable of unique behavior and biodistribution patterns not observed for small molecule analogues.¹⁰⁹ To this end, several strategies for the incorporation of imaging reporters within NPs have been introduced, allowing for NP visualization using, fluorescence,¹¹⁰ ultrasound,¹¹¹ CT,¹¹² MRI,¹¹³ and nuclear imaging.^{113,114} Of these modalities, MRI offers several advantages including exquisite anatomic co-registration with excellent tissue characterization, lack of ionizing radiation, and in general, provides high quality images at clinically relevant imaging depths. In turn, many NP-based MR imaging strategies have been explored using either inorganic^{111,112,115–119} or soft polymeric organic materials as contrast agents.^{120–123}

1.4.1 Molecular Basis for Gadolinium-based T_1 contrast agents

MRI images and signals are generated using similar basic principles to that of Nuclear Magnetic Resonance. A patient is placed in a low-field magnet to align the spin of protons, and radiofrequency (RF) pulses at the resonance frequency of water protons are introduced, tipping the magnetization of protons. As the protons relax back to equilibrium, the longitudinal ($1/T_1$) or transverse ($1/T_2$) relaxation rates are detected, and relative changes in these rates are processed to give a signal strength per voxel to generate an image with precise 3D information.¹²⁴ Contrast in an MRI image reflects differences in relaxation rates of water in different chemical environments. Contrast agents may be introduced to enhance the contrast in areas where the agent is present. Gadolinium-based contrast agents (GBCAs) are T_1 -weighted contrast agents in MRI that provide enhancement by shortening the longitudinal relaxation time of metal-bound water molecule protons resulting in brighter image intensity. GBCAs can affect

T_2 relaxation times as well, but the effect is not as great as that on T_1 relaxation rates. T_2 contrast agents include manganese or iron-based materials, and provide an alternative gadolinium-free drug for patients not eligible to receive GBCA, such as those with impaired renal function.

The effectiveness of a contrast agent is described as relaxivity, with the equation $r_1 = 1/T_1$, where $n = 1$ for longitudinal relaxation times or $n = 2$ for transverse relaxation. Relaxivity is normalized to concentration of contrast agent with units in $\text{mM}^{-1}\text{sec}^{-1}$. The gadolinium (III) ion on itself is toxic, and therefore must be sequestered with an organic chelate. Typical gadolinium chelating agents are octadendate ligands consisting of amine and oxygen binding moieties to the metal center, leaving 1 open site for a water molecule to bind to gadolinium, and can be macrocycles or linear.¹²⁵ The metal-ligand complexes exhibit very high thermodynamic equilibria (stability), as well as low kinetics of ligand exchange.¹²⁶ Despite the relative chemical inertness at neutral pH, in acidic conditions, ligands can be labile due to proton-associated dissociation, leading to instability of the metal complexes; linear chelates are more susceptible to this dissociation compared to macrocyclic ligands.¹²⁶ The gadolinium-chelate circulates in the blood stream as the Gd-L complex, thus obviating any negative interactions of the gadolinium ion in physiological processes or deposition *in vivo*.¹²⁵ Select examples of clinically approved GBCA are depicted in Fig. 1.4.¹²⁵

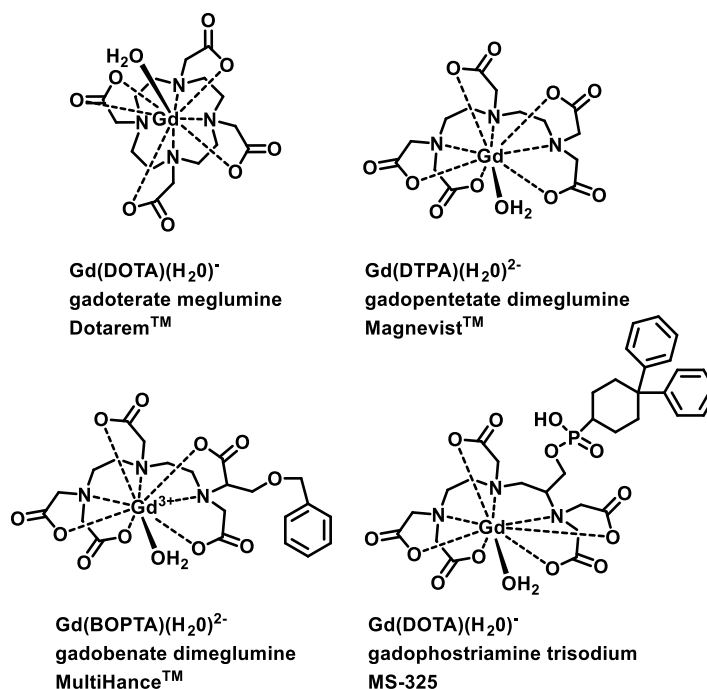


Figure 1.4 Clinically approved small molecule gadolinium based contrast agents.

The molecular basis driving relaxivity enhancements with GBCA stem from the paramagnetic contributions of the gadolinium-based molecule. Water molecules can interact with the Gd-chelate either through an inner sphere mechanism (the water molecules interacting directly with the metal) or second-sphere mechanism (bulk water exchange) (Fig. 1.5). The inner sphere contributions to relaxivity are predominant, and are described in equation 1 as¹²⁷:

$$\text{Equation 1: } r_1(\text{IS}) = q / [\text{H}_2\text{O}] / (T_{1m} + \tau_m)$$

where the q value is the hydration number, or number of water molecules bound to Gd; T_{1m} is the relaxation time of the water and τ_m is the water residency time (time spent bound to Gd). To increase relaxivity, then, one would aim to increase the q value, or decrease T_{1m} and τ_m . For examples highlighted in Fig. 1.4, q is 1. To increase q , a different type of ligand is required, with less than eight ligand sites, while maintaining appropriate thermodynamic stability and kinetic inertness. One such example is the hydroxypyridinonate (HOPO)-ligands developed by

the Raymond group.¹²⁸ To decrease the water relaxivity and residency times, there are many factors to consider. The derivation of these factors are discussed elsewhere¹²⁷ and depend on the field strength and the nature of the chelate (which can promote water exchange or alter the radius of Gd-water interaction).

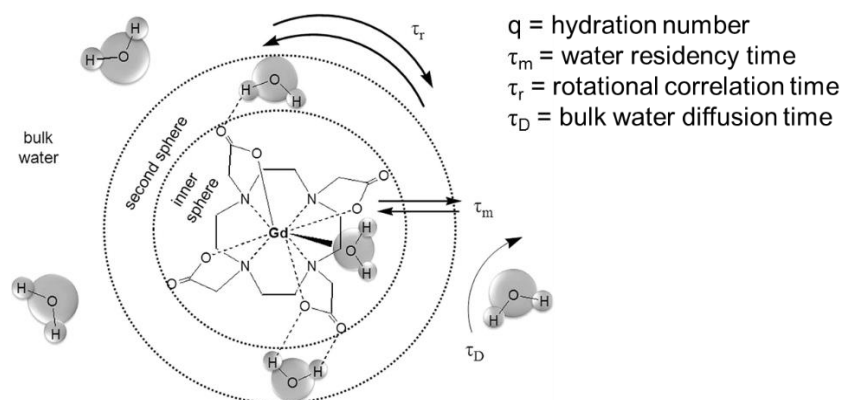


Figure 1.5 Molecular parameters of GBCA interacting with water to enhance relaxation time and contrast. Adopted with permission from Ref. 129, Copyright 2012 American Chemical Society.

Another approach to increasing relaxation rate is in altering the rotational correlation time (Fig. 1.5). The relaxation time of water is dependent on field strength, radius of the Gd-H(water) bond, and rotational correlation times τ_c . Rotational correlation time τ_c is dependent on the water residency time τ_m (the inverse of which is the water exchange rate, k_{ex}), the rotational correlation time τ_R and the electronic relaxation time T_{1e} . Conceptually, this means that coupling the Gd-L to a slow-tumbling macromolecule could significantly increase the relaxation time. Or, in another strategy, the ligand could be modified to shorten the radius of interaction between Gd-water or promote faster chemical exchange of water molecules in the inner sphere. Nuclear magnetic resonance dispersion (NMRD) profiles of clinical GBCA demonstrate that at clinically relevant field strengths, 1.5 T, rotational correlation time is most important for increasing relaxivity; Gd species whose diffusion rates are coupled to macromolecules demonstrate increases in relaxivity experimentally.¹²⁷ Further, simulations of

relaxivity for slow tumbling (10 ns), intermediate (1 ns) and fast (0.01 ns) rotation illustrate the field-strength dependence of relaxivity for different categories of contrast agents (Fig. 1.6). Although slow tumbling species (10 ns) model as very high-relaxivity species at low field strength, at higher field strengths there is no advantage of the macromolecule over a small molecule. The intermediate and small molecule species show stable relaxivity across field strength, with a small molecule having a lower relaxivity. This is important when thinking about designing the next generation of contrast agents for clinical translation: as technology has improved, clinics are moving towards higher field strength magnets. At the higher fields, GBCA appended to macromolecules may not provide the best results. Designing contrast agents for the future should address the variable relaxivities of these agents, and be tailored for specific applications.

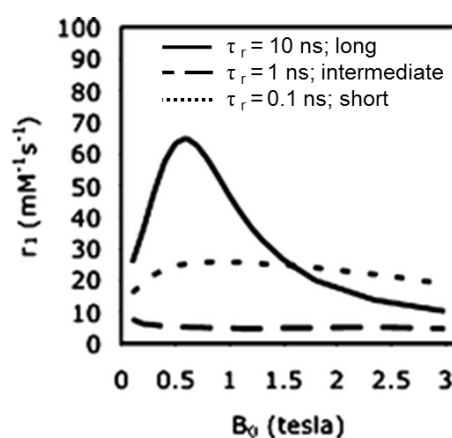


Figure 1.6 Effect of rotational correlation time on relaxivity at different field strengths. Reproduced from Ref. 127 with permission from The Royal Society of Chemistry.

Because of the vast improvements that slowing the rotational correlation time of a GBCA can have on the relaxivity, macromolecular, or NP-based contrast agents have been postulated as superior contrast agents for MRI based on the underlying physical parameters dictating MRI and high-relaxivity species.¹²⁷ Contrast agents are administered in 30% of scans, and are designed to provide contrast systemically, or at areas of interest. In our research, we

are interested in using MRI as a non-invasive imaging tool with clinical relevance. As such, in Chapter 3, strategies towards directly incorporating a gadolinium-chelate derivative in to a polynorbornene scaffold are described. The relaxivities are described, and *in vivo* imaging performed, demonstrated enhanced circulation times *in vivo* compared to a small molecule counterpart.

1.5 Albumin as a Drug Carrier

In the previous sections, the use of nanoparticles as drug carriers are discussed with regards to the potential use in nanomedicine and targeted drug delivery to tumor targets. While exploration of nanoparticles holds promise, there are still challenges to implementation in the clinic.^{2,4,129} Moving forward with a clinical translation of research in nanomedicines is difficult due to discussed problems associated with efficient nanodelivery, results in animal models, and subsequent translation to humans.²⁴ An alternative approach for drug delivery has emerged and uses an endogenous protein as a drug carrier and delivery vehicle as a simple yet elegant means towards more effective therapies. Specifically, human serum albumin, the most abundant blood protein in human plasma, has been shown to be an effective drug carrier, providing a platform that prolongs circulation of molecules bound to the protein, and offering favorable physiological interactions *in vivo*.^{130–132} This strategy has reached the clinical mainstream with several examples of therapeutic- or diagnostic- agents based on interactions with HSA on the market.^{130,133,134}

Human serum albumin (albumin, HSA), a 66.5 kDa protein, exists *in vivo* at very high concentrations (42-54 g/L), with a half-life of about 19 days.¹³⁵ Albumin has robust stability, is biodegradable and is amenable to covalent or non-covalent modifications for appending bioconjugates or drugs of interest.⁸ Native albumin acts as a carrier of various small molecules in the blood stream, especially hydrophobic molecules (e.g. hormones, fatty acids, and amino

acids) and because it is an endogenous protein, conjugates designed to interact with HSA are non-immunogenic. Successful examples of HSA drug carriers rely on two main features: (1) improved pharmacokinetics due to the extended blood half-lives achieved by hitchhiking on the long-circulating HSA thus allowing the potential for more efficacious drug delivery, and (2) improved targeting to disease targets.

The improvement of blood half-life for small molecules that have fast clearance profiles has been demonstrated for a range of molecules, especially with regards to diagnostic imaging applications.^{134,136,137} The extended circulation of specially designed diagnostic agents in the body can be visualized using a multitude of imaging techniques and offers the advantage of steady state imaging, and visualization of normal or abnormal vasculature. Blood half-life extension in the context of MRI is of interest for a wider window for *in vivo* imaging and clinical translatability. Several examples of gadolinium-based agents designed to interact with albumin have been clinically approved.^{127,134,138} For example, MS-325, gadofosveset trisodium, tradename Ablavar or Vasovist, was approved as a blood pool contrast agent for angiograms in the 2008.^{138–141} The Gd-agent is a diethylenetriaminepentaacetic acid (DTPA)-derivative with a phosphodiester linked bis-phenyl, where the hydrophobic moiety is designed to interact with hydrophobic pockets of HSA (Fig. 1.4).¹³⁴ In addition to enhanced blood circulation times, upon binding to albumin, the rotational correlation time of the Gd-based center is coupled to that of the slower tumbling protein, resulting in an enhancement of relaxivity *in vitro*. Gadobenate dimeglumine (tradename MultiHance),^{142,143} is another clinically approved blood pool imaging agent (Fig. 1.4). The DTPA ligand is modified with a phenyl ring, creating a hydrophobic moiety for interacting with HSA. Upon binding with HSA, relaxivity enhancements are observed, and the blood circulation time is prolonged compared to that of other Gd-based small molecule imaging agents (such as Dotarem). In these two examples, a hydrophobic moiety is installed on a linear Gd-chelate to promote hydrophobic interactions

with an endogenous protein for the purposes of improved blood circulation times, allowing for blood pool imaging applications. Of note is that neither Vasovist or MultiHance have been approved for tumor imaging applications.

Albumin has also been demonstrated to accumulate in tissues with abnormal vasculature or inflammation.^{12,144} In fact, albumin-Evans Blue “nanoparticles” were used by Matsumura and Maeda to describe the EPR effect in the 1980s.⁶ Since establishing that albumin proteins may experience an EPR effect at tumor sites, the protein has also been implicated as catabolites in tumors, an idea that hinges on the fast-growing cancer cells needing a nitrogen source for cell proliferation.^{14–16,131} Additionally, a subset of albumin-binding proteins is attributed to the mechanistic underpinnings for accumulation and efficacy of albumin-based drug carriers. Several albumin-binding proteins have been identified; the discussion here will focus on glycoprotein 60 (gp60), or albondin, and cell membrane receptor and extracellular, secreted protein, acidic and rich in cysteine, or SPARC.

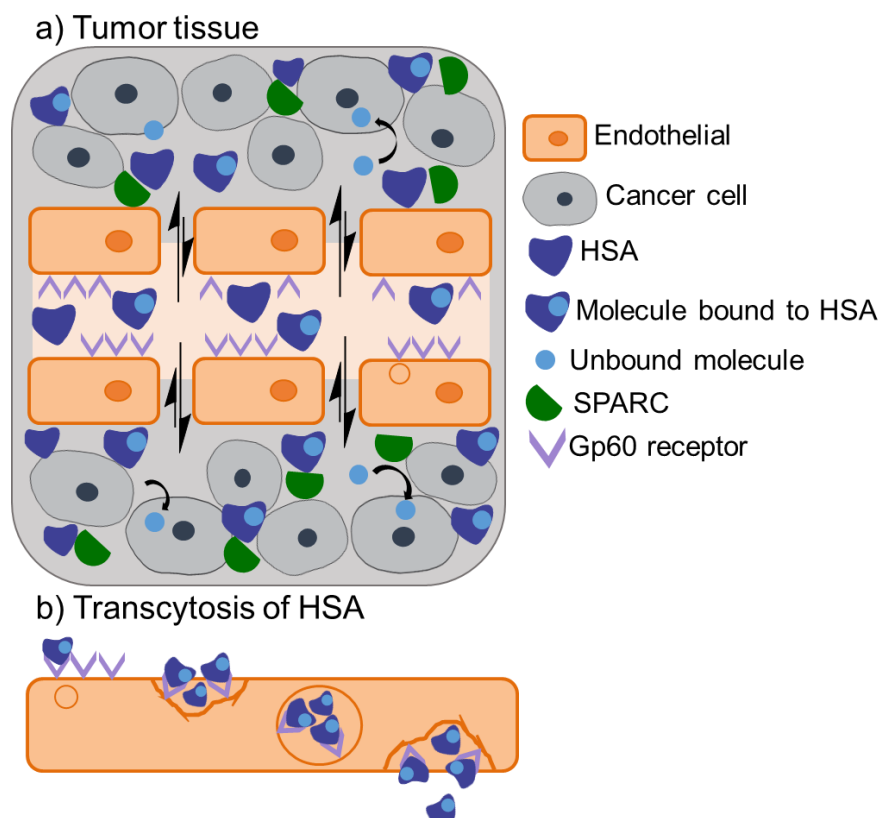


Figure 1.7 Depiction of albumin and albumin-bound molecules accumulating in tumor tissue.

It is understood that gp60, a 60 kDa glycoprotein, localized to the continuous endothelium cell surface, is selective for native albumin and facilitates the transcytosis of albumin from the capillaries to interstitial space.¹³¹ A host of detailed mechanistic studies reveals this receptor-mediated internalization occurs *via* a caveolin-dependent pathway trafficking proteins into the tissue without degradation.^{145–147} Receptor-mediated transcytosis is responsible for 50% of the albumin leaving the vasculature; fluid-phase transcytosis and passage through leaky vasculature (e.g. EPR effect) contributes to the remainder of albumin movement.^{131,145,147} Albumins that are modified or conformationally different are endocytosed by gp18 and gp30 receptors; these protein receptors are not localized to endothelial cells, but found throughout organ tissues, and are specific enough such that they do not recognize competent albumin. Gp18 and gp30 are considered scavenger proteins, and upon endocytosis,

degrade the protein. SPARC proteins are extracellular proteins, and like gp60, selectively bind albumin. It is suggested that SPARC-recognition of the albumin leads to the increased accumulation of albumin in tumor tissue, though there is no direct evidence of SPARC-mediated uptake of albumin in cancer cells. Nonetheless, SPARC shares a similar selectivity for albumin, hinting that the two protein receptors share a similar binding domain, despite extracellular location (SPARC) versus location on endothelial cells (gp60).¹⁴⁸

In addition to endothelial cell receptor gp60 and extracellular SPARC proteins specific for albumin, and gp18 and gp30 receptors for non-native albumin, several other membrane-bound albumin binding proteins have been identified: neonatal FC receptor (FcRn), heterogeneous nuclear ribonucleoproteins (hnRNPs), calreticulin, cubulin and megalin.¹³¹ Of these, hnRNP and calreticulin have been identified from human cancer cell membranes, yet their role in albumin-mediated uptake in tumor cells remains elusive.¹⁴⁹ Countless studies tracking HSA in tumor tissue confirms uptake of the protein in cells, yet the exact mechanism responsible for cancerous cell targeting remains vague; understanding this process is critical for improving cellular targeting of HSA drug carriers.

An illustrative example of therapeutic delivery based on HSA binding is the blockbuster drug Abraxane (ABX). Abraxane is described as a nanoparticle formulation of paclitaxel with HSA, wherein the hydrophobic taxane drug is formulated solvent-free with an endogenous protein. ABX is safer than a clinically comparable formulation of paclitaxel with Cremophor EL allowing for higher, safer dosings, with less side-effects than the formulation compound.¹⁵⁰ Developed by Abraxis and Desai in the early 2000s, ABX was approved for clinical use in 2005, and is now used for a host of indications.^{2,150–154} The mechanism of ABX targeting to tumors is attributed to selective transcytosis of the albumin-bound taxane across the endothelium to tumor tissue, where SPARC recognizes it, facilitating accumulation in the tumor site.^{153,155,156} The role of SPARC in ABX efficacy is highlighted by a clinical study that

showed enhanced efficacy of ABX in tumors with elevated SPARC levels.¹⁵⁷ It is important to note that the interactions between paclitaxel and albumin are non-selective, weak, hydrophobic and non-covalent interactions; nonetheless, the drug experiences advantageous effects from HSA as a carrier in the blood stream with selective accumulation in tumor sites, leading to greater therapeutic efficacy. The targeting effect to tumors of the HSA-drug conjugate is applicable to other therapeutics as well: docetaxel, doxorubicin and methotrexate approved formulations with HSA have demonstrated clinical efficacy.²

While the success of many albumin-carried drugs relies on non-covalent or covalent (not described here) interaction of warheads with albumin, few examples exist where a warhead is modified with a selective-binding moiety. Of the examples described above, imaging agents or therapeutic payloads in MS-325, MultiHance or ABX do not have highly specific binding regions, yet still display efficacy stemming from improved circulation times, and in the case of ABX, enhanced targeting to tumors by HSA. One of albumin's native functions in the body include transport of fatty acids. Detailed protein crystallographic studies demonstrate the specific binding of fatty acids of various carbon lengths in specific binding sites of the protein.^{158–163} This selective interaction of a long chain fatty acid with albumin was harnessed for the clinically approved drug Levemir, developed by Novo Nordisk and approved in 2004.¹³³ Levemir is the albumin formulation of an insulin polypeptide modified with myristic acid (C₁₄). Compared to free insulin, Levemir has increased blood circulation time and is more efficacious.

We were interested evaluating a long-chain fatty diacid, octadecanedioic acid (ODDA, C₁₈) for use in site-specific binding with HSA, and synthetic modifications to append interesting warhead molecules. Stearic acid (C₁₈) was shown to have a binding equilibrium with values ranging from $\sim 9 \times 10^8$ to $\sim 3.5 \times 10^7$ M for the first 5 binding molecules to the protein, with up to 7 molecules binding with the protein.^{160,162,163} Studies specifically investigating diacids, and ODDA, reveal that the diacids bind with albumin on the μ M range, at a lower

molar ratio of about 4 molecules fatty acid to albumin.^{161,164} The binding of long chain lipids is facilitated by a combination of non-polar interactions with hydrophobic binding pockets and cationic residues deep in the binding pocket, leading to electrostatic interactions. In our work, a novel platform technology has been developed, in which an octadecanedioic molecule is modified unilaterally to covalently link a warhead, either a therapeutic molecule, imaging agent, or some other compound of interest. The unmodified free acid remains to bind specifically and strongly with HSA in a reversible manner. Preliminary modeling of a novel ODDA-PTX molecule confirms a strong and specific interaction of the hydrophobic tail, anchored in the binding pockets with electrostatic interactions between cationic amino acid residues and the free acid (data not shown). The long chain FA acts as a means to “piggy-back” on to the endogenous protein, lending favorable blood circulation times and biodistribution. We sought to investigate the platform technology in regards to therapeutic small molecules, therapeutic peptides, and diagnostic/imaging agents.

1.6 Conclusions for Introduction and Dissertation Overview.

As overviewed in Fig. 1.1, there are many variables to consider when preparing nanoparticles for optimal *in vivo* function. This work will highlight characteristics of NPs that are vastly underutilized. Methods towards preparing polymeric NPs in a bottom-up approach to achieve interesting NP morphologies are presented in Chapter 2. Nanoparticles for *in vivo* imaging using MRI are described in Chapter 3. An alternative approach to NP drug delivery using a platform technology for hitchhiking on HSA is presented in Chapter 4. In using two fundamentally different approaches towards nanoparticle delivery to tumor tissue, polymeric and bioconjugate materials are designed and prepared, with evaluation in biological systems.

1.7 References

- (1) Duncan, R. *Nat. Rev. Drug Discov.* **2003**, 2 (5), 347–360.
- (2) Bobo, D.; Robinson, K. J.; Islam, J.; Thurecht, K. J.; Corrie, S. R. *Pharm. Res.* **2016**, 33 (10), 2373–2387.
- (3) Peer, D.; Karp, J. M.; Hong, S.; Farokhzad, O. C.; Margalit, R.; Langer, R. *Nat. Nanotechnol.* **2007**, 2 (12), 751–760.
- (4) Anselmo, A. C.; Mitragotri, S. *Bioeng. Transl. Med.* **2016**, 1 (1), 10–29.
- (5) Damia, G.; D’Incalci, M. *Eur. J. Cancer* **2009**, 45 (16), 2768–2781.
- (6) Matsumura, Y.; Maeda, H. *Cancer Res.* **1986**, 46 (8), 6387–6392.
- (7) Bertrand, N.; Wu, J.; Xu, X.; Kamaly, N.; Farokhzad, O. C. *Adv. Drug Deliv. Rev.* **2014**, 66, 2–25.
- (8) Maeda, H.; Ueda, M.; Morinaga, T.; Matsumoto, T. *J. Med. Chem.* **1985**, 28, 455–461.
- (9) Jain, R. K.; Stylianopoulos, T. *Nat. Rev. Clin. Oncol.* **2010**, 7 (11), 653–664.
- (10) Maeda, H.; Wu, J.; Sawa, T.; Matsumura, Y.; Hori, K. *J. Control. Release* **2000**, 65 (1–2), 271–284.
- (11) Greish, K. *J. Drug Target.* **2007**, 15 (7–8), 457–464.
- (12) Heneweer, C.; Holland, J. P.; Divilov, V.; Carlin, S.; Lewis, J. S. *J. Nucl. Med.* **2011**, 52 (4), 625–633.
- (13) Chen, Y.; Huang, J.; Zhang, S.; Gu, Z. *Chem. Mater.* **2017**, 29 (7), 3083–3091.
- (14) Le Fer, G.; Le Cœur, C.; Guigner, J.-M.; Amiel, C.; Volet, G. *Langmuir* **2017**, 33 (11), 2849–2860.
- (15) Ruenraroengsak, P.; Cook, J. M.; Florence, A. T. *J. Control. Release* **2010**, 141 (3), 265–276.
- (16) Bae, Y. H.; Park, K. *J. Control. Release* **2011**, 153 (3), 198–205.
- (17) Florence, A. T. *Int. J. Pharm.* **2007**, 339, 1–2.
- (18) Taurin, S.; Nehoff, H.; Greish, K. *J. Control. Release* **2012**, 164 (3), 265–275.
- (19) Prabhakar, U.; Maeda, H.; K. Jain, R.; Sevic-Muraca, E. M.; Zamboni, W.; Farokhzad, O. C.; Barry, S. T.; Gabizon, A.; Grodzinski, P.; Blakey, D. C. *Cancer Res.* **2013**, 73 (8), 2412–2417.
- (20) Hobbs, S. K.; Monsky, W. L.; Yuan, F.; Roberts, W. G.; Griffith, L.; Torchilin, V. P.;

- Jain, R. K. *Proc. Natl. Acad. Sci. U. S. A.* **1998**, 95 (8), 4607–4612.
- (21) Dreher, M. R.; Liu, W.; Michelich, C. R.; Dewhirst, M. W.; Yuan, F.; Chilkoti, A. *J. Natl. Cancer Inst.* **2006**, 98 (5), 335–344.
 - (22) Ernsting, M. J.; Murakami, M.; Roy, A.; Li, S. D. *J. Control. Release* **2013**, 172 (3), 782–794.
 - (23) Moghimi, S. M.; Hunter, A. C.; Andresen, T. L. *Annu. Rev. Pharmacol. Toxicol* **2012**, 52, 481–503.
 - (24) Wilhelm, S.; Tavares, A. J.; Dai, Q.; Ohta, S.; Audet, J.; Dvorak, H. F.; Chan, W. C. W. *Nat. Rev. Mater.* **2016**, 1, 1–12.
 - (25) Lammers, T.; Kiessling, F.; Ashford, M.; Hennink, W.; Crommelin, D.; Strom, G. *Nat. Rev. Mater.* **2016**, 1 (9), 16069.
 - (26) Chithrani, B. D.; Ghazani, A. A.; Chan, W. C. W. *Nano* **2006**, 668 (4), 662–668.
 - (27) Gratton, S. E. A.; Ropp, P. A.; Pohlhaus, P. D.; Luft, J. C.; Madden, V. J.; Napier, M. E.; DeSimone, J. M. *Proc. Natl. Acad. Sci. U. S. A.* **2008**, 105 (33), 11613–11618.
 - (28) Petros, R. a; DeSimone, J. M. *Nat. Rev. Drug Discov.* **2010**, 9 (8), 615–627.
 - (29) Albanese, A.; Tang, P. S.; Chan, W. C. W. *Annu. Rev. Biomed. Eng.* **2012**, 14 (1), 1–16.
 - (30) Elsabahy, M.; Wooley, K. L. *Chem. Soc. Rev.* **2012**, 41 (7), 2545.
 - (31) Morachis, J. M.; Mahmoud, E. A.; Almutairi, A. *Pharmacol. Rev.* **2012**, 64 (3), 505–519.
 - (32) Kamaly, N.; Xiao, Z.; Valencia, P. M.; Radovic-Moreno, A. F.; Farokhzad, O. C. *Chem. Soc. Rev.* **2012**, 41 (7), 2971–3010.
 - (33) Chu, K. S.; Hasan, W.; Rawal, S.; Walsh, M. D.; Enlow, E. M.; Luft, J. C.; Bridges, A. S.; Kuijter, J. L.; Napier, M. E.; Zamboni, W. C.; DeSimone, J. M. *Nanomedicine Nanotechnology, Biol. Med.* **2013**, 9 (5), 686–693.
 - (34) Tan, J.; Shah, S.; Thomas, A.; Ou-Yang, H. D.; Liu, Y. *Microfluid. Nanofluidics* **2013**, 14 (1–2), 77–87.
 - (35) Agarwal, R.; Journey, P.; Raythatha, M.; Singh, V.; Sreenivasan, S. V.; Shi, L.; Roy, K. *Adv. Healthc. Mater.* **2015**, 4 (15), 2269–2280.
 - (36) Banik, B. L.; Fattahi, P.; Brown, J. L. *Wiley Interdiscip. Rev. Nanomedicine Nanobiotechnology* **2016**, 8 (2), 271–299.
 - (37) Cabral, H.; Matsumoto, Y.; Mizuno, K.; Chen, Q.; Murakami, M.; Kimura, M.; Terada, Y.; Kano, M. R.; Miyazono, K.; Uesaka, M.; Nishiyama, N.; Kataoka, K. *Nat. Nanotechnol.* **2011**, 6 (12), 815–823.

- (38) Dobrovolskaia, M. A.; McNeil, S. E. *Nat. Nanotechnol.* **2007**, 2 (8), 469–478.
- (39) Champion, J. A.; Katare, Y. K.; Mitragotri, S. *J. Control. Release* **2007**, 121 (1), 3–9.
- (40) Park, J.; Maltzahn, G. Von; Zhang, L.; Derfus, A. M.; Simberg, D.; Harris, T. J.; Ruoslahti, E.; Bhatia, S. N.; Sailor, M. J. *Small* **2009**, 5 (6), 694–700.
- (41) Decuzzi, P.; Godin, B.; Tanaka, T.; Lee, S. Y.; Chiappini, C.; Liu, X.; Ferrari, M. *J. Control. Release* **2010**, 141 (3), 320–327.
- (42) Tao, L.; Hu, W.; Liu, Y.; Huang, G.; Sumer, B. D.; Gao, J. *Exp. Biol. Med.* **2011**, 236 (1), 20–29.
- (43) Venkataraman, S.; Hedrick, J. L.; Ong, Z. Y.; Yang, C.; Ee, P. L. R.; Hammond, P. T.; Yang, Y. Y. *Adv. Drug Deliv. Rev.* **2011**, 63 (14), 1228–1246.
- (44) Truong, N. P.; Whittaker, M. R.; Mak, C. W.; Davis, T. P. *Expert Opin. Drug Deliv.* **2014**, 5247 (August 2016), 1–14.
- (45) Geng, Y.; Dalhaimer, P.; Cai, S.; Tsai, R.; Tewari, M.; Minko, T.; Discher, D. E. *Nat. Nanotechnol.* **2007**, 2 (4), 249–255.
- (46) Christian, D. A.; Cai, S.; Garbuzenko, O. B.; Harada, T.; Zajac, A. L.; Minko, T.; Discher, D. E. *Mol. Pharm.* **2009**, 6 (5), 1343–1352.
- (47) Park, J. H.; Von Maltzahn, G.; Zhang, L.; Schwartz, M. P.; Ruoslahti, E.; Bhatia, S. N.; Sailor, M. J. *Adv. Mater.* **2008**, 20 (9), 1630–1635.
- (48) Meng, H.; Yang, S.; Li, Z.; Xia, T.; Chen, J.; Ji, Z.; Zhang, H.; Wang, X.; Lin, S.; Huang, C.; Zhou, Z. H.; Zink, J. I.; Nel, A. E. *ACS Nano* **2011**, 5 (6), 4434–4447.
- (49) Zhu, M.; Nie, G.; Meng, H.; Xia, T. *Acc. Chem. Res.* **2012**, 46 (3), 622–631.
- (50) Champion, J. A.; Mitragotri, S. *Proc. Natl. Acad. Sci. U. S. A.* **2006**, 103 (13), 4930–4934.
- (51) Blum, A. P.; Kammeyer, J. K.; Gianneschi, N. C. *Chem. Sci.* **2016**, 7 (2), 989–994.
- (52) Xiao, K.; Li, Y.; Luo, J.; Lee, J. S.; Xiao, W.; Gonik, A. M.; Agarwal, R. G.; Lam, K. S. *Biomaterials* **2011**, 32 (13), 3435–3446.
- (53) Greish, K.; Thiagarajan, G.; Herd, H.; Price, R.; Bauer, H.; Hubbard, D.; Burckle, A.; Sadekar, S.; Yu, T.; Anwar, A.; Ray, A.; Ghandehari, H. *Nanotoxicology* **2012**, 6 (7), 713–723.
- (54) Bremer, C.; Tung, C. H.; Weissleder, R. *Nat. Med.* **2001**, 7 (6), 743–748.
- (55) Olson, E. S.; Aguilera, T. a; Jiang, T.; Ellies, L. G.; Nguyen, Q. T.; Wong, E. H.; Gross, L. a; Tsien, R. Y. *Integr. Biol. (Camb)*. **2009**, 1 (5–6), 382–393.
- (56) Jiang, T.; Olson, E. S.; Nguyen, Q. T.; Roy, M.; Jennings, P. a; Tsien, R. Y. *Proc. Natl.*

Acad. Sci. U. S. A. **2004**, *101* (51), 17867–17872.

- (57) Scherer, R. L.; McIntyre, J. O.; Matrisian, L. M. *Cancer Metastasis Rev.* **2008**, *27* (4), 679–690.
- (58) Kulkarni, P. S.; Haldar, M. K.; Nahire, R. R.; Katti, P.; Ambre, A. H.; Muhonen, W. W.; Shabb, J. B.; Padi, S. K. R.; Singh, R. K.; Borowicz, P. P.; Shrivastava, D. K.; Katti, K. S.; Reindl, K.; Guo, B.; Mallik, S. *Mol. Pharm.* **2014**, *11* (7), 2390–2399.
- (59) Vartak, D. G.; Gemeinhart, R. A. *J. Drug Target.* **2007**, *15* (1), 1–20.
- (60) Coburn, J. M.; Kaplan, D. L. *Bioconjug. Chem.* **2015**, *26* (7), 1212–1223.
- (61) Law, B.; Tung, C. H. *Bioconjug. Chem.* **2009**, *20* (9), 1683–1695.
- (62) Razgulin, A.; Ma, N.; Rao, J. *Strategies for in vivo imaging of enzyme activity: an overview and recent advances*; 2011; Vol. 40.
- (63) Chien, M. P.; Thompson, M. P.; Barback, C. V.; Ku, T. H.; Hall, D. J.; Gianneschi, N. C. *Adv. Mater.* **2013**, *25* (26), 3599–3604.
- (64) Chien, M.-P.; Carlini, A. S.; Hu, D.; Barback, C. V.; Rush, A. M.; Hall, D. J.; Orr, G.; Gianneschi, N. C. *J. Am. Chem. Soc.* **2013**, *135* (50), 18710–18713.
- (65) Callmann, C. E.; Barback, C. V.; Thompson, M. P.; Hall, D. J.; Mattrey, R. F.; Gianneschi, N. C. *Adv. Mater.* **2015**, *27* (31), 4611–4615.
- (66) Nguyen, M. M.; Carlini, A. S.; Chien, M. P.; Sonnenberg, S.; Luo, C.; Braden, R. L.; Osborn, K. G.; Li, Y.; Gianneschi, N. C.; Christman, K. L. *Adv. Mater.* **2015**, *27* (37), 5547–5552.
- (67) Kannan, R. M.; Nance, E.; Kannan, S.; Tomalia, D. A. *J. Intern. Med.* **2014**, *276* (6), 579–617.
- (68) Gratton, S. E. A.; Pohlhaus, P. D.; Lee, J.; Guo, J.; Cho, M. J.; DeSimone, J. M. *J. Control. Release* **2007**, *121* (1–2), 10–18.
- (69) Schmid, G. M.; Miller, M.; Brooks, C.; Khusnatdinov, N.; LaBrake, D.; Resnick, D. J.; Sreenivasan, S. V.; Gauzner, G.; Lee, K.; Kuo, D.; Weller, D.; Yang, X. *J. Vac. Sci. Technol. B Microelectron. Nanom. Struct.* **2009**, *27* (2), 573.
- (70) Israelachvili, J. N.; Mitchell, D. J.; Ninham, B. W. *J. Chem. Soc. Faraday Trans. 2* **1976**, *72*, 1525.
- (71) Barnhill, S. A.; Bell, N. C.; Patterson, J. P.; Olds, D. P.; Gianneschi, N. C. *Macromolecules* **2015**, *48* (4), 1152–1161.
- (72) Nagarajan, R. *Langmuir* **2002**, *18*, 31–38.
- (73) Hayward, R. C.; Pochan, D. J. *Macromolecules* **2010**, *43* (8), 3577–3584.

- (74) Yu, K.; Eisenberg, A. *Macromolecules* **1998**, No. 97, 3509–3518.
- (75) Blanz, A.; Madsen, J.; Battaglia, G.; Ryan, A. J.; Armes, S. P. *J. Am. Chem. Soc.* **2011**, *133* (41), 16581–16587.
- (76) Cui, H.; Chen, Z.; Zhong, S.; Wooley, K. L.; Pochan, D. J. *Science* (80-.). **2007**, *317* (5838), 647–650.
- (77) Kempe, K.; Wylie, R. A.; Dimitriou, M. D.; Tran, H.; Hoogenboom, R.; Schubert, U. S.; Hawker, C. J.; Campos, L. M.; Connal, L. A. *J. Polym. Sci. Part A Polym. Chem.* **2016**, *54* (6), 750–757.
- (78) Zhang, L.; Eisenberg, A. *J. Am. Chem. Soc.* **1996**, *118* (13), 3168–3181.
- (79) Yu, K.; Eisenberg, A. **1996**, 9297 (96), 6359–6361.
- (80) Yu, K.; Zhang, L.; Eisenberg, A. *Langmuir* **1996**, *12*, 5980–5984.
- (81) Holder, S. J.; Sommerdijk, N. A. J. M. *Polym. Chem.* **2011**, *2* (5), 1018.
- (82) Shen, H.; Zhang, L.; Eisenberg, A. *J. Phys. Chem. B* **1997**, *101*, 4697–4708.
- (83) Adams, D. J.; Kitchen, C.; Adams, S.; Furzeland, S.; Atkins, D.; Schuetz, P.; Fernyhough, C. M.; Tzokova, N.; Ryan, A. J.; Butler, M. F. *Soft Matter* **2009**, *5* (16), 3086.
- (84) Won, Y.; Brannan, A. K.; Davis, H. T.; Bates, F. S. *J. Phys. Chem. B* **2002**, *106* (13), 3354–3364.
- (85) Jain, S. *Science* (80-.). **2003**, *300* (5618), 460–464.
- (86) Davis, H. T.; Bates, F. S. *Macromolecules* **2003**, *36*, 953–955.
- (87) Jain, S.; Bates, F. S. *Macromolecules* **2004**, *37* (4), 1511–1523.
- (88) Bang, J.; Jain, S.; Li, Z.; Lodge, T. P. *Macromolecules* **2006**, *39*, 1199–1208.
- (89) Rush, A. M.; James, C. R.; Gianneschi, N. C. In *Handbook of Metathesis Vol. 3: Polymer Synthesis*; Grubbs, R. H., Khosravi, E., Eds.; 2015; Vol. 3, pp 115–148.
- (90) Carrillo, A.; Kane, R. S. *J. Polym. Sci. Part A Polym. Chem.* **2004**, *42* (13), 3352–3359.
- (91) Liaw, D.-J.; Wang, K.-L.; Chen, T.-P.; Lee, K.-R.; Lai, J.-Y. *Polymer (Guildf)*. **2007**, *48* (13), 3694–3702.
- (92) Kelley, E. G.; Murphy, R. P.; Seppala, J. E.; Smart, T. P.; Hann, S. D.; Sullivan, M. O.; Epps, T. H. *Nat. Commun.* **2014**, *5*, 1–10.
- (93) Stubenrauch, K.; Moitzi, C.; Fritz, G.; Glatter, O.; Trimmel, G.; Stelzer, F. *Macromolecules* **2006**, *39* (17), 5865–5874.
- (94) Barnhill, S. A.; Bell, N. C.; Patterson, J. P.; Olds, D. P.; Gianneschi, N. C.

Macromolecules **2015**, *48* (4), 1152–1161.

- (95) Chen, C.; Wylie, R. A. L.; Klinger, D.; Connal, L. A. *Chem. Mater.* **2017**, *29* (5), 1918–1945.
- (96) Carlini, A. S.; Adamiak, L.; Gianneschi, N. C. *Macromolecules* **2016**, *49* (12), 4379–4394.
- (97) Nomura, K.; Abdellatif, M. M. *Polymer (Guildf)*. **2010**, *51* (9), 1861–1881.
- (98) Thompson, M. P.; Randolph, L. M.; James, C. R.; Davalos, A. N.; Hahn, M. E.; Gianneschi, N. C. *Polym. Chem.* **2014**, *5* (6), 1954–1964.
- (99) Leitgeb, A.; Wappel, J.; Slugovc, C. *Polymer (Guildf)*. **2010**, *51* (14), 2927–2946.
- (100) Kammeyer, J. K.; Blum, A. P.; Adamiak, L.; Hahn, M. E.; Gianneschi, N. C. *Polym. Chem.* **2013**, *4* (14), 3929–3933.
- (101) Chien, M. P.; Rush, A. M.; Thompson, M. P.; Gianneschi, N. C. *Angew Chem Int Ed Engl* **2010**, *49* (30), 5076–5080.
- (102) Rush, A. M.; Matthew P. Thompson; Tatro, E. T.; Gianneschi, N. C. *ACS Nano* **2014**, *7* (2), 1379–1387.
- (103) Rush, A. M.; Nelles, D. A.; Blum, A. P.; Barnhill, S. A.; Tatro, E. T.; Yeo, G. W.; Gianneschi, N. C. *J. Am. Chem. Soc.* **2014**, *136* (21), 7615–7618.
- (104) James, C. R.; Rush, A. M.; Insley, T.; Vukovic, L.; Adamiak, L.; Kral, P.; Gianneschi, N. C. *J. Am. Chem. Soc.* **2014**, *136* (32), 11216–11219.
- (105) Randolph, L. M.; LeGuyader, C. L. M.; Hahn, M. E.; Andolina, C. M.; Patterson, J. P.; Mattrey, R. F.; Millstone, J. E.; Botta, M.; Scadeng, M.; Gianneschi, N. C. *Chem. Sci.* **2016**, *7*, 4230–4236.
- (106) Kim, B. Y.; Rutka, J. T.; Chan, W. C. *N. Engl. J. Med.* **2010**, *363* (25), 2434–2443.
- (107) Uchegbu, I. F.; Siew, A. *J. Pharm. Sci.* **2013**, *102* (2), 305–310.
- (108) Wicki, A.; Witzigmann, D.; Balasubramanian, V.; Huwyler, J. *J. Control. Release* **2015**, *200C*, 138–157.
- (109) Choi, H. S.; Frangioni, J. V. *Mol. Imaging* **2010**, *9* (6), 291–310.
- (110) Srinivas, M.; Cruz, L. J.; Bonetto, F.; Heerschap, A.; Figdor, C. G.; de Vries, I. J. M. *Biomaterials* **2010**, *31* (27), 7070–7077.
- (111) Wang, C.-H.; Kang, S.-T.; Lee, Y.-H.; Luo, Y.-L.; Huang, Y.-F.; Yeh, C.-K. *Biomaterials* **2012**, *33* (6), 1939–1947.
- (112) Kinsella, J. M.; Jimenez, R. E.; Karmali, P. P.; Rush, A. M.; Kotamraju, V. R.; Gianneschi, N. C.; Ruoslahti, E.; Stupack, D.; Sailor, M. J. *Angew. Chemie, Int. Ed.*

2011, *50* (51), 12308–12311.

- (113) Fan, Q.; Cheng, K.; Hu, X.; Ma, X.; Zhang, R.; Yang, M.; Lu, X.; Xing, L.; Huang, W.; Gambhir, S. S.; Cheng, Z. *J. Am. Chem. Soc.* **2014**, *136* (43), 15185–15194.
- (114) Kaittanis, C.; Shaffer, T. M.; Thorek, D. L. J.; Grimm, J. **2014**, *19* (3–4), 143–176.
- (115) Cormode, D. P.; Sanchez-Gaytan, B. L.; Mieszawska, A. J.; Fayad, Z. A.; Mulder, W. J. *NMR Biomed* **2013**, *26* (7), 766–780.
- (116) Kim, B. H.; Lee, N.; Kim, H.; An, K.; Park, Y. I.; Choi, Y.; Shin, K.; Lee, Y.; Kwon, S. G.; Na, H. B.; Park, J. G.; Ahn, T. Y.; Kim, Y. W.; Moon, W. K.; Choi, S. H.; Hyeon, T. *J. Am. Chem. Soc.* **2011**, *133* (32), 12624–12631.
- (117) Mendonca Dias, M. H.; Lauterbur, P. C. *Magn. Reson. Med.* **1986**, *3* (2), 328–330.
- (118) Na, H. Bin; Song, I. C.; Hyeon, T. *Adv. Mater.* **2009**, *21* (21), 2133–2148.
- (119) Xie, J.; Liu, G.; Eden, H. S.; Ai, H.; Chen, X. *Acc. Chem. Res.* **2011**, *44* (10), 883–892.
- (120) Besenius, P.; Heynens, J. L.; Straathof, R.; Nieuwenhuizen, M. M.; Bomans, P. H.; Terreno, E.; Aime, S.; Strijkers, G. J.; Nicolay, K.; Meijer, E. W. *Contrast Media Mol. Imaging* **2012**, *7* (3), 356–361.
- (121) Bruckman, M. A.; Yu, X.; Steinmetz, N. F. *Nanotechnology* **2013**, *24* (46), 462001.
- (122) Davies, G. L.; Kramberger, I.; Davis, J. J. *Chem Commun* **2013**, *49* (84), 9704–9721.
- (123) Mi, P.; Kokuryo, D.; Cabral, H.; Kumagai, M.; Nomoto, T.; Aoki, I.; Terada, Y.; Kishimura, A.; Nishiyama, N.; Kataoka, K. *J. Control. Release* **2014**, *174*, 63–71.
- (124) Tirotta, I.; Dichiarante, V.; Pigliacelli, C.; Cavallo, G.; Terraneo, G.; Bombelli, F. B.; Metrangolo, P.; Resnati, G. *Chem. Rev.* **2015**, *115*, 1106–1129.
- (125) Caravan, P.; Ellison, J. J.; McMurry, T. J.; Lauffer, R. B. *Chem. Rev.* **1999**, *99* (9), 2293–2352.
- (126) Hao, D.; Ai, T.; Goerner, F.; Hu, X.; Runge, V. M.; Tweedle, M. J. *Magn. Reson. Imaging* **2012**, *36* (5), 1060–1071.
- (127) Caravan, P. *Chem. Soc. Rev.* **2006**, *35* (6), 512.
- (128) Datta, A.; Raymond, K. N. *Acc. Chem. Res.* **2009**, *42* (7), 938–947.
- (129) Therapeutics, N.; Approval, F. D. A.; Trials, C.; Eifler, A. C.; Thaxton, C. S. **2011**, *726*, 325–338.
- (130) Kratz, F. *J. Control. Release* **2008**, *132* (3), 171–183.
- (131) Merlot, A. M.; Kalinowski, D. S.; Richardson, D. R. *Front. Physiol.* **2014**, *5* AUG (August), 1–7.

- (132) Larsen, M. T.; Kuhlmann, M.; Hvam, M. L.; Howard, K. A. *Mol. Cell. Ther.* **2016**, *4* (1), 3.
- (133) Kratz, F.; Elsadek, B. *J. Control. Release* **2012**, *161* (2), 429–445.
- (134) Liu, Z.; Chen, X. *Chem. Soc. Rev.* **2016**, *45* (5), 1432–1456.
- (135) Neumann, E.; Frei, E.; Funk, D.; Becker, M. D.; Schrenk, H.-H.; Müller-Ladner, U.; Fiehn, C. *Expert Opin. Drug Deliv.* **2010**, *7* (8), 915–925.
- (136) Aime, S.; Botta, M.; Fasano, M.; Crich, S. G.; Terreno, E. *J. Biol. Inorg. Chem.* **1996**, *1* (4), 312–319.
- (137) Aime, S.; Chiaussa, M.; Digilio, G.; Gianolio, E.; Terreno, E. *J. Biol. Inorg. Chem.* **1999**, *4* (6), 766–774.
- (138) Caravan, P.; Cloutier, N. J.; Greenfield, M. T.; McDermid, S. A.; Dunham, S. U.; Bulte, J. W. M.; Amedio, J. C.; Looby, R. J.; Supkowski, R. M.; Horrocks, W. D.; McMurry, T. J.; Lauffer, R. B. *J. Am. Chem. Soc.* **2002**, *124* (12), 3152–3162.
- (139) Lauffer, R. B.; Parmelee, D. J.; Dunham, S. U.; Ouellet, H. S.; Dolan, R. P.; Witte, S.; McMurry, T. J.; Walovitch, R. C. *Radiology* **1998**, *207* (2), 529–538.
- (140) Muller, R. N.; Radüchel, B.; Laurent, S.; Platzek, J.; Piérart, C.; Mareski, P.; Vander Elst, L. *Eur. J. Inorg. Chem.* **1999**, 1999 (11), 1949–1955.
- (141) Parmelee, D. J.; Walovitch, R. C.; Ouellet, H. S.; Lauffer, R. B. *Invest. Radiol.* **1997**, *32* (12), 741–747.
- (142) Multihance® [package insert]. .
- (143) Spinazzi, A.; Lorusso, V.; Pirovano, G.; Kirchin, M. *Acad. Radiol.* **1999**, *6* (5), 282–291.
- (144) Levick, J. R. *Arthritis Rheum.* **1981**, *24* (12), 1550–1560.
- (145) Schnitzer, J. E. *Am. J. Physiol.* **1992**, *262* (1 Pt 2), H246-54.
- (146) Tiruppathi, C.; Song, W.; Bergenfeldt, M.; Sass, P.; Malik, A. B. *J. Biol. Chem.* **1997**, *272* (41), 25968–25975.
- (147) Schnitzer, J. E.; Oh, P. *J. Biol. Chem.* **1994**, *269* (8), 6072–6082.
- (148) Schnitzer, J. E.; Oh, P. *Am. J. Physiol.* **1992**, *263* (6), H1872-9.
- (149) Fritzsche, T.; Schnölzer, M.; Fiedler, S.; Weigand, M.; Wiessler, M.; Frei, E. *Biochem. Pharmacol.* **2004**, *67* (4), 655–665.
- (150) Ibrahim, N. K.; Desai, N.; Legha, S.; Formulation, N.; Soon-shiong, P.; Theriault, R. L.; Rivera, E.; Esmaeli, B.; Ring, S. E.; Bedikian, A.; Hortobagyi, G. N. *Clin. Cancer Res.* **2002**, *8* (May), 1038–1044.

- (151) Desai, N.; Trieu, V.; Yao, Z.; Louie, L.; Ci, S.; Yang, A.; Tao, C.; De, T.; Beals, B.; Dykes, D.; Noker, P.; Yao, R.; Labao, E.; Hawkins, M.; Soon-Shiong, P. *Clin. Cancer Res.* **2006**, *12* (4), 1317–1324.
- (152) Desai, N. P.; Trieu, V.; Hwang, L. Y.; Wu, R.; Soon-Shiong, P.; Gradishar, W. J. *Anticancer. Drugs* **2008**, *19* (9), 899–909.
- (153) Gradishar, W. J. *Expert Opin. Pharmacother.* **2006**, *7* (8), 1041–1053.
- (154) Miele, E.; Spinelli, G. P.; Miele, E.; Tomao, F.; Tomao, S. *Int. J. Nanomedicine* **2009**, *4*, 99–105.
- (155) Yardley, D. A. *J. Control. Release* **2013**, *170* (3), 365–372.
- (156) Desai, N.; Trieu, V.; Damascelli, B.; Soon-Shiong, P. *Transl. Oncol.* **2009**, *2* (2), 59–64.
- (157) Neuzillet, C.; Tijeras-Raballand, A.; Cros, J.; Faivre, S.; Hammel, P.; Raymond, E. *Cancer Metastasis Rev.* **2013**, *32* (3–4), 585–602.
- (158) Curry, S.; Mandelkow, H.; Brick, P.; Franks, N. *Nat. Struct. Biol.* **1998**, *5* (9), 827–835.
- (159) Choi, J.-K.; Ho, J.; Curry, S.; Qin, D.; Bittman, R.; Hamilton, J. a. *J. Lipid Res.* **2002**, *43* (7), 1000–1010.
- (160) Bhattacharya, A. A.; Grüne, T.; Curry, S. *J. Mol. Biol.* **2000**, *303* (5), 721–732.
- (161) Tonsgard, J. H.; Mendelson, S. A.; Meredith, S. C. *J. Clin. Invest.* **1988**, *82* (5), 1567–1573.
- (162) Spector, A. A. *J. Lipid Res.* **1975**, *16* (3), 165–179.
- (163) Ashbrook, J. D.; Spector, A. A.; Santos, E. C.; Fletcher, J. E. *J. Biol. Chem.* **1975**, *250* (6), 2333–2338.
- (164) Tonsgard, J. H.; Meredith, S. C. *Biochem. J.* **1991**, *276*, 569–575.

Chapter 2

Accessing Diverse Nanoparticle Morphologies *via* Ring Opening Metathesis Polymerization

2.1 Introduction

As we strive to create NPs for optimal performance *in vivo*, engineering the polymeric NP for favorable blood circulation profiles and accumulation at the target is crucial. NPs of non-spherical morphology are vastly underutilized in clinical applications, and combined with the unpredictability in assembled polymeric morphology, there is a motivation for experimentally exploring the role of polymer structure and self-assembly conditions in forming interestingly-shaped NPs.

As described in Chapter 1, vast numbers of research groups have explored polymeric self-assemblies with respect to their utility in a variety of medical applications and on a more fundamental level, design rules for controlling NPs with specific physicochemical properties. The two main strategies employed for imparting control on the NP morphology include dictating polymer chemical structure and architecture, that is the packing parameter considerations, and control over the self-assembly process, that is the thermodynamic and kinetic consideration. The approaches towards these two strategies involve chemical synthesis of the polymer (e.g. monomer selection, block length, dispersity) and control of the self-assembly process. This second strategy includes utilizing specific routes of assembly such as a solvent switch where solvent selection and mixing can alter the dynamics of assembly to

kinetically trap structures in a non-thermodynamic state. Towards this end, ionic polymerization techniques are commonly used to prepare polymers for study of self-assembly properties (there are many studies, discussed in Chapter 1, with exceptional work from Bates and Eisenberg). The work in this chapter relies on the ring-opening metathesis polymerization (ROMP) strategy to synthesize block copolymers to navigate biologically complex systems. As such, there is a need to understand how to best design and prepare polymers for specific nanoscale properties. We elect to use ROMP because of the synthetic control the living polymerization allows in preparing monodispersed blocks with specific molecular weights; this is crucial given that molecular architecture can alter the nanoassembly.

Previous work from the Gianneschi Lab and many others investigate polymer structure effects in the self-assembly process. In various studies, hydrophilic block of a block copolymer (BCP) was varied, along with ratio of hydrophilic-to-hydrophobic, and the overall polymer molecular weight (MW).¹⁻³ Phase diagrams were developed to characterize the range of morphologies that were accessed upon assembly in aqueous solution. Interestingly, identical polymers could access different morphologies based on the pathway for self-assembly, highlighting the nonergodic nature of polymer self-assemblies, and ability to kinetically trap locally stable structures using different solvent preparation procedures.

This chapter is primarily interested in strategies to modulate the hydrophobic block of an amphiphilic BCP. In some applications, the hydrophilic block of a polymer may be constrained, for example when incorporating peptides as targeting moieties, or incorporating a hydrophilic imaging agent. Therefore, it is imperative that we investigate the feasibility of using the hydrophobic block to affect polymer self-assembly structure. A library of polymers with different architectures is prepared in which a range of hydrophobic blocks, in both length and functionality, are chain extended with a hydrophilic poly(ethyleneglycol) monomer (PEG), followed by assembly using varied conditions. The resulting assemblies, while not predictive

or adhering to a defined phase diagram, did substantiate the hypothesis that nanoparticle morphology depends on both polymer architecture and self-assembly route.

A fluorinated hydrocarbon norbornene monomer was investigated as to feasibility in acting as a hydrophobic moiety in an amphiphile BCP. Perfluorohydrocarbons are interesting for their use in ultrasound contrast agents, in addition to the growing interest in ^{19}F -MRI. ^{19}F , not to be confused with the radioisotope ^{18}F used for positron emission tomography (PET), shares similar magnetic properties to a proton, and gives a distinct signal in NMR. The ^{19}F nucleus is in 100% natural abundance with a gyromagnetic ratio comparable to that of hydrogen, with 83% the sensitivity of the proton.⁴ Since only very small amounts of fluorine are present in the body, a contrast agent containing ^{19}F must be administered to generate a detectable signal. Fluorine MRI has been discussed as a new generation imaging technique, though clinical translatability is limited by the sensitivity to administered ^{19}F -containing agents, with some reports finding a detection limit of 126 mM ^{19}F atom for detection in phantoms at 3T.⁴

In addition to utility in imaging applications, the perfluorohydrocarbon monomer is investigated with interest in properties pertaining to the fluorophilic effect.⁵ This effect relies on the observation that fluorine is neither hydrophilic or hydrophobic, and prefers to interact with itself. In an amphiphilic polymer self-assembly process, this could prove advantageous as a strategy to drive aggregation in an aqueous environment: the fluorine-containing molecules aggregate together to minimize any contact with water. Results here articulate the utility of using fluorine to formulate polymeric NPs in water. Applications in ultrasound contrast agents were explored elsewhere.⁶ This work provides strategies towards using ROMP to make fluorine-containing NPs of various morphologies towards NP imaging agents.

2.2 Selection of Monomers and Preparation of Polymers

In many studies of polynorbornene amphiphiles, a norbornyl-phenyl is the hydrophobic block of the polymer. This monomer offers advantages such as ease of synthesis and fast polymerization kinetics. However, phenyl-based blocks are known to form relatively crystalline cores upon assembly. Due to strong hydrophobic interactions, the block readily packs together to minimize unfavorable interactions with water. The result is high T_g species ($> 100^\circ\text{C}$)¹ that requires high energy input to transition the core to a more mobile phase capable of undergoing chain rearrangement towards other equilibrium structures. In some cases, the resulting assembly structure is referred to as kinetically trapped, that is a structure that cannot reach thermodynamic equilibrium. Obtaining a kinetically trapped structure versus the thermodynamic structure can happen by modulating the assembly process. Utilizing different solvents and/or solvent mixtures for either blocks, one can access and subsequently trap the polymer structures along the path towards the most energetically stable structure before the kinetic structure can relax to the thermodynamic state.

This study investigates hydrophobic blocks of various functionalities, and the utility in using polymer structure to access kinetically trapped structures. Due to the less hydrophobic nature of the monomers selected for this study (Fig. 2.1), it was predicted that the BCPs prepared would lead to more diverse and exotic structures as the dynamics of polymer reorganization will be more favorable. All BCPs prepared here contained a (poly)ethyleneglycol (PEG, monomer **1**) hydrophilic block, which in all cases, was polymerized first, followed by the hydrophobic block, to ensure adequate solubility of the propagating block copolymer. Novel saturated hydrocarbons were prepared for investigation (norbornene- decylamine [Dec, monomer **2**], -hexylamine [Hex, monomer **3**] and -cyclohexanemethylamine [Cy, monomer **4**]) (Figs. 2.1 and 2.6). Monomers containing

naphthalene (Nap, monomer **5**), phenol (Phen, monomer **6**) and pyridine (Pyr, monomer **7**) moieties were utilized to further explore the scope of hydrophobic block. A control polymer containing -phenyl (-Ph, monomer **8**) was also synthesized.

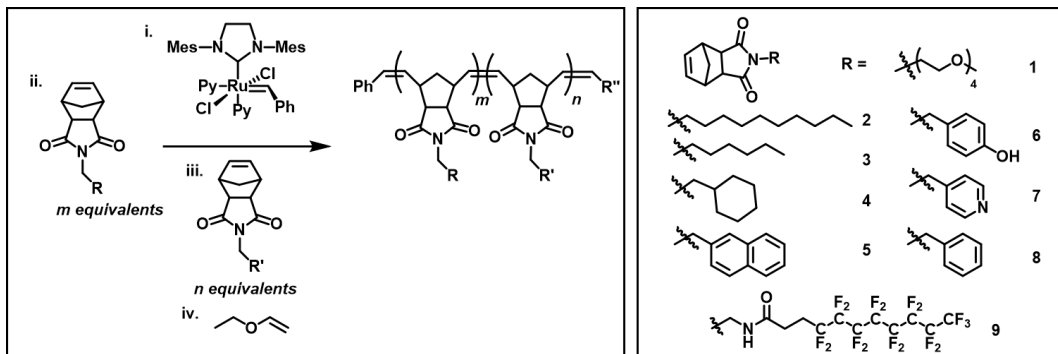


Figure 2.1 Ring opening metathesis polymerization (ROMP) scheme used to prepare all polymers. Monomers used for this study are described in the right panel.

Polymers **1-17** were synthesized via ROMP and characterized by SEC-MALS (Tables 2.1 and 2.3 and Figs. 2.7 and 2.8). All polymers demonstrated fidelity for living chain extension as evidenced by achieving desired target degrees of polymerization (based on equivalents *n* of monomer added to the living polymer chain) except for monomers **6** and **7**. Good polymerization control is shown by the lower polymer dispersities. The phenol and pyridine moieties are known to coordinate to the ruthenium catalyst, thus negatively impacting the polymerization.⁷ SEC traces for Polymers **P5**, **P6** and **P7** display broad peaks and shoulders indicative of lack of control during the polymerization. Once polymerized, the polymers were used as is for micellization procedures.

Table 2.1 Molecular Characterizations of **P1-P8**.

Polymer	Composition	Material Name	DP (m) ^a	DP (n) ^a	M_n ^b	Đ ^c
P1	1₁₈-b-2₂₄	PEG ₁₈ -b-Dec ₂₄	18 (75)	24 (25)[37]	13,690	1.012
P2	1₁₈-b-3₁₈	PEG ₁₈ -b-Hex ₁₈	18 (75)	18 (25) [27]	10,950	1.020
P3	1₁₈-b-4₂₂	PEG ₁₈ -b-Cy ₂₂	18 (75)	22 (25) [26]	11,970	1.019
P4	1₂₁-b-5₂₀	PEG ₂₁ -b-Nap ₂₀	21 (30)	20 (15)	13,880	1.167
P5	1₂₁-b-6₈₉	PEG ₂₁ -b-Phen ₈₉	21 (30)	89 (30)	31,870	1.039
P6	1₂₁-b-6₇₁	PEG ₂₁ -b-Phen ₇₁	21 (30)	71 (15)	27,150	1.020
P7	1₂₁-b-7₅₉	PEG ₂₁ -b-Pyr ₅₉	21 (30)	59 (30)	23,080	1.065
P8	1₁₄-b-8₂₀	PEG ₁₄ -b-Ph ₂₀	14 (20)	20(20)	10,060	1.015

^a The degree of polymerization (DP) m and n, are determined using SEC-MALS. Target DPs are in parentheses. For n, the reported DP was determined by SEC-MALS in DMF, while the number in brackets is the ¹H-NMR integration. ^b The number average molecular weight. The dispersity of copolymer (M_w/M_n).

2.3 Nanoparticle Formulation

A solvent switch method, was employed for all micellization procedures. In this method, a water miscible organic solvent is used to dissolve the polymer. After solubilizing the polymer in either acetonitrile (ACN), dimethylformamide (DMF), or dimethylsulfoxide (DMSO) solvent, MilliQ water was added dropwise to the polymer solution. Unless otherwise indicated, an equal volume of water was added, followed by transfer of solution to snakeskin dialysis tubing, with MW cutoff of 3500, and dialysis against water over two days to remove organic solvent. The resulting nanoparticles were used as is for further analysis. The nanoparticles were numbered according to the polymer used to formulate the particle, for example **NP1**, **NP2** and **NP3** were prepared from **P1**, **P2**, and **P3**, respectively.

Polymers **P1-3** contained identical hydrophilic block, and comparable hydrophobic degree of polymerization, with similar resulting polymer MWs. The resulting nanoparticles had several morphologies, depending on the polymer and the cosolvent used in the micellization procedure. **NP1** resulted in spherical NPs, regardless of the solvent selected (Fig.

2.2). NPs formulated from DMF and DMSO were approximately 20 nm in diameter by transmission electron microscopy (TEM), whereas NPs from ACN were slightly larger in diameter, and less uniform by TEM analysis. The observation of similar morphologies for **NP1** indicates that the polymer architecture is most important factor in forming NPs with distinct structures, and that there are multiple pathways (e.g. solvents) to access that structure. **NP2** prepared from ACN or DMSO resulted in non-discrete aggregates, while the micelles prepared from DMF solvent had an interesting diversity of high-aspect ratio nanoparticles, including branched micelles, rod-like micelles, and short worm-like structures. By using varied polymer structure and varied micellization conditions, NPs of various morphologies were prepared. Finally, **NP3** were predominantly spherical, with a few high-aspect ratio cylinders observed for the DMF micelle solution, compared to mostly large aggregates when prepared from DMSO. Here, solvent selection and polymer architecture are important in accessing equilibrium nanoassemblies.

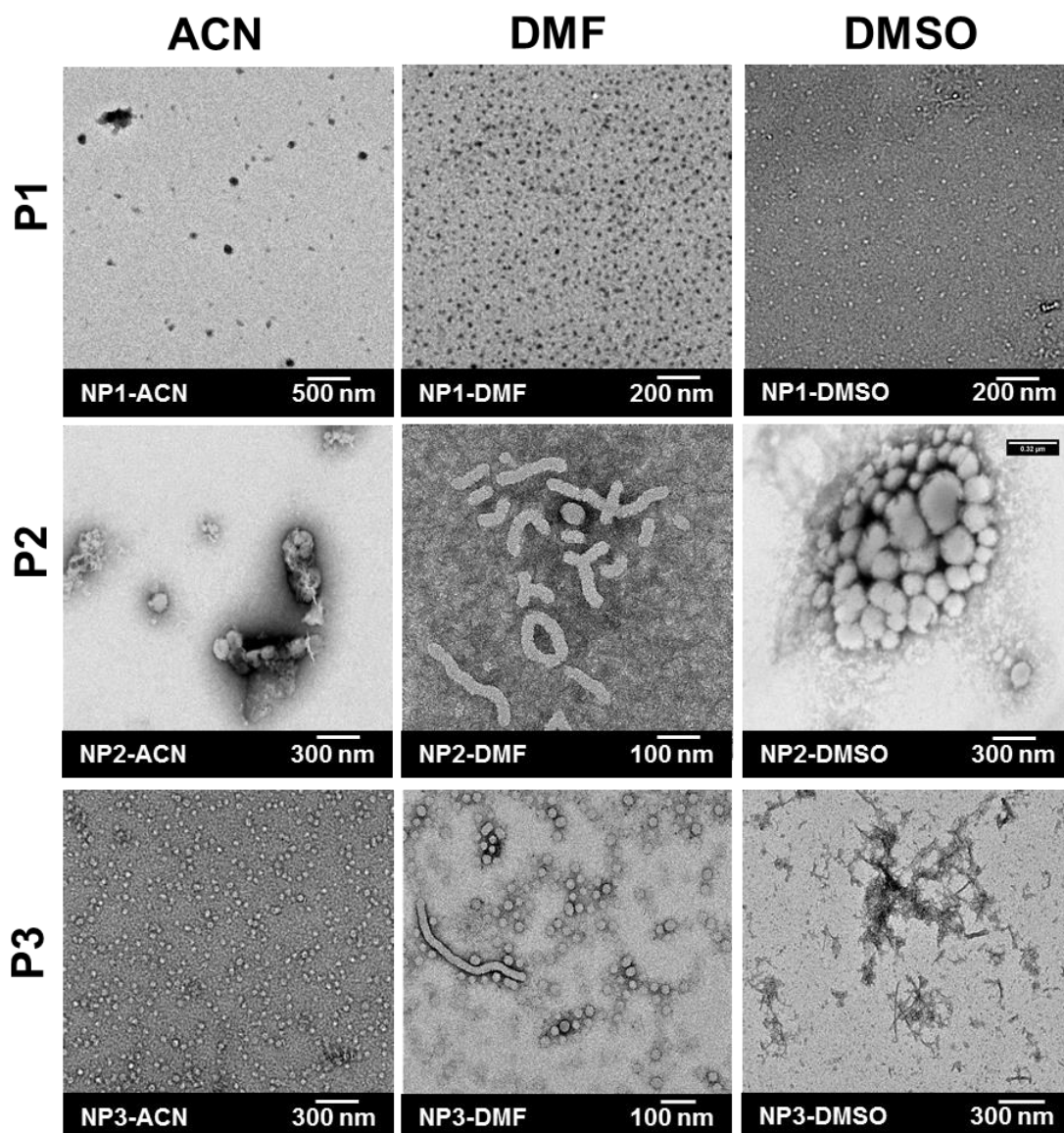


Figure 2.2 NPs 1-3, formed from P1-3, respectively. The solvent ACN, DMF or DMSO, is the solubilizing solvent, and was dialyzed away to leave fully aqueous solutions of the resulting NP, with representative TEM images here.

Next, the self-assembly conditions were further probed to investigate the effect on NP morphology. Interestingly, when **P2** was micellized with DMF solvent, different morphologies were accessed from those previously achieved (Fig 2.10). This is attributed to the strategy of using dynamics of self-assembly to achieve equilibrium structures. If undergoing a slow

addition of water, worm-like structures dominated the solution (Fig. 2.10a). When allowing for equilibration at low weight% water by stirring the solution overnight in 13% water in DMF, spherical nanoparticles of about 30-50 nm diameter were observed, indicating that the dynamics of assembly and rearrangement are important in reaching a stable structure (Fig. 2.10b). Upon removing DMF from the 13% water solution via dialysis, slightly smaller spheres around 25-30 nm were observed (2.10c). The dynamics of reorganization of polymer chains in this system is slow, and overnight equilibration at low weight percent water allows for reorganization to a lower energy state. The dynamics of assembly will depend on the polymer and solvent conditions; for all polymers herein, the hydrophobic block is relatively large, and upon water addition, the polymer solutions readily self-assemble in to trapped structures.

NPs 9-11 (Fig. 2.11) were prepared from **P9-11**. These polymers share the same monomer functionality as **P1-3**, but overall DP and molecular weights were much greater. In this small subset of the polymer library, the polymers were not as soluble in the solvents selected, but nevertheless some particles were observed. No particles were observed for **NP9** and **NP10** in DMSO, or **NP11** from both ACN and DMF. **P9** and **P10** formed spherical NPs around 25 nm, with **NP9**-DMF resulting in a distribution of smaller (25 nm) and larger (100 nm) NPs. **NP11** resulted in larger spherical particles with greater size distribution. **P9** had a bimodal distribution by SEC; two polymer populations can lead to greater particle dispersity if the polymers are trapped in different assemblies or the mixing of the polymers in solution is not good.

The **NP8**, (Fig. 2.12) was prepared from the control polymer **P8**, using a variety of solvents. **NP8** was formulated from ACN, DMF, tetrahydrofuran (THF) or trifluoroethanol (TFE, not used in previous formulations). THF and TFE were selected as less hydrophilic solvents, compared to ACN or DMF; the fluorinated solvent is particularly of interest for the fluoropolymers discussed in the next section. All processes resulted in spherical nanostructures,

though each of a different size (20 nm, 100nm, 15nm, and 20nm, respectively). The increase in size seems to correlate with decreasing polarity, with THF, the least polar solvent employed in this series, giving the smallest NPs. This might occur do to the favorable interaction between a very solvophobic hydrophobic block and less polar solvent. We were interested in whether NP formulation solutions in a mixed solvent system were kinetically trapped or able to equilibrate to a more energetically stable structure. To test this, the micelle solution for **P8** in DMF to water transition was imaged before dialyzing the organic solvent away: TEM of the 50% water solution reveals interesting flower-shaped morphologies, and appear to be comprised of an aggregated worm-like structure flanked by spherical structures. When the DMF was removed, the NPs relaxed to spherical morphology of ~100 nm diameter. Upon close inspection, the particles are bicontinuous structures, though without further probing with cryo-EM, for example, the internal structure cannot be ascertained.

NP5, 6, 7 and 17 were prepared from **P5, P6, P7 and P17**, respectively, and are shown in Fig. 2.13. These polymers demonstrated difficult solubility in organic solvent and upon addition of water during micellization and a very limited sampling of NPs were obtained under the conditions probed. Solubility problems perhaps stem from the hydrophobic nature of the aromatic functional moieties.

These studies highlight that diverse and stable morphologies may be formed through manipulation of the self-assembly process or by changing the polymer architecture. The dynamics of assembly was another strategy to formulate stable NPs. While not exhaustive or predictive, these strategies are feasible for manipulating the self-assembly of polymeric nanoparticles.

2.4 Fluorinated Monomer, Polymers, and Nanoparticles

Next, polymers were prepared in which the hydrophobic block consisted of a perfluorinated carbon chain (PFC, monomer **9**, Fig 2.1). This monomer has been used previously for applications in ultrasound contrast agents.⁶ In this series of polymers, PEG was polymerized first followed by the PFC to promote solubility and allow for easier characterization. It was anticipated that a poly(perfluorohydrocarbon) block would have differing solubility from the monomer; the strategy of polymerizing a solubilizing group first has been utilized in our group.⁸ The resulting polymers, fluorinated polymers 1-3 (**FP1-3**) were analyzed by SEC in chloroform (Table 2.2, Fig. 2.9). ¹H NMR was used in attempt to determine the degree of polymerization of the second (PFC) block,^{1,9} but in all cases, the integration values were extremely low (proton integration of polynorbornene backbone olefin peaks compared to terminal PEG -OCH₃ peak gave a degree of polymerization of the PFC block between 1 and 4). Even though deuterated chloroform, a non-polar solvent, was used for NMR, the polymer may still have aggregated in solution, shielding the protons of the polynorborne olefin backbone, and misrepresenting the actual integration value of protons of interest. Thus, the results from SEC in chloroform were used for reporting the molecular weights and degree of polymerization for **FP1-3**.

Table 2.2 Fluorinated polymer characterizations.

Polymer	Composition	Material Name	DP (m) ^a	DP (n) ^a	M _n ^b		Đ ^c	
					CHCl ₃	DMF	CHCl ₃	DMF
FP1	1₂₀-b-9₃₇	PEG ₂₀ -b-PFC ₃₇	20 (25)	37 (50)	32,540	525,900	1.278	1.093
FP2	1₁₆-b-9₄₀	PEG ₁₆ -b-PFC ₄₀	16 (20)	40 (20)	32,740	243,500	1.262	1.226
FP3	1₂₀-b-9₁₁₂	PEG ₂₀ -b-PFC ₁₁₂	20 (40)	112 (25)	83,690	490,400	1.013	0.1498

^a The degree of polymerization (DP) m and n, are determined using SEC-MALS. Target DPs are in parentheses. For n, the fluoro-block, the reported DP was determined by SEC-MALS in CHCl₃. ^b The number average molecular weight from SEC in CHCl₃ or DMF. ^c The dispersity of copolymer (M_w/M_n).

The polymers were solubilized in various organic solvents before slow transition in to water, and subsequent imaging of micelle solutions to assess morphology. Due to the fluorinated “hydrophobic” group, we probed the utility of a fluorinated solvent for polymer self-assembly in water, and the effects of solvents with varying polarity. The polymers were not soluble in highly polar solvents like DMF and DMSO, and these were subsequently omitted from the screen. Self-assembly from acetonitrile solution was attempted, but only **FP3** was soluble in the solvent.

All 3 **FPs**, when using the fluorinated solvent TFE for the solvent-switch formulation, resulted in similarly sized and relatively monodispersed spherical nanoparticles (**FNPs 1-3**, Fig. 2.3). Because of the nature of the fluorous effect, and the preference for fluorine to solubilize fluorine, using a fluorinated solvent with a perfluorinated polymer block is thought to provide excellent solubility of the core group. This solubility may provide the environment for the fluoro-block to arrange into similar and favorable architectures, leading to a similar morphology. Upon further experimentation with **FP2** and **FP3**, different morphologies were accessed depending on the cosolvent used (Figs. 2.4 and 2.5, respectively) which again supports the idea that nanoparticle morphology can be controlled during the self-assembly process by altering solvent conditions. For example, **FNP2**- THF yielded a [mostly] spherical morphology with some rod-like structures distributed on the grid. Micellization from a dioxane solution gave small branched-like structures. When the same polymer (**FP2**) was used to repeat the micellization procedure, the same phases were accessed (**FNP2'**): formulation from TFE gave spherical NPs, formulation from THF gave a mixture of rod-like structures and spheres, and micellization from a solution in dioxane resulted in a solution of branched-micelles and y-junction mixed phase. For **FP2** and **FNP2**, differential solubility of the fluoro-block by the less polar solvents (TFE, THF and dioxane) was critical for the polymers to arrange in to different structures. **FNP3** took the form of spherical NP when micellized from a TFE, THF or dioxane

solution, but when prepared from more polar acetonitrile, the NPS were rod-like in morphology. These results demonstrate (a) utility of using a perfluorinated monomer as a hydrophobic block, and (b) that solvent selection can affect the self-assembly of fluorinated polymers.

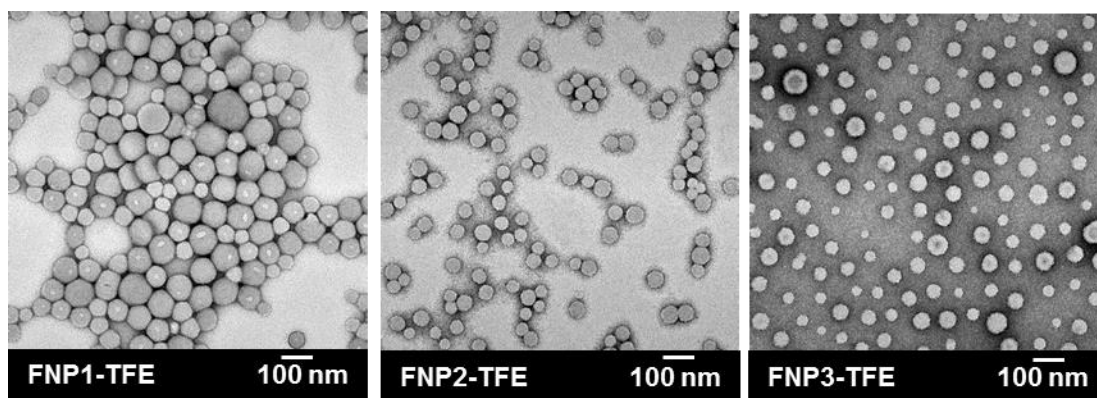


Figure 2.3 TEMs of **FNP1-3**, dialyzed from trifluoroethanol to water. All polymers gave spherical NPs with similar diameter.

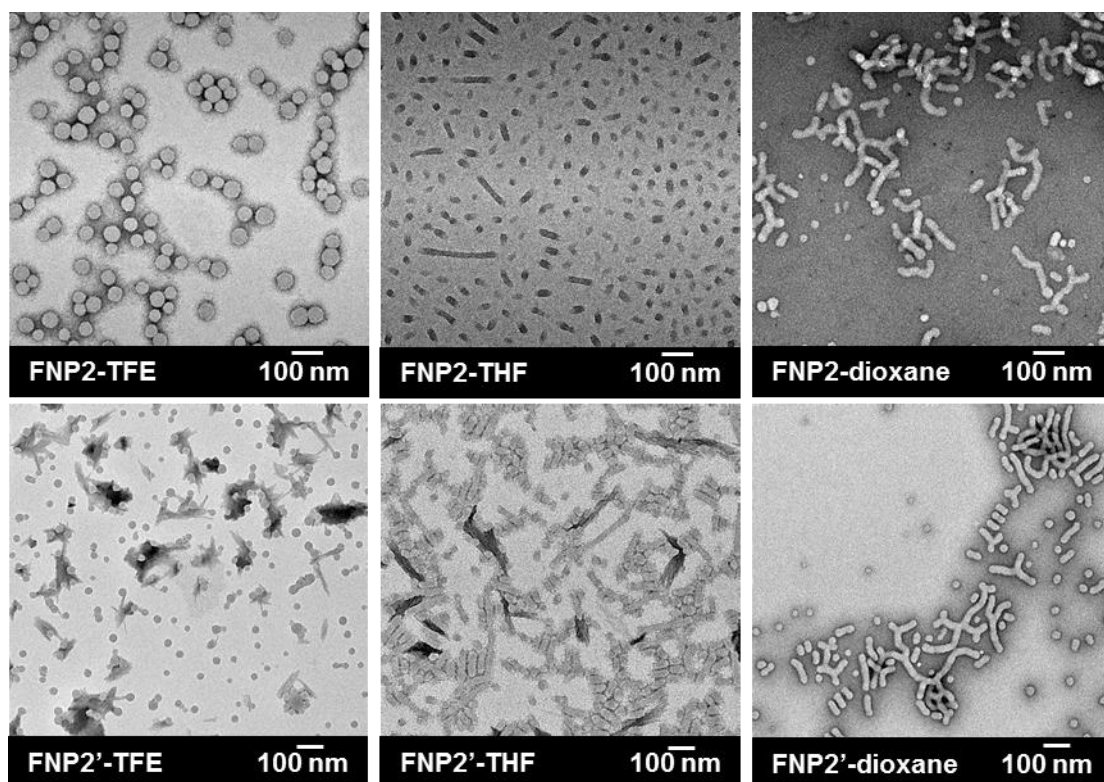


Figure 2.4 TEMs of **FNP2** prepared from different organic solvent conditions. The bottom panel is the repeat preparation of micelles under the same conditions (**FNP2'**) and demonstrates the reproducibility of micelle formation for this system.

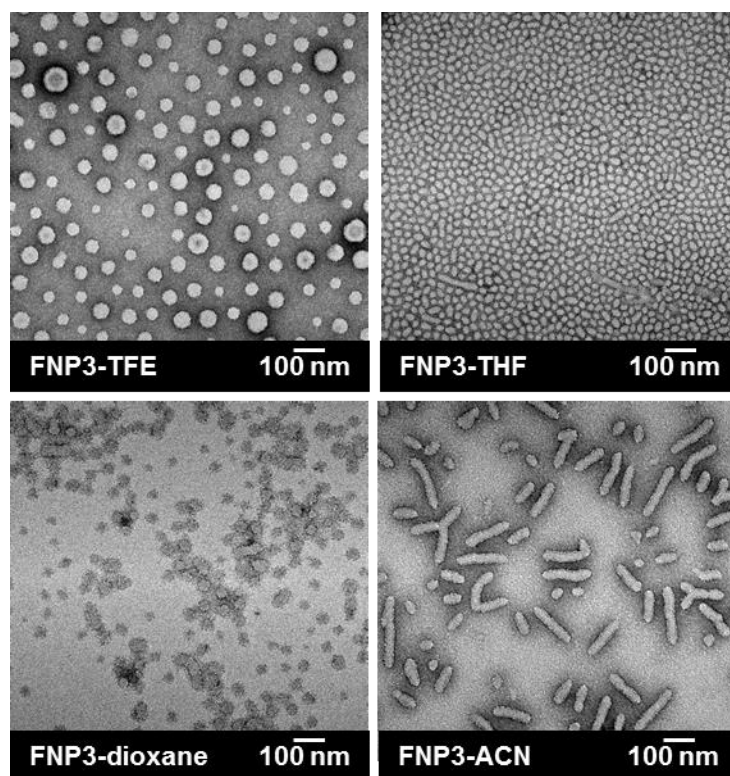


Figure 2.5 TEM of FNP3 prepared from different organic solvent conditions.

With the FNPs in hand, the solutions were investigated for a ^{19}F signal in NMR, but no signal from the micelle was observed for the nanoparticles. In a control experiment, polymer dissolved in organic solvent was subjected to NMR: a proton and fluorine NMR spectra were acquired, both nuclei showing the expected spectra. The observation of the micelle not giving a signal was similar to previously studied perfluorinated cores in polymeric nanoassemblies.¹⁰ The perfluorocarbon group is restricted in movement in the core, and does not give a signal in solution-phase NMR. Future work needs to be done to optimize these systems for utility in ^{19}F MRI applications.

2.5 Conclusions and Outlook

The design, synthesis, and formulation of organic polymers for self-assembled nanoparticles is an intriguing and rich area of research. The work described here complements

other published studies to show how polymer architecture, chemical functionality and manipulation of the self-assembly process can be utilized to prepare discrete nanoparticles towards biomedical applications. We are particularly interested in strategies to formulate nanoparticles of non-spherical morphologies. Towards this goal, we investigated a variety of hydrophobic functionalities in polynorbornene amphiphiles for probing trends in polymer self-assemblies, and demonstrated the ability to kinetically trap equilibrium structures of different phases.

This work demonstrates that varying the chemical identity of the hydrophobic block of an amphiphilic polymer, especially when selection of the hydrophilic block is restricted, serves as a tool in designing NPs with interesting morphologies. Omitting a low T_g hydrophobic block (-Ph), and instead using hydrocarbon groups like -decyl, -hexyl, and -cyclohexyl, non-spherical micelles were obtained. Additionally, by varying the organic cosolvent used in the micelle preparation procedure, it is possible to obtain many NP morphologies from one polymer. When using hydrophobic blocks with aromatic-type moieties (naphthalene, phenol and pyridine), the polymers in this study gave spherical NPs exclusively, if the polymers could be solubilized.

The most interesting results from this study demonstrated the robustness of a perfluorohydrocarbon monomer in synthesizing amphiphilic polynorbornene monomers, and their subsequent utility in preparing differently shaped NPs. Using a fluorinated cosolvent during micellization resulted in monodispersed spherical NPs, while using other less-polar solvents like dioxane and THF resulted in a diversity of morphologies.

Overall, these results indicate that tuning the hydrophobic moiety and self-assembly conditions can result in desired NP morphologies. Several research groups have employed this strategy in studies where NP structure was probed as a function of various parameters of overall molecular weight and ratio of hydrophilic to hydrophobic blocks to optimize polymer self-

assemblies. For example, in a study of polycatechol NPs as gadolinium-free MRI contrast agents, Li and coworkers employed the -hexyl hydrophobic moiety in the preparation of cylindrical micelles.¹¹ Future studies of nanoparticle self-assemblies should capitalize on using non-aromatic moieties and solvent conditions, especially where biomolecules like peptides must be incorporated in to the hydrophilic block.

Towards applying fluorinated polymer micelles in ¹⁹F-MR imaging, NP systems will need to be optimized. The perfluorohydrocarbon monomer used here is just one of many possible monomers, and the polymers structure can be further tuned. Contrast agents for ¹⁹F-MRI hold great promise for a new generation of *in vivo* imaging tools, especially useful since the nucleus probed is non-endogenous.

2.6 Acknowledgments

Monomers **1** and **5-8** were generously provided by Dr. Matthew Thompson.

2.7 Methods

All reagents were purchased from Sigma-Aldrich and used without further purification. ¹H (300 and 400 MHz) and ¹³C (100 MHz) NMR spectra were recorded on a Varian Mercury Plus spectrometer. Mass spectra were obtained at the UCSD Chemistry and Biochemistry Molecular Mass Spectrometry Facility. Polymer dispersities and molecular weights were determined by size-exclusion chromatography (SEC, Phenomenex Phenogel 5μ 10E3A, 1K-75K, 300 x 7.80 mm in series with a Phenomex Phenogel 5μ 10E3A, 10K-1000K, 300 x 7.80 mm (0.05 M LiBr in DMF or HPLC grade CHCl₃) using a Shimatzu pump equipped with a multi-angle light scattering detector (MALS, DAWN-HELIOS: Wyatt Technology) and a refractive index detector (Hitachi L-2490) normalized to a 30,000 MW polystyrene standard using dn/dc of 0.179. TEM was performed on a FEI Sphera microscope operating at 200 keV.

TEM grids were prepared by depositing small (3.5 μ l) aliquots of sample onto grids (formvar stabilized with carbon [5-10 nm] on 400 copper mesh, Ted Pella Inc.) that had previously been glow discharged using an Emitech K350 glow discharge unit and plasma-cleaned for 90 s in an E.A. Fischione 1020 unit. The sample grid was then stained with 1% uranyl acetate solution, rinsed with water (\sim 5 μ L), and excess liquid was removed. Micrographs were recorded on a 2K X 2K Gatan CCD camera

2.7.1 Monomer Synthesis

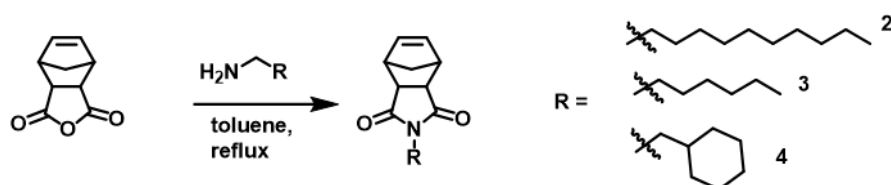


Figure 2.6 Synthetic scheme to prepare monomers **2**, **3** and **4**.

Synthesis of monomer **2**, **3** and **4**. The same reaction conditions were used for the synthesis of all monomers, in a similar manner previously published protocols.⁹ Briefly, *cis*-5-norbornene-*exo*-2,3-dicarboxylic anhydride (250 mg, 1.5 mmol), was dissolved in dry toluene, followed by the addition of a solution of decylamine, hexylamine or cyclohexanemethylamine (1.6 mmol, slight excess), (towards monomers 2, 3, or 4, respectively). The reaction was heated to reflux over night with a Dean Stark trap in place. After the reaction was complete, the solution was cooled, then washed with 3x with 1M HCl, then NaHCO_3 (sat). The organic phase was then dried over sodium sulfate, filtered and concentrated to give a yellow tinted viscous solution (monomer **2**, **3**) or white solid (monomer **4**).

Monomer 2- ^1H -NMR (CDCl_3)- (δ ppm): 0.85 (t, 3H, $-\text{CH}_3$), 1.19-1.33 (m, 15H, $6\times\text{CH}_2$ and H of CH_2), 1.45-1.55 (m, 3H total, $-\text{CH}_2$ and H of CH_2), 2.64 (s, 2H, $2\times\text{CH}$), 3.25 (s, 2H, $2\times\text{CH}$), 3.42 (t, 2H, $-\text{CH}_2$), 6.26 (s, 2H, $\text{CH}=\text{CH}$).

Monomer 3 $^1\text{H-NMR}$ (CDCl_3)- (δ ppm): 0.78 (t, 3H, CH_3), 1.11-1.28 (m, 7H total, $3\times\text{CH}_2$, H of CH_2), 1.39-1.52 (3H total, $-\text{CH}_2$ and H of CH_2), 2.58 (2H, $2\times\text{CH}$), 3.17 (2H, $2\times\text{CH}$), 3.36 (t, 2H, CH_2), 6.20 (s, 2H, $\text{CH}=\text{CH}$).

Monomer 4 $^1\text{H-NMR}$ (CDCl_3)- (δ ppm): 1.10-1.32 (3H, $1\times\text{CH}_2$ and H of CH_2), 1.49-1.77 (m, 10H, $4\times\text{CH}_2$ and H of CH_2 , H of CH_2), 2.69 (s, 2H, $2\times\text{CH}$), 3.31 (m, 4H, $-\text{CH}_2$ and $2\times\text{CH}$), 6.29 (s, 2H, $\text{CH}=\text{CH}$).

PEG monomer (1) and perfluorohydrocarbon monomer **9** were prepared as previously described.^{6,12,13}

2.7.2 Polymer Synthesis and Characterization

Third generation Grubbs catalyst was prepared as described previously.^{14,15} Briefly, the second generation catalyst ($[(\text{H}_2\text{IMes})(\text{PCy}_3)(\text{Cl})_2\text{Ru}=\text{CHPh}]$) was dissolved in dry toluene, and an excess of pyridine dropped in to a stirring solution. Then that solution was added dropwise to cold hexanes to precipitate the catalyst: $[(\text{H}_2\text{IMes})(\text{py})_2(\text{Cl})_2\text{Ru}=\text{CHPh}]$. Polymerizations were performed under a dry dinitrogen atmosphere with anhydrous, degassed solvents in a glove box. For all monomers in this study, polymerization kinetics were fast (detailed studies not determined here, but similar kinetics as described in Ref. 9) and after ~30 minutes, a small aliquot of the living polymer solution was removed, quenched and analyzed for block length and dispersity. Then the second monomer was dissolved and added to the solution and allowed to react another ~30 minutes. The reaction was quenched with ethyl vinyl ether, and analyzed for coblock molecular weight and dispersity using SEC-MALS in DMF (except where indicated). The polymer solution was concentrated then precipitated three time with cold ether to remove quenched “Ru” catalyst. The polymers were used as is for micellization procedures. Characterization for **P1-P8** is in Table 2.1, and for **P9-P17** is in Table 2.3. Fluorinated polymers (**FP**) 1-3 are described in Table 2.2. The SEC chromatograms are in

Figs. 2.6-2.8. In many cases, a PEG homopolymer was prepared, characterized, and split in to batches before addition of second monomer, hence these polymers have identical hydrophilic block.

Table 2.3 Molecular Characterizations of **P9-P17**.

Polymer	Composition	Material Name	DP (m) ^a	DP (n) ^a	M _n ^b	Đ ^c
P9	1₅₀-b-2₁₀₇	PEG ₅₀ -b-Dec ₁₀₇	50(50)	107(50)	50,660	1.2
P10	1₅₀-b-3₉₇	PEG ₅₀ -b-Hex ₉₇	50(50)	97(50)	42,680	1.028
P11	1₅₀-b-4₅₆	PEG ₅₀ -b-Cy ₅₆	50(50)	56(50)	32,080	1.055
P12	1₂₄-b-3₄₃	PEG ₂₄ -b-Hex ₄₃	24(30)	43(30)	19,160	1.010
P13	1₂₄-b-3₁₄	PEG ₂₄ -b-Hex ₁₄	24(30)	14(15)	11,900	1.013
P14	1₄₂-b-2₂₈	PEG ₄₂ -b-Dec ₂₈	42 (30)	28(30)	23,400	1.096
P15	1₄₂-b-2₄	PEG ₄₂ -b-Dec ₁₄	42 (30)	14(15)	19,370	1.132
P16	1₂₁-b-5₃₇	PEG ₂₁ -b-Nap ₃₇	21(30)	37(30)	19,270	1.039
P17	1₁₄-b-7₁₄	PEG ₂₁ -b-Pyr ₇₂	21(30)	72(15)	26,200	1.049

^a The degree of polymerization (DP) m and n, are determined using SEC-MALS. Target DPs are in parentheses. For n, the reported DP was determined by SEC-MALS in DMF. ^b The number average molecular weight. ^c The dispersity of copolymer (M_w/M_n).

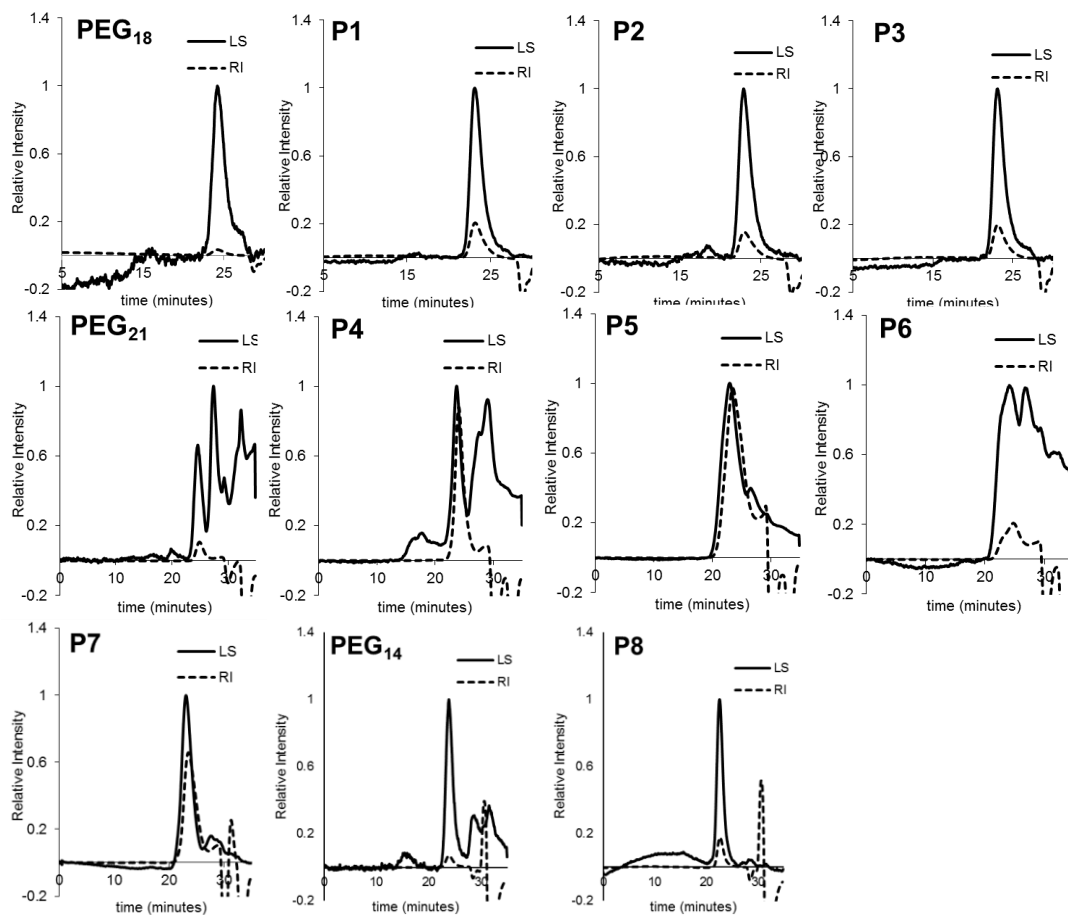


Figure 2.7 SEC-MALS traces for polymers **P1-P8**.

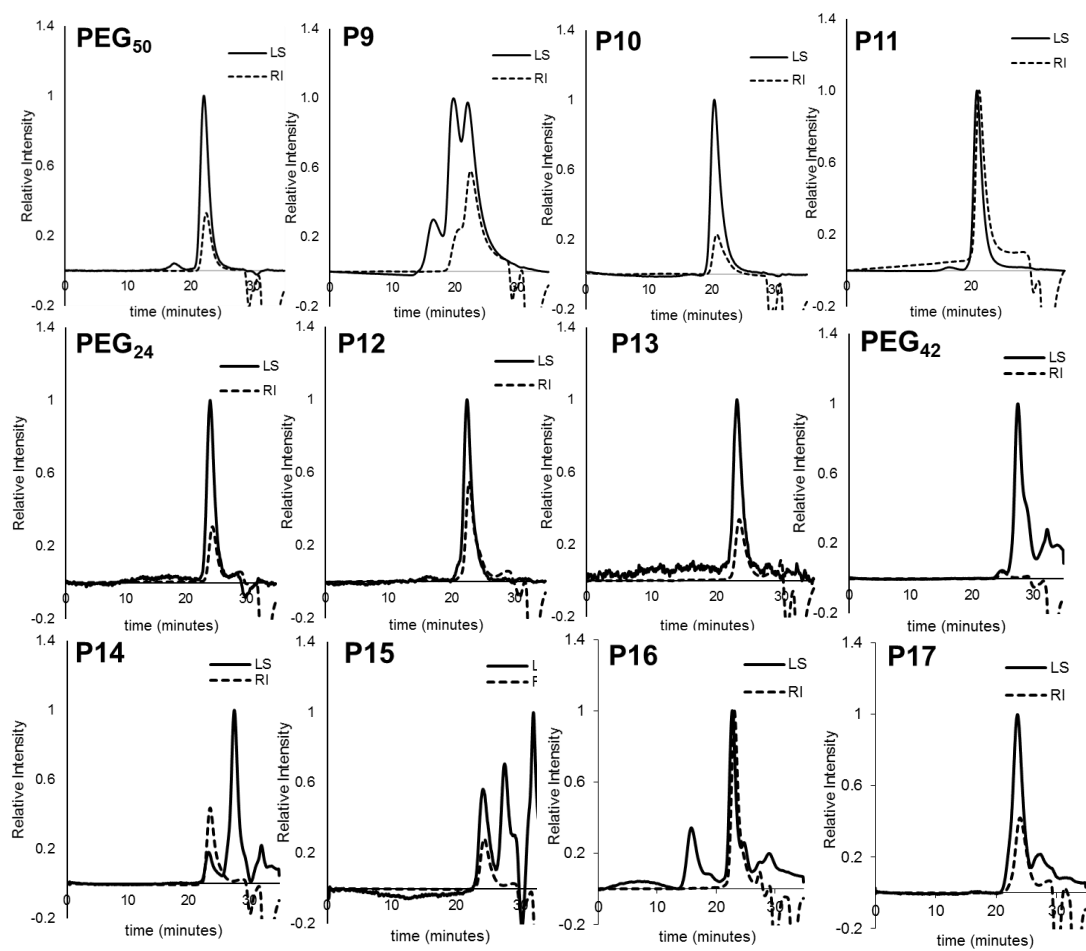


Figure 2.8 SEC-MALS traces for **P9-P17**.

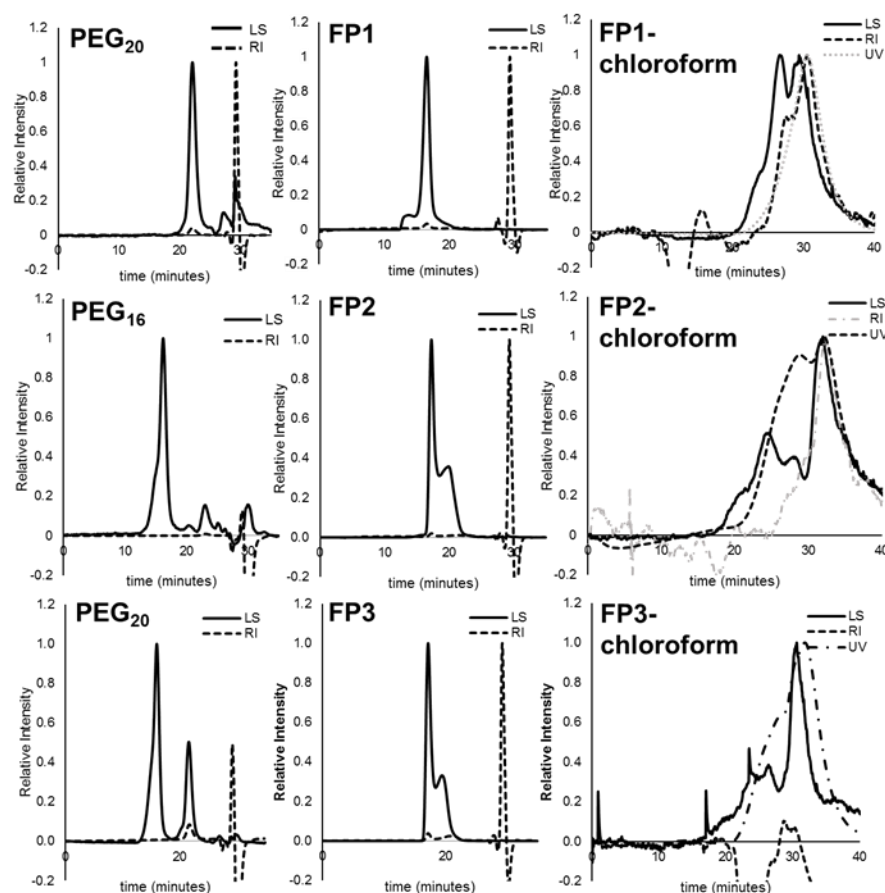


Figure 2.9 SEC-MALS traces for **FP1-3**. The first two chromatograms in each row are the PEG block followed by the coblock, run in DMF. In all cases, the polymers seemed to aggregate on the column and gave unrealistically high polymer MWs. Thus, these polymers were run with chloroform as a mobile phase, resulting in much cleaner analyses. The results of the coblock polymer run in chloroform was used to identify the polymer block lengths.

2.7.3 Formulation of Nanoparticles

General procedure: Polymers were solubilized in organic solvent (1-2 mg/mL). Water was added dropwise with gentle mixing until reaching a 1:1 v/v solution. The solution was then placed in snakeskin dialysis tubing with 3500 MWCO, and dialyzed against water, changing the dialysate two times. Nanoparticles were imaged using dry-state TEM. Samples were prepared as described in general methods section; all were negatively stained with uranyl acetate.

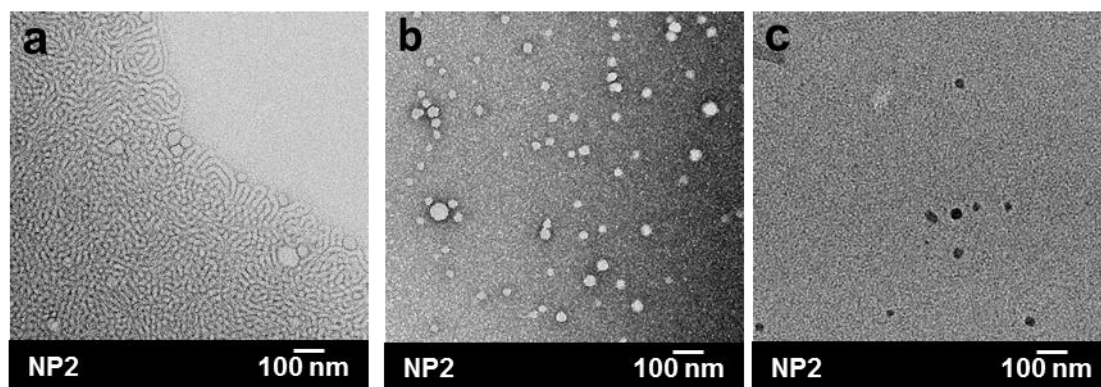


Figure 2.10 TEMs of NP2. Polymer 2 dialyzed from DMF to water, under the following conditions: a. slow addition of water, b. DMF + 13% v/v water, c: sample from previous panel dialyzed to remove solvent.

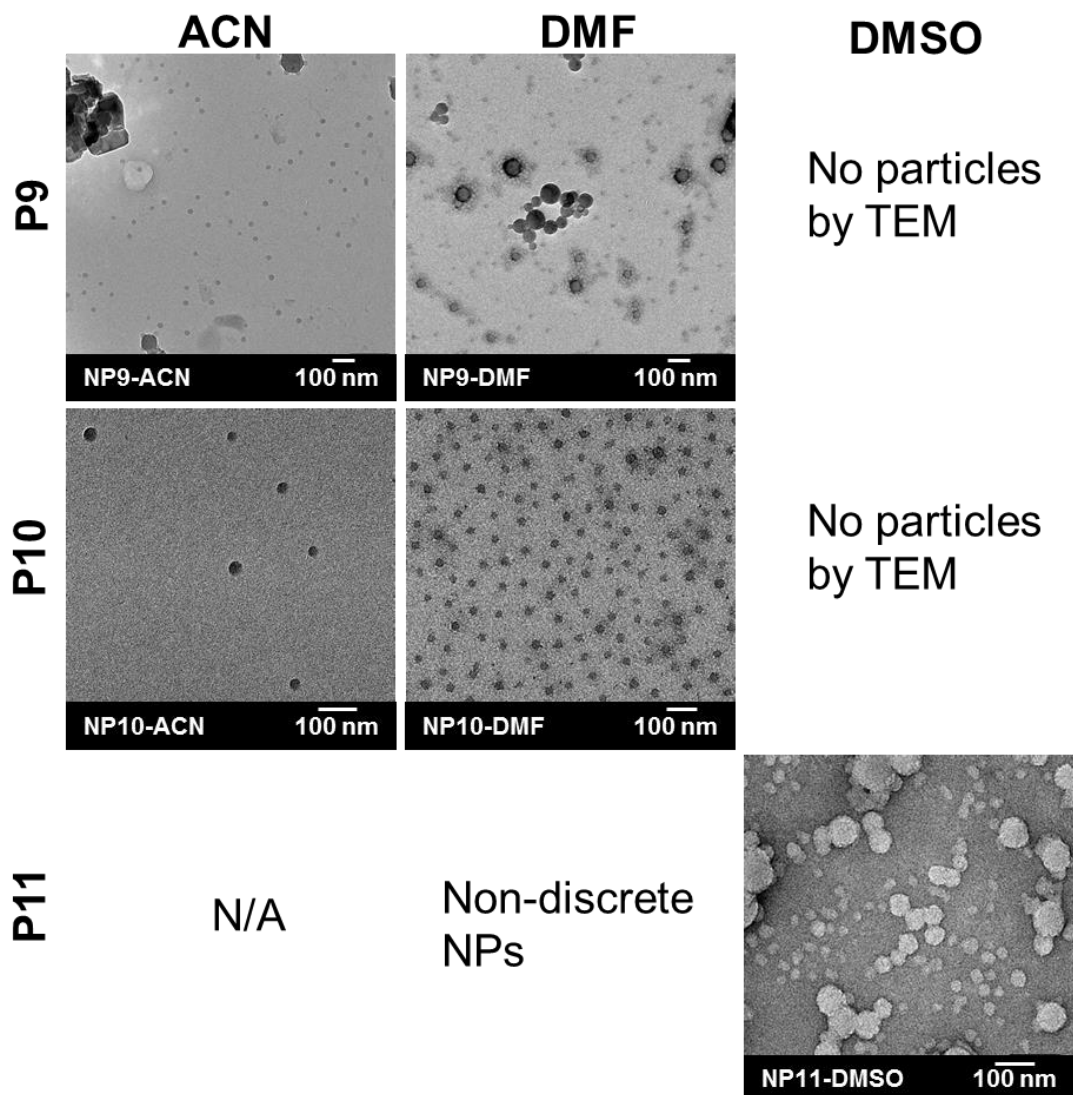


Figure 2.11 TEMs of NP9, NP10 and NP11, from polymers P9, P10 and P11, respectively. P9 and P10 first dissolved in DMSO did not result in any discrete structures when observed by TEM. P11 first dissolved in DMF did not yield discrete NPs either, and formulation using acetonitrile as a solvent was not done.

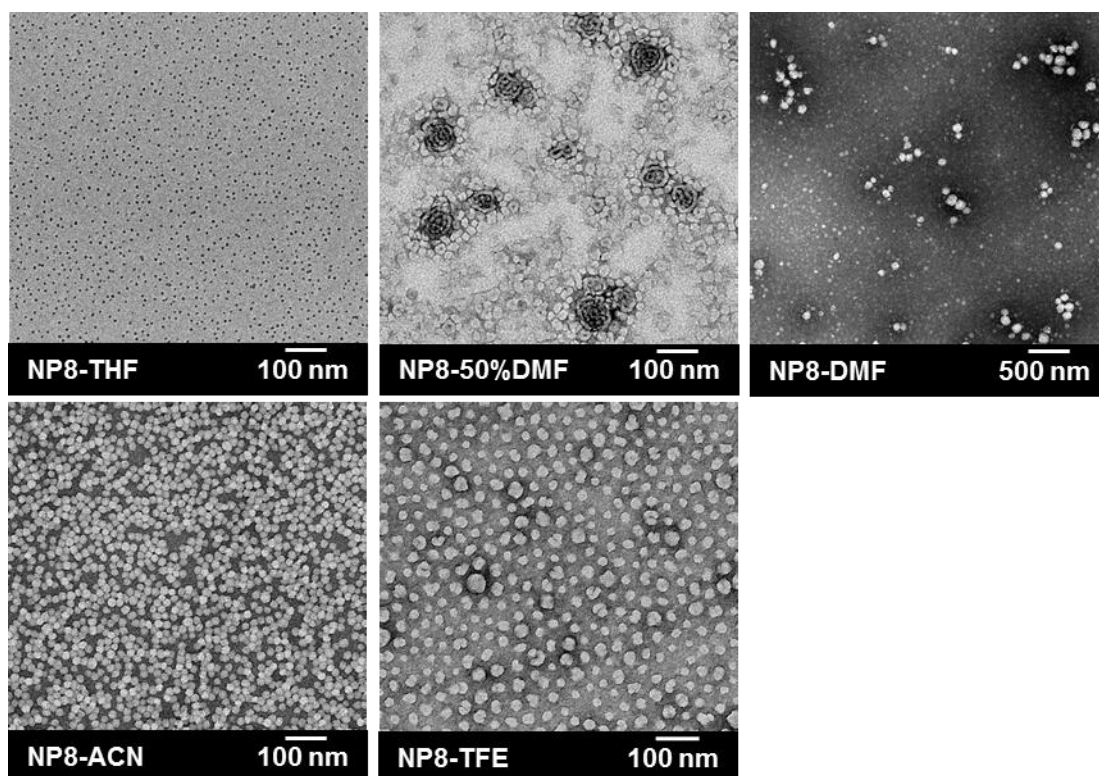


Figure 2.12 TEMs of NP8. Polymer 8 micellized under various solvent conditions. The solvent descriptions represent the initial solvent used, except for “NP8-50%DMF,” which is an image of the solution at 50% v/v water in DMF. That solution was then dialyzed in to 100% water to give the structures in “NP8-DMF.”

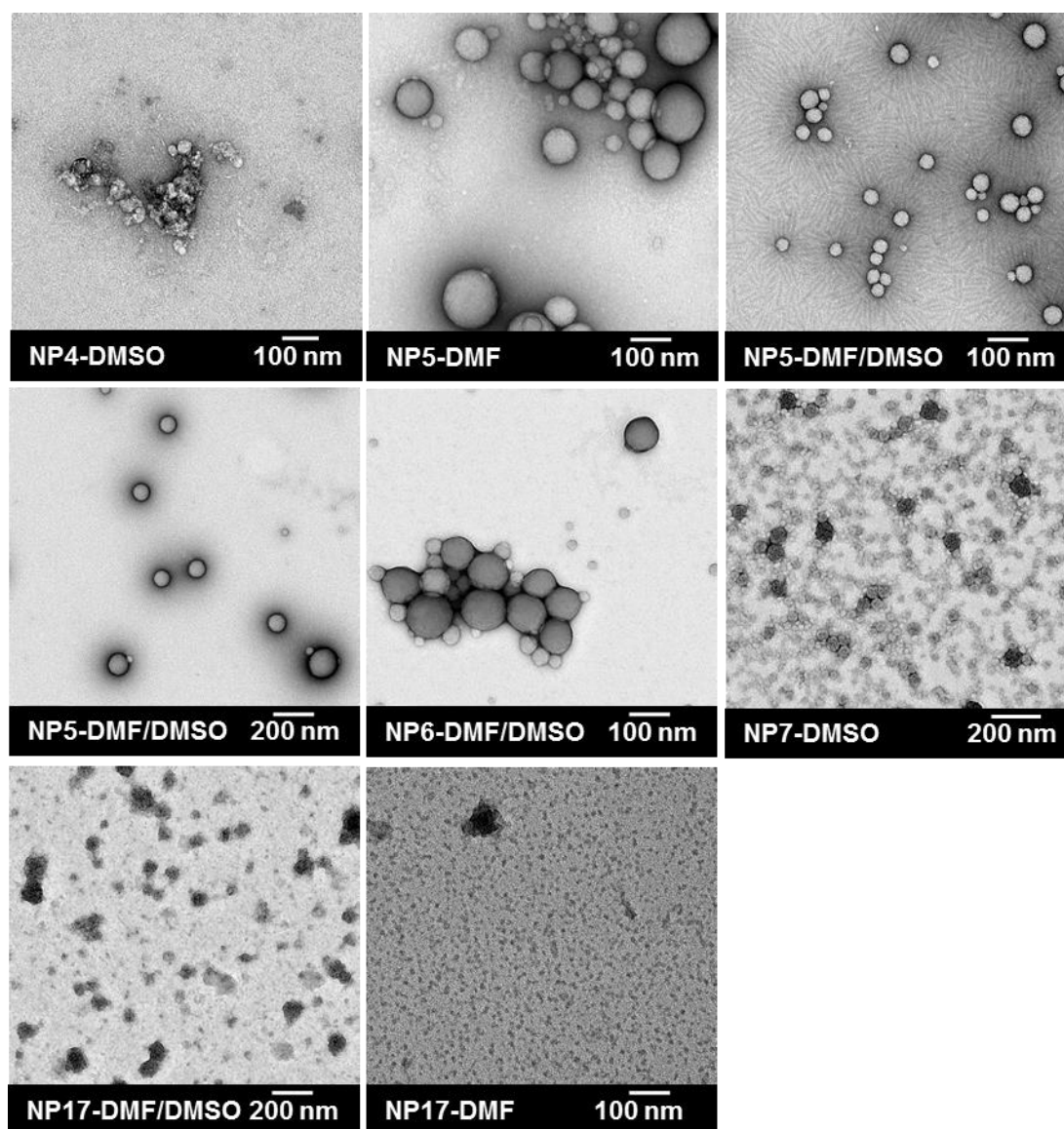


Figure 2.13 TEMs of NP4, NP5, NP6, NP7 and NP17. Discrete NPs were not observed for P9-P11 or P16-17. P12-P15 were not used in any NP formulation screens. The solvent description is the initial dissolution organic solvent and the solutions imaged are the dialyzed, 100% water micelle solutions. “DMF/DMSO” represents dissolution in a 1:1 v/v solvent mixture of DMF/DMSO.

2.8 References

- (1) Barnhill, S. A.; Bell, N. C.; Patterson, J. P.; Olds, D. P.; Gianneschi, N. C. *Macromolecules* **2015**, 48 (4), 1152–1161.
- (2) Won, Y.; Brannan, A. K.; Davis, H. T.; Bates, F. S. *J. Phys. Chem. B* **2002**, 106 (13),

3354–3364.

- (3) Jain, S.; Bates, F. S. *Science*. **2003**, *300*, 460–464.
- (4) Tirotta, I.; Dichiarante, V.; Pigliacelli, C.; Cavallo, G.; Terraneo, G.; Bombelli, F. B.; Metrangolo, P.; Resnati, G. *Chem. Rev.* **2015**, *115*, 1106–1129.
- (5) Cametti, M.; Crousse, B.; Metrangolo, P.; Milani, R.; Resnati, G. *Chem. Soc. Rev.* **2012**, *41* (1), 31–42.
- (6) Huang, Y.; Vezeridis, A. M.; Wang, J.; Wang, Z.; Thompson, M.; Mattrey, R. F.; Gianneschi, N. C. *J. Am. Chem. Soc.* **2017**, *139*, 15–18.
- (7) Kammeyer, J. K.; Blum, A. P.; Adamiak, L.; Hahn, M. E.; Gianneschi, N. C. *Polym. Chem.* **2013**, *4* (14), 3929–3933.
- (8) James, C. R.; Rush, A. M.; Insley, T.; Vukovic, L.; Adamiak, L.; Kral, P.; Gianneschi, N. C. *J. Am. Chem. Soc.* **2014**, *136* (32), 11216–11219.
- (9) Thompson, M. P.; Randolph, L. M.; James, C. R.; Davalos, A. N.; Hahn, M. E.; Gianneschi, N. C. *Polym. Chem.* **2014**, *5* (6), 1954–1964.
- (10) Nyström, A. M.; Bartels, J. W.; Du, W.; Wooley, K. L. *J. Polym. Sci.* **2008**, *49* (1), 511–512.
- (11) Li, Y.; Huang, Y.; Wang, Z.; Carniato, F.; Xie, Y.; Patterson, J. P.; Thompson, M. P.; Andolina, C. M.; Ditri, T. B.; Millstone, J. E.; Figueroa, J. S.; Rinehart, J. D.; Scadeng, M.; Botta, M.; Gianneschi, N. C. *Small* **2016**, *12* (5), 668–677.
- (12) Thompson, M. P.; Randolph, L. M.; James, C. R.; Davalos, A. N.; Hahn, M. E.; Gianneschi, N. C. *Polym. Chem.* **2014**, *5* (6), 1954–1964.
- (13) Kvach, M. V.; Tsybulsky, D. A.; Ustinov, A. V.; Stepanova, I. A.; Bondarev, S. L.; Gontarev, S. V.; Korshun, V. A.; Shmanai, V. V. *Bioconjug. Chem.* **2007**, *18* (5), 1691–1696.
- (14) Love, J. A.; Morgan, J. P.; Trnka, T. M.; Grubbs, R. H. *Angew. Chemie Int. Ed.* **2002**, *41* (21), 4035–4037.
- (15) Sanford, M. S.; Love, J. a; Grubbs, R. H. *Organometallics* **2001**, *20* (25), 5314–5318.

Chapter 3

MRI Contrast Agent Labeled Polymeric Nanomaterials for *In Vivo* Imaging

3.9 Introduction

The utility of macromolecular platforms, specifically polymeric and nanoparticle systems, in nanomedicine applications was discussed in detail in Chapter 1. It is highly desirable to develop nanoparticle platforms with their clinical translatability in mind, with regards to both therapeutic and diagnostic applications. This chapter focuses on diagnostic applications in nanomedicine, and specifically *in vivo* imaging using the magnetic resonance imaging (MRI) modality.

The Molecular Imaging and Contrast Agent Database, maintained by the National Center for Biotechnology Information at the National Institutes of Health, documents thousands of molecular imaging probes and contrast agents.¹ As of 2013, there are over one hundred FDA-approved contrast agents on the market for optical, X-ray, PET, ultrasound, CT and MR imaging modalities. We are interested in using MRI because it offers anatomic co-registration with excellent tissue characterization, lack of ionizing radiation, and in general, provides high quality images at clinically relevant imaging depths. In addition, the instrumentation and technical support for preclinical MR imaging is readily available to our lab. We are particularly interested in using gadolinium-based contrast agents (GBCAs) because these are by far the most commonly used MRI contrast agents.² There are examples of clinically

approved manganese and iron-oxide contrast agents for MRI, but we decided to investigate derivatives of the macrocyclic ligands for gadolinium contrast agents due to the relative ease of synthesis.

In the decades since the first GBCA was developed and clinically approved (Magnevist, 1980's) many researchers have investigated strategies for improving the efficacy of contrast agents.² This includes improving the relaxivity of the agent, or improving targeting to a site of interest, if applicable.²⁻⁴ As detailed in Chapter 1 and summarized here, increasing the relaxivity can be achieved by: 1) decreasing the molecular tumbling rate, 2) increasing the water exchange rate, or 3) increasing the q-value. When the tumbling rate is slowed, for example by coupling to a high molecular weight species (*eg* macromolecule or protein), further increases in relaxivity are limited by the water exchange rate.² To increase water exchange rates or q-value, the molecular structure of the chelate must be modified. A cartoon depiction of strategies to improve relaxivity of GBCA using macromolecular architectures is shown in Fig. 3.1, adopted from Caravan's Review highlighting such strategies, with the GBCA represented as a green circle.⁴ In panel a), the contrast agent is incorporated in macromolecular or polymeric form. In panel b), the contrast agent is appended to a nanoparticle, here represented on the surface of the particle; a similar architecture is envisioned for a dendritic structure containing a GBCA. In panel c), the contrast agent is fixed at the barycenter of a macromolecule. In all three scenarios, per-gadolinium relaxivity is increased due to the slower tumbling of the species. In a and b, if the contrast agent is not restricted, the agent may still spin on its axis, and thus the correlation is not fully matched to the macromolecule. In c, the contrast agent is somewhat restricted; relaxivity increases would then be limited by water exchange rates.

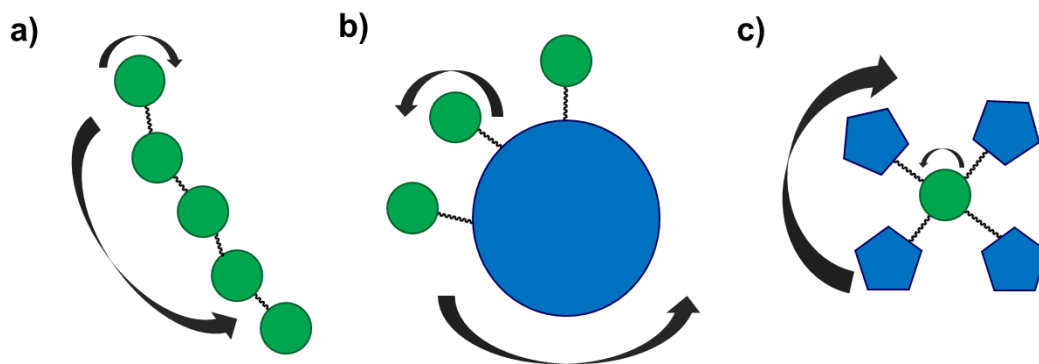


Figure 3.1 Scheme of macromolecular effects of GBCA. Adopted from Ref. 4. Appending a contrast agent to a macromolecule or nanoparticle slows the tumbling rate (represented by the large arrows), increasing relaxivity. Increases in relaxivity are then limited by local rotational correlation effects (represented by the small arrows), or slow water exchange rates

In this chapter, polymeric nanoparticle platforms incorporating a gadolinium-based contrast agent for magnetic resonance imaging are described. In this approach, the nanoparticles are expected to demonstrate increased relaxivity based on the coupling to a slower tumbling nanoparticle species (as in Fig. 3.1b). Towards this aim, we prepared amphiphilic block copolymers for the formation of micellar NPs, in which the hydrophilic block consists entirely of a Gd-based contrast agent for MRI. In developing this type of material, we sought a synthetic route through which the Gd^{3+} functionalized monomers are introduced directly into the polymer *via* a living polymerization approach, obviating the need for post-polymerization conjugation strategies, or ligand metalation processes.⁵⁻⁹ We then studied these materials as MRI contrast agents using *in vitro* techniques (nuclear magnetic resonance dispersion, NMRD) as well as *in vivo*, live animal imaging in mice.

First, the chemical tools for direct incorporation of a GBCA into the ROMP scheme are described. This is important in maintaining precise control of functionality and site-specific incorporation during synthesis of materials. Described here are the first examples of a directly polymerized norbornene-derived GBCA monomer and chain transfer agent (CTA) using

ROMP (Fig. 3.2). Having both tools at one's disposal allows for synthesis of highly tailorable materials, with a range of options for modulation of polymer architecture.

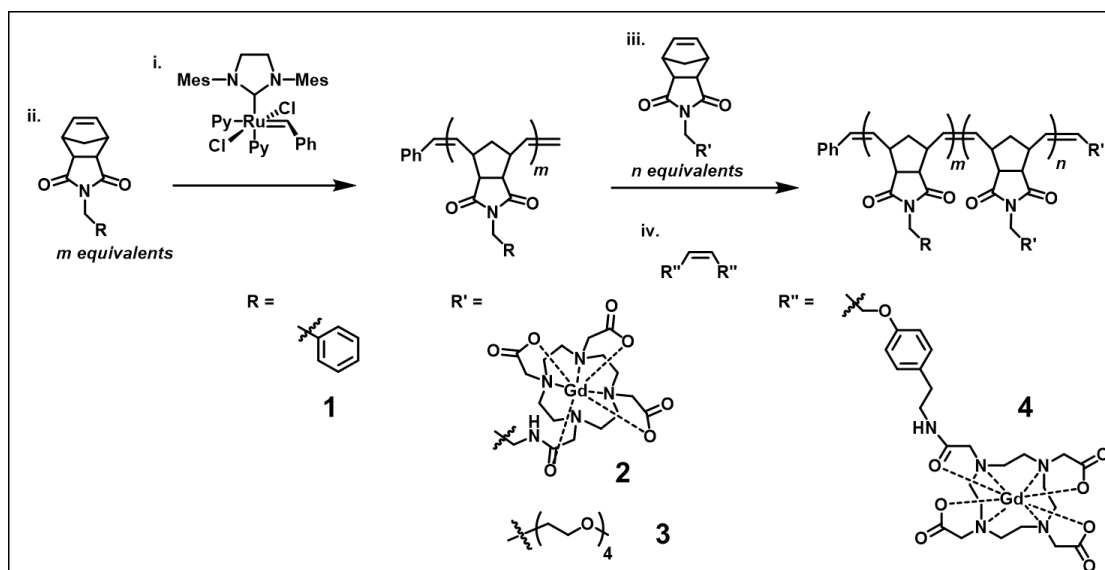


Figure 3.2 ROMP scheme for incorporation of a gadolinium-containing monomer or chain transfer agent. This scheme was followed for all polymers in the chapter. Depending on the ratio of the blocks, the polymer amphiphiles assemble in to different nanoparticle structure.

With these chemical tools in hand, polymers were synthesized and formulated into nanoparticles. These NPs were then evaluated in biologically relevant systems using MRI. While current FDA approved clinical agents are mostly small molecules, it is well known that macromolecular contrast agents could provide a better platform for diagnostic type materials: macromolecule GBCA have higher relaxivities, longer blood circulation times, and favorable properties that researchers have explored extensively. Serendipitously, two differently shaped NPs were formulated: spheres and fibers. These materials allowed us to probe the following questions in subsequent studies: 1) how is the relaxivity of a material affected when GBCA is incorporated into polymeric NPs as a discrete block, and 2) how does shape affect the relaxivity? The materials were then evaluated *in vivo* for their contrast ability. Further, with the two different shapes, would there be detectable differences in the biodistribution of the

materials correlated to their shapes? Another application of direct incorporation of GBCA is presented as a CTA; this approach was evaluated and utility demonstrated with a stimuli-responsive peptide-polymer-based platform.

The impact of this work lies in the ability to tailor soft materials to a particular imaging application. Ultimately, our goal for this work was to establish strategies to incorporate clinically translatable imaging agents suitable for *in vivo* imaging of targeted polymeric nanoparticle systems developed in the Gianneschi Lab. With the monomer and CTA in hand, along with well-defined methods for characterization of these polymers, materials can be formulated for diagnostic purposes. To date, there are no clinically approved, targeted contrast agents despite the rich literature investigating targeting of nanoparticle diagnostics. Using a targeted NP with a reporter like gadolinium in conjunction with cancer therapy may allow for sensitive detection of non-resected tumor, or metastases, and is a long-term work of this research.

3.10 Graft-Through Polymerization of a Gd-DOTA Moiety

In this section, graft-through polymerizations of a Gd-DOTA-monoamide monomer are described (DOTA = -1,4,7,10-tetraazacyclododecane-1,4,7,10-tetraacetic acid). The polymers are subsequently formulated as nanoparticles, and *in vitro* studies are described. To our knowledge, this represents the first demonstration of a Gd³⁺-labeled polymer prepared entirely by direct polymerization. Examples of Gd³⁺-labeled polymers and soft NPs to date have employed post-polymerization metal chelation, requiring subsequent purification steps and removal of excess Gd³⁺.¹⁰ In work from the Kiessling group, one arm of a hydroxypyridinone (HOPO)-Gd³⁺ chelate was directly polymerized using ROMP, followed by reaction with the other ligands to form the complete chelate, and subsequent metalation. This polymeric GBCA demonstrated higher relaxivities compared to other clinically approved

contrast agents, but no enhancement over the small molecule HOPO ligands originally developed by Raymond.^{11,12} In our work, direct, graft-through polymerization of a metalated, monomer derivative of a GBCA offers a strategy that circumvents post-polymerization modifications and metalations.

3.10.1 Synthesis of Gd-DOTA Norbornyl Monomers

Monomer **2** (Figs. 3.2 and 3.18) is a novel compound, synthesized specifically for direct incorporation of a modified Gd-DOTA moiety *via* living, ring-opening metathesis polymerization (ROMP).^{13,14} The norbornenyl-Gd-DOTA monoamide enables visualization with standard T₁-weighted MRI. Importantly, **2** is complexed to Gd³⁺ prior to its incorporation into synthetic polymers.

Briefly, a NB-amine was reacted with a mono-NHS activated DOTA. The reaction was capped with acetic anhydride, then neutralized before metalation with Gd(OAc)₃. The product was purified using semi-preparative HPLC. The four reactive acids on DOTA proved problematic in the synthesis, with respect to the yield. While the N-hydroxysuccinimide (NHS)-DOTA was selected initially as the reactive reagent, the NHS was prone to hydrolysis before introducing the material in to the reaction vessel, and therefore did not enhance selectivity. The DOTA-derived monomer could also be synthesized using differently protected ligands. The tris-*t*Bu monoacid ligand is readily available commercially, and is now more commonly used in our lab. A key feature of the monomer is that gadolinium is pre-chelated with the organic ligand, obviating the need for most polymerization metalation and purifications. Subsequently, the pure monomer was used in further polymerization studies.

3.10.2 Preparation and Characterization of Polymers with Gd-DOTA as Hydrophilic Entity

We prepared amphiphilic block copolymers from hydrophobic monomer **1** (-phenyl, Ph) and hydrophilic monomer **2** (Gd). Gratifyingly, we could avoid post-polymerization modifications, given that **2** was consumed during ROMP reactions (Figs. 3.22 and 3.23). Because gadolinium is paramagnetic, peak broadening in the ^1H -NMR prevents the monitoring of polymerization progression, and therefore HPLC provides a method to monitor reaction progress. Polymers were characterized using SEC-MALS, (Figs. 3.22 and 3.23), and summarized in Table 3.1.

Table 3.1 Polymer Characterization.

Polymer	Composition	Material Name	DP m ^a	DP n ^a	M _n ^b	Đ ^c	Used to make NP:
P1	1 ₂₁₀ - <i>b</i> - 2 ₄	Ph ₂₁₀ - <i>b</i> -Gd ₄	210	4	55,740	1.004	SMN
P2	1 ₄₂ - <i>b</i> - 2 ₂	Ph ₄₂ - <i>b</i> -Gd ₂	42	2	11,910	1.024	FMN

^a The degree of polymerization (DP) m and n, are determined using SEC-MALS. ^b The number average molecular weight. ^c The dispersity of copolymer (Mw/Mn).

3.10.3 Nanoparticle Formulation and Characterization

Following synthesis, polymers were self-assembled using a solvent switch method. Solutions of **P1** and **P2** were subjected to slow transition from DMSO to water *via* dialysis, inducing the assembly of micellar NPs. NP structure was determined by transmission electron microscopy (TEM) and scanning TEM (STEM). For **P1**, negative stain TEM revealed spherical micellar nanoparticles with low dispersity (with average diameter of 25 nm and standard deviation of 2.9 nm, and are hereafter referred to as SMN, Fig. 3.3b and 3.4).

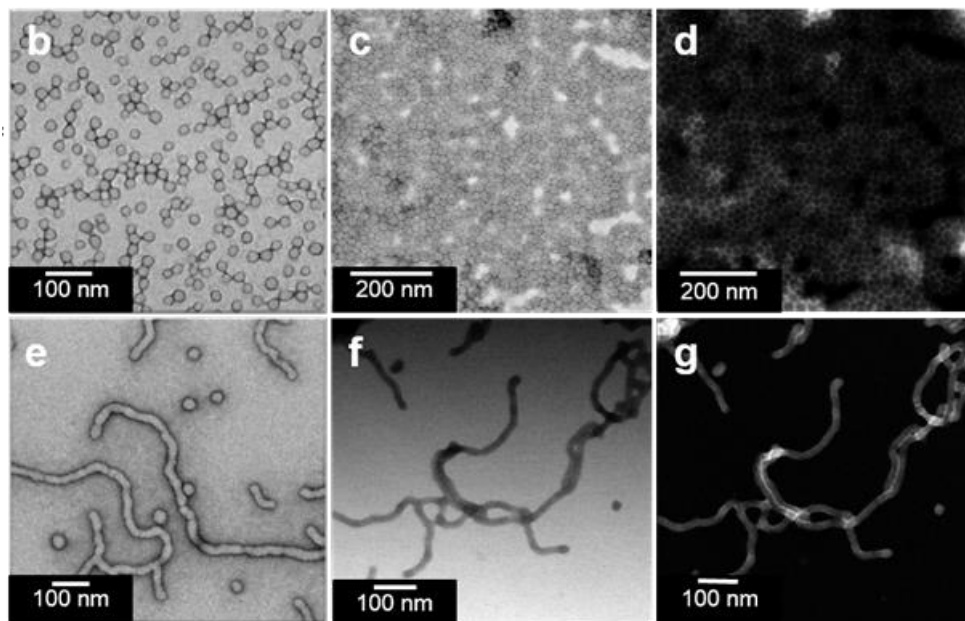


Figure 3.3 Particle characterization by electron microscopy of spherical micellar nanoparticles (SMNs) and fibril-shaped micellar nanoparticles (FMNs). (b) Negative stained TEM of SMN. (c) Unstained BF-STEM of SMN. (d) Unstained HAADF-STEM of SMN. (e) Negative stained TEM of FMN. (f) Unstained BF-STEM of FMN. (g) Unstained HAADF-STEM of FMN

Unstained, bright field STEM (BF-STEM) demonstrated close packing of NPs with dark rings around the coronas, as would be expected for a NP bearing a heavy element (i.e. Gd^{3+}) in the corona (Fig. 3.3c). This is supported by unstained, high-angle annular dark field (HAADF) STEM coupled with energy-dispersive X-ray spectroscopy (EDS), which confirmed the presence of Gd^{3+} in the shell of the particle indicated by bright halos (Z-contrast) around the outer edges and characteristic X-ray edges of Gd^{3+} (Figs. 3.3d and 3.27).

Similar microscopy characterization was performed on NPs derived from **P2**. Negative stain TEM, unstained BF-STEM, and unstained HAADF-STEM analysis revealed a predominantly fibrillar morphology, with Gd^{3+} present within the shell (Fig. 3.3e-g). STEM-EDS also confirms Gd^{3+} on the shell of the particles (Fig. 3.28). We refer to these predominantly fibril-shaped NPs as fibrillar micellar nanoparticles (FMN), but note that the FMN formulation

was not an entirely homogeneous phase, containing a minor component of spherical NPs. Indeed, mixed phases are common for cylindrical micelles.¹⁵ However, FMN represents approximately 95% of the sample, as determined by TEM image analysis (Fig. 3.5 and Table 3.2).

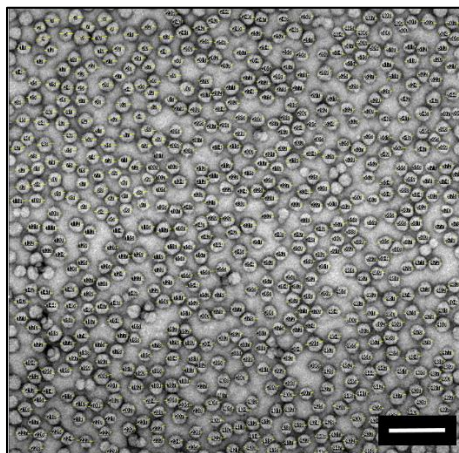


Figure 3.4 SMN phase analysis. TEM image analyzed for sphere diameter uniformity (scale bar = 100 nm). Diameters of particles were measured in ImageJ. 604 particles were counted, and found to have an average diameter of 24.7 nm, with a standard deviation of 2.9 nm.

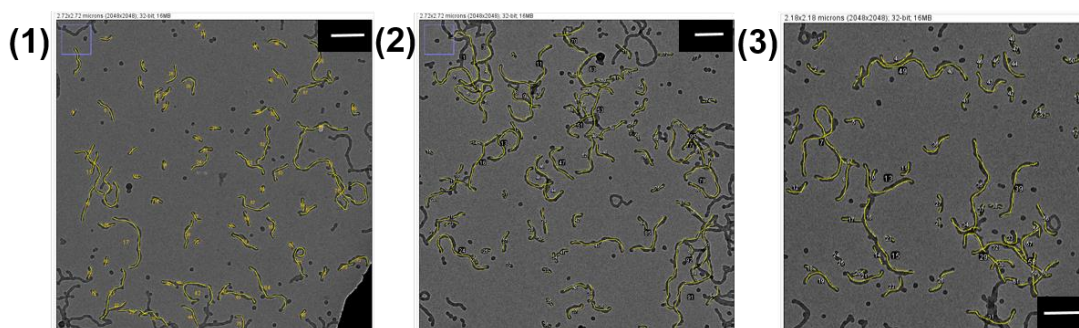


Figure 3.5 FMN phase analysis. Three TEM images were analyzed for % volume fibrillar phase (scale bar = 250nm). Lengths of fibrillar particles were measured in ImageJ, as indicated by the yellow lines above in representative TEM images (1)-(3), above. Diameter of the fibers was assumed to be the same as the spheres, and volume was calculated using the average sphere radius. Volume of the spheres was calculated accordingly, and summation of volume of tabulated spheres and fibers was used to determine respective ratios, as listed in Table 3.2.

Table 3.2 Measured volumes of spheres and non-spheres in FMN.

Image #	Total measured volume (nm³)	Fraction non-sphere	% non-sphere
1	0.013	0.941	94.2
2	0.021	0.963	96.3
3	0.011	0.948	94.8
Average % volume non-sphere			95.1

Importantly, the two NP formulations are stable as SMN or FMN for periods in excess of 14 months in aqueous media (Figs. 3.25 and 3.26). Moreover, cryo-TEM revealed that NPs remain identifiable following incubation in blood serum at 37 ° C for one week (Figs. 3.6 and 3.7).

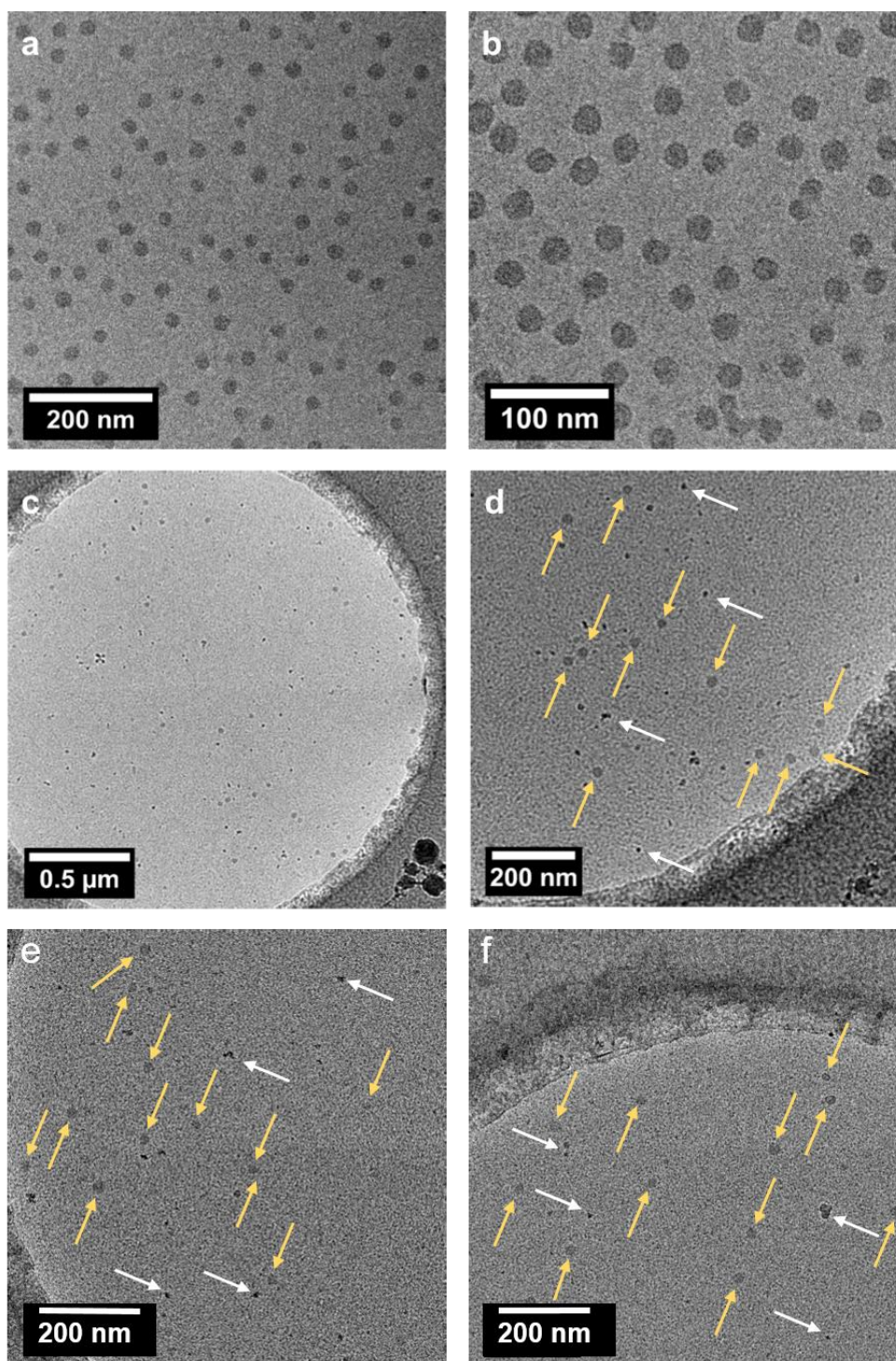


Figure 3.6 Stability of Nanomaterials in biological milieu: Cryo-TEM of SMN in Water and Blood Serum for 1 week. a) and b) Cryo-TEM of SMN in water. c) - f) Cryo-TEM of SMN in blood serum after 1 week. 10 uL of SMNs in water was added to 10 uL of blood serum. Sample volume was reduced to 10 uL by evaporation under reduced pressure and stored at 37 °C for 1 week prior to imaging. Yellow arrows in d, e and f indicate SMN, while white arrows indicate examples of ice artifacts stemming from cryo sample preparation.

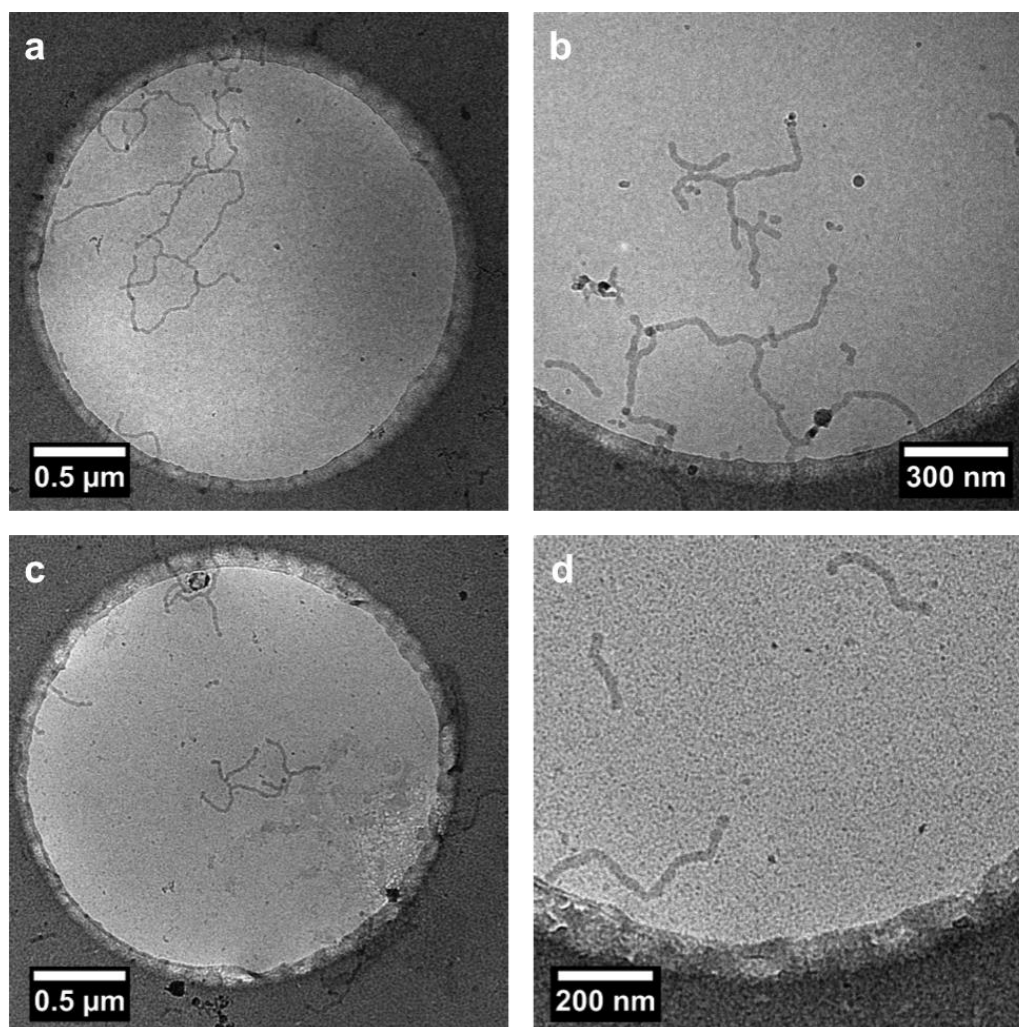


Figure 3.7 Stability of Nanomaterials in biological milieu: Cryo-TEM of FMN in Water and Blood Serum. a) and b) Cryo-TEM of FMN in water. c) and d) Cryo-TEM of FMN in blood serum. 10 uL of FMNs in water was added to 10 uL of blood serum. The sample volume was reduced to 10 uL by evaporation under reduced pressure and stored at 37 °C for 1 week prior to imaging.

3.10.4 *In Vitro* Relaxivity

SMN and FMN were further characterized by nuclear magnetic resonance dispersion (NMRD) analysis to investigate the basic magnetic properties as related to their utility as MRI contrast agents. At 37 °C and neutral pH, the NMRD profile of both NPs show the characteristic line-shape of macro-/supramolecular structures due to a reduction in rotational tumbling rate (Fig. 3.8);^{3,16} this is markedly distinct from the NMRD line-shape of Gd-DOTA. Notable

features in the NMRD profile of the NPs include a region of constant relaxivity at low field strengths (~ 0.01 MHz – 0.5 MHz, 0.0002 – 0.01 T) for SMN and FMN, with FMN displaying an elevated per Gd^{3+} relaxivity over SMN at all field strengths. Both NPs have a maximum relaxivity at ~ 20 MHz (0.5 T); SMN has a maximum per Gd^{3+} r_{1p} of $15.6 \text{ mM}^{-1}\text{sec}^{-1}$, while FMN demonstrates a favorably elevated r_{1p} of $18.5 \text{ mM}^{-1}\text{sec}^{-1}$ (Table 3.3; for detailed description of NMRD fit parameters, see Fig. 3.29). We note that the higher per Gd^{3+} relaxivities of SMN and FMN as compared to the mononuclear Gd-DOTA at 20 MHz (Table 3.3) are competitive (i.e. within the same order of magnitude) with other nanoparticle and polymer-based systems.^{17,18} Further, although all three of these systems converge to similar relaxivities at high frequencies, r_1 enhancement for SMN and FMN over Gd-DOTA is still pronounced both at 3 T (FMN: +210%; SMN: +169%). Such enhancement is largely due to the improved rotational dynamics for the two paramagnetic NPs combined with an exchange rate of coordinated water sufficiently fast as not to strongly limit the relaxivity.

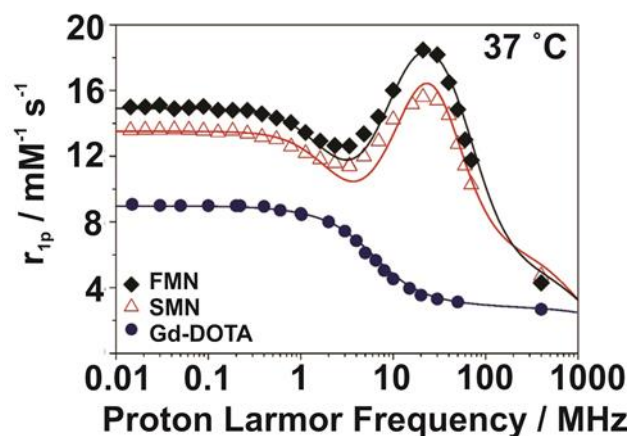


Figure 3.8 ^1H NMRD profiles for Gd-DOTA, SMN, and FMN.

Table 3.3 Relaxation parameters obtained from the analysis of NMRD profiles reported in Fig. 3.8.^a

	$^{20}r_{1p}$ (mM ⁻¹ s ⁻¹)	Δ^2 (10 ¹⁹ s ⁻²)	τ_V (ps)	τ_{RL} (ns)	τ_{RG} (ns)	S^2	τ_M (ns) ^b
SMN	15.6	0.9	52	0.19	5.9	0.20	560
FMN	18.5	0.7	53	0.15	2.8	0.25	350
Gd-DOTA	3.5	1.0	7	/	0.04	/	122

^a The fitting parameters a , ^{310}D , q and r were fixed to the values of 4.0 Å, 3.10x10⁻⁵ cm² s⁻¹, 1 and 3.0 Å, respectively; ^b let to vary between 100 and 900 ns.

3.11 *In Vivo* Analysis of Gadolinium-Containing SMN and FMN

Next, we performed an *in vivo* pilot study to determine if the Gd³⁺-labeled NPs would provide sufficient contrast in live mice imaged via MRI. Intraperitoneal (IP) injections were chosen based on the lab's interest in direct injection of therapeutic nanoparticles to the peritoneal cavity to localize delivery to areas affected by malignancies such as ovarian cancer. There are limited examples in the literature that study the IP delivery of nanoparticles as a means of systemic introduction.^{19–23} By using IP injections, we hoped to understand how materials distribute in the IP space and reach systemic circulation, critical information in the investigation of nanoparticle treatment strategies.

In these studies, C57/BL6 mice were first anesthetized and imaged by MRI prior to injection. For all formulations of contrast agent studied (Gd-DOTA, SMN, and FMN, $n = 3$ for each material), T₁-weighted images obtained immediately after injection demonstrate significant IP signal due to the Gd³⁺ reporter displayed on all injected samples (Fig. 3.9). Each animal was then imaged up to several hours post-injection to track retention in the peritoneal cavity. At two hours following IP injection, no enhanced signal was observed in the IP space of animals following injection of Gd-DOTA (Fig. 3.10). However, measurable signal was

clearly observed in the IP spaces of animals injected with either SMN or FMN (Figs. 3.10 and 3.30). This enhancement demonstrates that the NP formulations are retained in the IP space longer than Gd-DOTA. In addition, MRI of the urinary bladder of animals following injection of Gd-DOTA demonstrated rapid accumulation of Gd-DOTA, indicating clearance through renal excretion, as expected (Fig. 3.11). This was markedly delayed and less intense in the case of SMN or FMN. When looking at the liver (Fig. 3.12) there appears to be some signal enhancement in the organ, though the MRI scans nor corresponding quantitative T_1 analysis indicate definitive accumulation in the liver tissue. The apparent signal could be an image or motion artifact.

While accumulation in the bladder for Gd-DOTA is quite clear, and follows the known clearance of small molecule contrast agents, detection of the NPs over the time points imaged was difficult. This could be for several reasons, including slow clearance of NP formulations from the IP space. Low concentrations of the Gd reporter are distributed throughout the body, and may be below the threshold of detection for MRI. Imaging 1, 2 or 7 days after injection of material also did not show contrast enhancement via MRI, and *ex vivo* organ analysis at 1 week indicates more than 99% of material is eliminated (Fig. 3.33). Because we were interested in how shape might affect short term biodistribution, we next designed an experiment for more sensitive quantification of gadolinium using ICP-MS methods, with the aim of determining biodistribution at shorter time points.

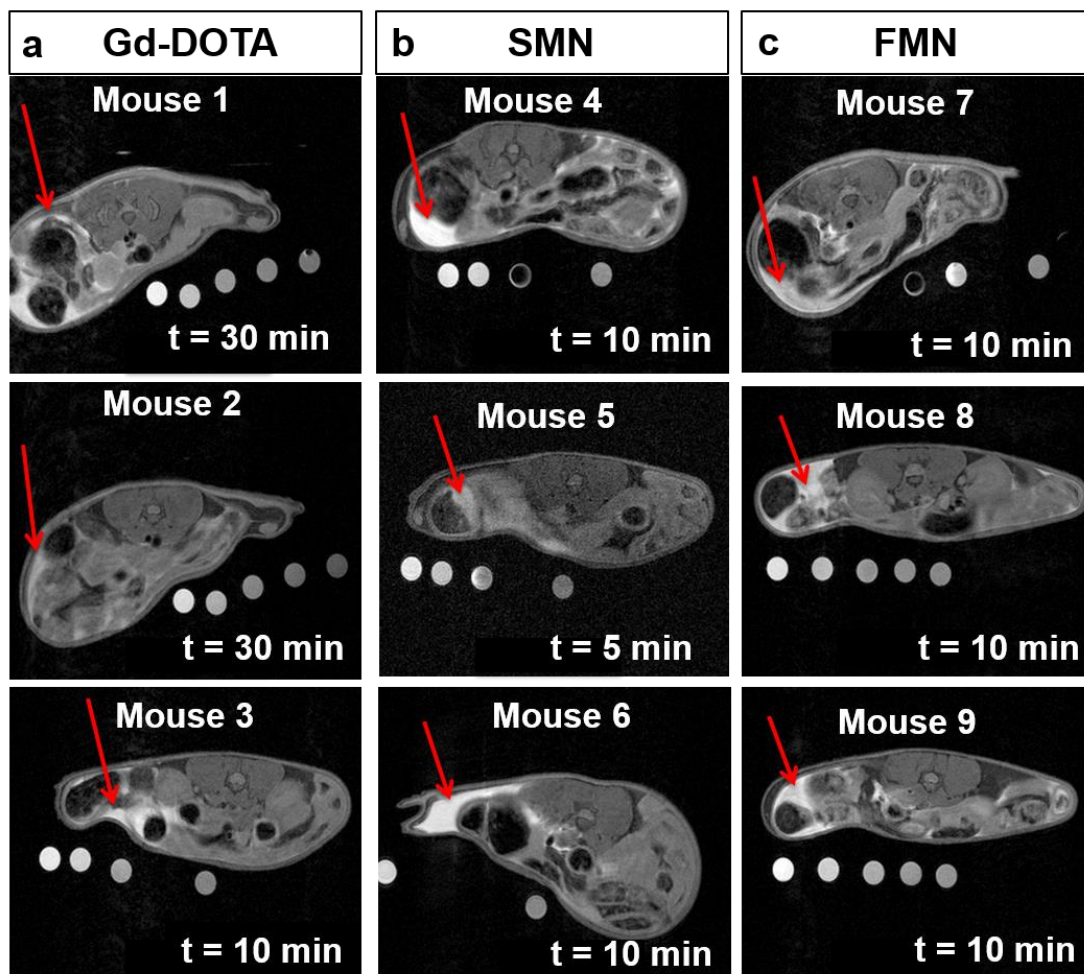


Figure 3.9 Anatomical MRI post-injection of contrast agent demonstrating successful introduction of materials IP. Red arrows indicate contrast surrounding the bowel loops. a) Anatomical image of mice 1 – 3, 10 – 30 minutes post-IP injection of Gd-DOTA. b) Anatomical image of mice 4 – 6, 5 – 10 minutes post-IP injection of SMN. c) Anatomical image of mice 7 – 9, 10 minutes post-IP injection of FMN.

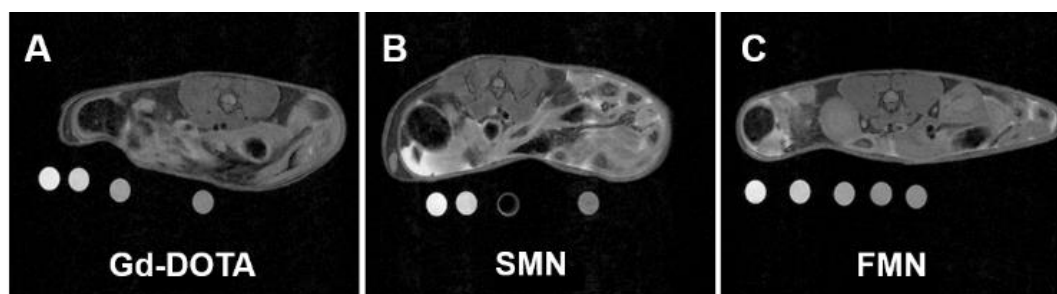


Figure 3.10 Axial T₁-weighted images of the abdomen approximately 2 hours following IP injection of a) Gd-DOTA, b) SMN, and c) FMN. See Fig. 3.28 for additional images of IP space at 2 hours. Phantoms, containing dilutions of the same material, were placed underneath the animal during scanning and used to correct for inter-scan variability. See methods section for further description of analysis.

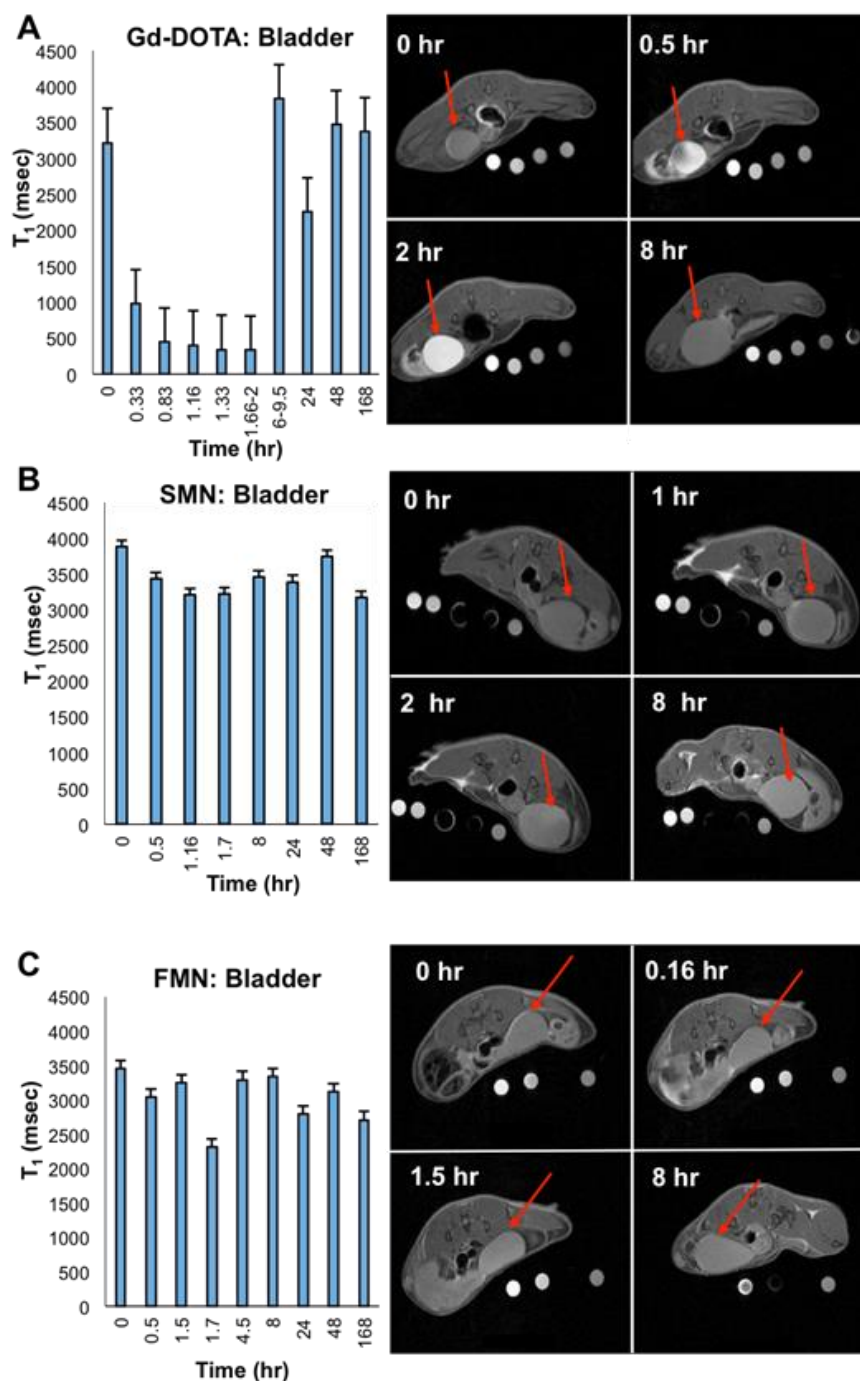


Figure 3.11 Time progression of signal enhancement, quantified as T_1 , and corresponding axial T_1 -weighted images of the bladder after IP-injection of a) Gd-DOTA, b) SMN, and c) FMN. For mice 1-9, multiple regions of interest were sampled, normalized by comparing the relaxivity of phantoms for each scan to the pre-injection phantom relaxivity, averaged over the organ in the scan, then converted to T_1 . For sampled time points of each material, T_1 times were averaged, and standard error generated for $n = 3$ mice. Red arrows indicate the urinary bladder.

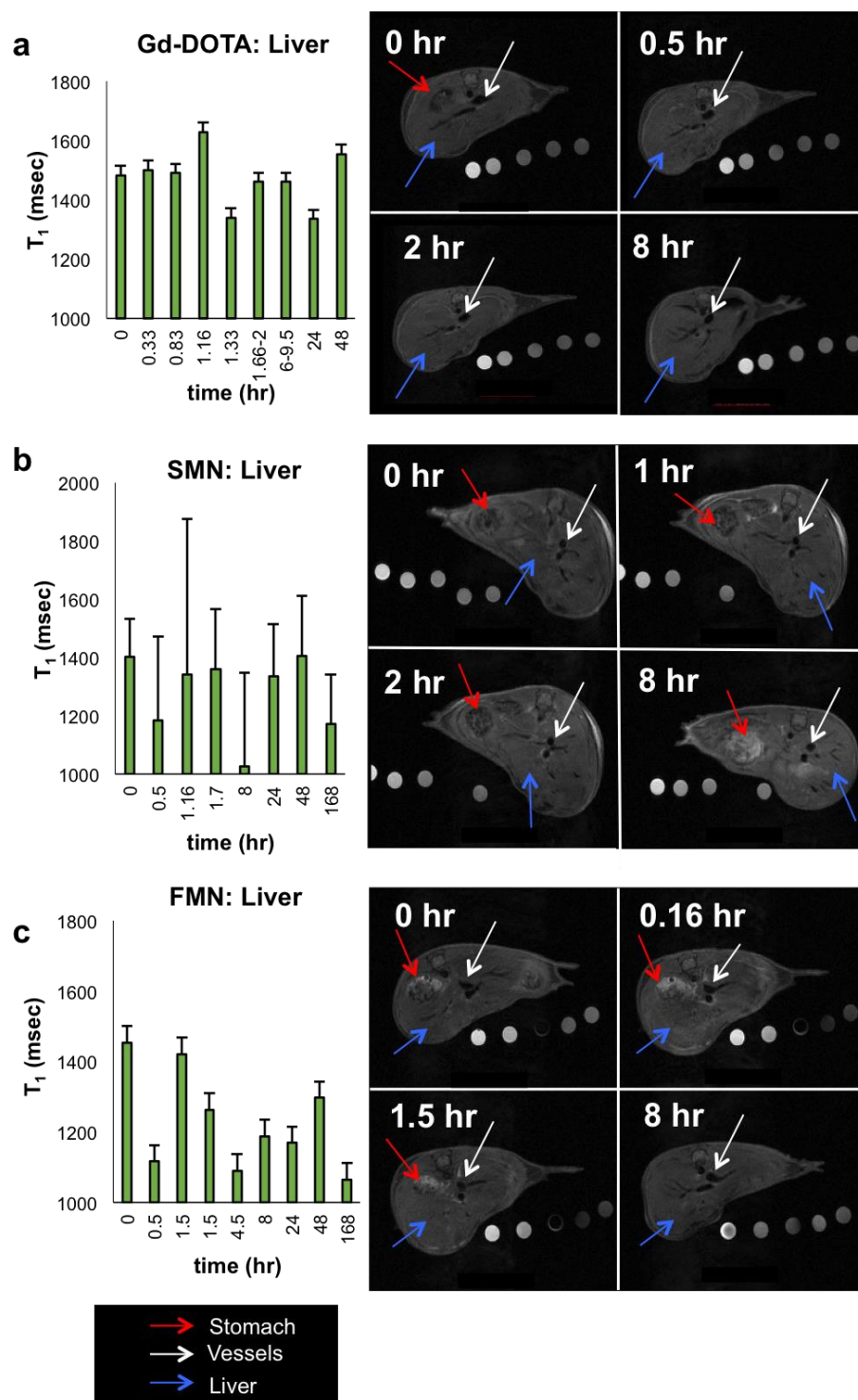


Figure 3.12 Time progression of contrast enhancement, reported as T_1 , and corresponding anatomical scans of the liver after IP-injection of a) Gd-DOTA, b) SMN, and c) FMN. Any contrast enhancement in the stomach is due to food, not injected material. Red arrows indicate the stomach, white arrows indicate a vessel, and blue arrows indicate part of the liver.

3.11.1 *Ex Vivo* Analysis

We next performed an *ex vivo* biodistribution analysis to gain insight as to where NPs localized *in vivo* following IP injection. As whole body MRI demonstrated possible signal enhancement in the liver following injection of NPs (Fig. 3.12), we designed a quantitative analysis of Gd^{3+} in the liver, spleen, and bowel accumulation of NPs following IP injection. At 2, 12 or 24 hours post-IP injection, animals ($n = 3$ for each group) were sacrificed and the spleen, liver, gut (includes intestines and stomach), kidney, heart and bladder were harvested. The tissues were homogenized in acid then analyzed by ICP-MS or ICP-OES for gadolinium content. The only tissues displaying significant signal were the spleen, liver and gut and therefore only these organs are included in this summary. The results are summarized in Figs. 3.13, 3.31 and 3.32 for individual animal profiles. Notably, the observation of hepatic uptake and non-detectable accumulation in the kidney via *ex vivo* analysis, is consistent with that of others who have observed NP accumulation in the liver following IP injection.^{24,25}

In these initial *in vivo* analyses of the materials, there was no clear conclusion to be made from the small sample size, but the following trends were observed. SMN appeared to accumulate in the spleen and liver ($n = 3$) at higher concentrations than the bowel at 2 and 24 hours (Fig. 3.13). FMN showed less accumulation in the spleen or liver as compared to SMN at 2 hours post-injection ($n = 3$). The slightly higher concentration of material in the spleen and liver at 12 hours indicates sustained RES clearance throughout the first 24 hours post-injection. Interestingly, at 1 week post-injection (Fig 3.33), the total % of injected dose is slightly higher for FMN compared to SMN (0.03% versus 0.01%), though both materials are mostly cleared from the body by this point. These data suggest that both NPs are cleared relatively slowly from the IP space, and while no statistically significant data was generated from the small sample size, there appears to be differences in accumulation and clearance for the spherical particles compared to the fibrillar particles.

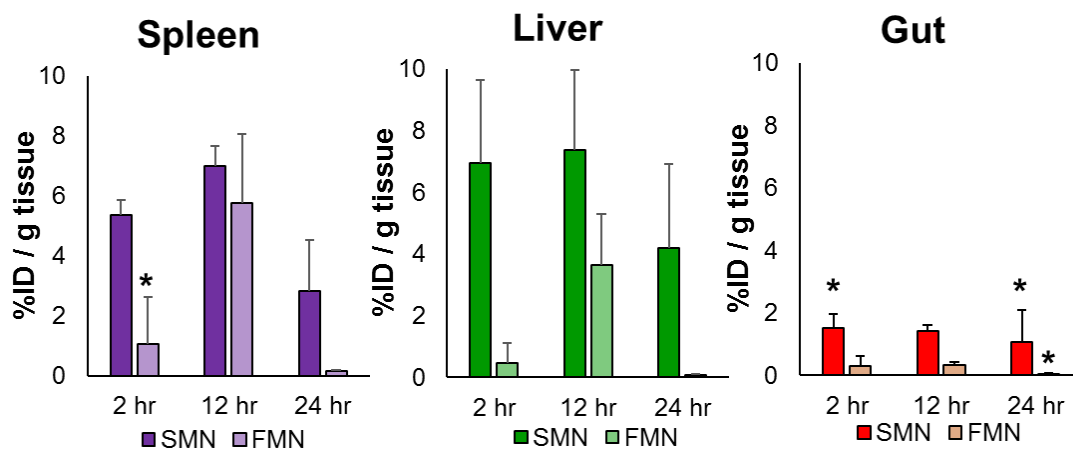


Figure 3.13 Accumulation of SMN and FMN in the spleen a), liver b), and bowel c), at 2, 12 or 24 hours following IP injections as detected by the presence of Gd by ICP-MS and ICP-OES. For each time point $n = 3$, except where indicated with *, where $n = 2$. Error bars represent standard deviations.

3.12 Incorporation of Gd-DOTA as a Chain Transfer Agent

In some cases, a functional unit may be incorporated into a polymer as a chain transfer agent rather than as a monomer. In the Gianneschi Lab we have developed a suite of functional chain transfer reagents for end-labeling polymers using ROMP.⁸ By using a symmetric functional olefin, polymerization reactions can be terminated such that the functional agent is incorporated on the end. This gives us a handle for synthesizing more complex polymer architectures, with control over the incorporation of exactly one functional unit on the polymer backbone. Functional termination agents to incorporate functional units have been described, but none, to our knowledge, incorporating a Gd-based imaging agent.

One exploratory aim for using the termination agent was to evaluate location of a contrast agent in a polymer or polymeric nanoparticle architecture and how that might affect the relaxivity properties of a material. For example, we envisioned a polymer scheme in which the contrast agent could be localized on the corona of a NP or buried inside the hydrophobic

core (Fig. 3.14, top and bottom, respectively). Based on more detailed discussions in Chapter 2, we know that phenyl-based hydrophobic blocks of polymer amphiphiles result in high T_g , crystalline cores. In labeling a polymer at the terminus of a hydrophobic block, we hypothesize that the gadolinium center would be buried in the core versus localized on the corona. A gadolinium-based contrast agent must be accessible to water to affect the local water relaxation times. If the gadolinium center is buried in the crystalline-like core where water is excluded, this will theoretically result in an OFF signal. Other examples in the literature describe situation in which gadolinium centers are constricted at the barycenter of a macromolecule; the result in this scenario is a constriction of the metal-center, lower tumbling rates, and increased relaxivities (Fig. 3.1c).⁴ Another scenario might be that the hydrophilic GBCA sits at the core-shell interface and does interact with water; in this case, rotation of the gadolinium center may be constricted and instead lead to an increase in relaxivity, rather than an OFF signal.

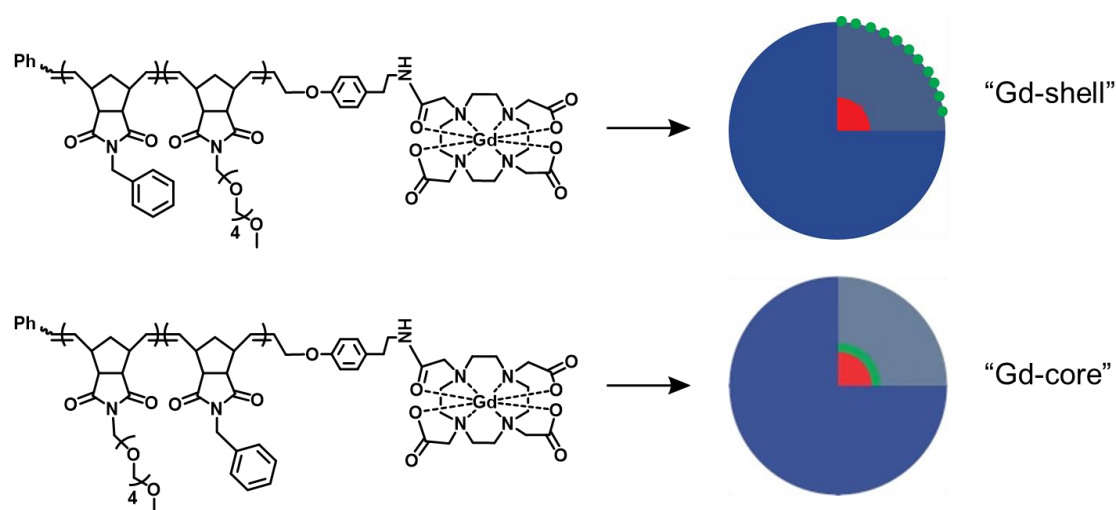


Figure 3.14 Polymer amphiphiles end-terminated with Gd-DOTA moiety. Upon polymer self-assembly in aqueous environment, the Gd-label is envisioned to sit either at the corona-water interface or buried within the assembly.

With these design principles in mind, the Gd termination agent of interest was first synthesized and then incorporated into polymers. These materials were subsequently formulated into nanoparticles and studied.

3.12.1 End-labeling of Polymers

First a Gd-DOTA -containing chain transfer agent (Gd-CTA) was prepared and characterized according to the schemes in Figs. 3.19-3.21. Next, a series of test amphiphilic polymers were prepared in which a phenyl-based norbornene monomer was polymerized as the hydrophobic block, and a PEG-monomer was polymerized as the hydrophilic block (Fig. 3.14). If the Gd-CTA was desired to be on the end of the hydrophobic block to form “Gd-core” particles, PEG was polymerized first, followed by -Ph then termination with Gd-CTA. Conversely, if Gd-CTA was desired to be on the hydrophilic end to form “Gd-shell” particles, -Ph was polymerized first, followed by PEG then Gd-CTA. Aliquots of the polymerization reaction were removed following polymerization of the first and second blocks for characterization by SEC-MALS (Table 3.4, Fig. 3.24). Then, at least 1.2 eq of Gd-CTA were added to the reaction mixture.

Table 3.4 Polymers End-labeled with gadolinium-containing CTA.

Polymer	Composition	Material	DP m ^a	DP n ^a	M _n ^b	Đ ^c	Used to make NP:
P3	1₁₉-b-3₁₀₇	Ph ₁₉ -b-PEG ₁₀₇ -Gd	19	107	43,930	1.017	NP3 “Gd-shell”
P4	3₁₁₂-b-1₁₀	PEG ₁₁₂ -b-Ph ₁₀ -Gd	112	10	63,840	1.078	NP3 “Gd-score”
P5	1₁₅-b-3₇	Ph ₁₅ -b-PEG ₇ -Gd	15	7	6,370	1.044	NP3 “Gd-shell”
P6	3₃₂-b-1₄	PEG ₃₂ -b-Ph ₄ -Gd	32	4	14,180	1.018	NP3 “Gd-core”

^a The degree of polymerization (DP) m and n, are determined using SEC-MALS. ^b The number average molecular weight. ^c The dispersity of copolymer (Mw/Mn).

The kinetics of termination were not determined, but the consumption of the material was tracked over 24 hours. This could not be monitored using traditional methods of ^1H -NMR because gadolinium is paramagnetic and affects peak broadening in the NMR spectrum.⁹ After the Gd-CTA was added to reaction mixture, small aliquots were removed and analyzed by HPLC for the presence of unreacted Gd-CTA. This was compared to a standard curve for Gd-CTA to determine reaction completion. After a few hours the concentration decreased, indicating consumption; an excess of Gd-TA was added to ensure complete incorporation. The reaction was quenched with ethyl vinyl ether to deactivate the catalyst, and ensure any living polymers in the reaction were quenched. Polymers were then analyzed by SEC-MALS, using the same dn/dc as the diblock polymers before functional termination. No significant peak shift for polymers with or without the functional unit was observed, though the refractive index of the polymers changed upon addition of functional Gd-CTA.

3.12.2 Nanoparticle Formulation

Polymers were self-assembled using the solvent-switch method, as described above. Polymer was dissolved in organic solvent at a concentration of about 1 mg/mL, then water slowly added up to 50/50 v/v%. The solution was then transferred to either dialysis cups or snakeskin tubing, depending on the volume/scale of the NP formulation, and dialyzed against 2L water. The water was refreshed 3 times over 3 days. Solutions were then removed from dialysis containers, and analyzed by DLS and TEM to evaluate the quality of NP (shape, size, dispersity). The results are described in Fig. 3.15.

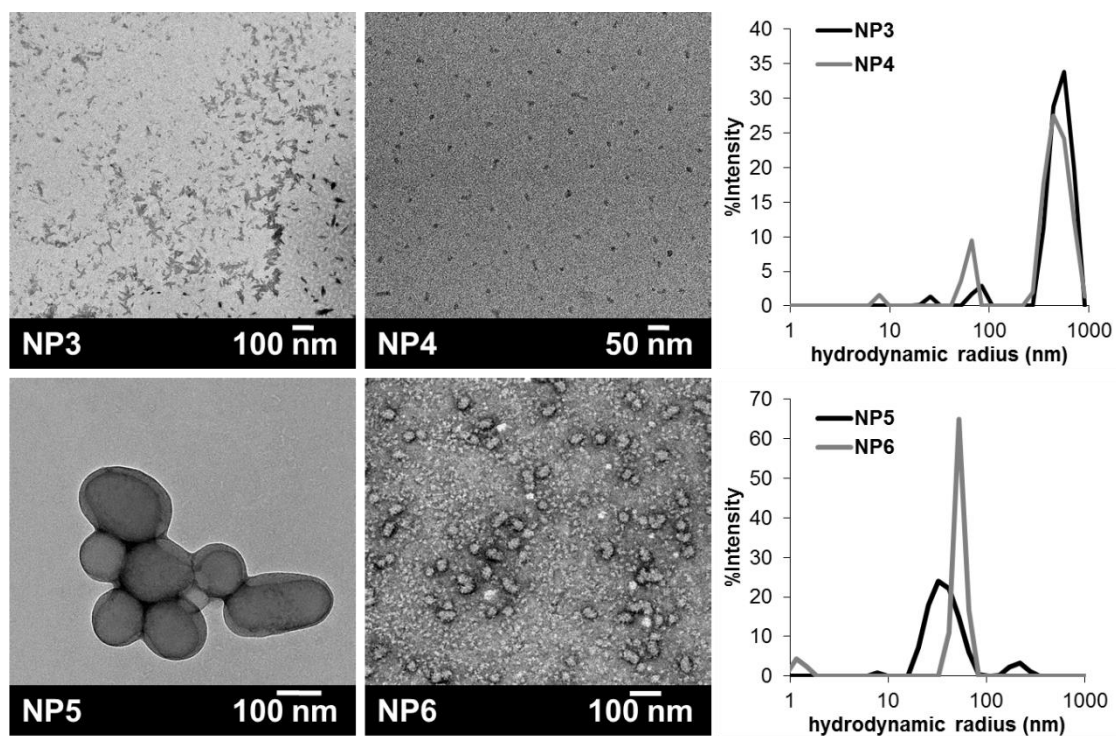


Figure 3.15 TEM images and DLS of **NP3-6** and dynamic light scattering, formulated from polymers **P3-6**, end-labeled with a gadolinium-containing CTA. For DLF of NP3-6, the % intensity was plotted for each of the nanoparticle solutions. **NP3-4** were unfiltered solutions: aggregates are readily apparent at hundreds of nanometers, while the peaks at about 90 and 60 nm are from the particles. **NP5-6** were filtered prior to measurement and display radius of about 30 and 50 nm, respectively. The discrepancy from the observed diameters by TEM are not uncommon in DLS analysis: as is apparent here, these NPs readily aggregate in solution, and the TEM samples are readily prone to staining and drying artifacts.

3.12.3 Application of End Termination of Polymers with Gd-Based Agent

Next relaxivity of materials was evaluated at 300 MHz using an inversion recovery experiment. Control experiments measuring the relaxivity of a standard compound, Gd-DOTA, resulted in expected relaxivity determination ($\sim 4 \text{ mM}^{-1}\text{sec}^{-1}$, see Fig. 3.34). However, there was a systematic experimental error in measuring the relaxivity of the gadolinium NPs 3-6. The solutions were made in deuterated water, which was believed to be a source of the tremendous experimental error. Using ^2H , a spin-inactive nucleus, effectively changes the concentration of ^1H protons that were detected during the experiment. The results are depicted in Fig. 3.34 but

due to the large experimental error, should not be taken as representative data. Another possible source of error may have been the concentration used in determining the per mM relaxivity, though this error was circumvented by verifying gadolinium concentration with ICP-MS.

3.13 Applications of Peptide Polymeric Materials with a MRI

Contrast Agent

In the previous sections, application of polymeric nanoparticles containing a GBCA were described and studied, wherein the only targeting property of the material was its shape (SMN versus FMN). As discussed in Chapter 1, the Gianneschi lab is interested in developing peptide polymer materials in which the specific peptide sequence is used as a stimuli-responsive unit. Here, two example applications of peptide polymer materials containing a GBCA are described.

The Gianneschi group has developed an active accumulation method for nanoparticles at tumor targets using enzymes. Peptide polymer amphiphiles (PPAs) contain an optimized sequence for matrix metalloproteinases (MMPs), proteins that are upregulated in tumor extracellular space. The MMPs recognize NPs and impart a phase change, causing particles to both accumulate at, and stick in, the tumor tissue. This EDAPT [enzyme-directed assembly of particles in tissue] method has been demonstrated as a proof-of-concept using *in vivo* fluorescence imaging. (A cartoon depiction of EDAPT provided in Chapter 1, Fig. 1.3.) MRI of targeted nanoparticle systems is highly desirable, owing to its clinical translatability, with other advantages over optical detection, including deep-tissue imaging and mitigation of background auto-fluorescence of biologic tissue.

We were curious if we could make similar PPAs incorporating a GBCA using the norbornyl Gd-DOTA monomer. ROMP was used to polymerize amphiphiles that contain: 1) a

hydrophobic core block, 2) a peptide-containing block, blended with a carboxylic acid, and 3) a gadolinium-based contrast agent, as shown in Fig. 3.16. The peptide sequence selected is the same as used in previous studies, and contains the optimized sequence “GPLGLAG” and solubilizing residues after that.^{5,26–28} Based on previous observations, the peptide sequence may experience steric crowding in the polymer architecture, and must be blended to decrease density to allow enzyme access.²⁹ The gadolinium based contrast agent is polymerized as a short block.

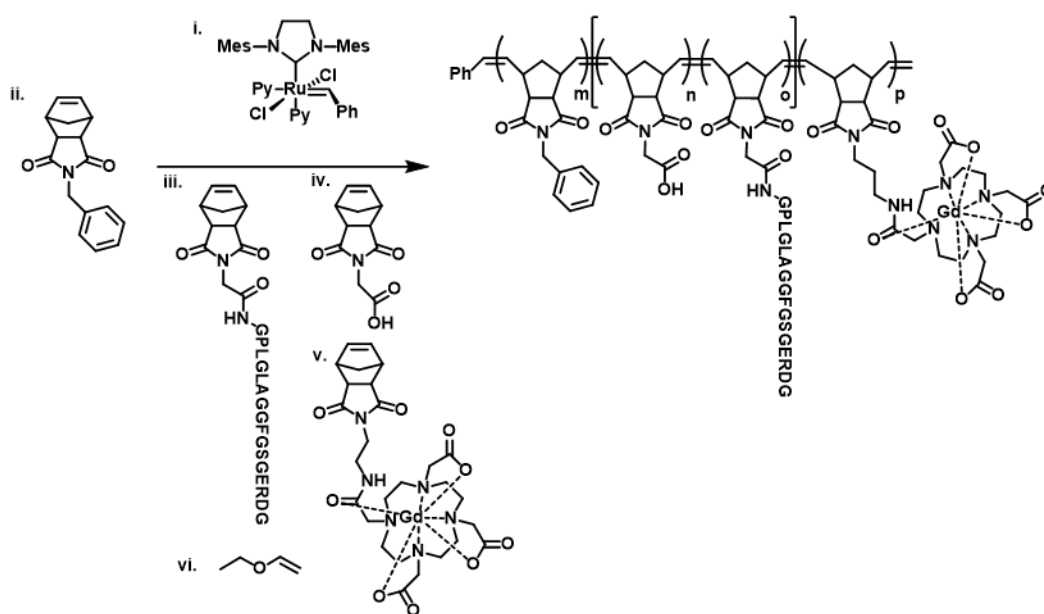


Figure 3.16 Polymer scheme for enzyme-responsive, MRI-labeled materials. $m = 25$, $n = 3$, $o = 4$, $p = 2$.

The polymer was used to prepared micelles using similar methods as described in previous sections. The particles were spherical in morphology and about 30 nm in diameter. The particles were subjected to enzymatic treatment using a model enzyme, thermolysin. Results are described in Fig. 3.17.

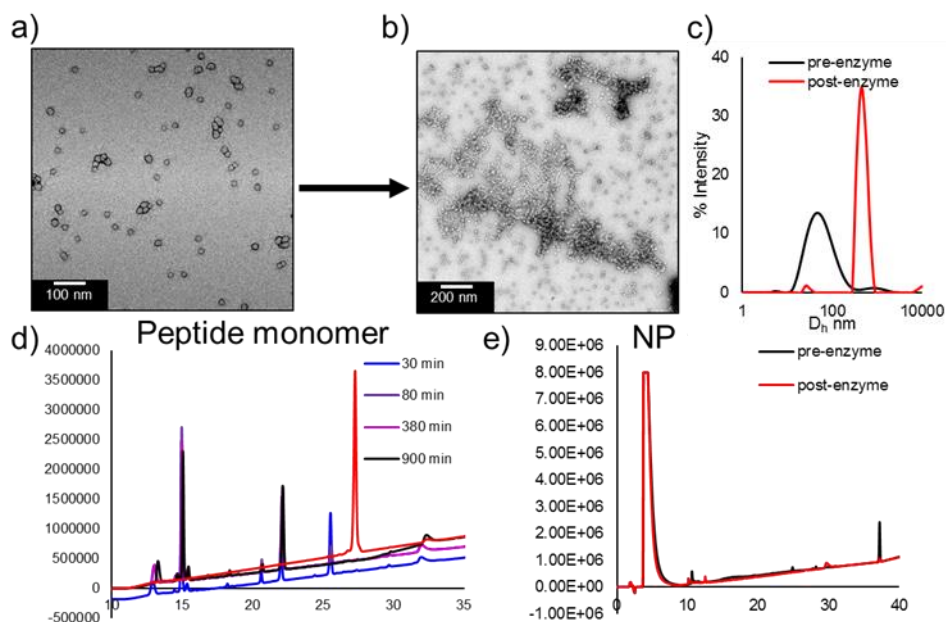


Figure 3.17 Evaluation of enzyme-responsive polymeric nanoparticles. a) TEM of nanoparticles. b) TEM of particles after treatment with enzyme, showing not change in morphology. c) DLS of particles before and after treatment. It appears there may be some aggregation after treatment (red trace), but the TEM confirms that it is most likely the particles sticking together, no changing morphology. d) Example HPLC of control peptide monomer treated with thermolysin, showing the various cleavage products expected over time. 3) HPLC of the nanoparticle solution over time. No cleavage products were detected by HPLC.

Despite the polymers give discrete, uniform spherical nanoparticles, under the conditions probed, they were not responsive to enzyme treatment. DLS seemed to show aggregation post-enzyme treatment, but this is most likely just the particles sticking together in solution, a property seen in the TEM of the particles post-treatment. The control treatment of peptide monomer only confirmed that the enzyme was active. Therefore, there was most likely a problem with the nanoparticle architecture that prohibited the enzyme activity and morphology switch. Future work using this type of enzyme-responsive unit should optimize the polymer size, degree of polymerization of peptide block, and the spacing of monomers to prevent crowding of the peptide sequence from inhibiting the enzyme. Nevertheless, this is a

feasible way to prepare polynorbornene materials that incorporate a targeting and imaging moiety.

In another project, enzyme- and heat-responsive elastin peptide-like polymer amphiphiles containing a gadolinium contrast agent are studied.³⁰ The polymers were end-labeled with the gadolinium-containing CTA, and used as a probe to measure effects of phase transitions on relaxivity. While no changes in relaxivity were observed, the relaxivities of the polymers in solution, $\sim 3\text{--}4\text{ mM}^{-1}\text{sec}^{-1}$, are consistent with the relaxivity of the small molecule chelate, rather than a macromolecular species. This is evidence that free rotation of the chelate, as opposed to coupling of rotation time to the polymer, is occurring in this polymer architecture.

3.14 Conclusions and Outlook

In this chapter, strategies towards preparing polymeric materials containing a gadolinium-based contrast agent are described. First, a new synthetic method for labeling polymers and NPs with a Gd^{3+} -based contrast agent through direct polymerization of a monomer is described. This procedure ensures that the entire shell of the nanoparticle consists of Gd^{3+} -labeled monomers, and can be extended to more complex polymers synthesized through ROMP, for example those incorporating a targeting moiety. This route led to the preparation of two different phases of NP, one entirely spherical (SMN), the other predominantly fibrillar (FMN). Preliminary *in vivo* MRI and *ex vivo* elemental analyses suggest that these differently shaped NPs derived from chemically identical starting materials show promise for imaging following IP injection. We note that the concept of shape dependent *in vivo* behavior of NPs has been observed in the context of intravenous (IV) injection by Discher, Caruso, Mitragotri, and others,^{31–38} but to the best of our knowledge, this report represents the first to begin to address the effects of NP shape following the clinically important IP injection route. Indeed, direct delivery of small molecule chemotherapeutic agents *via* intraperitoneal

(IP) injection is a well-established therapeutic paradigm in the treatment of human metastatic ovarian, pancreatic and gastric malignancies.^{21,22,39-41} Interestingly, there is research investigating the importance of NP size in efficacy of nanoscale formulations for enhanced delivery and targeting to peritoneal malignancies when introduced *via* IP.²⁰ These studies note that small NPs easily clear from the peritoneum owing to the larger stomata openings (lymphatic duct openings), while larger NPs and micrometer size NPs are retained more easily. Additionally, cationic charges on the NPs favors greater retention due to greater interactions with macrophages in the cavity.⁴² The studies presented herein suggest the favorable retention of FMNs in the IP cavity compared to small spherical NP. Future studies will build on these initial *in vivo* observations to further explore and exploit NP physicochemical properties for greater retention and targeting to tissues in the intraperitoneal space, especially with regards to therapies specific for peritoneal malignancies like ovarian cancer.. Using a norbornyl-monomer of the GBCA as a hydrophilic block in a block copolymer amphiphile, two differently shaped nanoparticles were prepared. These nanoparticles exhibited increased relaxivity, as expected for a macromolecular contrast agent, and were used to study the shape effects of nanoparticles *in vivo*. MRI studies of nanoparticles injected *via* intraperitoneal injection demonstrated retention in the IP space compared to a small molecule contrast agent, and the materials appeared to exhibit differences in bioaccumulation and RES clearance. The small sample size prohibits definitive conclusions. Nevertheless, the imaging strategies performed in this study were the first examples of MRI imaging in live animals in our group, one of few studies in the literature comparing head-to-head spherical versus cylindrical NPs *in vivo*, and to the best of our knowledge one of the few that evaluates biodistribution qualitatively using MRI.

Retention of nanoparticles in the IP space represents an important delivery strategy for therapeutics treating diseases of the IP cavity. In the future, it would be interesting to sample from the IP cavity over time to quantitatively determine the concentration of materials; this

could be accomplished using lavage techniques for sampling from the IP space.²³ The Gianneschi Lab develops therapeutic polymeric nanoparticles designed to treat ovarian cancer specifically,⁴³ and on-going work should evaluate the differences in efficacy of NP drug delivery using the IP versus IV route of administration. Based on our observations and the observations of others, large, high-aspect ratio nanoparticles should be the goal for optimal peritoneal cavity retention.

Ultimately, using an end-label for incorporation of GBCA (via the CTA) is not an effective strategy for developing materials for *in vivo* imaging. Though MRI is very sensitive, there does need to be a minimal local concentration to observe contrast enhancement. Due to the architecture of polymers that only incorporate one gadolinium atom per polymer chain, and the limitations of solubility of polymeric nanoparticles in solution, concentration of contrast agent in solution will limit detectability *via* MRI, unless the relaxivity enhancements from the architecture are extremely favorable. From the latter perspective, members of the Gianneschi group are pursuing alternative ligand types for gadolinium based contrast agents., in particular, the HOPO-class of ligands, with a q-value of two.¹²

3.15 Acknowledgements

Chapter 3 is adapted, in part, from material as it appears in Chemical Science 2016. Randolph, Lyndsay M.; LeGuyader, Clare L. M.; Hahn, Michael E.; Andolina, Christopher M.; Patterson, Joseph P.; Mattrey, Robert F.; Millstone, Jill E.; Botta, Mauro; Scadeng, Miriam; and Gianneschi, Nathan C. The dissertation author is a co-primary investigator and author of this paper.

3.16 Methods

All reagents were purchased from Sigma-Aldrich or Macrocyclics and used without further purification. RP-HPLC, semi-preparative RP-HPLC, NMR, mass spectrometry analyses, and SEC-MALS were performed using the same equipment and methods as described in Chapter 2 (2.7 Methods).

3.16.1 Monomer Synthesis

Monomer 1, (N-Benzyl)-5-norbornene-exo-2,3-dicarboximide was prepared as previously described. Synthesis of Gd-DOTA-MA monomer **2**. See Fig. 3.2 for chemical structures. 2-(2-aminoethyl)-3a,4,7,7a-tetrahydro-1H-4,7-methanoisoindole-1,3(2H)-dione was prepared as previously described,²² (50 mg, 0.158 mmol) and dissolved with DOTA-NHS•HPF₆•CF₃CO₂H (100 mg, 0.131 mmol) (purchased from Macrocyclics) in pyridine (0.655 mL). The reaction solution was placed on a vortex overnight. Acetic anhydride (0.309 mL, 3.28 mmol) was added and the reaction mixture was mixed on a vortex mixer for 10 min. Gd(OAc)₃ (160 mg, 0.393 mmol) was then added to the remaining solution and placed back on the vortex overnight. The reaction was concentrated to dryness to give a light brown residue. The product was then purified by semi-preparative RP-HPLC over a 50-minute linear gradient from 8% to 15% acetonitrile in water with 0.1% TFA (50 mg, 75%) (Fig. 3.18 for

HPLC chromatogram and mass spectra). LRMS (ESI) 748.21 $[M+H]^+$, 770.17 $[M+Na]^+$, HRMS, expected $[M+H]^+$: 748.1936, found: 748.1932.

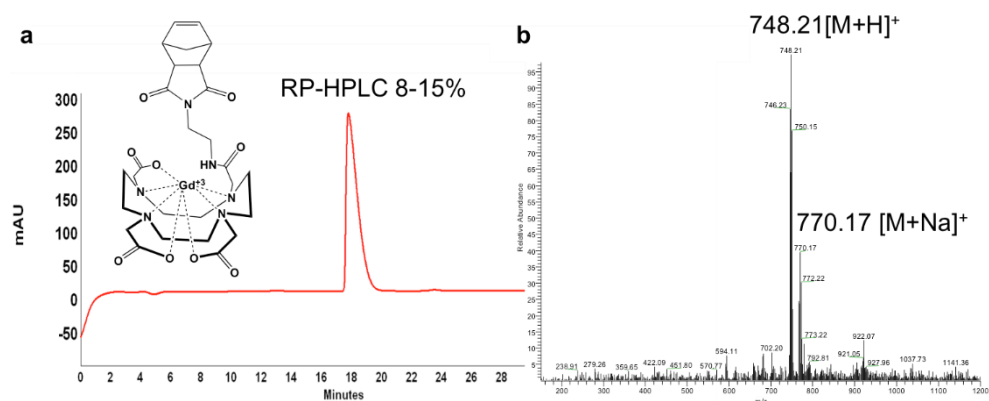


Figure 3.18 Monomer **2** characterization following purification by RP-HPLC. a) Analytical RP-HPLC chromatogram of purified monomer **2** and b) LR-ESI-MS.

3.16.2 Symmetric Chain Transfer Agent Synthesis

The “Gd-CTA” was synthesized as described in Fig. 3.19. Using a symmetric diamine⁴⁴ dissolved in pyridine, a slight excess (2.1) of equivalents of “DOTA-NHS” (Macrocyclics) was added and the two reagents were allowed to react at room temperature overnight. The reaction was monitored for completion using HPLC, then purified by prep-HPLC optimized gradient of 15-23% acetonitrile in water with 0.1% TFA. The functional termination agent was then metalated by the addition of $Gd(OAc)_3$ and vortexed vigorously over two days. The reaction was analyzed by ESI-MS and purified by semipreparative HPLC using normal buffer conditions and monitoring at 214 nm. In all cases, % yield was low, presumably because of multiple reactive sites on both the macrocyclic ligand and symmetric terminating agent precursor. Alternatively, the Gd-CTA could be prepared in a one pot synthesis as described in Wang *et al.*,³⁰ in which a DOTA-tris(tert-butyl ester) was stirred with an amine functionalized symmetric olefin, acid deprotected then purified by RP-HPLC, followed by metalation at pH 6, and re-purification by HPLC.

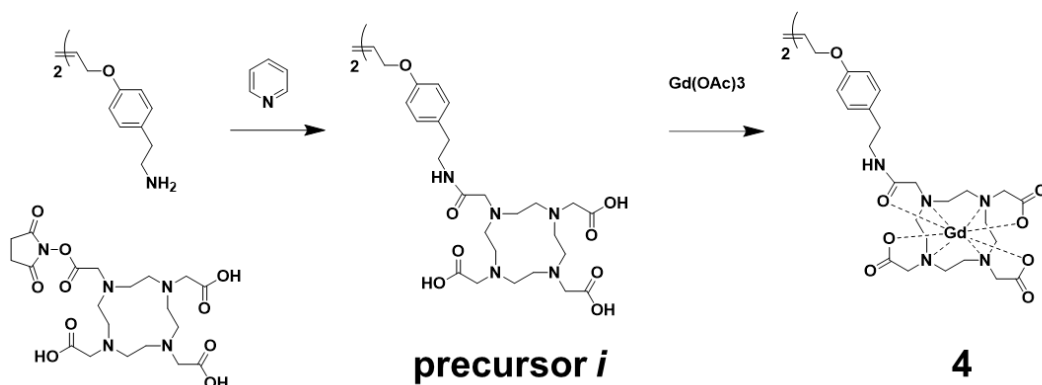


Figure 3.19 Scheme to prepare Gd-CTA.

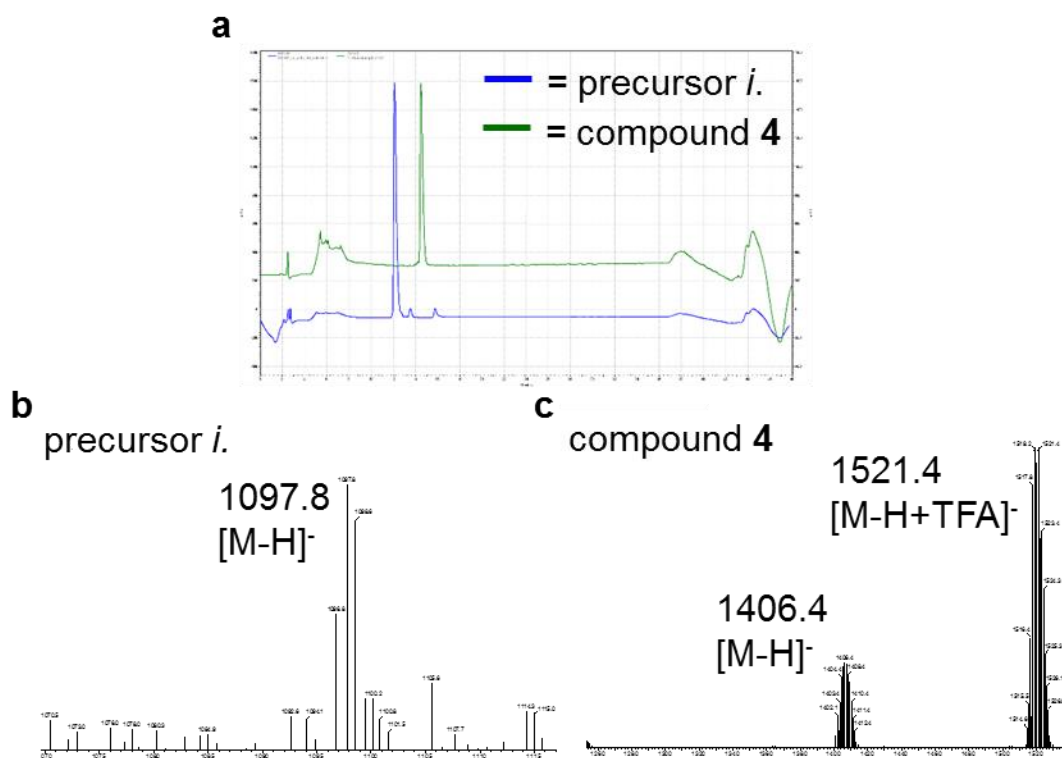


Figure 3.20 Characterization of Gd-CTA. a) The RP-HPLC chromatogram of purified organic ligand precursor *i* in blue, and the metalated Gd-TA, compound **4** in green. ESI-MS *i* and compound **4** are shown in b and c, respectively. b) Expected mass is 1098.56. c) Expected mass is 1408.36.

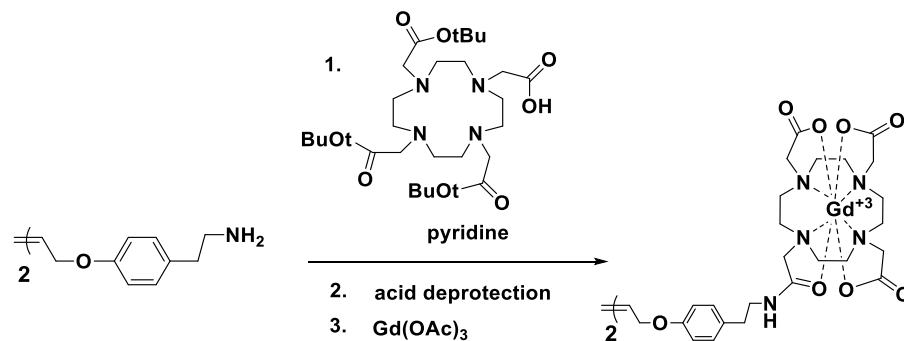


Figure 3.21 Alternative preparation of Gd-CTA. Described as in Ref. 42.

3.16.3 Polymer Synthesis and Characterization

Polymerizations were performed under a dry dinitrogen atmosphere with anhydrous, degassed solvents in a glove box. Initiator $(\text{IMesH}_2)(\text{C}_5\text{H}_5\text{N})_2(\text{Cl})_2\text{Ru}=\text{CHPh}$ was prepared as described by Sanford et al⁴⁵ and in Chapter 2.

Synthesis of P1. A solution of the initiator (2.44 mg, 0.00335 mmol) in anhydrous 7:2 $\text{CH}_2\text{Cl}_2:\text{CH}_3\text{OH}$ (0.129 mL) was added to a stirred solution of **1** (68 mg, 0.268 mmol) in a mixture of anhydrous 7:2 $\text{CH}_2\text{Cl}_2:\text{CH}_3\text{OH}$ (2.97 mL) in a glove box. The reaction was left to stir in a glove box for 20 min, after which an analytical aliquot (approximately 32% by volume) was removed and mixed with an excess of ethyl vinyl ether for 30 min, then dried under high vacuum to give a homopolymer of **1** as a solid. To the remaining reaction mixture, a solution of **2** (25 mg, 0.0335 mmol) in anhydrous 7:2 $\text{CH}_2\text{Cl}_2:\text{CH}_3\text{OH}$ (0.08 mL) was added immediately following analytical aliquot removal. The reaction was monitored by analytical RP-HPLC (using the same conditions described above for compound **2**, see Fig. 3.22a) to ensure complete consumption of **2**. The mixture was left to stir in a glove box for 90 min and then quenched with excess ethyl vinyl ether (0.0251 mL) for 20 minutes, which was concentrated to dryness to give a greenish solid. This was used without further purification until particle formation. The homopolymer and block-copolymer were analyzed by SEC-MALS as shown in Fig. 3.22b.

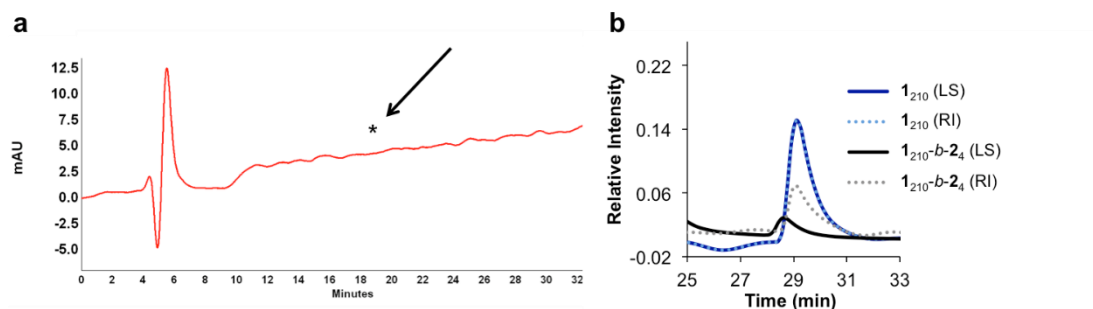


Figure 3.22 Characterization of **P1**, **1₂₁₀-b-2₄**. a) Analytical RP-HPLC chromatogram of reaction mixture demonstrating consumption of monomer **2**. Expected retention time of monomer **2** is highlighted with an asterisk. b) SEC-MALS and RI analyses of homopolymer **1** and block copolymer **1₂₁₀-b-2₄** in CHCl₃.

Synthesis of P2. In a similar manner to the polymerization procedures described above, a solution of the initiator (3.9 mg, 0.005 mmol) in anhydrous CH₂Cl₂ (0.8 mL) was added to a stirred solution of monomer **1** (61 mg, 0.24 mmol) in anhydrous CH₂Cl₂ (1.4 mL) in a glove box. After 20 min, an analytical aliquot (approximately 20% by volume) was removed and mixed with an excess of ethyl vinyl ether for 30 min, and dried under high vacuum to give a homopolymer of **1** as a solid. To the remaining reaction mixture, a solution of monomer **2** (25 mg, 0.033 mmol), in anhydrous CH₃OH (0.625 mL) was added immediately following aliquot removal. The reaction was monitored by analytical RP-HPLC (using the same conditions described above for compound **2**, see Fig. 3.23a) to ensure complete consumption of monomer **2**. After 90 min, the polymerization was quenched with excess ethyl vinyl ether for 30 minutes. A small aliquot was removed for subsequent analysis. This material was carried on without further purification until particle formation. The homopolymer and block-copolymer were analyzed by SEC-MALS, as shown in Fig. 3.23b.

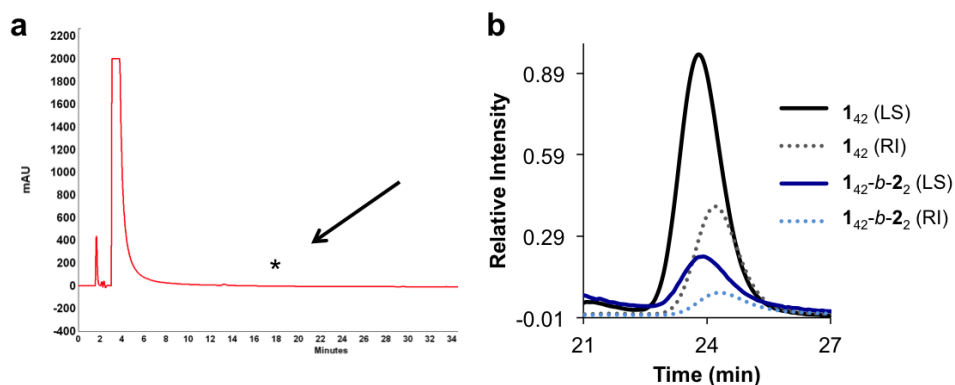


Figure 3.23 Characterization of **P2** $1_{42-b-22}$. a) Analytical RP-HPLC chromatogram of the reaction mixture demonstrating consumption of monomer **2**. Expected retention time of monomer **2** is highlighted with an asterisk. b) SEC-MALS and RI analyses of homopolymer **1** and block copolymer $1_{42-b-22}$ in 0.05 M LiBr in DMF.

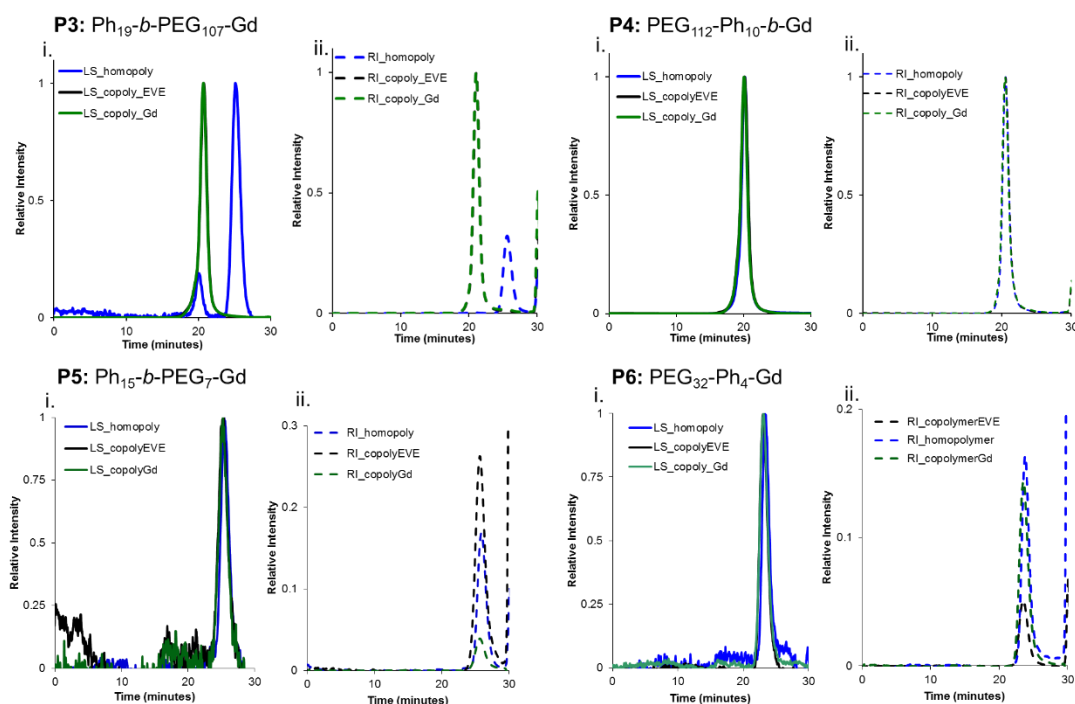


Figure 3.24 SEC-MALS traces for **P3-6**. Polymers end-labeled with Gd-CTA. In each panel, i. are the light scattering traces, and ii. are the RI traces. Blue traces are for the homopolymer, black is the copolymer end terminated with ethyl vinyl ether (control) and green is for the copolymer end-labeled with Gd-CTA.

3.16.4 Formulation of Polymeric Nanoparticles

SMN (**P1**, 1_{210-b-24}). **P1** (75 mg, 1.35 μ mol) was dissolved in DMSO (2.5 mL) and the solution was sonicated until fully dissolved. A solution of 1:1 DMSO:H₂O (2.5 mL) was added drop wise. The cloudy polymer mixture was sonicated for 15 minutes, then transferred to a 3,500 MWCO snakeskin dialysis tubing (Pierce) and dialyzed against a 1:1 DMSO:H₂O solution (2L). After 24 hours, the milky solution was removed from dialysis and H₂O was added drop wise (2.5 mL) to the polymer mixture. This mixture was then transferred to a 10,000 MWCO snakeskin dialysis tubing and dialyzed against 2L of H₂O. After 24 hours, H₂O (2.5 mL) was added to the dialysis bag and the dialysate was refreshed with 2L of H₂O. Dialysis was allowed to continue for 24 hours. The sample was removed from dialysis and the tubing was rinsed with H₂O (3 x 1mL) into the polymer sample. The sample was further diluted with 25 mL of H₂O, which was then sonicated for 9 hours. The sample was placed in a centrifuge at 4000 rcf for 6 min. The supernatant was used for all further analysis.

FMN (derived from **P2** 1_{42-b-22}). Half of the reaction volume from the synthesis of **P2** was diluted to 2 mg/mL with respect to the starting materials with 7:2 CH₂Cl₂:CH₃OH. This solution was placed into a 3,500 MWCO snakeskin dialysis tubing and dialyzed against DMSO for 4 hours. The sample was then dialyzed against 4:1 DMSO:H₂O for 4 hours, followed by 3:2 DMSO:H₂O for 4 hours, followed by 2:3 DMSO:H₂O for 4 hours, followed by 1:4 DMSO:H₂O for 4 hours, then 2 x H₂O for 4 hours each to yield an opalescent sample, which was used as is for all further analysis.

NPs 3-6 were formulated as above.

3.16.5 Characterization of Nanomaterials

Transmission Electron Microscopy. Dry-state TEM was prepared as described in Chapter 2, stained with a 1% uranyl acetate solution. Samples for Cryo-TEM were prepared by depositing

3.5 μL of sample to a freshly glow discharged Quantifoil R2/2 TEM grid. The grids were blotted with filter paper under high humidity to create thin films and rapidly plunged into liquid ethane. The grids were transferred to the microscope under liquid nitrogen and kept at < -175 $^{\circ}\text{C}$ while imaging.

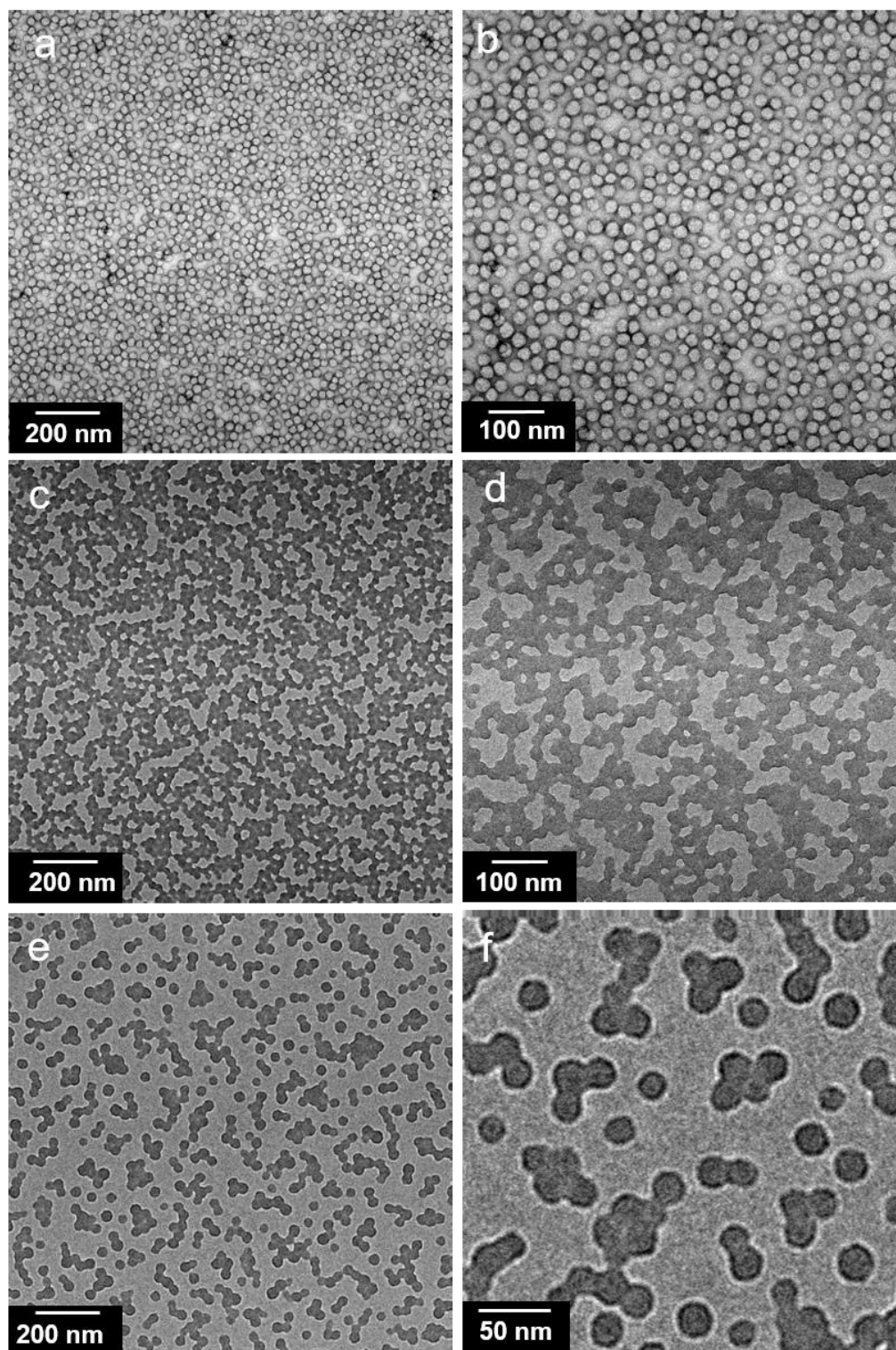


Figure 3.25 TEM of SMN, imaged 14 months after preparation. A and b are negatively stained with 1% uranyl acetate. C-f are not stained.

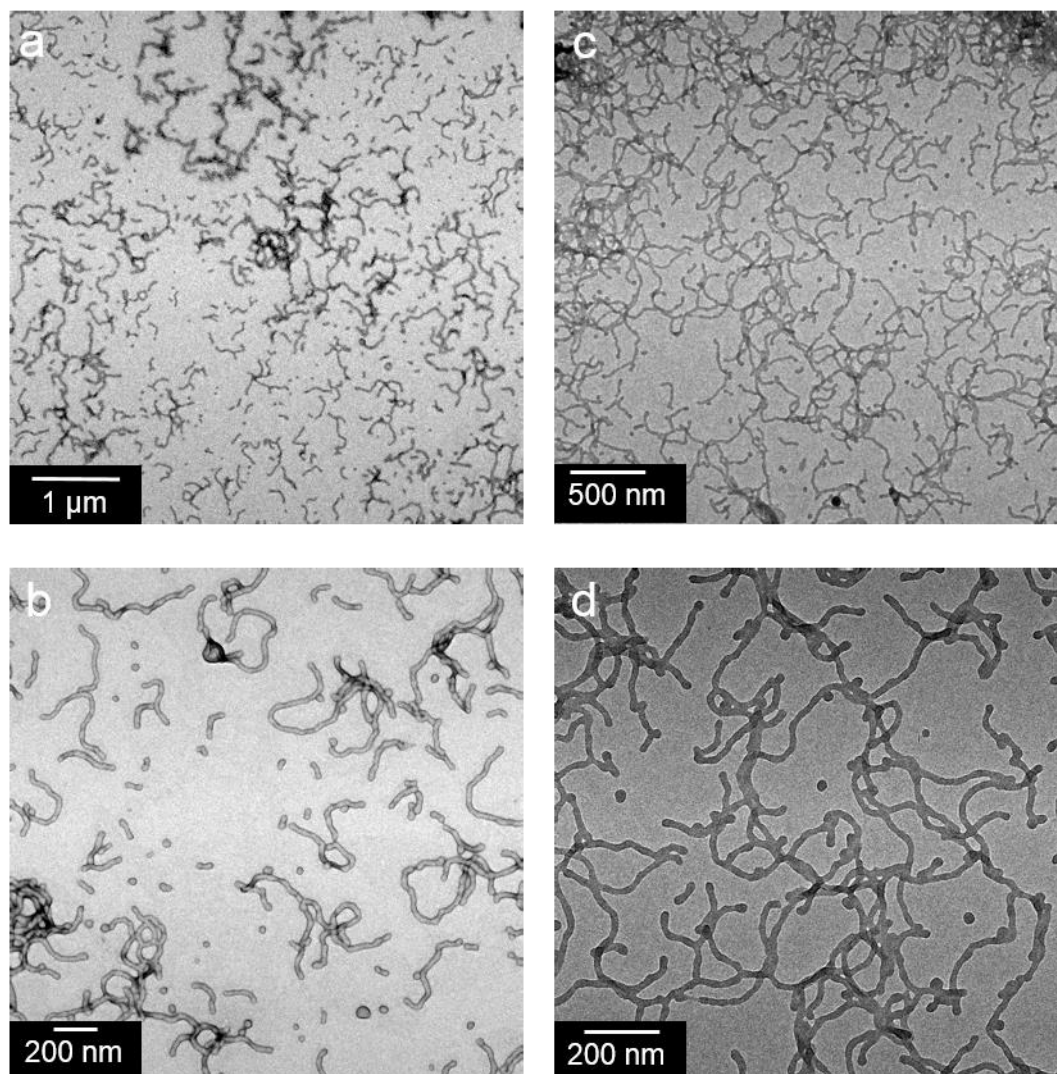


Figure 3.26 TEM of FMN, imaged 14 months after preparation. A and b are negatively stained using 1% uranyl acetate/ c and d are not stained.

For STEM-EDS, images were acquired on a JEOL JEM 2100F TEM equipped with an INCA (Oxford) EDS detector at the University of Pittsburgh, PA. Samples were prepared by drop-casting 5 μ L of sample onto TEM grids (ultrathin 5 nm A-type carbon with 400 mesh Copper) followed by slow drying covered on the bench top for at least 3 hours. Samples were then dried under vacuum for 24-48 hours to remove contamination that would interfere with STEM-EDS. STEM-EDS data was collected for 180 - 600 s at specific points, using the largest probe size (1.5 nm electron beam diameter) with a 200 kV accelerating voltage. Images were

collected in bright field (BF) and high-angle annular dark field (HAADF) modes, and grid background subtraction taken.

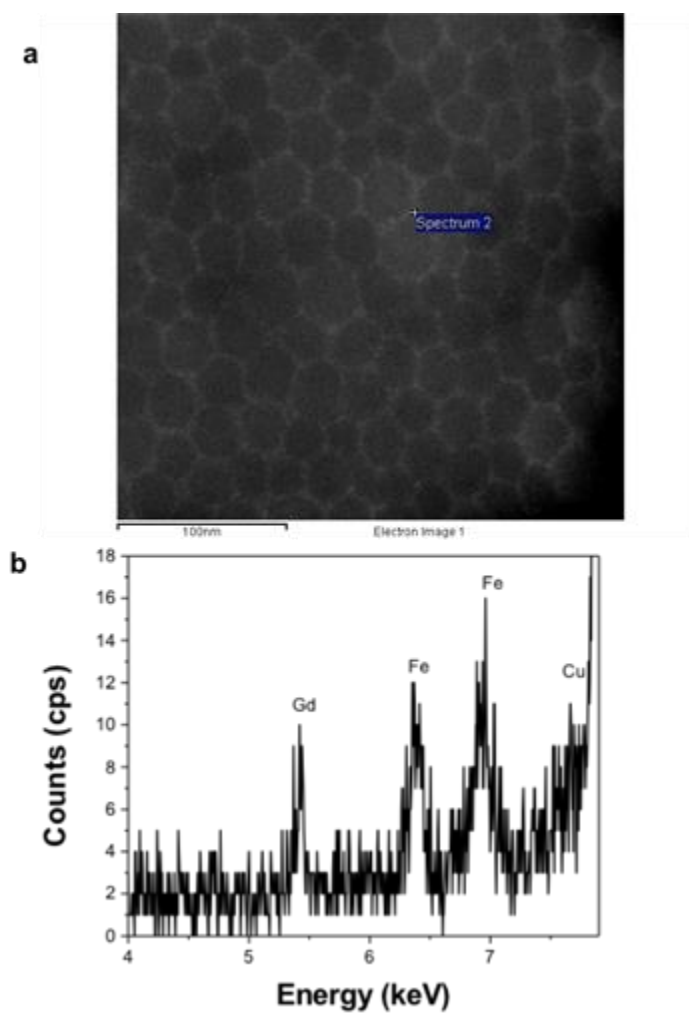


Figure 3.27 STEM-EDS Analysis of SMN. a) STEM-HAADF of SMN with area chosen for EDS analysis (annotated as spectrum 2). b) EDS of SMN from the area selected in (a). Iron and copper signals are artifacts from the specimen holder and copper grid.

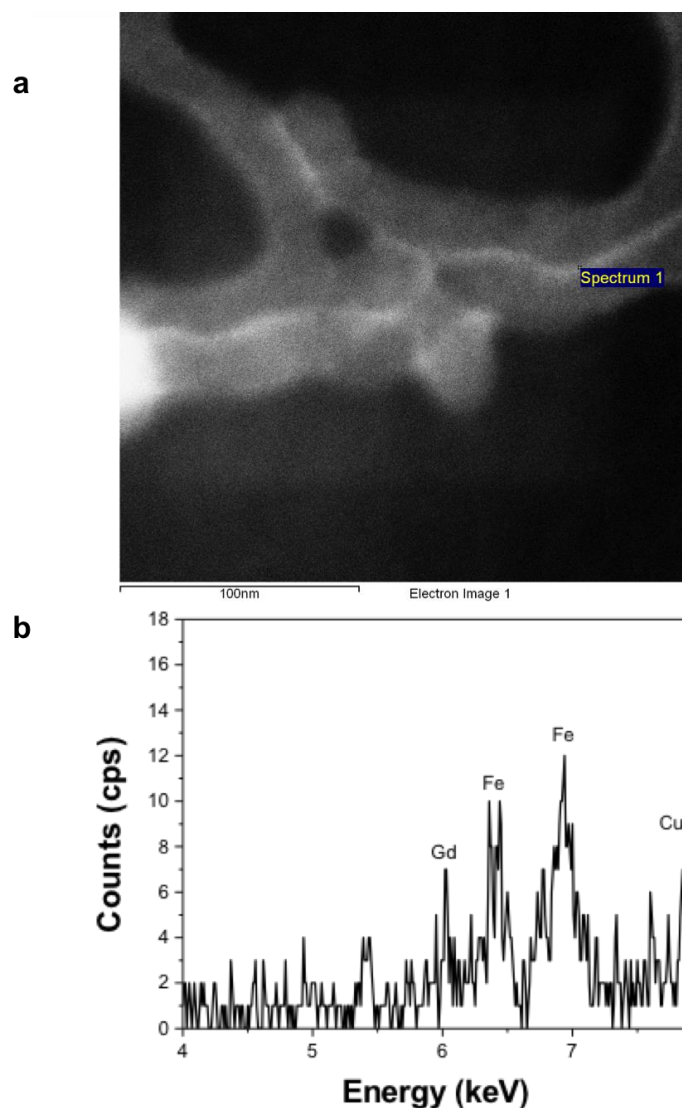


Figure 3.28 STEM-EDS Analysis of FMN. a) STEM-HAADF of FMN with area chosen for EDS analysis (annotated as spectrum 1). b) EDS of FMN from the area selected. Iron and copper signals are artifacts from the specimen holder and copper grid.

3.16.6 ^1H NMRD Profiles, Fitting Parameters, and Description

Proton $1/T_1$ NMRD profiles were measured on a Fast Field-Cycling Stellar SMARTracer NMR Relaxometer (Stelar, Mede (PV), Italy) over a continuum of magnetic field strengths from 0.00024 to 0.25 T (corresponding to 0.01-10 MHz proton Larmor frequencies). The relaxometer operates under computer control with an absolute uncertainty in $1/T_1$ of $\pm 1\%$.

Additional data points in the range 20-70 and 400 MHz were obtained on a Bruker WP80 NMR electromagnet adapted to variable-field measurements (15-80 MHz proton Larmor frequency) Stellar Relaxometer and Jeol ECP spectrometer (9.39 T), respectively. The ^1H T_1 relaxation times were acquired by the standard inversion recovery method with typical 90° pulse width of 3.5 μs , 16 experiments of 4 scans. The temperature was controlled with a Stellar VTC-91 airflow heater equipped with a calibrated copper–constantan thermocouple (uncertainty of ± 0.1 $^\circ\text{C}$). The temperature was determined by previous calibration with a Pt resistance temperature probe. The nuclear magnetic relaxation dispersion (NMRD) profiles allow a detailed characterization of the paramagnetic solutes in terms of a large set of structural and dynamic parameters. The experimental profiles were measured in aqueous solution at 310 K and neutral pH. The best fit parameters, listed in Table 3.3, were obtained using the standard equations for the inner sphere (IS) and outer sphere (OS) relaxation contributions and by fixing the values of the following parameters: the hydration number ($q = 1$), the Gd-H₂O distance ($r = 3.0$ Å), the distance of closest approach of the bulk water molecules ($a = 4.0$ Å) to the metal ion, the relative diffusion coefficient ($D = 3.1 \times 10^{-5} \text{ cm}^2\text{s}^{-1}$).^{3,16,46}

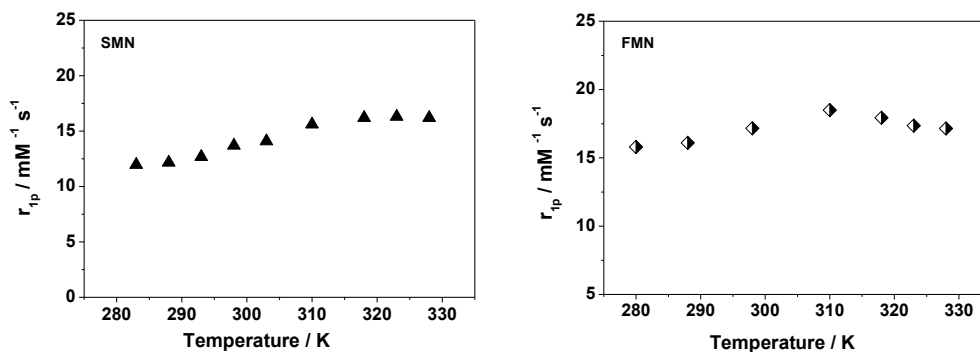


Figure 3.29 NMRD Proton relaxivity as a function of temperature for SMN (left) and FMN (right) at 20 MHz and pH=7.2 In the case of SMN (left) the relaxivity increases with temperature up to about 320 K and then it remains stable at higher temperatures. This behavior is associated with a longer value of the residence lifetime, which implies a more pronounced limiting effect on relaxivity. In the case of FMN (right panel) the profile is characterized by a broad peak centered at about 305-315 K: this implies that around physiological temperatures relaxivity reaches a maximum value and it is not limited by the relatively slow exchange of the bound water molecule. A good fit of the NMRD data was obtained with $^{298}\tau_M$ values of 350 and 560 ns for FMN and SMN, respectively, in full agreement with the temperature-dependence study.

In the case of the paramagnetic nanoparticles, the analysis of the NMRD profiles takes into account the occurrence of a relatively fast local rotation of the metal complex superimposed to the global motion of the nanoparticle (Lipari–Szabo approach).^{47,48} This model allows for the separation of the contribution of the overall global rotation of the paramagnetic nanoparticle ($\tau_{RG} = 5.9$ and 2.8 ns for SMN and FMN, respectively) from the contribution of a faster local motion ($\tau_{RL} = 0.19$ and 0.15 ns for SMN and FMN, respectively) associated with the rotation of the coordination polyhedron about the linker connecting the complex to the nanoparticle. The large difference between the two correlation times indicates that the system is rather flexible and its relaxivity limited by the relatively short value of τ_{RL} . The correlation of the two types of motions is described by the parameter S^2 whose value is comprised between zero (completely independent motions) and one (totally correlated motions). The parameters for electronic relaxation (Δ^2 , τ_V) were used as empirical fitting parameters and do not have a precise physical meaning for these macromolecular systems.^{49,50} The temperature dependence

of proton relaxivity was also measured at 0.5 T in order to obtain an independent evaluation of the residence lifetime τ_M of the coordinated water molecule (Fig. 3.29).

3.16.7 *In Vitro and In Vivo MRI*

MR images were acquired on a Bruker 7.0 T magnet with Avance II hardware equipped with a 72 mm quadrature transmit/receive coil. Axial MR images were acquired using a standard T1-weighted sequence with a repetition time of 3249.2 ms, time to echo of 7.6 ms, with fat suppression, a matrix of 256 x 256, field of view (FOV) of 4.00 x 3.00 cm, resolution of 156 x 117 microns, slice thickness of 1.00 mm, inter-slice distance of 1.00 mm, 80 slices. T₁ shortening was determined by selecting regions of interest (ROI) using Software ParaVision Version 5.1 from T1-T2 map with the following parameters: Times to echo of 11, 33, 55, 77, and 99 ms and 6 repetition times of 5000, 3000, 2500, 2000, 1500, and 1200 ms, and a flip angle of 180°.

All animal procedures were approved by University of California, San Diego's institutional animal care and use committee, protocol S10145. Female mice (C57Bl/6) weighing 18 grams were purchased from Harlan Sprague Dawley, and were anesthetized with 3% isoflurane in O₂ and subjected to baseline MRI imaging before injection. A total of nine mice (three sets of three) were injected with 550 μ L of an aqueous 0.4 mM Gd-DOTA, SMN, or FMN intraperitoneally and imaged continuously under anesthesia for two hours and then again at selected time points of approximately 3h, 4h, 5h, 6h, 7h, 8h, 24h, 48h, and 1 week (each measurement made under anesthesia). Images of successful IP injections can be found in Fig. 3.9.

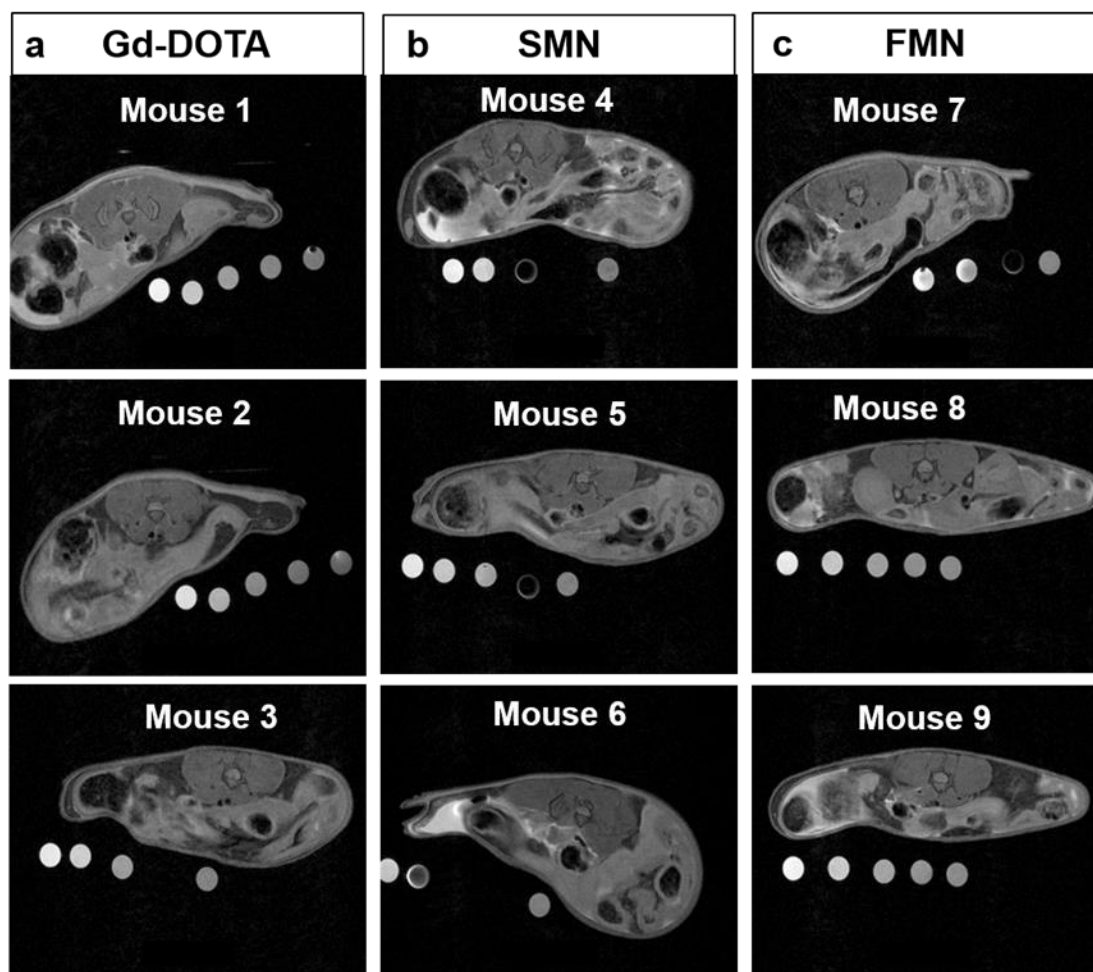


Figure 3.30 Anatomical MRI of IP space at two hours post-injection demonstrating no signal enhancement (for Gd-DOTA) or signal enhancement (for SMN and FMN): NP formulations are retained in the IP space longer than Gd-DOTA. (a) Anatomical image of mice 1 – 3, two hours post-IP injection of Gd-DOTA. (b) Anatomical image of mice 4 – 6, two hours post-IP injection of SMN. (c) Anatomical image of mice 7 – 9, two hours post-IP injection of FMN.

3.16.8 Analysis of T_1 Data

To correct for minor scan-to-scan variations due to noise, T_1 was normalized to pre-injection phantom relaxivities. Phantoms of Gd-DOTA, SMN or FMN, were included in each scan corresponding to the material injected. Concentrations selected were 0.41, 0.12, 0.033, 0.0095, and 0.0027 mM with respect to Gd^{3+} in H_2O . Pre-injection relaxivities were generated for each mouse by averaging $1/T_1$ (r_1) values (sec^{-1}) for each phantom concentration over selected slices of the mouse. (The selected slices were those in which the organs of interest

were visible.) For each scanning time point after injection, an average $1/T_1$ for 5 phantoms were calculated and compared to the pre-injection relaxivity value to generate an adjustment factor for the scan of interest. Relaxivity values generated from phantoms for each scan were within (+/-) 1 - 20% of the pre-injection phantom relaxivity. After organ ROI T_1 was converted to $1/T_1$, each were multiplied by the adjustment factor. $1/T_1$ was averaged over each organ and then converted back to T_1 (msec). Normalized T_1 were averaged over three mice for each time point sampled and each material. Error for urinary bladder and liver are standard errors, over three mice for each material, using normalized T_1 for each specific time point sampled.

3.16.9 *Ex vivo* ICP-MS Analysis of Organs

Mice were sacrificed using a lethal overdose of >5% isofluorane and selected organs harvested. The liver, bowel and spleen were dissected, placed in separate tubes and their masses were recorded individually. Mass of the entire liver, bowel and spleen was recorded, added to concentrated nitric acid (900 μL), and placed on a shaker overnight, vented. The following morning, concentrated H_2O_2 (50 μL) was added to each of the organ solutions and placed back on the shaker, vented, for approximately 30 min. An aliquot (200 μL) of the digested organs was added to distilled DI water (800 μL) and submitted to Exova for ICP-MS analysis to determine Gd^{3+} concentration. The final concentration of Gd^{3+} in each organ normalized to organ mass. Individual animal profiles at 2, 12 and 24 hours and average gadolinium concentration detection at 1 week are described in Figs. 3.31-3.33.

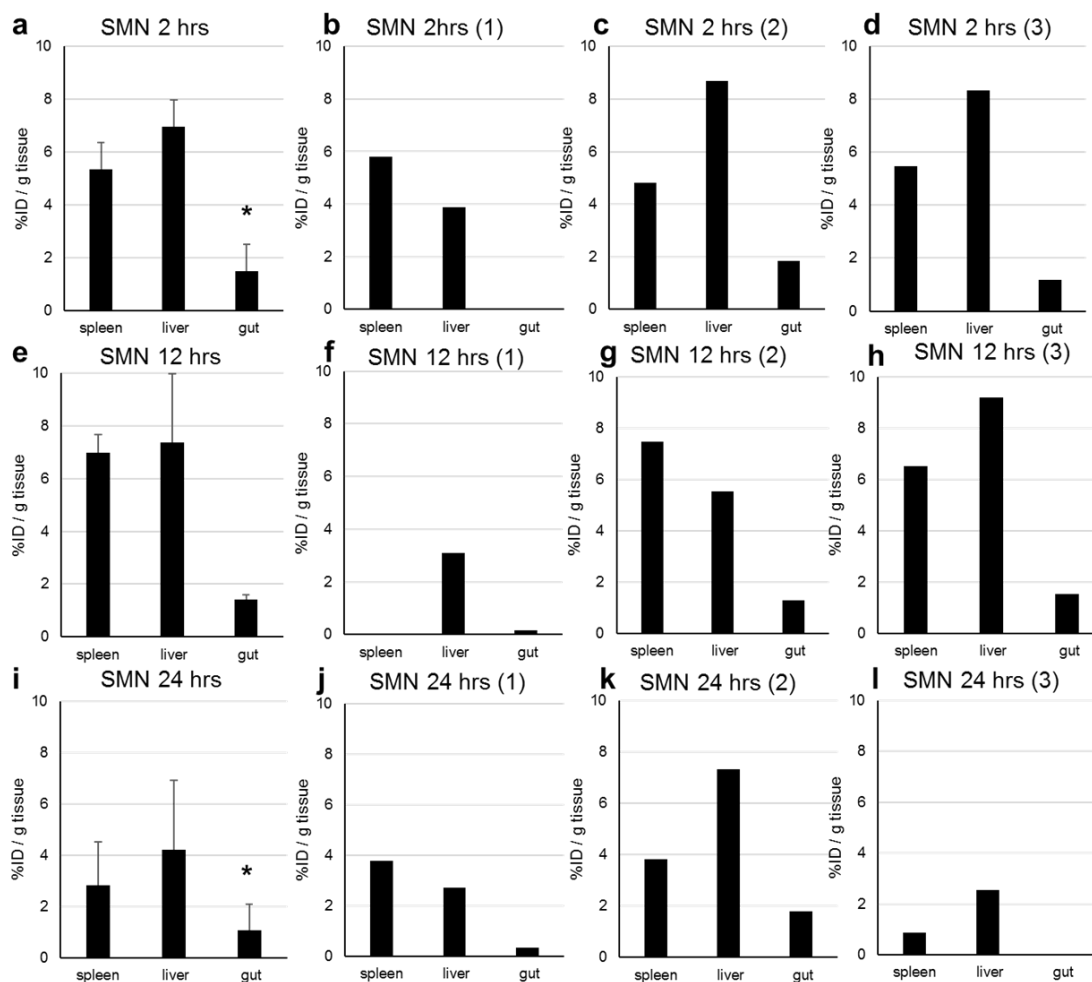


Figure 3.31 Average and three individual mice for SMN at 2, 12 and 24 hrs. Graphs a, e and i are the average of three mice. Graphs b-d, are individual mice sacrificed at 2 hours post injection. Graphs f - h are individual mice sacrificed at 12 hrs, Graphs j-k are individual mice sacrificed at 24 hrs. Error bars are for n= 3 mice except where annotated with *, where n = 2.

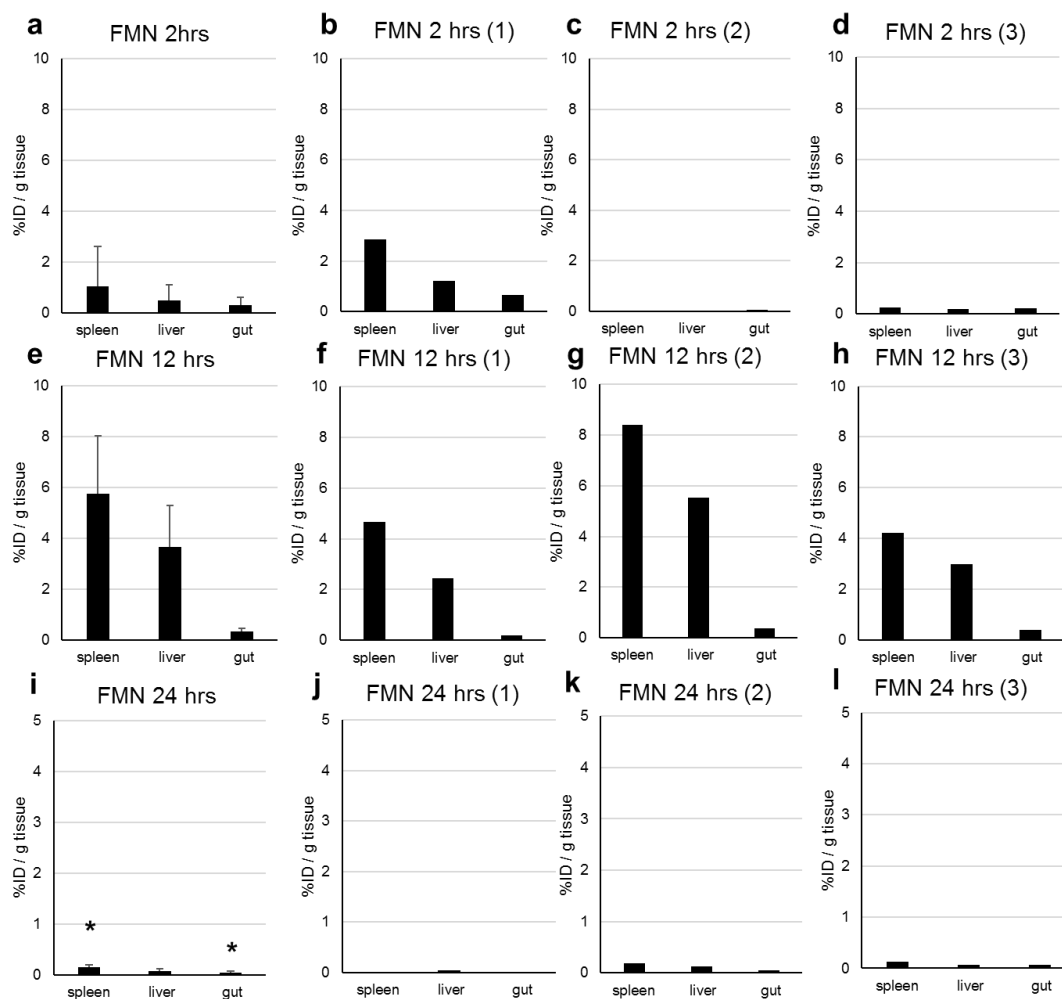


Figure 3.32 Average and three individual mice for FMN at 2, 12 and 24 hrs. Graphs a, e and i are the average of three mice. Graphs b- d, are individual mice sacrificed at 2 hours post injection. Graphs f- h are individual mice sacrificed at 12 hrs. Graphs j- l are individual mice sacrificed at 24 hrs. Error bars are for n= 3 mice except where annotated with *, where n = 2.

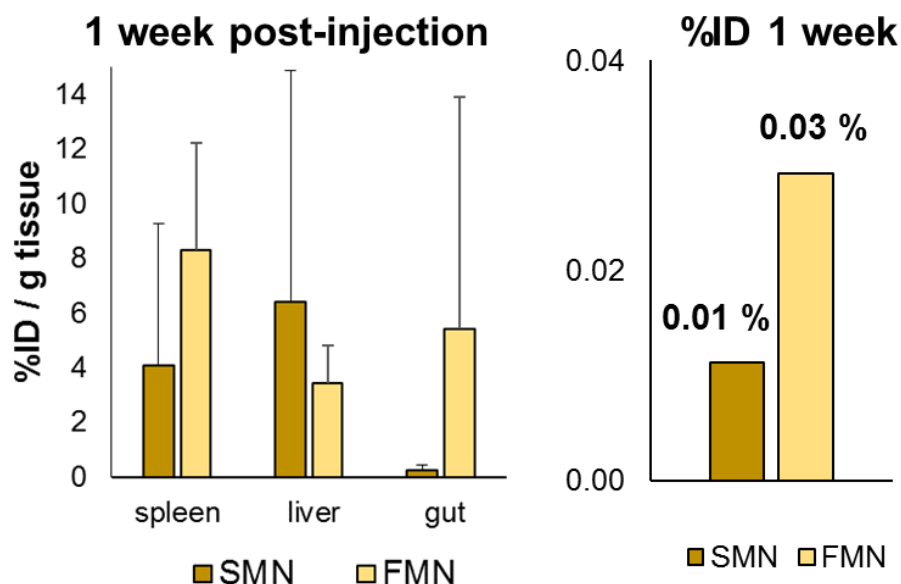


Figure 3.33 Detection of gadolinium in mice 1 week post injection. %ID/g tissue in spleen, liver and gut for SMN and FMN. Total % of injected dose (spleen, liver and gut) at 1 week

3.16.10 Concentration Determination of Gadolinium in Aqueous Nanoparticles

Standard Curve for Gd^{3+} Concentration Determination. A 0.1 M stock solution of GdCl_3 in H_2O was prepared. From this stock, concentrations of 3.0, 1.0, 0.5, and 0.01 mM of Gd^{3+} in 2:3:5 $\text{HNO}_3:\text{H}_2\text{O}:\text{D}_2\text{O}$ were made. T_1 relaxations were determined for each concentration of Gd^{3+} using inversion recovery experiments on a 300 MHz Varian NMR instrument. $1/T_1$ were averaged for three separate samples at the same concentration, then plotted to give a relaxivity of free Gd^{3+} of $13.8 \text{ mM}^{-1}\text{sec}^{-1} \pm 0.830$ with an R^2 value of 0.9992.

General Procedure to Determine Concentration of Gd^{3+} for SMN and FMN. In order to determine Gd^{3+} concentration, the metal was first stripped from the chelate using concentrated nitric acid. 80% HNO_3 in water (115 μL) was added to an aliquot of each sample (115 μL). Each mixture was then heated at 65 $^\circ\text{C}$ for approximately 12 hours. The sample was diluted with 230 μL of D_2O and T_1 was determined using an inversion recovery experiment on

a 300 MHz Varian NMR. Based the standard curve created above, the concentration of Gd^{3+} in stock solutions of SMN and FMN were determined to be 0.408mM and 0.444mM, respectively.

3.16.11 Relaxivity Measurements for CTA Polymer Nanoparticles

The T1 times of serial dilutions of Gd-DOTA, NP3 or NP4 were determined on a 300 MHz Varian NMR using an inversion recovery experiment, as described above. The results are depicted as plots of concentration of gadolinium in mM versus $1/T_1$ in seconds. The results are inconclusive.

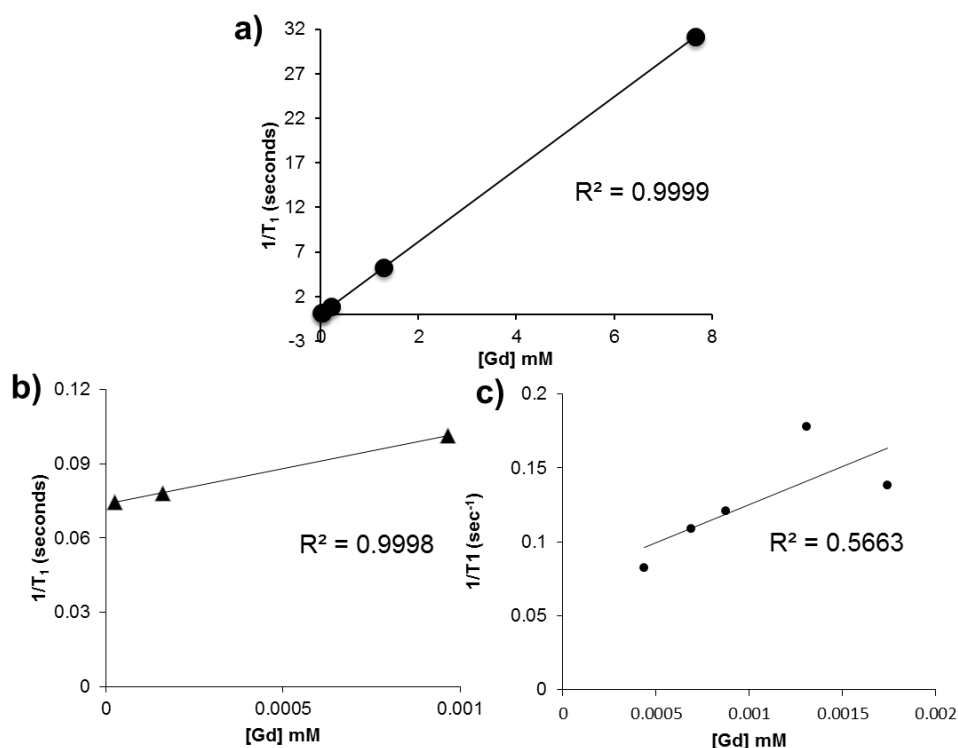


Figure 3.34 Relaxivity measurements using inversion recovery experiments at 300 MHz, with R-squared of the linear best fit inset. a) relaxivity plot for Gd-DOTA, the control compound. Relaxivity was measured as $4 \text{ mM}^{-1}\text{sec}^{-1}$. b) One example plot for NP3, “Gd-shell” particles. A relaxivity measurement of $28 \text{ mM}^{-1}\text{sec}^{-1}$ is based on estimated concentration. A second measurement of this particle also generated a relaxivity of about 28 (not pictured). When concentration was adjusted based on measured concentration (ICP-MS) the relaxivity was in turn adjusted to $227 \text{ mM}^{-1}\text{sec}^{-1}$. c) One example plot for NP4, “Gd-core” particles. A relaxivity measurement of $52 \text{ mM}^{-1}\text{sec}^{-1}$ is based on estimated concentration. When concentration was

adjusted based on measured concentration (ICP-MS) the relaxivity was in turn adjusted to 1450 mM⁻¹sec⁻¹. The linear regression fit for data sets a and b were satisfactory, but not good for plot c. No conclusions can be made from these experiments.

3.17 References

- (1) Information, N. C. for B. Molecular Imaging and Contrast Agent Database (MICAD) <https://www.ncbi.nlm.nih.gov/books/NBK5330/> (accessed Apr 7, 2017).
- (2) Pierre, V. C.; Allen, M. J.; Caravan, P. *J Biol Inorg Chem* **2014**, *19* (2), 127–131.
- (3) Caravan, P.; Ellison, J. J.; McMurry, T. J.; Lauffer, R. B. *Chem. Rev.* **1999**, *99* (9), 2293–2352.
- (4) Caravan, P. *Chem. Soc. Rev.* **2006**, *35* (6), 512.
- (5) Chien, M. P.; Thompson, M. P.; Barback, C. V.; Ku, T. H.; Hall, D. J.; Gianneschi, N. C. *Adv. Mater.* **2013**, *25* (26), 3599–3604.
- (6) James, C. R.; Rush, A. M.; Insley, T.; Vukovic, L.; Adamiak, L.; Kral, P.; Gianneschi, N. C. *J. Am. Chem. Soc.* **2014**, *136* (32), 11216–11219.
- (7) Rush, A. M.; Nelles, D. A.; Blum, A. P.; Barnhill, S. A.; Tatro, E. T.; Yeo, G. W.; Gianneschi, N. C. *J. Am. Chem. Soc.* **2014**, *136* (21), 7615–7618.
- (8) Thompson, M. P.; Randolph, L. M.; James, C. R.; Davalos, A. N.; Hahn, M. E.; Gianneschi, N. C. *Polym. Chem.* **2014**, *5* (6), 1954–1964.
- (9) Hahn, M. E.; Randolph, L. M.; Adamiak, L.; Thompson, M. P.; Gianneschi, N. C. *Chem. Commun.* **2013**, *49* (28), 2873–2875.
- (10) Allen, M. J.; Raines, R. T.; Kiessling, L. L. *J. Am. Chem. Soc.* **2006**, *128* (20), 6534–6535.
- (11) Klemm, P. J.; Floyd, W. C.; Smiles, D. E.; Fréchet, J. M. J.; Raymond, K. N. *Contrast Media Mol. Imaging* **2012**, *7* (1), 95–99.
- (12) Datta, A.; Raymond, K. N. *Acc. Chem. Res.* **2009**, *42* (7), 938–947.
- (13) Leitgeb, A.; Wappel, J.; Slugovc, C. *Polymer (Guildf)*. **2010**, *51* (14), 2927–2946.
- (14) Bielawski, C. W.; Grubbs, R. H. *Prog. Polym. Sci.* **2007**, *32* (1), 1–29.
- (15) Blanz, A.; Madsen, J.; Battaglia, G.; Ryan, A. J.; Armes, S. P. *J. Am. Chem. Soc.* **2011**, *133* (41), 16581–16587.
- (16) Aime, S.; Botta, M.; Terreno, E. In *Advances in Inorganic Chemistry*; Academic Press, 2005; Vol. Volume 57, pp 173–237.

- (17) Villaraza, A. J.; Bumb, A.; Brechbiel, M. W. *Chem. Rev.* **2010**, *110* (5), 2921–2959.
- (18) Liu, Y.; Zhang, N. *Biomaterials* **2012**, *33* (21), 5363–5375.
- (19) Lu, Z.; Wang, J.; Wientjes, M. G.; Au, J. L.-S. *Future Oncol.* **2010**, *6* (10), 1625–1641.
- (20) Dakwar, G. R.; Shariati, M.; Willaert, W.; Ceelen, W.; De Smedt, S. C.; Remaut, K. *Adv. Drug Deliv. Rev.* **2016**, *108*, 13–24.
- (21) Ishigami, H.; Kitayama, J.; Kaisaki, S.; Hidemura, A.; Kato, M.; Otani, K.; Kamei, T.; Soma, D.; Miyato, H.; Yamashita, H.; Nagawa, H. *Ann. Oncol.* **2010**, *21* (1), 67–70.
- (22) Xie, Y.; Long, Q.; Wu, Q.; Shi, S.; Dai, M.; Liu, Y.; Liu, L.; Gong, C.; Qian, Z.; Wei, Y.; Zhao, X. *RSC Adv.* **2012**, *2* (20), 7759–7771.
- (23) Tsai, M.; Lu, Z.; Wang, J.; Yeh, T. K.; Wientjes, M. G.; Au, J. L. S. *Pharm. Res.* **2007**, *24* (9), 1691–1701.
- (24) Jung, C.; Kaul, M. G.; Bruns, O. T.; Du i, T.; Freund, B.; Heine, M.; Reimer, R.; Meents, A.; Salmen, S. C.; Weller, H.; Nielsen, P.; Adam, G.; Heeren, J.; Ittrich, H. *Circ. Cardiovasc. Imaging* **2014**, *7* (2), 303–311.
- (25) Abdelhalim, M.; Mady, M. *Lipids Health Dis.* **2011**, *10* (1), 1–9.
- (26) Chien, M. P.; Carlini, A. S.; Hu, D.; Barback, C. V.; Rush, A. M.; Hall, D. J.; Orr, G.; Gianneschi, N. C. *J. Am. Chem. Soc.* **2013**, *135* (50), 18710–18713.
- (27) Callmann, C. E.; Barback, C. V.; Thompson, M. P.; Hall, D. J.; Mattrey, R. F.; Gianneschi, N. C. *Adv. Mater.* **2015**, *27* (31), 4611–4615.
- (28) Nguyen, M. M.; Carlini, A. S.; Chien, M. P.; Sonnenberg, S.; Luo, C.; Braden, R. L.; Osborn, K. G.; Li, Y.; Gianneschi, N. C.; Christman, K. L. *Adv. Mater.* **2015**, *27* (37), 5547–5552.
- (29) Blum, A. P.; Kammeyer, J. K.; Gianneschi, N. C. *Chem. Sci.* **2016**, *7* (2), 989–994.
- (30) Wang, Z.; Li, Y.; Huang, Y.; Thompson, M. P.; LeGuyader, C. L. M.; Sahu, S.; Gianneschi, N. C. *Chem. Commun.* **2015**, *51* (96), 17108–17111.
- (31) Christian, D. A.; Cai, S.; Garbuzenko, O. B.; Harada, T.; Zajac, A. L.; Minko, T.; Discher, D. E. *Mol. Pharm.* **2009**, *6* (5), 1343–1352.
- (32) Geng, Y.; Dalhaimer, P.; Cai, S.; Tsai, R.; Tewari, M.; Minko, T.; Discher, D. E. *Nat. Nanotechnol.* **2007**, *2* (4), 249–255.
- (33) Müllner, M.; Dodds, S. J.; Nguyen, T.-H.; Senyschyn, D.; Porter, C. J. H.; Boyd, B. J.; Caruso, F. *ACS Nano* **2015**, *9* (2), 1294–1304.
- (34) Champion, J. A.; Mitragotri, S. *Proc. Natl. Acad. Sci. U. S. A.* **2006**, *103* (13), 4930–4934.

- (35) Liu, Z.; Cai, W.; He, L.; Nakayama, N.; Chen, K.; Sun, X.; Chen, X.; Dai, H. *Nat. Nanotechnol.* **2007**, *2* (1), 47–52.
- (36) Tao, L.; Hu, W.; Liu, Y.; Huang, G.; Sumer, B. D.; Gao, J. *Exp. Biol. Med.* **2011**, *236* (1), 20–29.
- (37) Hu, X.; Hu, J.; Tian, J.; Ge, Z.; Zhang, G.; Luo, K.; Liu, S. *J. Am. Chem. Soc.* **2013**, *135*, 17617–17629.
- (38) Hu, X.; Liu, G.; Li, Y.; Wang, X.; Liu, S. *J. Am. Chem. Soc.* **2015**, *137* (1), 362–368.
- (39) Basel, M. T.; Balivada, S.; Wang, H.; Shrestha, T. B.; Seo, G. M.; Pyle, M.; Abayaweera, G.; Dani, R.; Koper, O. B.; Tamura, M.; Chikan, V.; Bossmann, S. H.; Troyer, D. L. *Int. J. Nanomedicine* **2012**, *7*, 297–306.
- (40) Di Pasqua, A. J.; Huckle, J. E.; Kim, J. K.; Chung, Y.; Wang, A. Z.; Jay, M.; Lu, X. *Small* **2012**, *8* (7), 997–1000.
- (41) Markman, M. *Crit. Rev. Oncol. Hematol.* **1999**, *31* (3), 239–246.
- (42) Dadashzadeh, S.; Mirahmadi, N.; Babaei, M. H.; Vali, A. M. *J. Control. Release* **2010**, *148* (2), 177–186.
- (43) Proetto, M. T.; Anderton, C. R.; Hu, D.; Szymanski, C. J.; Zhu, Z.; Patterson, J. P.; Kammeyer, J. K.; Nilewski, L. G.; Rush, A. M.; Bell, N. C.; Evans, J. E.; Orr, G.; Howell, S. B.; Gianneschi, N. C. *ACS Nano* **2016**, *10* (4), 4046–4054.
- (44) Matson, J. B.; Grubbs, R. H. *Macromolecules* **2010**, *43* (1), 213–221.
- (45) Sanford, M. S.; Love, J. A.; Grubbs, R. H. *J. Am. Chem. Soc.* **2001**, *123* (27), 6543–6554.
- (46) Andre, Ä. P.; Toth, E.; Fischer, H.; Seelig, A.; Mäcke, H. R.; Merbach, Ä. E. *Chem. Eur. J.* **1999**, *5*, 2977–2983.
- (47) Lipari, G.; Szabo, A. *J. Am. Chem. Soc.* **1982**, *104* (17), 4559–4570.
- (48) Lipari, G.; Szabo, A. *J. Am. Chem. Soc.* **1982**, *104* (17), 4546–4559.
- (49) Ferreira, M. F.; Mousavi, B.; Ferreira, P. M.; Martins, C. I. O.; Helm, L.; Martins, J. A.; Geraldes, C. F. G. C. *Dalt. Trans.* **2012**, *41* (18), 5472–5475.
- (50) Zhang, Z.; Greenfield, M. T.; Spiller, M.; McMurry, T. J.; Lauffer, R. B.; Caravan, P. *Angew. Chemie Int. Ed.* **2005**, *44* (41), 6766–6769.

Chapter 4

Fatty Acid Conjugates for Hitchhiking on Albumin: Diagnostic and Therapeutic Applications

4.18 Introduction

Synthetic nanoparticles are widely explored for nanomedicine applications, yet efficient tissue targeting *in vivo* remains a challenge. As an alternative to polymeric nanomaterials, a protein drug carrier is proposed. Harnessing human serum albumin's endogenous and naturally evolved role as a hydrophobic molecule carrier, we designed conjugates of warheads with diagnostic or therapeutic application to hitchhike on the protein. The designed gadolinium-based contrast agents and paclitaxel based warheads are covalently attached to a long chain fatty acid. Through specific conjugate design, these “protein nanoparticles” experience prolonged circulation and accumulation profiles compared to small molecule counterparts.

Preliminary exploratory work of the proposed fatty acid (FA) platform technology examined a paclitaxel (PTX) pro-drug conjugate (PTX-FA) of octadecandioic acid (ODDA, C₁₈) formulated with albumin in treatments of tumor-burdened mice. While detailed *in vivo* experiments are out of the scope of this thesis, representative data provides evidence of the efficacy of the novel platform in xenograft models (Fig. 4.1). With evidence that a therapeutic drug formulated with albumin could target and suppress tumor growth with safer administration

compared to a clinical standard, Abraxane (ABX), we turned to investigating the scope of this platform.

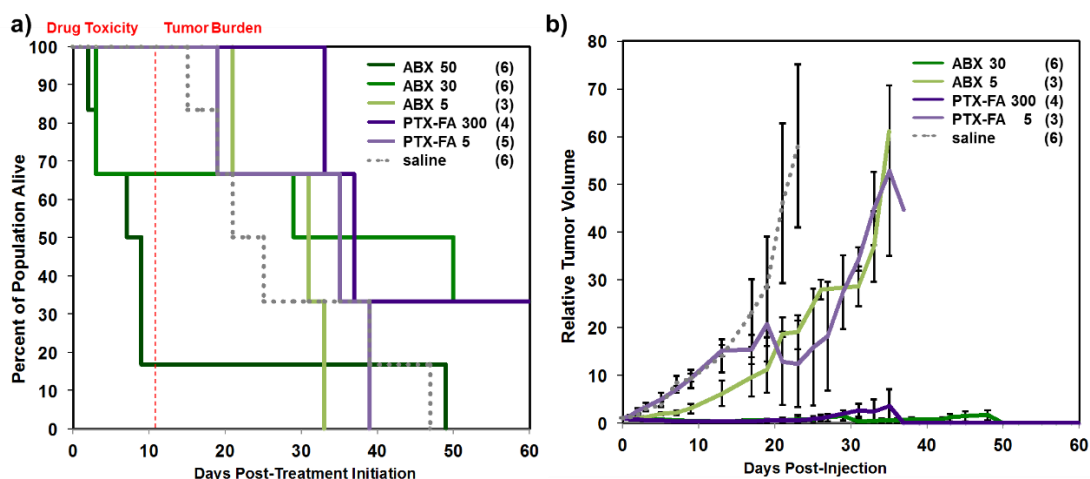


Figure 4.1 PTX-FA + HSA was tested head-to-head against Abraxane in a xenograft HT-1080 tumor model. Tumor-burdened animals were dosed with respect to mg of paclitaxel per kg body weight (mg/kg) 3 times total, every 4 days (q4dx3). Panel (a) shows a Kaplan-Meier survival plot. The tumor growth plots in panel (b) show efficacy in suppressing tumor growth at various dosings. On-going *in vivo* studies are investigating optimal therapeutic dosings in the HT-1080 model, as well as other tumor models of interest.

A gadolinium-based contrast agent conjugate of ODDA was envisioned for use as a blood pool contrast agent and a targeting imaging agent. Described herein is a Gd-DOTA moiety modified with ODDA, its characterization *in vitro* with regards to enhancement of relaxivity, and its utility in *in vivo* imaging, with subsequent blood circulation and bioaccumulation profiles generated. We hypothesized that utilizing this platform for an imaging agent would provide key information regarding utility of the diacid-albumin interaction for favorable *in vivo* properties: hijacking the albumin for prolonged circulation time of the gadolinium based contrast agent (GBCA) will provide a longer window of opportunity for imaging and favorable biodistribution, circumventing problems with existing small molecule clinical contrast agents. Furthermore, when the small molecule fatty acid conjugate binds with HSA, the rotational correlation time of the species will slow down, as it

is coupled to a macromolecular species; this will cause an increase in relaxivity. We compare a fatty acid Gd-DOTA conjugate (FA-Gd) head-to-head to MultiHance and Gd-DOTA to understand behavior in blood circulation time and bioaccumulation, especially targeting tumor tissue.

In the second part of this chapter we sought to establish a screening tool to evaluate the toxicity of novel fatty acid-conjugates, and examine effects of modifications of the conjugate with respect to toxicity. Comprehensive *in vitro* toxicity for several fatty acid-derivatives was performed. Initial mechanistic studies using a surrogate fatty acid-fluorescein probe provided preliminary information regarding cancer cell uptake of fatty acid conjugates under the investigated conditions.

4.19 Fatty Acid Conjugates as Diagnostic Agents

Of interest in the drug delivery field are methods to prolong the circulation time of small molecule diagnostic agents, and to enhance their targeting at the region of interest. The FA platform presents a means to address both of these challenges, and designing MRI contrast agents to bind with HSA is a strategy employed by other clinical and academic examples.¹

A fatty acid conjugate of a modified Gd-DOTA chelate was prepared and examined for its relaxivity properties. The FA-Gd was formulated with HSA then evaluated *in vivo* for imaging capabilities, blood circulation time enhancement, and well as targeting to a tumor. A cartoon overview of this FA-Gd platform is depicted in Fig. 4.2.

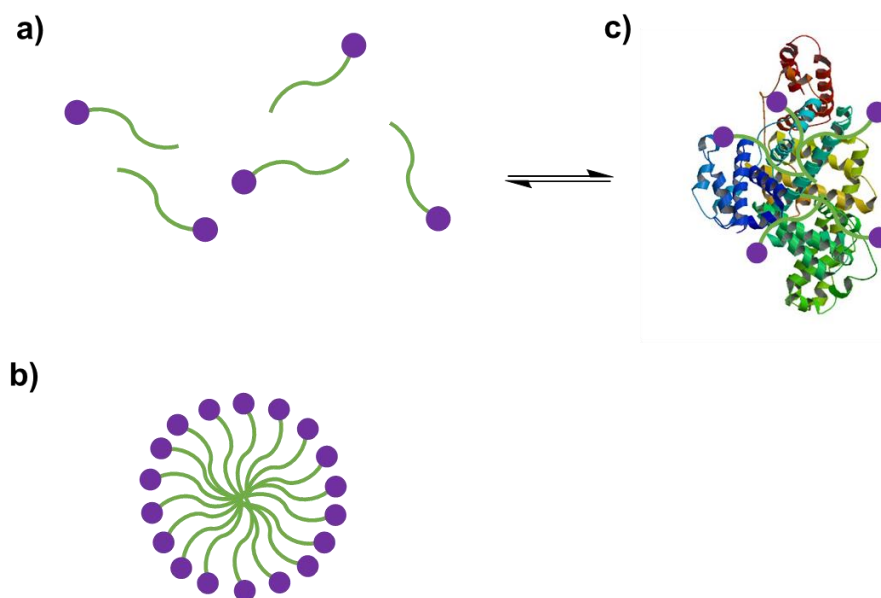


Figure 4.2 A cartoon of FA-Gd conjugates of a diagnostic warhead, designed to selectively interact with HSA. a) represents the ODDA hydrophobic tail (green) and Gd-DOTA moiety (purple dot). The small molecule conjugate is amphiphilic and may aggregate, as in panel (b). Panel c) represents 5 molecules of ODDA-conjugate binding to HSA; equilibrium arrows are used because it is a reversible process.

4.19.1 Synthesis and Formulation Strategy

The fatty-acid-chelate for gadolinium was prepared in a similar strategy to previously prepared fatty-acid conjugates.² The mono-methyl ester ODDA was activated as the pentafluorophenol (-PFP) ester to give a good leaving group, then reacted with a commercially available, mono ethylamide, tris-*t*-butyl DOTA derivative (Fig. 4.3). Subsequent exposure to acidic then basic conditions removed the *t*-butyl and methyl-ester protecting groups. The free fatty-acid-DOTA ligand was then metalated with gadolinium at neutral pH and purified using RP-HPLC to give the FA-Gd-DOTA compound (FA-Gd) (Fig. 4.19).

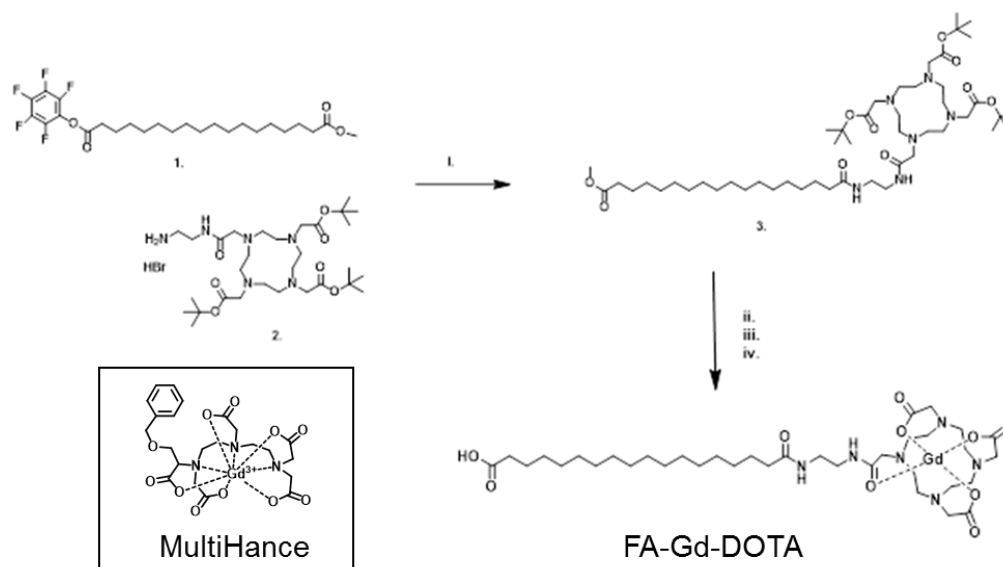


Figure 4.3 The synthetic strategy for preparing FA-Gd-DOTA. Detailed methods included in method section.

Before use in further experiments, free Gd^{3+} was removed from the aqueous solution of FA-Gd using a basic precipitation method. The purified solution was confirmed to have no free metal using the Arsenazo assay.³

The FA-Gd compound contains a hydrophobic fatty acid chain and a hydrophilic DOTA moiety. The compound is amphiphilic in nature, and found to be fully soluble in aqueous conditions. To probe whether the compound aggregates in solution as a small molecule surfactant, a pyrene critical micelle concentration (CMC) assay was performed.⁴ Under physiological conditions (DPBS, pH ~7.5), FA-Gd was found to have a CMC of about ~ 1mM (Fig. 4.21). A CMC concentration is important to keep in mind while measuring other physicochemical parameters of the compound, especially relaxivity, where macromolecular species have drastically different properties than small-molecule constituents.

4.19.2 Relaxivity Measurements

To evaluate the efficacy of FA-Gd as a potential contrast agent, the relaxivity was compared to clinically relevant contrast agents. Relaxivity was measured at 1.4 T using a Bruker minispec over a range of concentrations. FA-Gd was measured either on its own or in the presence of HSA, and compared to MultiHance, gadobenate dimeglumine (inset Fig. 4.3, MH), and Gd-DOTA with HSA. Measurements were repeated with different stock solutions. The results are described in Fig 4.4 and Table 4.3. FA-Gd has a relaxivity of $3.9 \text{ mM}^{-1}\text{sec}^{-1}$, but when formulated in the presence of excess HSA to form FA-Gd + HSA, the relaxivity increases to $13.5 \text{ mM}^{-1}\text{sec}^{-1}$. FA-Gd + HSA demonstrates higher relaxivity than MultiHance formulated with HSA, which had a measured relaxivity of $5.8 \text{ mM}^{-1}\text{sec}^{-1}$. FA-Gd + HSA also demonstrated higher relaxivity than Gd-DOTA (Dotarem™, gadoterate meglumine) in the presence of HSA, which had a relaxivity of $6.0 \text{ mM}^{-1}\text{sec}^{-1}$. These experiments confirm the advantage of formulating the FA-Gd with HSA: as a small molecule, and below the CMC (fully solvated), FA-Gd has a relaxivity in the regime of other small molecules. For samples at concentrations at or above the CMC, relaxivity enhancement was greater, presumably from effects of macromolecular aggregates of FA-Gd (data not reported, but omitted from analysis). When formulated with HSA, the FA-Gd molecule binds strongly with HSA, which imparts a relaxivity enhancement from coupling the tumbling time of the Gd chelate to that of the slower tumbling protein. This interaction was expected, and similarly demonstrated for other protein-binding small molecule Gd chelates.^{5,6} We tested our formulation with MH head-to-head, showing that our formulation had higher relaxivity compared to clinical MH. The favorable relaxivity of our complex could be attributed to the more selective and strong binding affinity for a fatty-acid-type molecule compared to the non-specific hydrophobic binding moiety in MH.

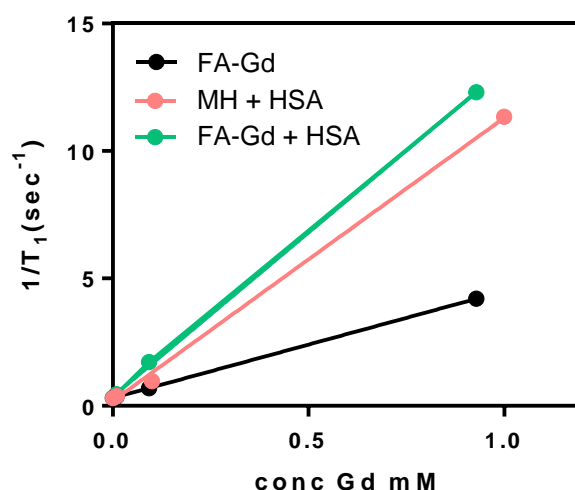


Figure 4.4 Representative relaxivity plots comparing FA-Gd, MultiHance (MH) formulated with HSA and FA-Gd formulated with HSA.

An experiment was performed in which FA-Gd was formulated at different ratios to HSA. In fact, because the interaction between FA-Gd and HSA is non-covalent, despite the predicted strong binding constant, the molecule exists in equilibrium between a bound and unbound state with HSA (Fig. 4.2. equilibrium between species a and c). The previously discussed experiments were done with excess protein to favor a FA-Gd + HSA bound complex. Formulation of FA-Gd in the presence of varying ratios of HSA sought to tease out any effects of relaxivity from a mixture of protein-bound and unbound FA-Gd. Under the conditions probed, there seemed to be little to no effect of the ratio of FA-Gd to HSA (Table 4.4).

4.19.3 *In Vivo* Evaluation

To evaluate contrast enhancement, differentiation in circulation time, and bioaccumulation *in vivo*, the FA-Gd was formulated and introduced in a xenograft model bearing an HT-1080 tumor. FA-Gd was formulated with HSA at a 5:1 molar ratio with respect to Gd; this formulation emulates the on-going *in vivo* efficacy work with PTX-FA. Three types

of *in vivo* experiments were performed: blood half-life, imaging and biodistribution. Three materials were tested: FA-Gd, MH and Gd-DOTA formulated with HSA at low and high doses, in either healthy or tumor-burdened animals.

First, preliminary studies investigated the feasibility of using our novel materials for MRI imaging in healthy animals. Imaging using a 4.7 T preclinical MRI scanner, imaging was performed in conjunction with blood half-life studies. These preliminary results indicated that both FA-Gd and MH circulate in the bloodstream of healthy mice hours post tail-vein injection (Figs. 4.22 and 4.27). FA-Gd had slightly higher serum concentration compared to MH at the same time point, indicating an enhancement of circulation time with our formulation strategy (Fig. 4.27). MRI scans revealed contrast enhancement at the gall bladder, clearance via the hepatobiliary system (Fig. 4.22). At the same timepoint, MH did not have a significant contrast enhancement in the gall bladder. With these results in hand, we pursued investigation of our materials in a tumor-burdened animal.

In the next study, FA-Gd and MH were introduced *via* tail-vein injection in tumor-burdened mice. A conservative dosing of Gd-material was used (“low dose” for FA-Gd = 100 nmol, for MH = 50 nmol). MRI imaging immediately post-injection, and at 2 hours and 4 hours post-injection show contrast enhancement at the gall bladder out to 4 hours post-injection (Figs. 4.23 and 4.24). The contrast is apparent despite the low plasma concentration of gadolinium, confirmed with blood draws and analysis via ICP-MS (Fig. 4.28), indicating clearance from the blood via hepatobiliary system and accumulation at this organ. Inspection of the tumor-region did not show obvious contrast enhancement expected from either formulation. At 24 hours, animals were imaged, and no contrast was visible. The animals were then scarified, perfused with saline, then organs harvested and digested for biodistribution analysis. The experimental procedures are described in more detail in the methods section, along with the biodistribution results (Figs. 4.30 and 4.31). In summary, while gadolinium was detected in the

heart, liver, kidney, spleen, lung and tumor, there were no significant trends across the small sample size ($n = 3$). Additionally, total percent recovery of injected dose was low in all animals ($< 0.3\%$), and in some organs the concentration detected was below the limit of quantification using ICP-MS.

The third round of studies in tumor-burdened animals used a significantly higher dosing regimen, dosing at $1\ \mu\text{mol Gd}$ per animal, using $200\ \mu\text{L}$ tail-vein injections of a $5\ \text{mM}$ solution. In this study, FA-Gd, MH and Gd-DOTA were compared head-to-head to determine the blood circulation half-life and imaging capabilities. The animal receiving FA-Gd and MH showed contrast enhancement at the gall bladder out to six hours post-injection (Fig. 4.5 and 4.25). Gd-DOTA did not provide contrast enhancement at any of the multiple-hour time points. For all mice receiving contrast agents, no significant change in signal was detected at the tumor site.

Analysis of blood serum corroborated the prolonged blood circulation time of the gadolinium-based contrast agent formulations. Before injection, then immediately post-injection, and 1, 4, 7 and 24 hours post-injection, blood samples were drawn and serum separated and analyzed for gadolinium content. For each material, 3 animals were evaluated, and the average gadolinium concentrations are reported in Fig. 4.6, with individual animal profiles in Fig. 4.29. Minutes after injection, the dose is distributed in the blood volume of the mouse, giving the max concentration in the blood: the concentration of gadolinium for all samples is comparable in this first time-point post-injection. At 1 hour, there is already a significant drop-off in gadolinium concentration for all samples, though the FA-Gd has a distinctly higher concentration compared to MH or Gd-DOTA. Our determination of the half-life of MH is consistent with the reported elimination half-life of 1.17-2 hours.⁷ This was shorter than that for FA-Gd, indicating a prolonged and favorable blood circulation time of the reporter agent containing a fatty-acid moiety. At the 7 hour blood analysis point, the average

concentration of gadolinium in the blood is 270 ppb, compared to 4 ppb for both MH and Gd-DOTA. Despite the clearance of most of the material from the blood around this time point, and formulation of a GBCA with the FA, e.g. FA-Gd serves as a strategy for extending the circulation time and thus imaging window for experiments utilizing a GBCA. In addition, we confirmed hepatobiliary clearance of MH, and observed our FA-Gd material clearing *via* this mechanism (Fig. 4.5). This is a significant result because it represents an alternative formulation strategy for a GBCA that may be more suitable for patients experiencing decreased renal function. The MR experiments performed in this chapter were not-optimized; on-going and future work will need to evaluate targeting effects to the tumor, which was not observable *via* MR imaging under the conditions employed here.

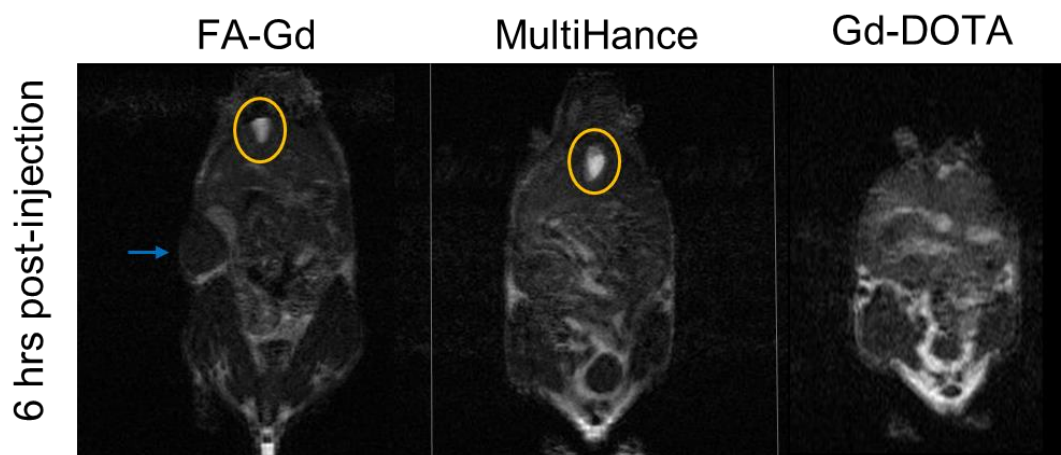


Figure 4.5 Representative MRI scans for tumor-burdened mice receiving high dose of FA-Gd, MH or Gd-DOTA. Yellow circle highlights the signal intensity in the gall bladder; the blue arrow indicates the tumor, when present in the slice shown.

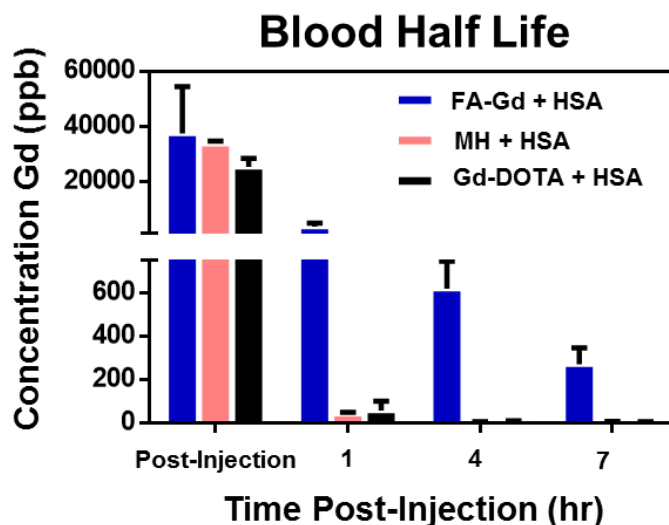


Figure 4.6 Blood Half-life. FA-Gd, MultiHance (MH), and Gd-DOTA, formulated with HSA, and injected *via* tail vein in a tumor-burdened animal (HT-1080 xenograft).

4.20 Fatty Acid-Taxol Conjugates for Therapeutic Applications

Preliminary investigation of C_{18} conjugates involved derivatives of paclitaxel, with the aim to compare efficacy head-to-head with Abraxane. The taxol-conjugate (PTX-FA, Fig. 4.10) was formulated with HSA to yield, then evaluated for efficacy *in vivo*. Different formulations yielded PTX-FA + HSA (1:1), PTX-FA + HSA (2:1) and PTX-FA + HSA (5:1), where the number describes equivalents of PTX-FA to albumin protein. On-going *in vivo* studies focus on the PTX-FA + HSA (5:1) formulation because of the higher loading of taxol per protein. Based on promising results, this technology has been further evaluated for mode of action and pharmacokinetic/pharmacodynamic studies: those results are out of the scope of this dissertation, but relevant experimental data is provided for context.

4.20.1 Stability of PTX-FA

PTX-FA was prepared under standard amide coupling conditions, per published procedures.² The stability of the PTX-FA compound was evaluated using HPLC to confirm

that hydrolysis of the prodrug could be achieved. Briefly, PTX-FA was dissolved in organic solvent with either acidic, neutral or basic water added at a low enough concentration such that the small molecule did not precipitate. The control solution in organic solvent did not contain water. The solutions were incubated for 24 hours, then analyzed by HPLC to detect degradation of the parent compound. Before incubation, pure PTX-FA had a retention time of about five minutes. The control solution showed no change after 24 hours, while the PTX-FA subject to acidic conditions yielded partial degradation, with the PTX cleavage product appearing at two minutes. Under basic conditions, all PTX-FA was cleaved. This assay demonstrates that PTX-FA is a labile prodrug of PTX, and that liberation of the active PTX occurs readily under basic conditions, but not as readily under acidic conditions. This is important when looking towards the toxicity of PTX-FA or formulations thereof *in vitro* and *in vivo*.

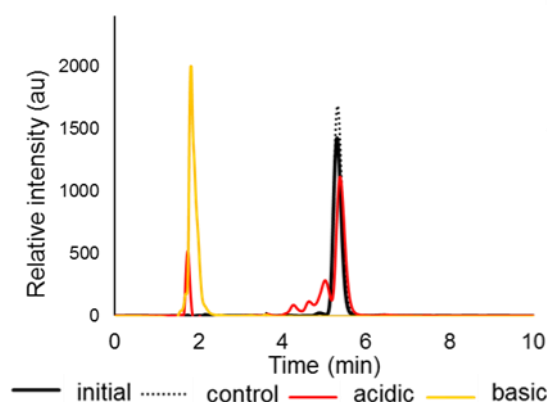


Figure 4.7 HPLC traces of PTX-FA under various experimental conditions.

4.20.2 Formulation of PTX-FA with Albumin

To formulate PTX-FA with its carrier protein HSA, the two components were combined in a mixed-solvent solution, lyophilized, then resuspended in DBPS prior to use in further experiments. HSA was dissolved in MilliQ water at 1X, while PTX-FA was dissolved in t-butanol at 10X. The two were combined, mixed, flash frozen in liquid nitrogen, then

lyophilized to give a white powder. Details on concentrations used in formulation are described in the methods section. PTX-FA and HSA could be combined at increasing ratios of PTX-FA to protein. HSA has at least five strong binding sites for long-chain fatty acids, and formulations of 1:1 molar ratio PTX-FA to HSA, 2:1 and 5:1 were explored. Using the higher-loading (5:1), higher dosing of taxol is achieved.

4.20.3 *In Vitro* Toxicity

With the PTX-FA in hand, and a strategy for formulating with HSA, the toxicity of the small molecule and its formulated counterpart were evaluated *in vitro*. First, the toxicity was tested against HeLa cells, a human cervical cancer line. After comparing toxicity of the commercially available paclitaxel compound to PTX-FA and PTX-FA + HSA, toxicity was tested against a range of cancer cell lines, including: HT-1080 (human fibrosarcoma), H522 (human lung), HT-29 (human colon), PANC-1 (human pancreas/duct cancer), and HepG2 (human liver carcinoma/hepatocellular carcinoma). All toxicity studies described herein were performed in the same manner so that results may be directly compared, though the experiments are not optimized for each treatment condition. The initial *in vivo* efficacy, described in a later section, was evaluated for an HT-1080 xenograft model, so establishing an *in vitro* assay for comparison of the HT-1080 line to other cancer lines was critical. HT-29, PANC-1 and H522 were also tested in xenograft models. HepG2 is of particular interest because of its known interactions with HSA- and we envisioned this as a cancer model wherein strong HSA interactions would provide even more favorable results with respect to specificity and efficacy. Ongoing experiments are evaluating the genes for specific cell receptors responsible for HSA targeting to HepG2 cells specifically.

Viability experiments with HeLa cells reveals that PTX-FA is not as toxic as the parent PTX compounds (Fig. 4.8a). This could be attributed to the fact that PTX-FA is a prodrug, and

over the time of the experiment, not all PTX is liberated. Additionally, PTX-FA might be seen differently by the cells: the long chain fatty-acid may provide an alternate pathway for the molecule to be taken into the cell. The conditions used *in vitro* also appear to affect toxicity. For example, treatment with serum-free media (Opti-MEM, OM) decreases the toxicity of PTX, but not drastically in PTX-FA. Cell culture media with serum proteins may associate with the small molecule drug, affecting its mode of action, or interaction with the cell. Preliminary mechanistic studies evaluating the effects of formulation and treatment conditions on cell uptake were performed and provide some insight in to this problem (see section 4.5).

Formulations with HSA were shown to be toxic to cells: the 1:1 and 2:1 molar ratio (PTX-FA: HSA) had comparable toxicities to PTX-FA, while the 5:1 ratio had lower IC₅₀ values, but did not impart full cell death on HeLa cells (Fig. 4.8b). A comparison of different formulations of PTX-FA in the presence and absence of serum proteins in media is presented in Fig. 4.2c. Across the board, treatments in serum-free media are more toxic than treatments of the same compounds in serum-containing media. This could be attributed to serum proteins of FBS interacting with PTX-FA, sequestering them and hindering hydrolysis of PTX or preventing cell-membrane interactions. PTX was significantly more toxic than PTX-FA or when formulated with HSA: this is not surprising as the formulation with HSA must undergo more steps before reaching its target in the cell nucleus. While toxicity is still on a similar order of magnitude as free PTX, the novel prodrug compounds present a strategy towards higher dosing with diminished toxicity, as is evident by *in vitro* cell culture studies.

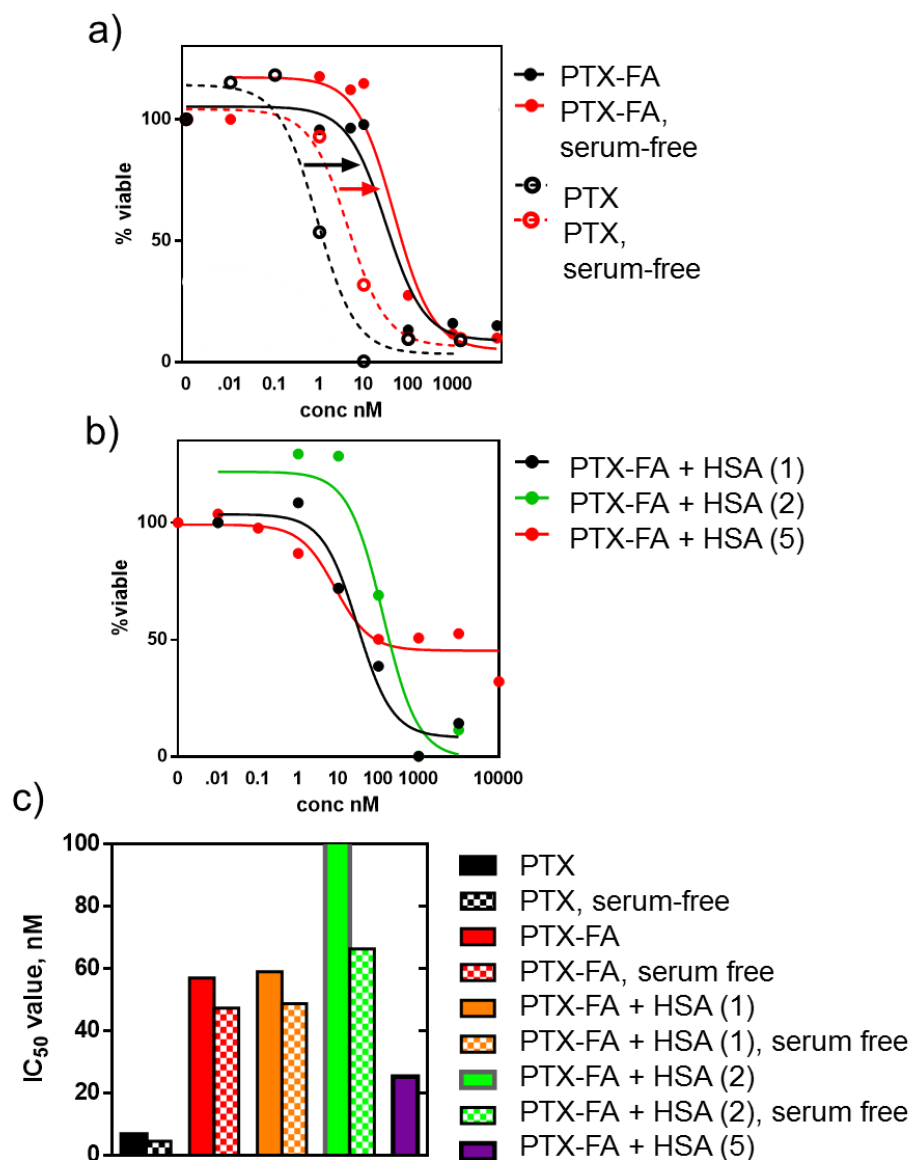


Figure 4.8 Representative IC₅₀ curves for conjugates of PTX, and formulations thereof. a) PTX, PTX-FA in normal media (in black), or serum-depleted media (in red). The dashed lines are commercially available PTX; the solid lines are the synthetic small molecule PTX-FA. b) Formulations with HSA. 1:1 ratio (black solid), 2:1 ratio (blue), or 5:1 ratio (red). c) A comparison of all compounds and treatment conditions. More representative IC₅₀ curves and a summary of all trials are in Figs. 4.32 and 4.33 and Table 4.5.

A comparison of the toxicity of fatty acid conjugates across different cell lines shows that PTX-FA and formulation with HSA are comparable in toxicity in HeLa, HT-1080, HT-29 and HepG2 (Fig. 4.9). While the compounds are not as toxic in PANC-1 or H522 cell lines,

there is still evidence of cytotoxicity. This corroborates unpublished data that shows efficacy of PTX-FA suppressing tumor growth in PANC-1 and H522 xenograft tumor models (not shown). A table summarizing toxicity of various compounds in the cell lines is provided in Table 4.1, with representative IC₅₀ curves in Figs. 4.34-4.38 and Tables 4.6-4.10

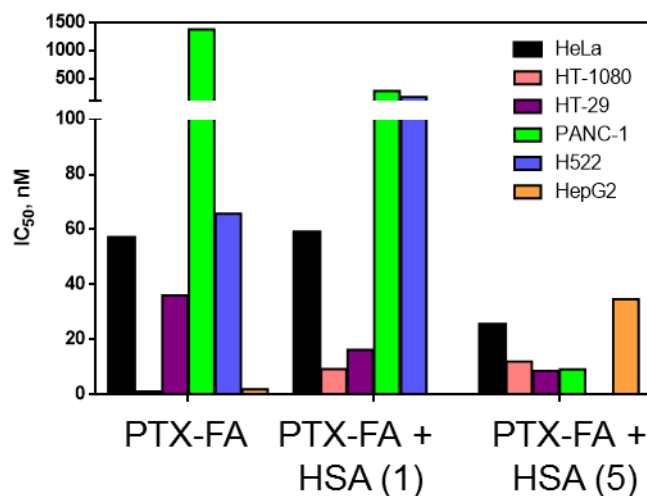


Figure 4.9 IC₅₀ plots of PTX-FA and formulation with HSA across 6 cell lines. The values shown here are toxicity in complete media. Tables summarizing all experiments on the various cell lines are included in Tables 4.6 through 10.

Table 4.1 IC₅₀ values PTX-FA and PTX-FA + HSA (1), (2), and (5) in various cell lines.

Cell line	PTX-FA	PTX-FA + HSA (1)	PTX-FA + HSA (2)	PTX-FA + HSA (5)
HeLa	57.05	59.00	278.25	25.375
HT-1080	1.11	9.27	47.6	12
HT-29	36.1	16.3	9.24	8.62
PANC-1	1381	283	N/A	9.09
H522	65.8	182	N/A	N/A
HepG2	1.89			34.6

4.20.4 *In Vivo* Efficacy

The PTX-FA formulations with HSA were tested head-to-head against Abraxane in a xenograft HT-1080 tumor model. Tumor-burdened animals were dosed with respect to mg of paclitaxel per kg body weight (mg/kg) 3 times total, every 4 days (q4dx3). Select results are shown in Fig. 4.1. Panel (a) shows a Kaplan-Meier survival plot. Favorable survival plots were seen for animals receiving 30 or 50 mg/kg ABX and 5 or 300 mg/kg PTX-FA + HSA. Animal death before the last dose was attributed to toxicity of the therapeutic, whereas animal death past 12 days from the start of the therapy (e.g. saline) was attributed to tumor overgrowth and morbidity. ABX at medium (30 mg/kg) and high dosing (50 mg/kg) showed some drug toxicity, however if the animals survived the initial dosing of taxanes, it had a good chance of efficacy against the tumor. The lowest dose of ABX (5 mg/kg) was ineffective, showing similar results to the saline control. PTX-FA was tolerated well by the animals, and prolonged animal survival, compared to saline. Of note is that the animals could tolerate the PTX-FA 300 dose, providing evidence of a safer formulation strategy, which in turn allows for higher dosing of therapeutic, and greater efficacy. The tumor growth plots in panel (b) show efficacy in halting tumor growth at various dosings. ABX at 30 mg/kg and PTX-FA at 300 mg/kg are comparable with regards to suppressing tumor growth. ABX and PTX-FA at the same dose (5 mg/kg) show comparable ability to suppress tumor growth, which is not as effective as the higher doses, but better than the saline control. On-going *in vivo* studies are investigating optimal therapeutic dosings in the HT-1080 model, as well as other tumor models of interest.

4.21 Exploring the Scope of the Fatty Acid Platform

We next explored the scope of the fatty acid platform by testing a variety of taxol-derivatives wherein the carbon chain length and attachment was varied. The compounds were evaluated *in vitro* using the established cytotoxicity assays as described in the previous

sections. Just as several agents have been formulated with albumin in a method similar to the Abraxane formulation with paclitaxel,⁸ we demonstrate that our approach could also be tailored to make other conjugates of warheads of interest. Methotrexate, camptothecin, and peptide conjugates are briefly described and evaluated for their therapeutic nature. Methotrexate (MTX) is used a folate antagonist, used to treat solid tumors and rheumatoid arthritis, among other diseases.^{9,10} Camptothecin (CPT) is a quinoline alkaloid class of cytotoxins, approved for treatment of several types of cancers, including colorectal, ovarian, cervical and small-cell lung cancer.¹¹ A KLA peptide (KLAKLAKKLAKLAK, or KLAKLAK₂) was chosen for evaluation because of its known characterizations and utility, and because of its mode of action: the in-tact peptide must be in the cytosol where it inserts in to and disrupts the membrane of mitochondria, causing cell apoptosis.¹²

4.21.1 Other Paclitaxel-Derivatives

The importance of the 18-carbon fatty acid chain for utility in HSA-binding was evaluated by synthesizing fatty-acid -paclitaxel conjugates with modified carbon chains and linkers.² Specifically, the length of the chain, saturation and the role of any additional linker was evaluated. Four new PTX-prodrugs were prepared in a similar manner to PTX-FA (see Fig. 4.10 for structures). This is not an exhaustive exploration of compounds of interest. Examples are specifically chosen to support the claim that this is a generalizable platform technology. Future studies might investigate different fatty acid derivatives to tune properties such as binding kinetics and equilibria. The hexadecanedioic acid (C₁₆-PTX) and eicosanedioic acid (C₂₀-PTX) conjugates simply vary the fatty acid chain length, while maintaining the terminal free acid and ester linkage to paclitaxel. The octadec-9-enedioic acid (C_{18unsat}-PTX) conjugate has 9-10 trans-unsaturation, and maintains the ester link to paclitaxel; the unsaturation may provide a kink in the fatty acid chain, affecting its binding with HSA. A final

derivative contained a mono-methyl-ester protected acid, with a 6-amino-hexanoic acid linker to ester-attached paclitaxel; this compound is labeled “C_{6linked}-PTX” here forth, referring to the extended linker carbon length.

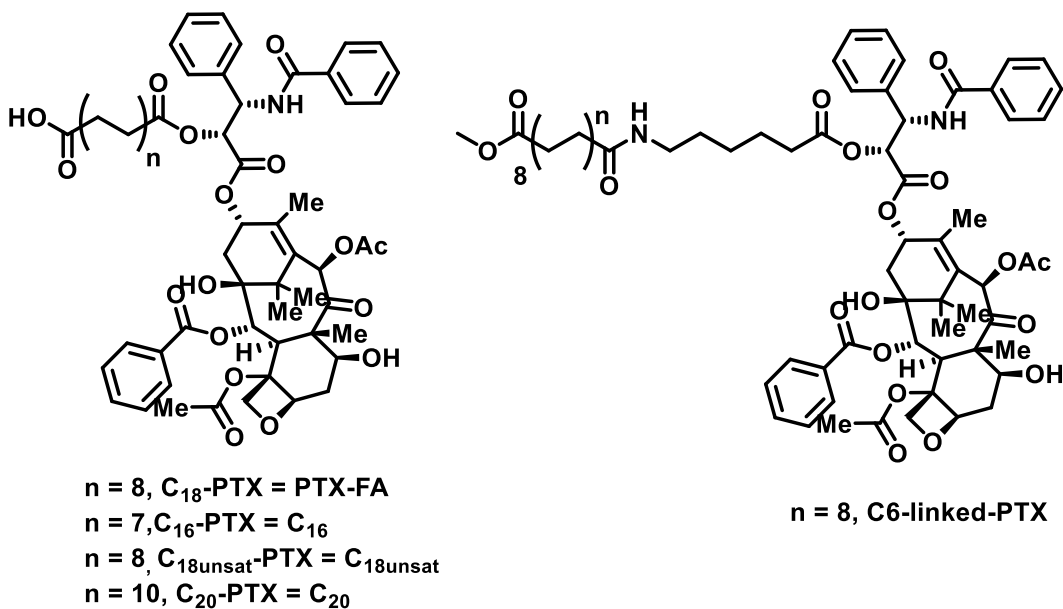


Figure 4.10 Various fatty acid-PTX conjugates evaluating key features of the fatty acid compounds.

As described in the introduction, HSA has specific binding for various fatty acid derivatives, and we have seen that clinical drugs modified with a myristic (C₁₄) acid exhibit favorable interactions with the protein (reference fatty acid binding differences and Levemir). We were curious how extending or shortening the length of our ODDA probe might affect the function of the prodrug. The aim was to use the cytotoxicity assay as a surrogate screen for fatty acid conjugate activity, alleviating the need for resource-intensive *in vivo* studies to screen for efficacy. Cytotoxicity experiments in HeLa cells revealed that the C_{18unsat}- and C₂₀-PTX compounds had similar toxicity to PTX-FA, whereas C₁₆-PTX was less toxic, and the C_{6linked}-PTX was significantly less toxic (Fig. 4.11 and Table 4.2). It is interesting that two less carbons had such an impact on toxicity, and may be attributed to slightly decreased hydrophobicity of

the chain affecting interactions with serum proteins or the cell membrane. The decrease in toxicity of the C_{6linked}-PTX was less surprising: the methyl-protected ester may have impacted the solubility of the complex or led to differing interactions with the serum proteins present. Alternatively, the 7 extra atoms in the chain may have proved too many, affecting how it was “seen” by serum-proteins or the cell. The free acid was not present on C_{6linked}-PTX conjugate (methyl-ester protecting group maintained), and represents the only example in this study where the ionic interaction with the pit of the binding pocket was altered (a positive residue sits inside key binding pockets of HSA, allowing for strong interactions with negatively charged carboxylates). There are countless iterations of long-chain fatty acid with linkers to find an optimal binding moiety with HSA optimized for the warhead. Other avenues of exploration include further optimizing chain and linker length, altering the non-functional terminus of the fatty acid to have a noncharged moiety (e.g. stearic acid derivative) or tuning the cleavable linker using functional groups such as carbonates, carbamates, or other labile linkers.^{13,14}

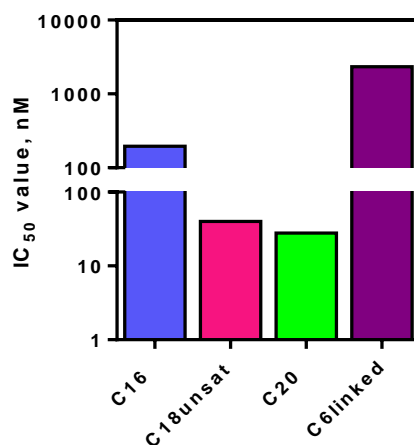


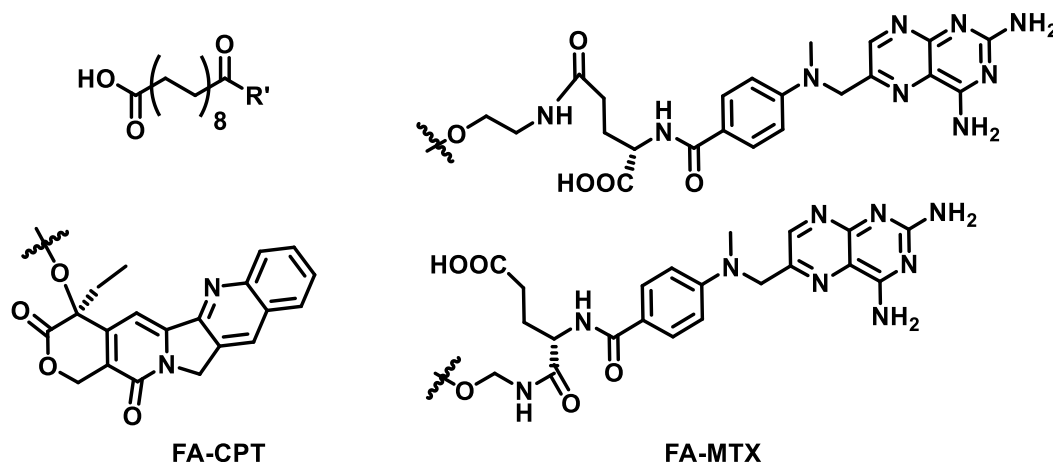
Figure 4.11 Cytotoxicity of taxane-type conjugates in HeLa cells. These are representative IC₅₀ plots. For Repeat experiments, see Fig. 4.39 and Table 4.11.

Table 4.2 IC₅₀ values PTX-FA, C₁₆-PTX, C_{18unsat}-PTX, C₂₀-PTX and C_{6link}-PTX in HeLa cells.

Compound	PTX-FA	C ₁₆ -PTX	C _{18unsat} -PTX	C ₂₀ -PTX	C _{6link} -PTX
IC ₅₀ (nM)	57.04	195.6	40.0	27.8	2329

4.21.2 Other Categories of Therapeutic Agents

To demonstrate the broad applicability of this platform technology, two other small molecule cytotoxic drugs were prepared and evaluated with an initial screen for toxicity *in vitro*: camptothecin and methotrexate. Both FA-CPT and FA-MTX were only prepared as ester-linked C₁₈ fatty acid conjugates. FA-MTX required an amino-linker between the carboxylic acids of the MTX and the dicarboxylic acid, and the product was a mixture of isomers, both of which are described in Fig. 4.12.

**Figure 4.12** FA-CPT and FA-MTX: cytotoxic drugs modified with a ODDA.

With FA-CPT and FA-MTX in hand, the compounds were tested for activity against HeLa cells using the same protocol as for the paclitaxel conjugates, and compared to their parent compounds (Fig. 4.40 and Tables 4.12 and 4.13). CPT and MTX were found to have IC₅₀ values of 49.8 nM and 6.0 nM. The conjugates had non-optimal IC₅₀ curves, with a response of about 50% viability up to 50 μ M for FA-MTX and FA-CPT. The drastic difference

in toxicity from the respective parent compounds was unexpected. This may be to poor solubility of the conjugates, or steric hindrance of the fatty acid and the labile ester bond of the pro-drug form. Experiments at higher concentrations will need to be performed along with optimization of the cytotoxicity assay for these compounds. CPT- and MTX-derivatives have been found to be cytotoxic for a number of cell lines,^{10,11} so subsequent testing to evaluate cytotoxicity of our fatty-acid conjugates should be done in other cell lines.

4.21.3 Peptide Conjugates

The fatty acid platform is amendable to therapeutic compounds other than small molecule cytotoxins, specifically peptides. The “KLA” peptide was of interest for its therapeutic function in cells.¹² The FA-KLA conjugate was prepared by first synthesizing the KLA peptide using standard solid phase peptide synthesis. After the last lysine residue was coupled to the peptide, an excess of mono TIPS-protected ODDA was washed over the resin to couple the fatty acid to the peptide. The FA-peptide conjugate (FA-KLA, Fig. 4.13) was then cleaved from the resin using acidic conditions, which also served to deprotect the TIPS protected acid group. The compound was purified under dilute conditions using preparatory RP-HPLC. A formulation with HSA proved straightforward because the FA-KLA was fully soluble in aqueous solution. FA-KLA and HSA were prepared at 2X concentration in DPBS then added in 1:1 volume to get a 1X concentration of FA-KLA + HSA, where the FA-KLA and albumin are at a 1:1 mol ratio.

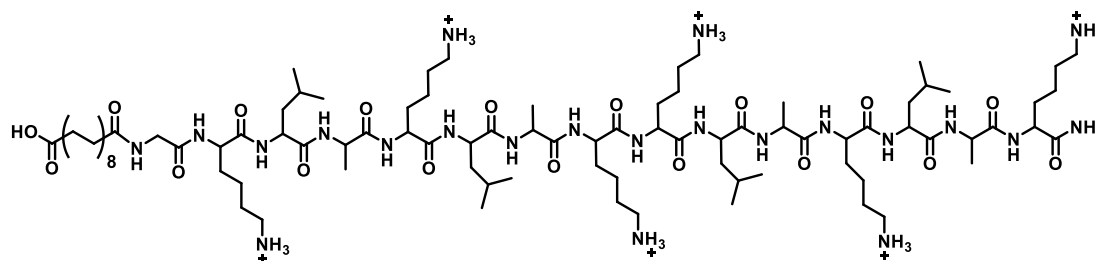


Figure 4.13 A “KLA peptide” conjugate, FA-KLA.

With FA-KLA in hand, preliminary cytotoxicity experiments were performed. In HeLa cells, FA-KLA had an IC_{50} of about 38 μ M in media, or 17 μ M in serum-free media, while when formulated with HSA, cell viability had a minimal response with treatments up to 1mM (restricted by solubility of HSA at high concentrations) (Fig. 4.41 and Table 4.14). The lack of toxicity of FA-KLA when formulated with HSA was apparent in both competent and serum-free media. This was an interesting result since the KLA peptide must be in the cytosol to impart function (e.g. cell death), and it was hypothesized that HSA would be critical for chaperoning the FA-conjugate in to the cell. However, without formulation with HSA, and even without serum proteins in the treatment media, the FA-KLA could impart cell death, and was thus inside the cell. Two hypotheses could relate to how FA-KLA was able to get in the cell. In one instance the amphiphilic-type molecule (hydrophilic peptide, hydrophobic fatty acid residue) might aggregate in aqueous conditions, and the cell might “see” the compound as a nanoscaled aggregate, allowing internalization via an endocytotic pathway. A crude DLS experiment looking at aggregation at increasing concentration predicted that an approximate critical aggregation concentration was around mM. Below that (e.g. the concentrations used in viability experiments), the FA-KLA should be fully solvated and aggregated at higher concentrations. This may explain why treatments at 1mM of FA-KLA began to show a response in viability: the cell was seeing and internalizing a macromolecular aggregate, rather than a solvated peptide-conjugate. Minimal differences between treatments in media with or without serum proteins suggests that protein association is not part of the mechanism for getting in to cells. Alternatively, the FA-KLA maybe be invoking a fatty-acid transport mechanism for cell uptake, though no further studies support that idea at this time. When sequestered upon formulation with HSA, the KLA activity is greatly diminished, suggesting that formulation with a protein carrier may be shielding the material from accessing the cell cytosol or mitochondria. Further optimization of this system and assay is necessary, though it is promising

that FA-KLA shows toxicity in cells. This is on the same order of toxicity compared to what was seen previously in our group, where a multivalent (polymeric) version of the KLA peptide is toxic around 10 μM , while free peptide is not toxic up to 100 μM .¹⁵

4.22 Cellular Internalization of Fatty Acid Conjugates

Toxicity of compounds was preliminary evaluated using *in vitro* viability assays for FA-conjugates and their formulations with HSA. The deviation in toxicity across compounds, and especially toxicity of free FA-KLA, prompted initial investigation of mechanism of internalization of materials *in vitro*. Importantly, the toxic paclitaxel-, camptothecin-, and methotrexate-derived materials were ester-linked prodrugs of the parent compounds. The free compounds must be inside the cell to prove toxic, based on their targets and mechanism of action. The FA-conjugates may enter the cell in-tact, then hydrolyze to release the toxic compound, or alternatively, may undergo hydrolysis outside the cell, followed by diffusion of active compounds in to the cytosol and subsequent cell death. The KLA compound must be inside the cell in order to have activity: its target is the mitochondria. The FA-KLA conjugate, however, is amide-linked and thus in order to be toxic, the conjugate must be inside the cell. A few scenarios might explain how the conjugate on its own may be internalized: passive diffusion in the cell, hydrophobic interactions with the hydrophobic cell membrane, internalization *via* a fatty-acid uptake pathway, or aggregation in solution such that the cell “sees” the material as an aggregate rather than a dispersed small molecule leading to endocytosis, as described in the previous section.

To get a basic understanding of internalization pathway, cell uptake studies were performed using a fluorescein labeled FA-conjugate surrogate. The FA-Fluor was prepared in a similar manner as the other ODDA-conjugates (Fig. 4.14). A fluorescein-labeled FA-KLA conjugate was also prepared using biorthogonal protecting groups during SPPS. These

materials could then be formulated with (or without) HSA and introduced in cells to evaluate differences in cell uptake using standard flow cytometry methods.

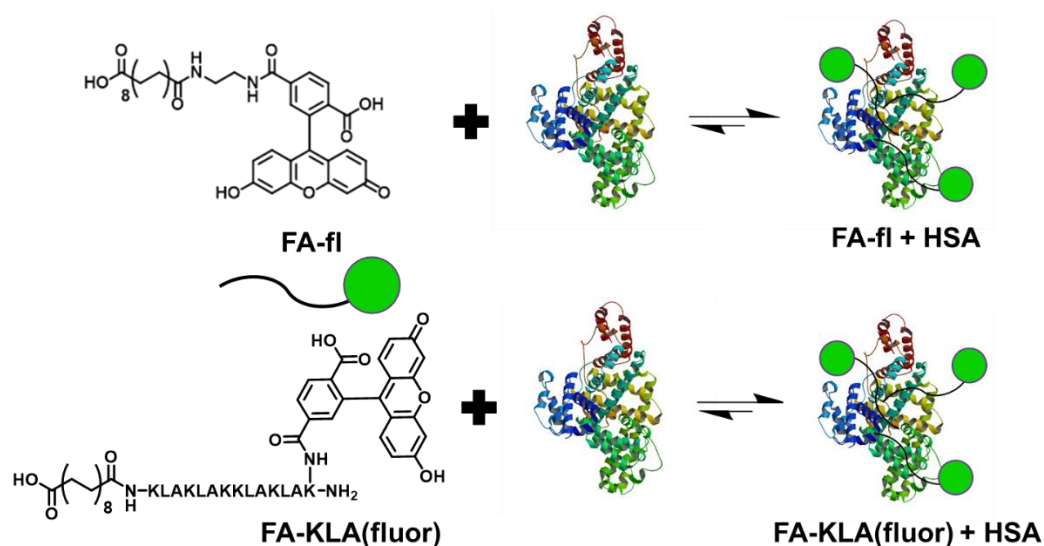


Figure 4.14 Fluorescein conjugates formulated with HSA to evaluate cell uptake pathway.

4.22.1 Cell Uptake Evaluated by Flow Cytometry

Concentration dependence of uptake of FA-fl was evaluated for effects of the treatment media, e.g. serum proteins. As shown in Fig. 4.15, cell-associated fluorescence signal increased with treatment concentration, with the greatest increases in signal for treatments of FA-fl (a) in serum-free media. Interestingly, FA-fl + HSA (b) in media had modest increases in fluorescence compared to DPBS control, with treatments in serum-free conditions, demonstrating slightly higher increases in fluorescence. The differences in signal increase from FA-fl compared to formulation with HSA is counter to the hypothesis that HSA chaperones cargo in to all cells: if this hypothesis were true, cells treated with FA-fl + HSA would be expected to show higher fluorescence increases compared to FA-fl. Experiments using DMEM without FBS supplementation yielded similar results as the serum-free OptiMEM media (results not pictured): OptiMEM was used as the “serum-free media” for all experiments in this

section. This may demonstrate effects of serum-protein opsonization of FA-fl or FA-fl + HSA and so was evaluated along-side regular, serum-containing media.

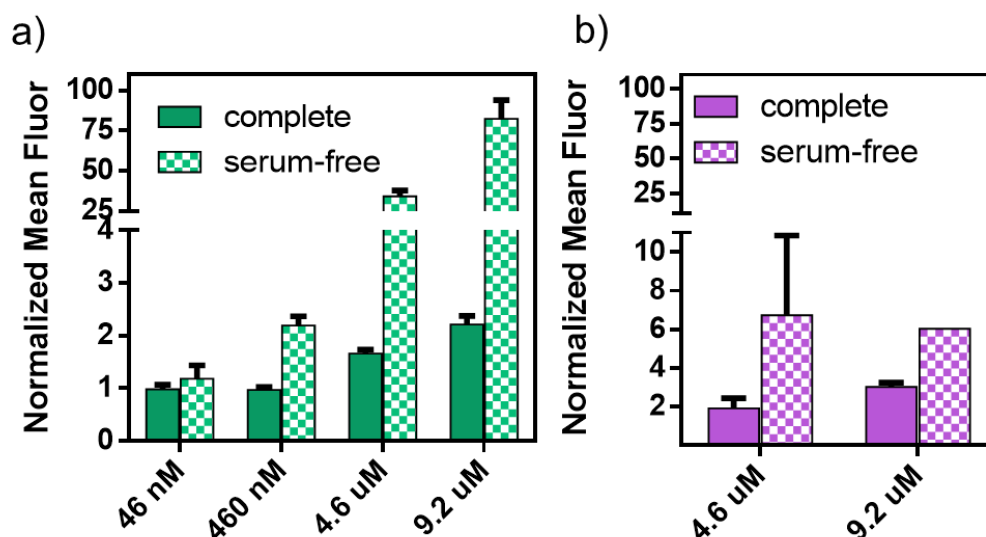


Figure 4.15 Concentration dependent uptake of (a) FA-fl and (b) FA-fl + HSA in complete media or serum-free media in HeLa cells. Formulation with HSA was made at 1:1 conjugate: albumin ratio. Representative cell scattering dot-plots and histograms showing clear population shifts, are also described in the methods section (Fig 4.42-4.44) These data are gated healthy populations, and the treatment solution did not seem to affect the viability of the cells.

The observed preferential cell uptake of FA-fl under serum-free conditions is also observed in other select cell lines (Fig. 4.16). Similar to HeLa cells, HT-1080, HT-29 and HepG2 cells treated with FA-fl in serum-free media demonstrated the highest increase in fluorescence signal. FA-fl + HSA also demonstrated increases in fluorescence, with not as drastic increases in fluorescence for treatments in serum-free media compared to the unformulated conjugate. The surprising result of higher fluorescence signal for the FA-fl in serum-free media prompted preliminary mechanistic studies of cell uptake.

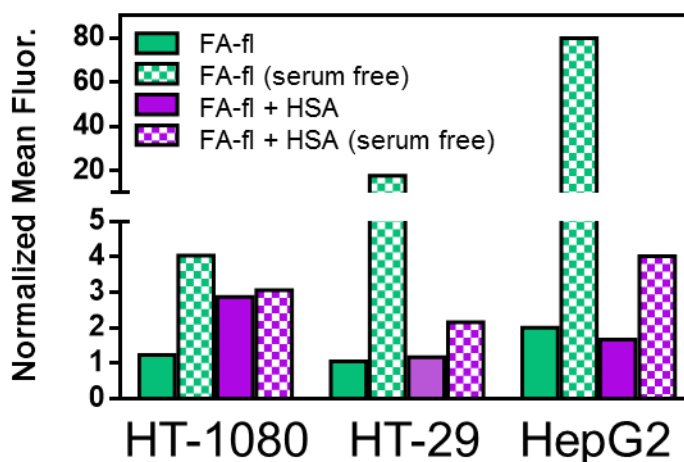


Figure 4.16 Internalization of FA-fl in other cell lines. All treatments at 4.6 μ M fluorescein. Representative cell scattering dot-plots and histograms showing clear population shifts, are also described in the methods section. Treatments did not significantly affect cell viability. Representative dot plots and histograms showing population shifts in Fig. 4.27-4.32.

In addition to FA-fl and formulation with HSA, a fluorescein-labeled FA-KLA conjugate was prepared and is depicted in Fig 4.14. FA-KLA(fluor) and FA-KLA(fluor) + HSA were used to treat HT-1080, HT-29 and HepG2 cells (Fig 4.17). In HT-1080 cells a large increase in fluorescence for both formulations was observed, both in complete and serum-free media; this represents greater increases in signal compared to that from FA-fl or FA-fl + HSA treatments. In HT-29 cells increases in signal were observed for both materials. Interestingly, there appeared to be little advantage for formulating the peptide conjugate with HSA or treatment in serum-free media, which is on contrast to the results observed with FA-fl in serum-free conditions. HepG2 cells demonstrated the greatest relative increases in fluorescence, with FA-KLA(fluor) generating a marginally higher fluorescence signal than when formulated with HSA.

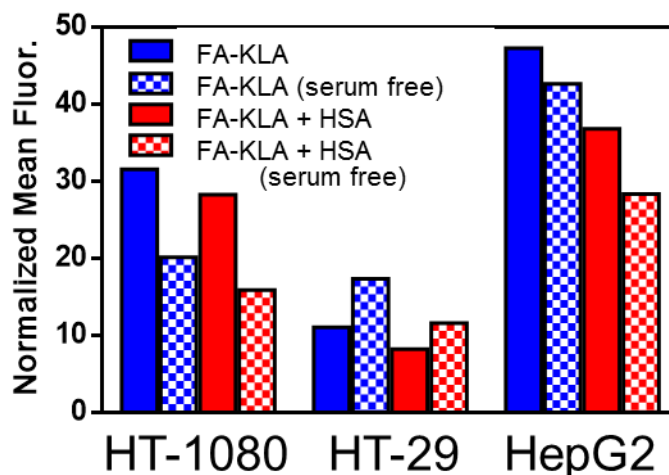


Figure 4.17 Internalization of fluorophore labeled peptides (FA-KLA(fluor)) in different cell lines. HeLa was not evaluated. All treatments were at 4.6 μ M with respect to fluorophore, and formulation with HSA were at a 1:1 mol ratio of peptide to albumin. Dot plots and histograms are in Figs. 4.45-4.50.

4.22.2 Evaluation of Mechanism of Action

To elucidate possible mechanisms leading to differences in uptake between FA-fl and HSA formulations therefore, experiments were performed to probe active versus passive mechanism, and using a metabolic inhibitor, M β CD. This inhibitor depletes cholesterol-rich membranes associated in the lipid-rafts involved in the clathrin-independent/caveolae-mediated endocytosis pathway, which is the mechanism cited for HSA transcytosis across the endothelial emmbrane.^{16,17} The FA-fl or FA-fl + HSA were prepared in media or serum-free media, then used to treat HeLa cells for 1 hour at 37°C or 4°C. Incubation at 4°C would shut-off any active internalization pathway: a relative decrease in signal would indicate that an energy-dependent pathway was responsible for cell uptake. If a caveolae-mediated endocytotic pathway played a role in cell uptake, treatment with the metabolic inhibitor would disrupt this pathway, and again, a relative decease in signal would occur.

For FA-fl, regardless of media composition, fluorescence signal was maintained for incubation at 4°C versus 37°C (Fig.4.18a). This suggests that the process of FA-fl entering cells

is non-energy dependent. This might occur if the small molecule passively diffused through the membrane as other small molecules are known to do, or the hydrophobic tail passively inserts in to, or associates with, the cell membrane. For the latter, a thorough wash of the cells and a heparin wash should remove material not inside the cell or its membrane, and although the heparin wash was not included for the cell uptake experiments, the preliminary cell uptake experiments found that the heparin wash had no effect on the cell fluorescence. Co-incubation with M β CD did not affect cell uptake of FA-fl compared to controls or treatment of FA-fl without inhibitor at 37°C, indicating that a caveolae mediated-pathway may not be responsible for FA-fl uptake. For FA-fl + HSA (Fig.4.10b), signal increase was higher upon incubation at 4°C, again suggesting a non-metabolic dependent pathway for uptake of the complex; M β CD did not negatively affect uptake. An alternative explanation for the effects seen for FA-fl + HSA formulations is that the FA-fl may be in its unbound form under these conditions and thus interacting with the cell [passively] as a small molecule.

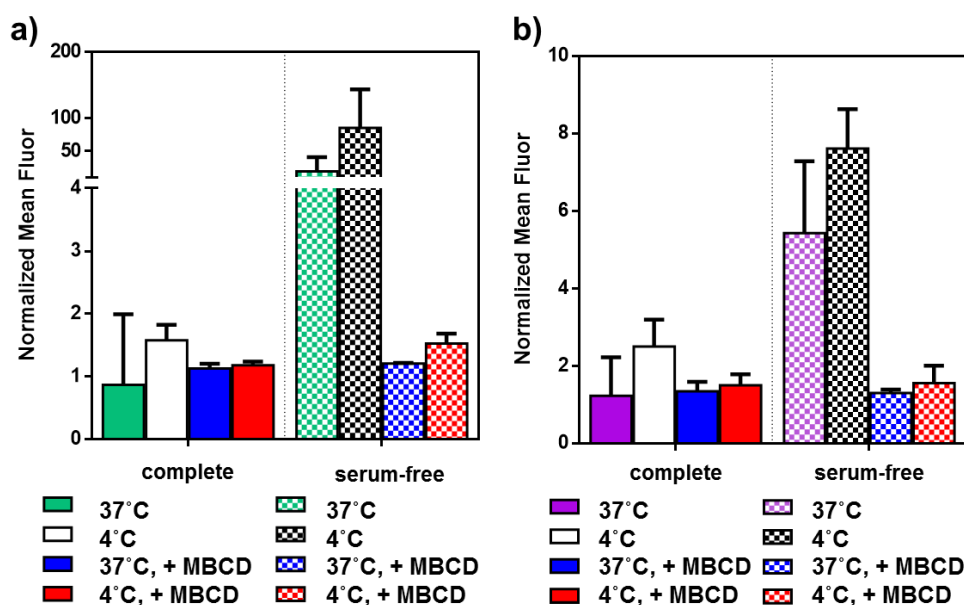


Figure 4.18 FA-fl (a) or FA-fl + HSA (b) treatment of HeLa cells under various conditions, all at 4.6 μ M with respect to fluorescein. All data normalized to vehicle, which is 1. Representative dot plots and histograms in Fig. 4.51-4.53.

These experiments demonstrate that fatty-acid conjugates may be passively diffusing in to cells due to their small molecular weights. To elucidate differences in uptake of free fatty-acid conjugate compared to complexation with albumin, HSA should be labeled with another fluorophore, complementary to fluorescein. Further experiments are on-going in the lab and focused on investigating both HSA-receptor proteins and fatty-acid transport proteins (FATPs). Regardless of the mode of internalization, the cytotoxic FA-conjugates were able to demonstrate toxicity across cell lines, either through passive or active mechanisms in to the cell, with availability of ester bond cleavage revealing the active form of the drug.

4.23 Conclusions and Outlook

Taking advantage of endogenous protein-small molecule interactions for improved pharmacokinetics via prolonged blood circulation times is an exciting opportunity for enhanced

drug delivery of many classes of drugs. Human serum albumin represents an ideal platform for hitchhiking a small molecule drug to enhance circulation time and targeting to some tissue, such as cancerous and inflamed tissue. Clinical success stories such as Abraxane and Levemir indicate utility and promise of designing molecules for more efficient drug delivery. Inspired by naturally occurring interactions of long-chain fatty acids with HSA, a platform technology utilizing ODDA-modified with various warheads was developed and tested to show efficacy in therapeutic and diagnostic applications. Therapeutic efficacy of PTX-FA demonstrates that our novel formulation is safer than the comparable ABX, allowing for higher dosing and a greater therapeutic window. Ongoing pharmacokinetic and pharmacodynamic studies are investigating detailed absorption, distribution, and metabolism of PTX-FA, and dose-dependence thereof. Other *in vitro* experiments discussed herein and preliminary *in vivo* studies (not included here) indicate that PTX-FA is efficacious against various cell lines. In the diagnostic realm, a gadolinium-based fatty-acid derivative demonstrated favorable relaxivity properties *in vitro*, and utility as a blood-pool imaging agent.

Based on interest in understanding the mechanism leading to successful targeting of HSA and HSA-bound molecules to tumor targets, *in vitro* cell experiments preliminarily investigated a FA-fluorescein molecule for mechanism of action getting in to a cell. Other have attributed ABX success to EPR effects, gp60-mediated transcytosis, and SPARC recognition for localization at the tumor cell, though mechanisms investigating cell uptake of warhead remain elusive. It is suggested that albumin mediates internalization of warheads in to cancer cells where payload is delivered, though detailed studies have not been done, and are out of the scope of this work. Ongoing collaborative studies are working to identify genes for cancer cell receptors for PTX-FA formulations of paclitaxel. Using CRISPR-Cas9 technologies, a range of endocytotic and fatty-acid receptors are being probed for their role in PTX-FA uptake.

Identifying the mode and species internalized by cancer cells will allow researchers to even more specifically target cancer tissue and cells.

Also of note in the albumin-mediated world is how formulation of HSA with a chemically-modified fatty acid might affect how the protein is seen in the body, specifically albumin-specific receptors like gp60, gp18 and gp30. It was discussed that gp60 is specific for native albumin, while gp18 and gp30 specific for modified albumin. Not investigated here is how a natural carrier molecule (ODDA) chemically modified with a bulky hydrophobic or hydrophilic small molecule (paclitaxel or gd-DOTA) affects its binding with albumin. This could be done with computational modeling, and experimental cell work investigating efficiency of transcytosis of modified fatty-acids in endothelial cells or specificity towards albumin receptors. (reference for experimental transcytosis exps).

The results from cell toxicity and uptake studies highlight effects that experimental conditions may have on the results of the experiment. For example, differences in toxicity of PTX-FA and PTX-FA + HSA are evident, and are also dependent on serum-containing media used in the experiments. Cell uptake studies reveal that FA-fluorescein more readily associates with cells compared to when formulated with albumin. The latter uptake experiment suggests that a fatty-acid conjugate with a non-labile linker (e.g. FA-fl) may internalize in to cells via a fatty-acid uptake mechanism. More detailed experiment are necessary to conclude this as the mechanism for cell association, but this idea is important when considering the efficacy of the PTX-FA molecule.

PTX-FA is a prodrug of the active moiety PTX, which is linked *via* an ester moiety, allowing for hydrolysis and release of free taxol, which inside the nucleus binds microtubules, halting cell reproduction. Thus, it is imperative that taxol is both releases from the fatty-acid carrier and is in the cell. There is an interplay of PTX-FA and protein binding equilibrium and kinetics, as well as PTX-FA hydrolysis kinetics. We know that hydrolyzed PTX is in cancer

cells based on reduction in tumor volume in *in vivo* models, but it is unknown in which form (e.g. PTX-FA, PTX-FA + HSA, or PTX) it is internalized in the cell. More detailed equilibrium experiments looking at the binding equilibrium of PTX-FA with albumin under physiologic conditions may reveal information about how tightly bound the modified FA-molecules are with the protein. Isothermal calorimetry (ITC) experiments were attempted using PTX-FA, but due to the many possible binding sites of PTX-FA with HSA, the experiments did not yield reliable binding coefficients. Future investigation of PTX, PTX-FA and PTX-FA + HSA should look at interplay between binding kinetics, hydrolysis kinetics, and how these compounds are recognized by the cancer cell, including investigation of albumin-mediated internalization mechanisms, as described above. Investigation of the role and specificity of the fatty acid chain was investigated with regards to taxol conjugates. C16, C18, C20 and C6link, conjugates of taxol were prepared and tested for toxicity. All compounds were shown to have similar toxicities in HeLa cells, even when compared to PTX-FA, though no information about binding equilibria or hydrolysis kinetics was obtained. While literature indicates binding constant of C18 is strongest compared to (other chain lengths),¹⁸ depending on the application and interaction with albumin, the exact synthetic structure of the FA-conjugate can easily be modulated.

The results from the *in vivo* evaluation of the diagnostic agent were promising. We achieved desired enhancement of blood serum circulation time using our strategy of formulation with HSA, and a change in profile compared to clinical small molecule standards, including one (MH) designed to interact with HSA for enhanced circulation and a second (Gd-DOTA) not specific for blood pool imaging. While contrast enhancement was observed using a preclinical 4.7 T MRI, we were unable to determine using MRI if the material was accumulating at the tumor target. It is important to point out that blood circulation or clearance time does not necessarily equate to elimination half-lives. Materials are subject to metabolism

and deposition or accumulation in various organs, in addition to elimination. While metabolic experiments were not performed for these materials, the accumulation at the tumor-target site and off-target organs was evaluated *ex vivo* at 24 hours, but no significant trends in accumulation were detected. Future work will need to work out the proper dosing and imaging parameters for using this novel diagnostic agent.

The platform technology described here is widely amendable to various therapeutic treatments. Ongoing projects in the Gianneschi lab are investigating fatty acid conjugates of: RNA, other peptides, other therapeutic small molecules (include methotrexate, docetaxel, camptothecin), other metal based therapeutic molecules (platinum or gold-based), other imaging agents (cyanine dyes) and combinatorial therapies. This formulation strategy is only limited by synthetic accessibility of the fatty-acid conjugate.

4.24 Acknowledgments

Chapter 4, in part, was published as a patent: “Modified Cytotoxins and Their Therapeutic Use.” Callmann, Cassandra; Thompson, Matthew P.; LeGuyader, Clare L. M.; Bertin, Paul A. and Gianneschi Nathan C. 2016. The dissertation author was a contributing author on this reference.

Chapter 4, in part, was also published as a patent entitled “Modified MRI Contrast Agents and Uses Thereof.” LeGuyader, Clare L. M.; Thompson, Matthew P.; Callmann, Cassandra; Ditri, Treffly; Bertin, Paul A.; Gianneschi, Nathan C. 2017. The dissertation author is the primary investigator of this material.

Chapter 4 also contains material that is currently being prepared for submission for publication: Callmann, C.; Thompson, Matthew P.; Barback, Christopher; LeGuyader, Clare L. M.; Hennis, Robert; Henriksen, Niel; Jaremko, Matthew; Momper, Jeremiah; Burkart,

Michael; Bertin, Paul A. and Gianneschi, Nathan C. The dissertation author is a contributing author of this pending manuscript.

Sha He and the Almutairi Group at UCSD are acknowledged for the use of their bench-top relaxometer, used to measure relaxivity of all samples in this chapter.

This work was supported in part by resources in the Environmental and Complex Analysis Laboratory located at the University of California, San Diego.

4.25 Methods

4.25.1 General Synthetic Methods

General synthetic and analytical methods were performed in a similar manner to that described in previous chapters. Paclitaxel, camptothecin and other reagents were obtained from Fischer. ODDA was provided by Elevance Renewable Sciences.

Synthetic methods of key intermediates and compounds are detailed in Ref. 2 (Mono-TIPS-FA, PTX-FA, FA-MTX, C₁₆-PTX, C₂₀-PTX, C_{18unsat}-PTX and C_{6linked}-PTX). The FA-CPT and FA-Gd-DOTA compounds are described here because they are novel compounds prepared by this dissertation author.

Synthesis of FA-Gd-DOTA (FA-Gd). (Fig. 4.3) The first intermediate, compound 1, was prepared per Ref. 2. i. Compound 1 (0.284 mmol) was dissolved in chloroform and compound 2 (0.188 mmol, purchased from Macrocyclics) was predissolved in chloroform then added to reaction flask. The reaction mixture was stirred under N₂ for 2 days, or until all of 2 was consumed. The product compound 3 was purified by flash chromatography using a 10% methanol in DCM mobile phase.

ii. Pure compound 3 was dissolved in chloroform. TFA was added and reaction stirred overnight, or until full t-butyl deprotection. After deprotection confirmed, the organic solution was concentrated and the product precipitated with ether three times.

iii. Next, the resulting precipitate was dissolved in a 1:1 methanol:water solution. Excess NaOH was added and the reaction mixture stirred vigorously at room temperature. After deprotection was confirmed by MS and HPLC, metalation was performed:

iv. Fully deprotected ligand was dissolved in water and 1.2 equivalents of GdCl_3 were added. Adjust pH to neutral using HCl. Gently heat in oil bath at 60°C . Purify via semi-prep HPLC, 75% MeOH/water+0.1%TFA. Lyophilize to give white powder. Expected mass: 897.38.

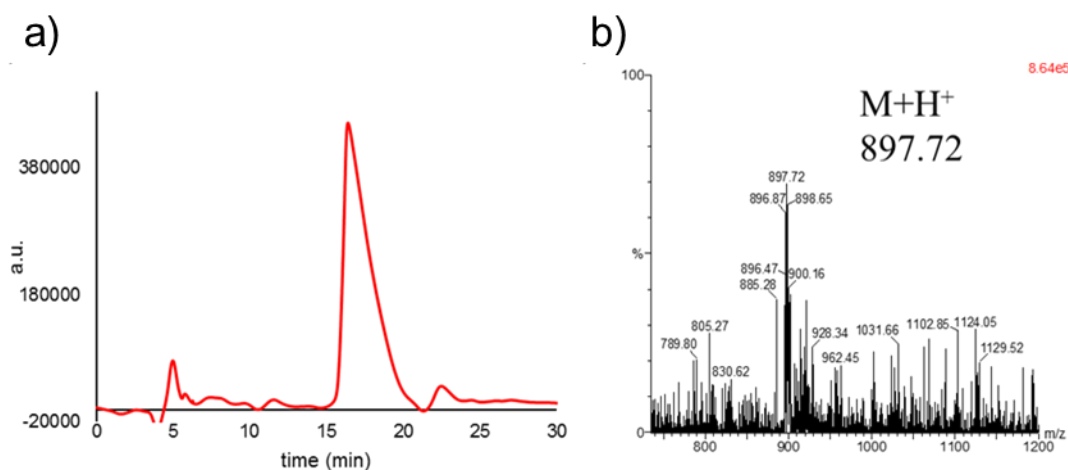


Figure 4.19 Semi-preparative RP-HPLC purification of FA-Gd-DOTA, and ESI-MS, positive ion mode, low resolution.

Synthesis of FA-CPT. ODDA was stirred in DMF solution along with EDC, DMAP and Camptothecin. After reaction was complete, reaction solution was concentrated, brought up in DCM, then washed 2x 1M HCl and 1x H_2O . The organic layer was dried over MgSO_4 , filtered and concentrated. Crude FA-CPT was purified first by flash chromatography using a gradient elution (100% DCM \rightarrow 10% methanol in DCM); then purified by prep RP-HPLC using a 70-90% acetonitrile in water + 0.1% TFA gradient, monitoring at 260 nm. The purified product was lyophilized to remove the HPLC solvents, leaving a yellow-tinted powder. ^1H -NMR (CDCl_3), 400 MHz. Chemical shifts: δ (ppm): 8.41 (s, 1H), 8.23 (d, 1H, $J = 8.4$ Hz), 7.95 (d, 1H, $J = 8.1$ Hz), 7.84 (t, 1H, $J = 8.5$ Hz), 7.68 (t, 1H, 7.1 Hz), 7.26 (s, 1H), 5.68

(d, 1H, $J = 17.2$ Hz), 5.42 (d, 1H, $J = 17.2$ Hz), 5.31 (s, 2H), 2.49 (m, 2H), 2.35 (t, 2H, $J = 8.0$ Hz), 2.29 (m, 1H), 2.17 (m, 1H), 1.70-1.59 (m, 4H), 1.39-1.11 (m, 24H), 0.98 (t, 3H, 7.4 HZ).

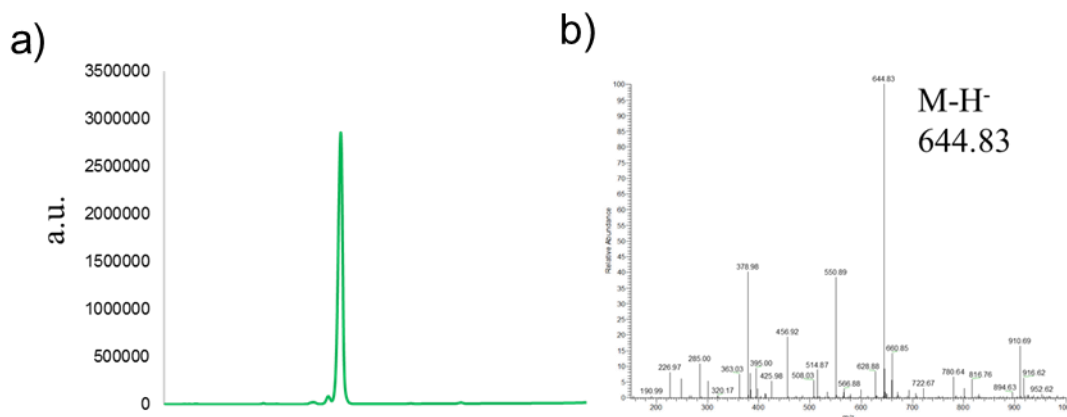


Figure 4.20 HPLC trace after prep-HPLC purification of FA-CPT. ESI-MS, low resolution.

4.25.2 Critical Micelle Concentration Determination

The fluorescence spectrum of pyrene is sensitive to small changes in solvent environment, specifically the vibrational bands I and III ($\lambda_{em} = 373$ and 384 nm). To determine critical micelle concentration, the concentration of surfactant versus ratio of I_I to I_{III} was plotted. The change in slope of this relationship indicates CMC. Stock pyrene solution was prepared at $2 \mu\text{M}$ in spectral grade methanol. Solutions containing increasing concentration of FA-Gd and constant concentration of pyrene were prepared. Fluorescence was measured using a Photon Technology International fluorescence detector, with excitation at 334 nm, and emission slit widths of 8 nm and 2 nm for $\lambda_{em} = 373$ and 384 nm, respectively.

Concurrently, DLS was measured on the same solutions. As concentration increased, changes intensity count were expected as the surfactant aggregates. Because DLS is not as

sensitive as fluorescence of pyrene vibrational bands, the distinction of CMC value was not as clear, though appears around the same concentration as determined in the pyrene assay.

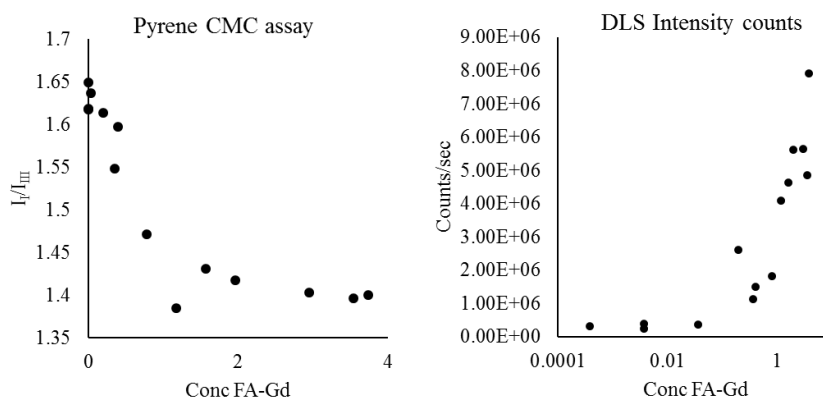


Figure 4.21 Critical micelle concentration using pyrene assay and DLS. For the DLS experiment, concentration was plotted on a log scale to more clearly see a transition in intensity counts.

4.25.3 Relaxivity Measurements

Relaxivity measurements were performed using a Bruker minispec mq60 relaxometer (60 MHz, 1.41 T, 37°C). Samples were prepared the day of measurement as a 2X concentrated stock solution of the small molecule Gd-containing compound, either FA-Gd or Multihance. For the FA-Gd only, serial dilutions were made to obtain the experimental solutions. For the formulations in the presence of HSA, a 2x HSA solution was prepared (using defatted HSA, Sigma) in DPBS such that the experimental solution would have an excess of protein. Equal volumes of the 2X FA-Gd and HSA solutions were mixed together and serial dilutions were made from this solution.

The aqueous sample was loaded in to an NMR tube, and T_1 times measured using the following parameters: Pulse separations from 10ms to 10,000 ms, with 10 data points. Delay sampling window = 0.05 ms, sampling window = 0.02 ms, time for saturation curve display = 3s. The inverse of T_1 time was plotted versus mM concentration of Gd, which was determined

from ICP-MS. Correlation coefficients (R^2 values) were found to be at least 0.99 in almost all data sets, indicating good linear correlation. Experiments were repeated and the relaxivities averaged. Relaxivity with varying ratios of FA-Gd to HSA are reported in Table 4.4. Experiments with FA-Gd at concentrations above the CMC were omitted due to poor fit with the rest of the dilution series: this is presumably from a macromolecular effect of FA-Gd aggregates versus unimer FA-Gd. A student t-test confirmed that FA-Gd in the presence of HSA had a significantly higher relaxivity than FA-Gd ($p < .03$) and significantly higher relaxivity than MH + HSA ($p < .06$).

Table 4.3 Relaxivity Data.

formulation	Relaxivity ($\text{mM}^{-1}\text{sec}^{-1}$)	R^2 fit
FA-Gd	2.45	0.999
	6.51	0.999
	4.19	0.99999
	2.42	0.991
FA-Gd + HSA	8.48	0.999
	20.87	0.9898
	12.87	0.997
	11.86	0.9793
MH + HSA	6.64	0.9997
	4.97	0.999
Gd-DOTA + HSA	5.98	0.92

Table 4.4 Relaxivity measurements FA-Gd, varying ratios with HSA.

Mol FA-Gd	Mol HSA	Relaxivity (mM ⁻¹ sec ⁻¹)	R ²
1	5	8.48	0.999
1	1	8.92	0.9999
5	1	8.07	0.9999
10	1	8.53	0.999

4.25.4 General *In Vivo* Imaging Methods

All animal studies and procedures were performed in accordance with IACUC, protocol S10145. Xenograft nu/nu mice, female, 4-6 weeks old, were inoculated with 10⁶ HT-1080 cells as a bolus injection, subcutaneously (as previously described¹⁹). After ~10 days, tumors had grown to an average volume of ~400 mm³, as measured with calipers, using the formula: W2 *(L/2) and ready for experimenting. Animals were injected via tail vein with 100 µL of stock solution of Gd-containing compound. Animals were anesthetized with 3% isoflurane in oxygen, at a flow rate of 2 mL/minute.

MR images were taken using an MR solutions table top preclinical scanner (MRSolutions 4000MRS MR), with integrated anesthesia and animal monitoring systems, using pre-programmed scan sequences (scout, 4.7 T FSE T₁w coronal; 4.7 T FSE T₁w axial). Images were acquired at strategic timepoints to monitor for increased contrast and/or accumulation in the tumor. Slices highlighting the tumor and whole body are pictured in Figs. 4.22-4.25 For the preliminary imaging and half-life studies, animals received 45.7 nmol of gadolinium for FA-Gd + HSA, and 755.9 nmol of gadolinium for MultiHance (low dose). Healthy animals received 1 µmol gadolinium, as did the follow-up studies in tumor-burdened mice comparing FA-Gd, MH and Gd-DOTA head-to-head.

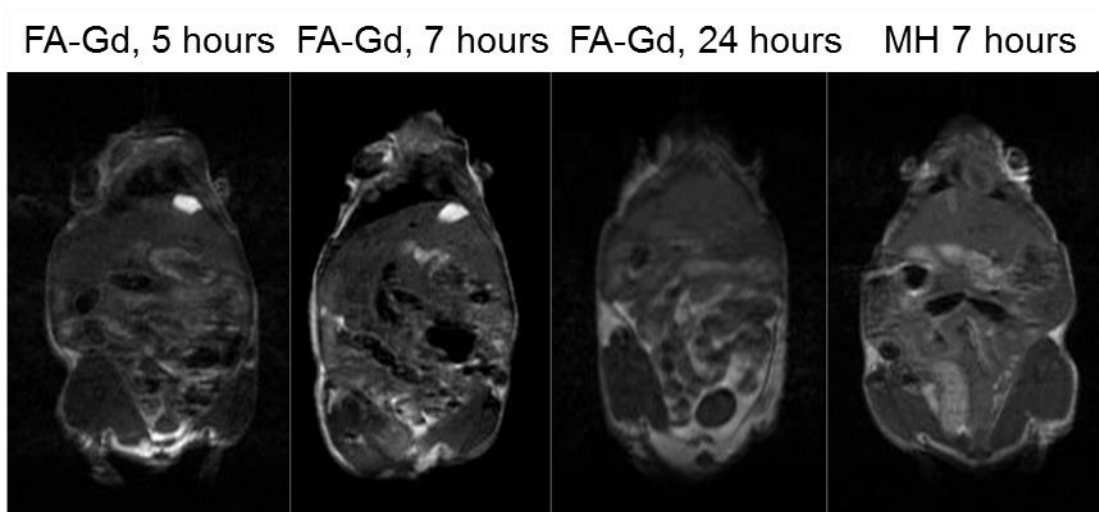


Figure 4.22 MRI scans of healthy animals receiving 1 μmol FA-Gd or MH. For FA-Gd, contrast enhancement is clearly visible in the gall bladder out to 7 hours, and recovers to baseline at 24 hours, indicating clearance from the animal. The animal receiving MH did not show distinct enhancement at the same 7 hour timepoint; this material is cleared faster from the blood.

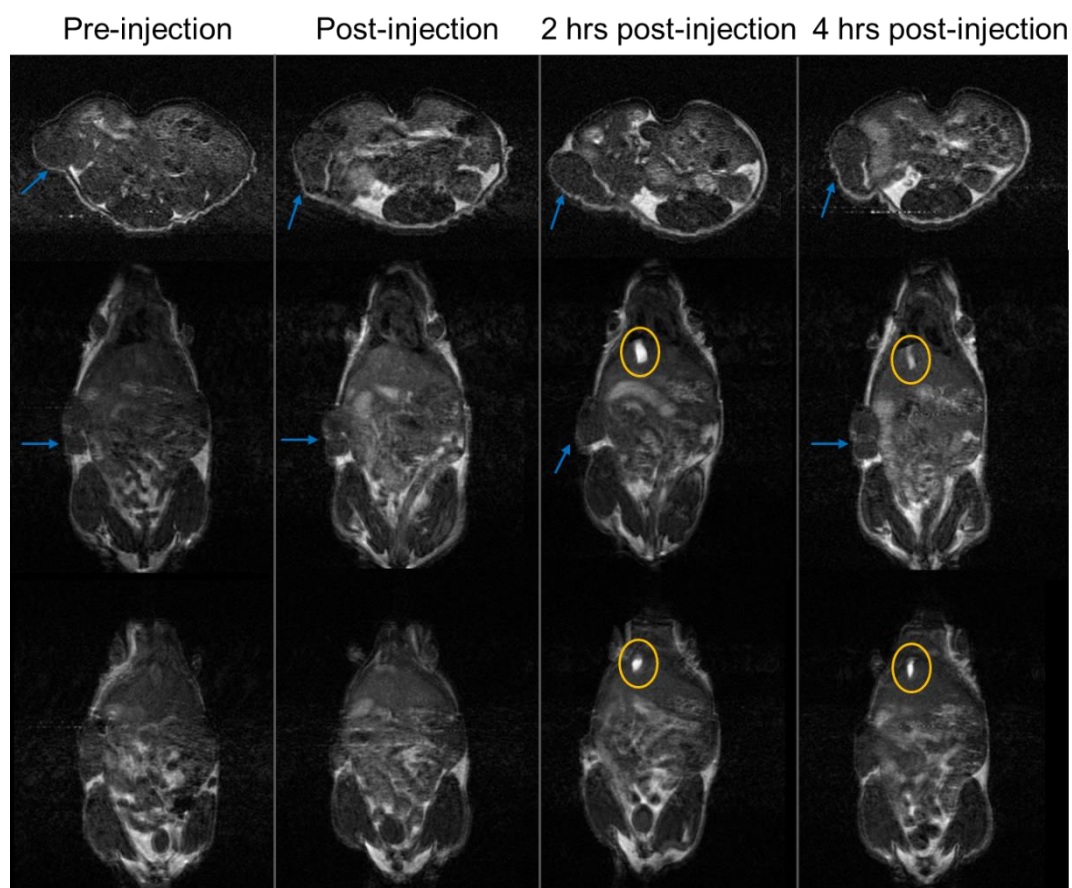


Figure 4.23 Representative MRI scans of tumor-burdened mouse receiving FA-Gd at low dose. Contrast is clearly visible out to 4 hours post-injection in the gall bladder, indicated with a yellow circle. The tumor is indicated with the blue arrow.

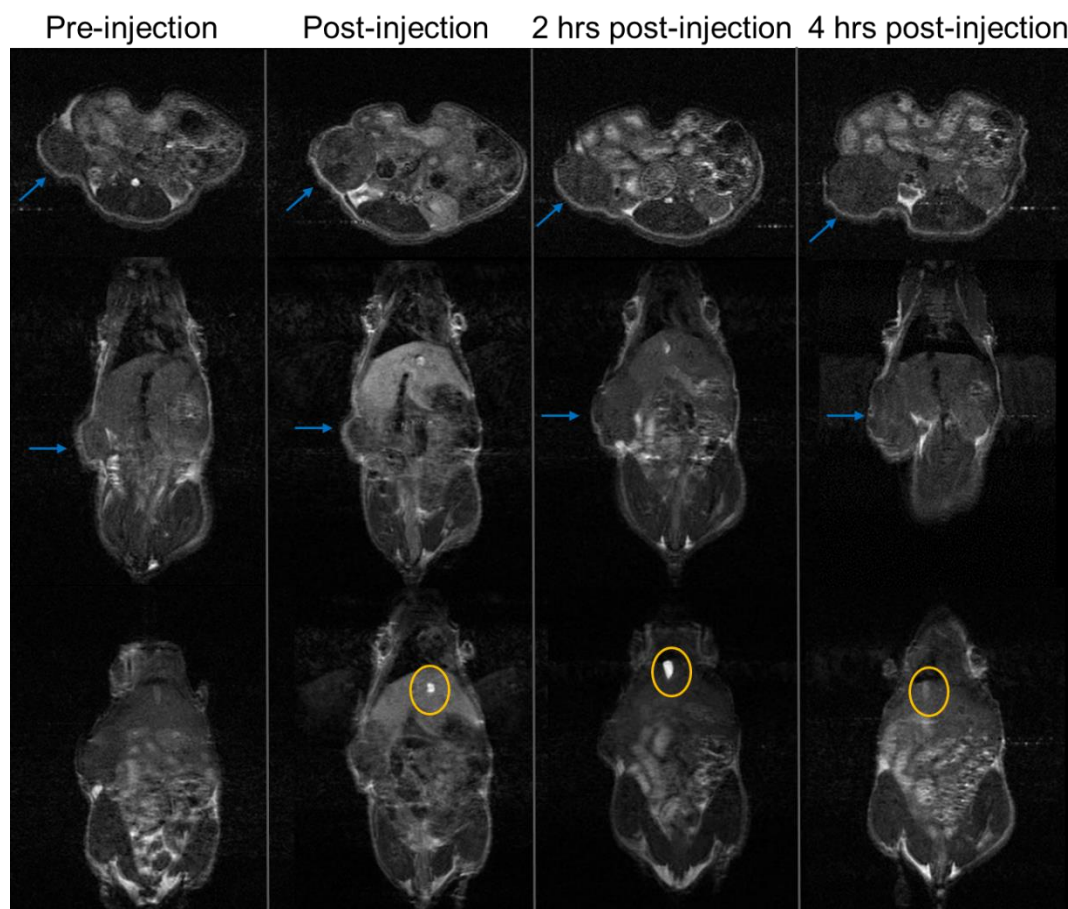


Figure 4.24 Representative MRI scans of tumor-burdened mouse receiving MH at low dose. Contrast is visible out to 4 hours post-injection in the gall bladder, indicated with a yellow circle. The tumor is indicated with the blue arrow.

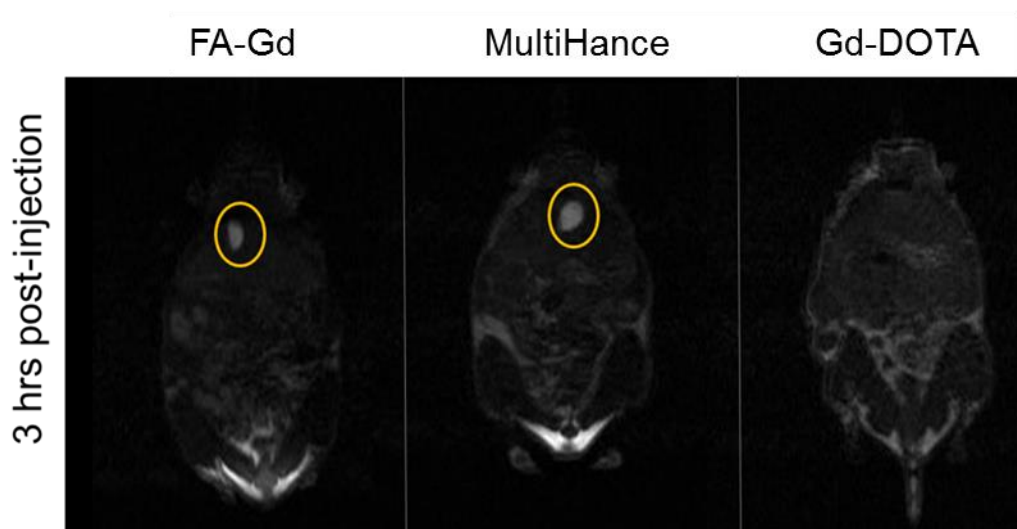


Figure 4.25 Representative MRI scans for tumor-burdened mice receiving high doses of FA-Gd, MH or Gd-DOTA. Contrast is visible for FA-Gd and MH, but not for Gd-DOTA.

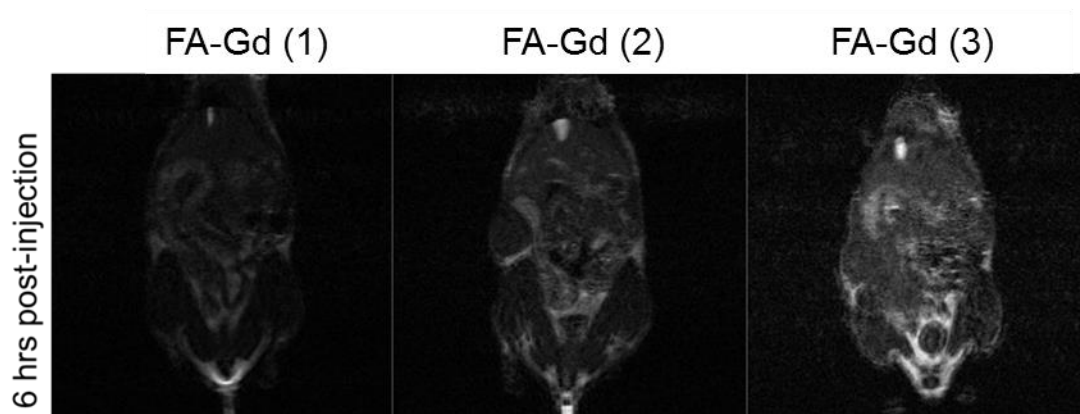


Figure 4.26 MRI scans of tumor-burdened animals receiving FA-Gd. All three animals imaged demonstrate contrast enhancement out to 6 hours post-injection in the gall bladder. (Animal 2 is identical image to that in Fig. 4.5).

4.25.5 Blood Half -Life Studies and Protocols

Blood half-life of FA-Gd, MultiHance and Gd-DOTA were evaluated head to head by analyzing for gadolinium concentration in blood plasma. Blood samples were collected via retro-orbital blood draw pre-injection (0 point) then 1, 2, 4, 7 and 24 hours post injection in to heparanized borosilicate glass pipettes. Whole blood aliquots were immediately spun down at

1500 rpm for ten minutes to separate plasma from red blood cells. 25 μ L of plasma was isolated, and stored at -80°C until acid digested, after which the sample was diluted for analysis by ICP-MS.

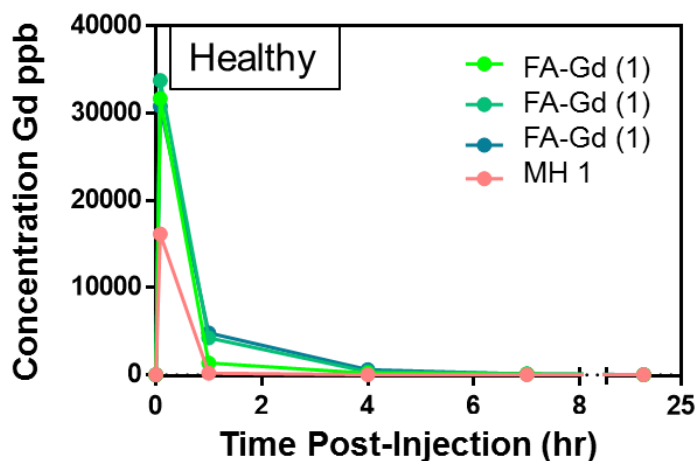


Figure 4.27 Blood half-life healthy animals. High dose (1 μ mol Gd). 3 animals receiving FA-Gd, 1 animal for MultiHance.

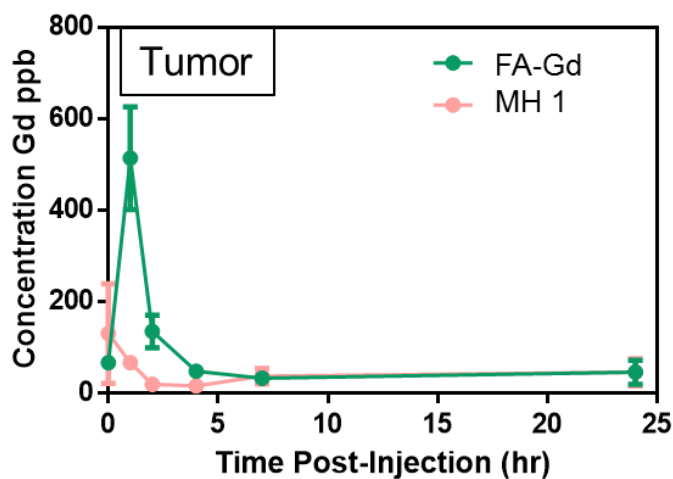


Figure 4.28 Pilot study, blood half-life tumor-burdened animal, average of $n=3$. Low dose.

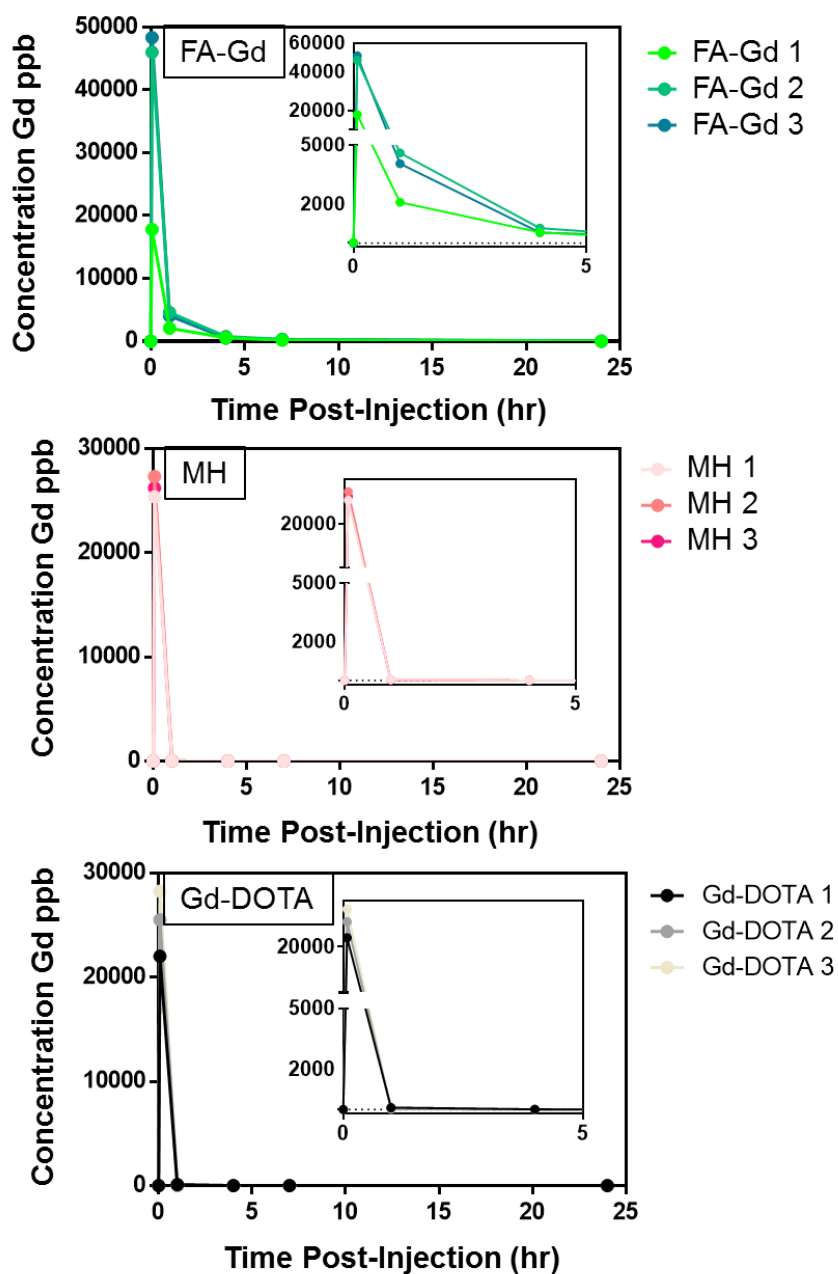


Figure 4.29 Blood Half Life, tumor-burdened animal. 3 animals each, FA-Gd, MH and Gd-DOTA. Inset highlights changes in serum concentration in the first 5 hours post-injection.

4.25.6 General *Ex Vivo* Analysis Methods

At time points of interest (e.g. 24 hours), mice were sacrificed using a CO₂ overdose. If the animals were perfused, a butterfly needle was used, and ~20 mL of saline was flushed through over ~20 minutes. The heart, kidney, liver, spleen, lung, tumor mass, were collected,

weighed then digested in concentrated HNO_3 (900 μL , or 500 μL for the liver). For the non-perfused animals, after CO_2 overdose was administered, cervical dislocation was performed prior to beginning dissection and organ harvest. Organs were digested as above. After the tissues were homogenized, aliquots were diluted to a final volume of 5 mL at a final acid concentration of 5% for ICP-MS analysis.

For ICP: for all experiments in this chapter, ICP analysis was done at the UCSD ECAL facility, using a Thermo Scientific iCAP RQ ICP-MS. Calibration standards ranged from .01 to 10,000 ppb in 5% nitric acid. Biodistribution data in Fig. 4.30 is represented as %ID/g tissue, a standard way to normalize amount of material in tissues of different masses. Plots comparing total amounts of material detected at 24 hours both as total ng Gd detected and % of injected dose are reported for each material and each animal.

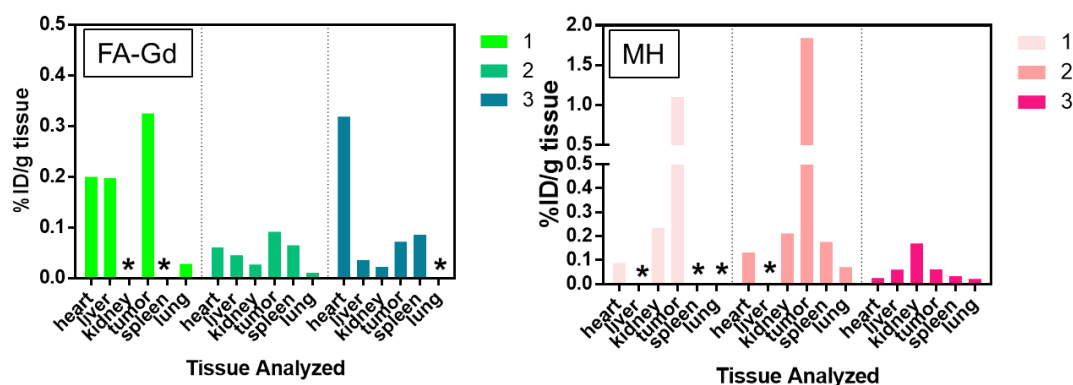


Figure 4.30 Biodistribution in tumor-burdened animals, Low Dose. Individual animal profiles looking at normalized accumulation in organs of interest: heart, liver, kidney, tumor, spleen and lung. These animals were perfused prior to organ harvest. 3 animals received FA-Gd, at a dose of 100 nmol gadolinium (15,725 ng) and 3 animals received MH at a dose of 50 nmol (7,862.5 ng). * denotes no detection by ICP-MS.

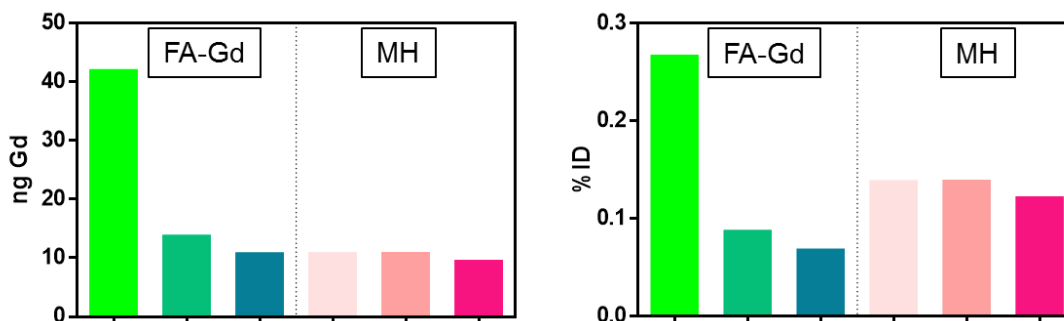


Figure 4.31 Plots describing total ng of Gd detected in the animal (sum organs) and %injected dose are described; these plots correspond to the animals in Fig. 4.30, which were perfused prior to organ harvest.

4.25.7 General Cell Culture Methods

All cell lines were obtained from an in-house sub-culture originally purchased from ATCC. Cells were incubated at 37°C at 5% CO₂ using Dulbecco's modified eagle medium, DMEM (high glucose, no glutamine, Life Technologies/Gibco, Cat 11960044) supplemented with 10% FBS (heat inactivated, Omega Scientific, Cat FB-02), and 1x of sodium pyruvate (100x = 100mM, Life Technologies, Cat 11360070), non-essential amino acids (Life Technologies, Cat 11140050), GlutaMAX (Life technologies Cat 35050061) and antibiotics (Penicillin-Streptomycin, Life Technologies Cat 15140122). Opti-MEM reduced serum medium (Life Technologies, Cat 31985070) was used as is, and DMEM without phenol red (Life Technologies, Cat 31053028) was supplemented as in other DMEM. Cell cultures were maintained by sub-culturing in flasks every 4-7 days when cells became confluent using trypsin-EDTA, 0.25% (Life Technologies, Cat 25200114).

4.25.8 Cytotoxicity

Cytotoxicity of compounds was evaluated using the CellTiter Blue (CTB) assay (Promega, cat G8081). Treatments of fatty acid-conjugates were prepared as 1000x serial stock dilutions in DMSO, then diluted into media for 1X, 0.1% DMSO treatment solutions. PTX-FA + HSA formulations and FA-KLA were prepared as concentrated solutions in DPBS, then

diluted in media for treatment solutions. Cells were plated in 96-well plates, 1 day before treatment, at the following densities: HeLa at 3,000 cells/well, HT-1080 at 4,500 cells/well, HT-29 at 7,500 cells/well, PANC-1 at 10,000 cells/well, H522 at 10,000 cells/well, and HepG2 at 4,500 cells/well. After 24 hours, plating media was removed, then treatments of 100 μ L were added to the wells. After 3 days, the media was removed and replaced with 100 μ L complete DMEM without phenol red. Then 20 μ L of CTB reagent was added, and the cells incubated for two hours at 37°C. Fluorescence was measured at 590 nm with excitation at 560 nm using a Perkin Elmer EnSpire plate reader. Average background fluorescence of CTB reagent in media without cells was subtracted from average fluorescence readings of the experimental wells (three wells per treatment concentration). Viability was calculated as the average background-subtracted signal in a well compared to that of a negative control well (cells treated with vehicle, either 0.1% DMSO/media or media). Viabilities were fit in GraphPad Prism using a non-linear, dose-dependent inhibition curve. The IC_{50} numbers given in the table reflect the concentration at which the cell death is 50% of the maximum response. The $\log(IC_{50})$ and error in $\log IC_{50}$ are reported, and reflects the standard error in the fit. Where applicable, average viabilities are reported; these averages reflect experiment-to-experiment variability. Of note is the high variability from experiment-to-experiment. This could come from error in concentration determination of the compound of interest, or a treatment solution in which the organic compound precipitates. Future studies should include a validation of concentration of treatment and freshly prepared treatment solutions.

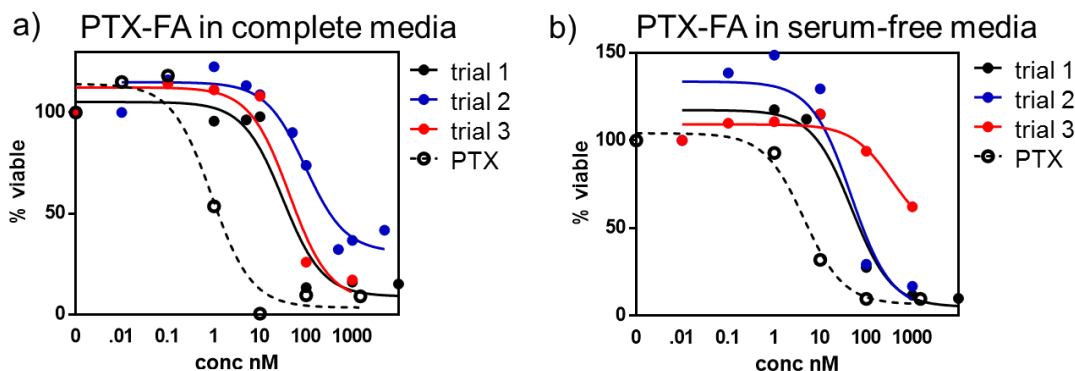


Figure 4.32 Representative IC_{50} curves for PTX-FA conjugates compared to parent PTX compound in complete versus serum-free media, with 0.1% DMSO to solubilize the organic compounds, in HeLa cells. In both cases, the conjugates are not as toxic as the parent compound. There is also not much different in toxicity between treatments in complete media (a) versus serum-free media (b). Three repeats for the PTX-FA compound are shown here, with IC_{50} values for each trial reported in Table 4.5.

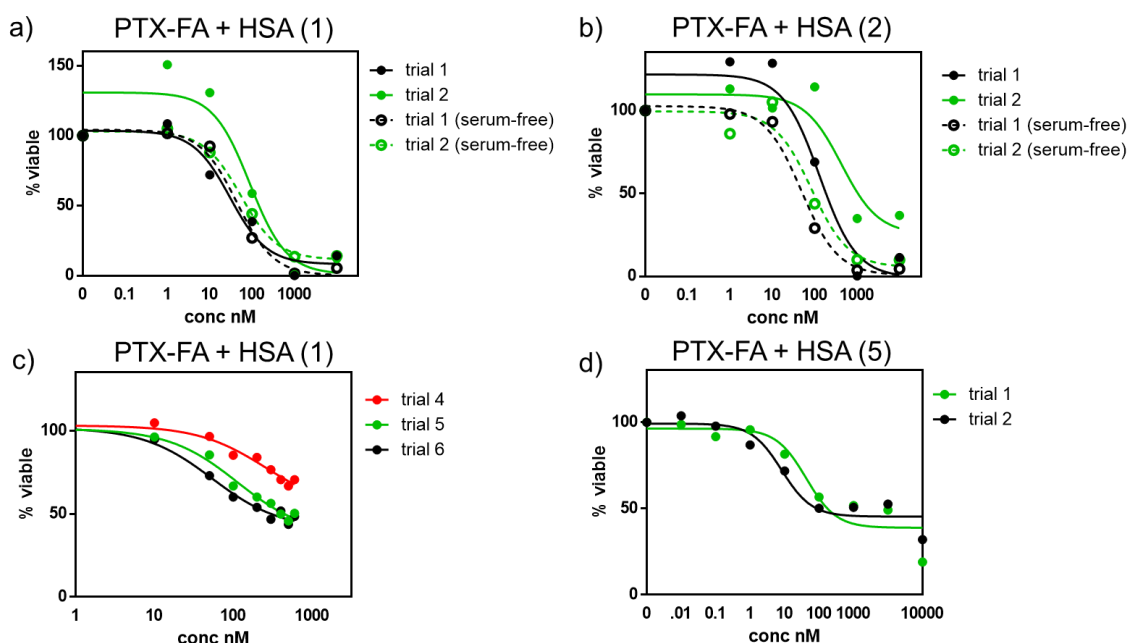


Figure 4.33 Representative IC_{50} curves for PTX-FA formulations with HSA in HeLa cells. The concentrations are given with respect to taxol concentration. Additionally, there is no great difference in toxicity in the serum-free media (dotted plots in panels a) and b)). Panel c) shows examples of cytotoxicity experiments where the treatment concentration was not high enough to generate a complete IC_{50} curve and these results were excluded from overall analyses. In panel d), it is interesting that even at very high concentrations ($\sim 10 \mu M$), full cell death does not occur, whereas at comparable concentrations for the other formulations, viability is very low. IC_{50} values for each trial reported in Table 4.5.

Table 4.5 Toxicity of PTX, PTX-FA, and formulations with HSA in HeLa cells. Evaluation in complete media and serum-free media (OM) are reported.

Compound	Media conditions		Log IC ₅₀	std error log (IC ₅₀)	IC ₅₀ nM	avg	stdev
PTX	DMEM	trial 1	-7.917	0.1045	12.1	6.73	5.6
		trial 2	-8.143	0.1991	7.2		
		trial 3	-9.049	0.1057	0.893		
PTX	OM	trial 1	-8.334	0.373	4.64	4.54	0.1
		trial 2	-8.353	0.0649	4.43		
PTX-FA	DMEM	trial 1	-7.504	0.3078	31.37	57.05	34.8
		trial 2	-7.365	0.326	43.18		
		trial 3	-7.015	0.1773	96.6		
PTX-FA	OM	trial 1	-7.32	0.149	47.9	47.35	0.8
		trial 2	-7.33	0.4995	46.8		
PTX-FA + HSA (1)	DMEM	trial 1	-7.522	0.2551	30.1	59.00	40.9
		trial 2	-7.056	0.3937	87.9		
		trial 3*	-6.582	0.2206	261.7		
		trial 4*	-6.948	0.1132	112.7		
		trial 5*	-7.267	0.1015	54.1		
PTX-FA + HSA (1)	OM	trial 1	-7.359	0.1397	43.8	48.80	7.1
		trial 2	-7.27	0.08076	53.8		
PTX-FA + HSA (2)	DMEM	trial 1	-6.886	0.3259	129.9	278.25	209.8
		trial 2	-6.37	0.4964	426.6		
PTX-FA + HSA (2)	OM	trial 1	-7.316	0.1333	48.4	66.40	25.5
		trial 2	-7.074	0.2687	84.4		
PTX-FA + HSA (5)	DMEM	trial 1	-8.084	0.2529	8.25	25.38	24.2
		trial 2	-7.372	0.3616	42.5		

*omitted from average.

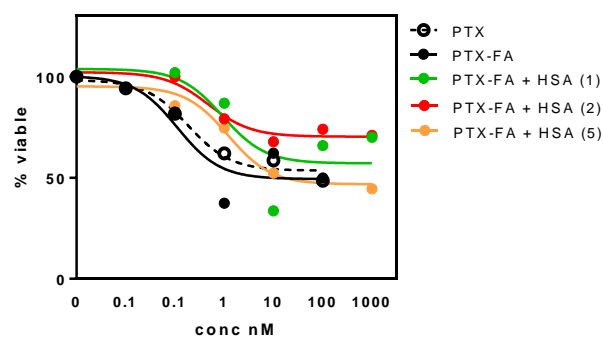


Figure 4.34 Representative IC_{50} curves for PTX-FA and formulations with HSA in HT-1080 cells. All experiments were done in using complete media. IC_{50} values for each trial reported in Table 4.6.

Table 4.6 Toxicity of PTX, PTX-FA, and formulations with HSA in HT-1080 cells. Evaluation in complete media are reported.

Compound	$\log IC_{50}$	std error $\log (IC_{50})$	IC_{50} nM
PTX	-8.738	0.2055	1.83
PTX-FA	-8.953	0.4755	1.11
PTX-FA + HSA (1)	-8.033	0.8264	9.27
PTX-FA + HSA (2)	-8.323	0.2649	47.6
PTX-FA + HSA (5)	-7.922	0.1245	12

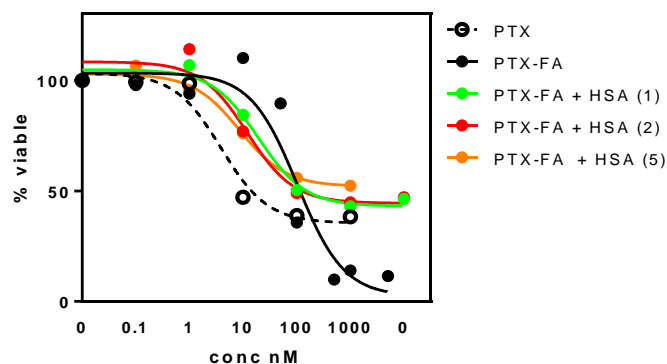


Figure 4.35 Representative IC_{50} curves for PTX-FA and formulations with HSA in HT-29 cells. Evaluation of toxicity in complete media is reported. IC_{50} values for each trial reported in Table 4.7.

Table 4.7 Toxicity of PTX, PTX-FA, and formulations with HSA in HT-29 cells. Evaluation in complete media are reported.

Compound	log IC ₅₀	stdev log IC ₅₀	IC ₅₀ nM	avg	std dev
PTX	-8.409	0.2406	3.9		
PTX-FA	-9.129	1.278	0.743		
PTX-FA	-6.989	0.2349	102.5	36.1	57.5
PTX-FA	-8.294	0.1672	5.08		
PTX-FA + HSA (1)*	-6.675	0.2506	211.6		
PTX-FA + HSA (1)*	-6.318	0.3546	481.3		
PTX-FA + HSA (1)	-7.88	0.201	13.2	16.2	4.31
PTX-FA + HSA (1)	-7.715	0.167	19.3		
PTX-FA + HSA (2)	-8.183	0.2993	6.57		
PTX-FA + HSA (2)	-7.925	0.262	11.9	9.235	3.768879
PTX-FA + HSA (5)	-8.064	0.1336	8.62		

*omitted from average.

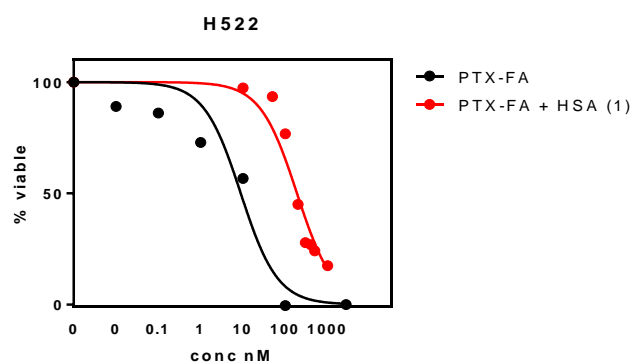


Figure 4.36 Representative IC₅₀ curves for PTX-FA and formulations with HSA in H522 cells. Evaluation of toxicity in complete media is reported. IC₅₀ values for each trial reported in Table 4.8.

Table 4.8 Toxicity of PTX-FA and formulations with HSA in H522 cells. Evaluation in complete media are reported.

Compound	log IC ₅₀	stdev log IC ₅₀	IC ₅₀ nM	avg	stdev
PTX-FA	-7.807	0.1417	15.6	65.8	70.9
PTX-FA	-6.936	0.1413	115.9		
PTX-FA + HSA (1)	-6.818	0.1312	152	182.3	42.9
PTX-FA + HSA (1)	-6.672	0.1685	212.6		

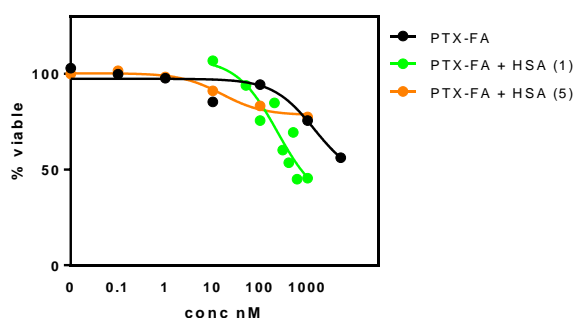


Figure 4.37 Representative IC₅₀ curves for PTX-FA and formulations with HSA in PANC-1 cells. Evaluation of toxicity in complete media is reported. IC₅₀ values for each trial reported in Table 4.9.

Table 4.9 Toxicity of PTX-FA and formulations with HSA in PANC-1 cells. Evaluation in complete media are reported.

Compound	log IC ₅₀	stdev log IC ₅₀	IC ₅₀ nM	avg	stdev
PTX-FA	-5.86	0.3674	1381		
PTX-FA + HSA (1)	-6.325	0.5044	473.1		
PTX-FA + HSA (1)	-6.835	0.2824	146.2	283.4	169.6
PTX-FA + HSA (1)	-6.636	0.3553	231		
PTX-FA + HSA (5)	-8.606	0.3241	2.48	9.09	9.3
PTX-FA + HSA (5)	-7.805	0.1381	15.7		

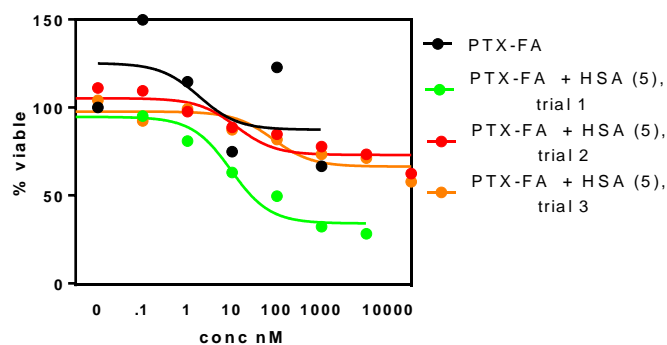


Figure 4.38 Representative IC_{50} curves for PTX-FA and PTX-FA + HSA (5:1) formulations in HepG2 cells. Evaluation of toxicity in complete media is reported. IC_{50} values for each trial reported in Table 4.10.

Table 4.10 Toxicity of PTX-FA and formulations with HSA in HepG2 cells. Evaluation in complete media are reported.

Compound	$\log IC_{50}$	stdev $\log IC_{50}$	IC_{50} nM	avg	stdev
PTX-FA	-8.738	0.9402	1.89		
PTX-FA + HSA (5)	-8.025	0.1348	9.44		
PTX-FA + HSA (5)	-7.906	0.4158	12.4	34.6	41.1
PTX-FA + HSA (5)	-7.086	0.3833	82.1		

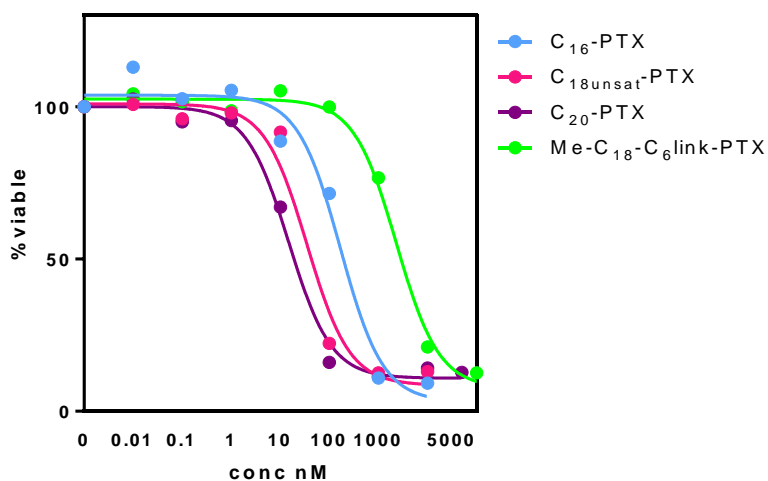


Figure 4.39 Representative IC₅₀ curves for C₁₆-PTX, C_{18unsat}-PTX, C₂₀-PTX and Me-C₁₈-C₆link-PTX in HeLa cells. Evaluation of toxicity in complete media is reported. IC₅₀ values for each trial reported in Table 4.11.

Table 4.11 Toxicity of C₁₆-PTX, C_{18unsat}-PTX, C₂₀-PTX and Me-C₁₈-C₆link-PTX in HeLa cells. Evaluation in complete media are reported.

Compound		Log IC ₅₀	Std.Error Log IC ₅₀	IC ₅₀ nM	avg	stdev
C16-PTX	trial 1	-6.681	0.1044	208.3	195.6	24.1
	trial 2	-6.775	0.1576	167.8		
	trial 3	-6.677	0.184	210.6		
C20-PTX	trial 1	-7.754	0.1528	17.6	27.8	20.1
	trial 2	-7.293	0.2017	50.9		
	trial 3	-7.827	0.0822	14.9		
C18unsat-PTX	trial 1	-7.237	0.1087	57.9	40.03	16
	trial 2	-7.565	0.1923	27.2		
	trial 3	-7.456	0.1669	35		
Me-C18-C6-link-PTX	trial 1	-5.633	0.0792	2329	N/A	N/A

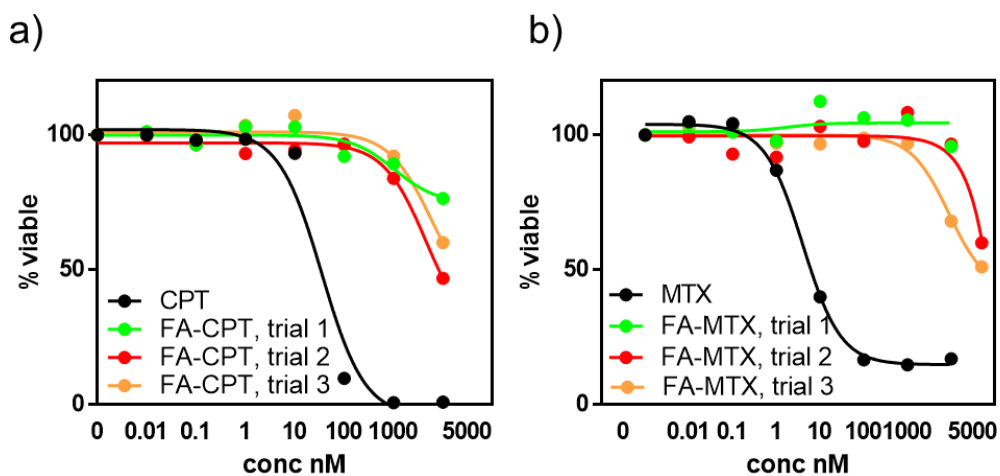


Figure 4.40 Cytotoxicity of MTX, FA-MTX and CPT, FA-CPT in HeLa.

Table 4.12 Toxicity of control (parent) compounds CPT and MTX.

Compound	log IC ₅₀	std error log IC ₅₀	IC ₅₀ nM	avg	std dev
CPT	-7.036	0.2723	92		
CPT	-7.453	0.1864	35.2	49.8	37.1
CPT	-7.652	0.1356	22.3		
MTX	-8.111	0.3208	7.75		
MTX	-8.069	0.05742	8.54	6.01	3.72
MTX	-8.759	0.09587	1.74		

Table 4.13 Toxicity of FA-CPT and FA-MTX in HeLa cells.

Compound		highest dosing	viability
FA-CPT	trial 1	10 uM	77%
FA-CPT	trial 2	10 uM	47%
FA-CPT	trial 3	10 uM	60%
FA-MTX	trial 1	10 uM	95%
FA-MTX	trial 2	50 uM	60%
FA-MTX	trial 3	50 uM	51%

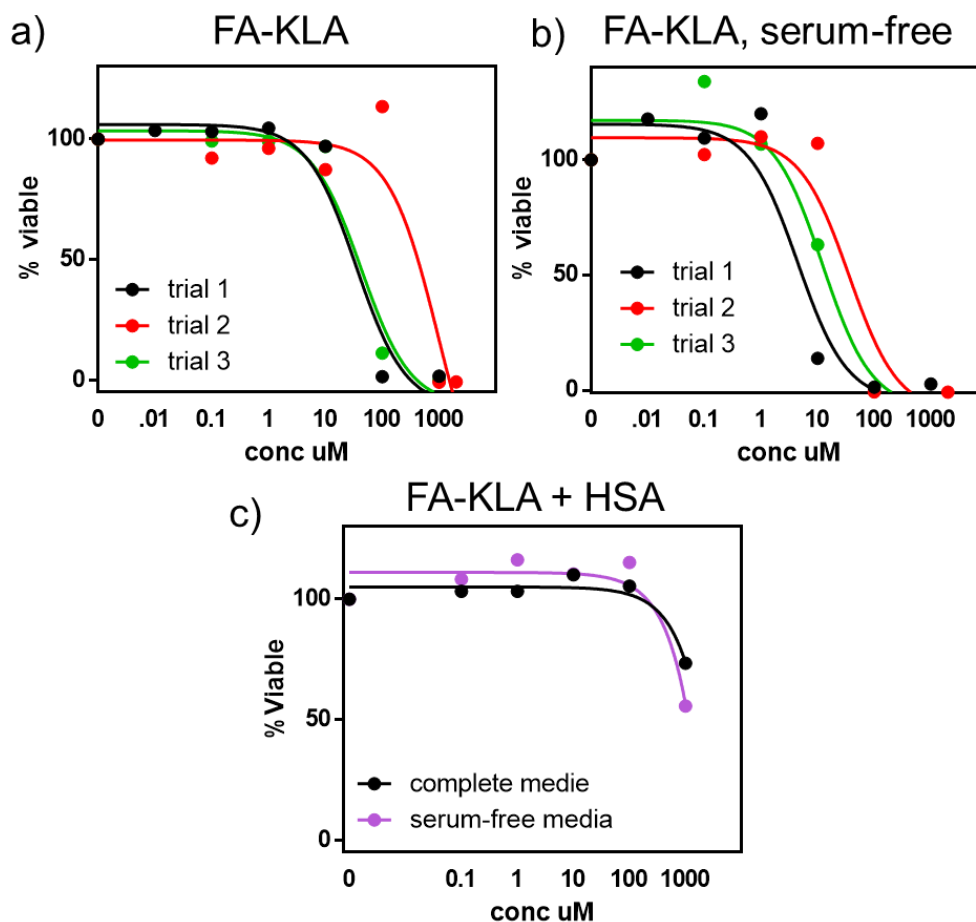


Figure 4.41 Representative IC₅₀ curves for FA-KLA and FA-KLA + HSA in HeLa cells. Evaluation of toxicity in complete media is reported and serum-free media is reported. IC₅₀ values for each trial reported in Table 4.14.

Table 4.14 Toxicity of FA-KLA and FA-KLA + HSA in HeLa cells. Evaluation in complete media as and serum-free media (OM) is reported.

Compound	condition		log IC ₅₀	std error log IC ₅₀	IC ₅₀ uM	avg	stdev
FA-KLA	DMEM	trial 1	-4.458	0.2741	34.9	38.7	5.4
		trial 2	-3.01	0.6444	978		
		trial 3	-4.371	0.2609	42.5		
FA-KLA	OM	trial 1	-5.348	0.3241	4.49	17.6	16.4
		trial 2	-4.444	0.3295	36		
		trail 3	-4.912	0.2561	12.3		
FA-KLA + HSA		trial 1			-	-	-

4.25.9 Cell Uptake Experiments

Flow cytometry was used to elucidate the association of a fluorescein-fatty acid compound or FA-KLA with fluorescein tag with a cell. Flow cytometry analysis gives an idea of cell-associated fluorescence coming from the treatment solutions, over that of background cell fluorescence (control cells). 24 hours prior to treatment, 100,000-120,000 cells were plated in each well of a 24-well plate. After one day, media was removed, then treatment solution of fluorescein-containing treatment solution was added (500 μ L of treatment solution prepared as in the cytotoxicity experiments: 0.1%DMSO/media for FA-fl, treatments, media only for all other compounds and formulations). The cells were incubated for 1 hour at 37 °C. Control cells were treated with the vehicle (media) for a background fluorescence signal. After incubation, treatment solution was removed, then cells washed with DPBS 3 times. A heparin wash (0.5mg/mL solution) was performed with 5 minute incubations. [This step would remove negative components of a treatment solution from the cell surface. It was found that omitting the heparin wash did not significantly affect results from flow cytometry analysis (results not shown).] Next, cells were lifted from the wells by incubating with 250 μ L 0.25%trypsin/EDTA solution for 10 minutes. The trypsinization solution was quenched with 500 μ L complete media, and cells mixed well, before transferring to an eppendorf with 750 μ L DPBS. Eppendorfs were centrifuged for 5 min at 300 g, to pellet out cells; supernatant was aspirated, then cell pellet suspended in 70 μ L cold DPBs. Cells were stored as is in eppendorfs on ice until analysis.

4.25.10 Cell Uptake Mechanistic Experiments

In the experiments examining mechanism of uptake of materials, the following considerations were taken: cells were incubated with material for 1 hour in a fridge at 4°C. This would inhibit any active uptake mechanism. For the M β CD inhibitor (Fischer, cat C4555), prior

to treatments, 37 μ L of a 128 mM M β CD solution in DPBS was added to the wells containing 500 μ L DMEM for a final concentration of 9.5 mM. The cells were incubated at 37°C or 4°C. Then, for experiments in complete media, the treatment solutions were added directly to the wells: for FA-fl, 5 μ L of a 460 μ M solution in DMSO was added to give a final concentration of 4.6 μ M. For FA-fl + HSA, 33 μ L of a 70 μ M solution in DPBS was added to give a final concentration of 4.6 μ M. For experiments in serum-free media, after the 30 minute incubation with M β CD, all media and M β CD was aspirated, then treatment solutions of 4.6 μ M FA-fl in 0.1%DMSO/OM with 9.5 mM M β CD or 4.6 μ M FA-fl + HSA in OM with 9.5 mM M β CD were added. The cells were incubated for 1 hour at either 37°C or 4°C. Then the same procedure as above was used to harvest the cells.

4.25.11 Flow Cytometry Analysis

A BD-Accuri C6 Plus flow cytometer was used for all analyses. Immediately before analysis, cells were gently vortexed, and visually confirmed to be distinct cells in suspension using light microscopy. Each analysis was performed for 10,000 events using slow fluidics mode (14 μ L/min). All samples were gated to a healthy cell population, with the gate generated from the analysis of the vehicle control cells. Fluorescein channel (FL1-A) was analyzed, and fluorescence intensity count normalized to the fluorescence count for control cells. Representative scattering plots for different cell types (HeLa, HT-1080, HT-29, HepG2) are shown for treatments with media or serum-free media (Opti-MEM). In most cases, there was no significant change in population with the serum-free media or with the various treatment solutions. The exception is when performing mechanistic uptake studies with the M β CD inhibitor. Extended incubation time (multiple hours) with M β CD is known to negatively affect cell viability; the resulting scattering plots (Figs. 4.51, 4.52) shows a large decrease in healthy

cell gated population. The scatter plots and histograms below are representative of data presented in Figs. 4.15-4.17.

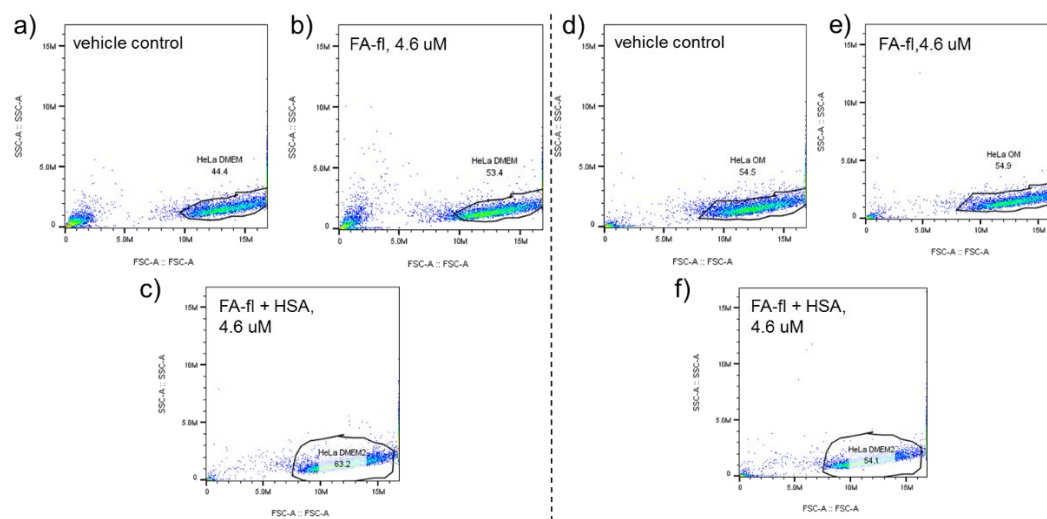


Figure 4.42 Dot plots showing forward scattering (FSC, x axes) versus side scattering (SSC, y axes) for representative experiment of HeLa cells treated with FA-fl or FA-fl + HSA, and gating used for healthy cell populations. Points close to origin are from cellular or other debris. A) is cells treated with complete media, vehicle control (gate = 44.4%). B) cells treated with 4.6 μ M FA-fl in complete media (gate = 53.4%); c) FA-fl + HSA formulation, 4.6 μ M in complete media (gate = 63.2%); d) serum-free media, vehicle control (gate = 54.5%); e) 4.6 μ M FA-fl in serum-free media (gate = 54.9%); f) FA-fl + HSA formulation, 4.6 μ M in serum-free media (gate = 54.1%). Select histograms showing population shifts in fluorescence intensity is shown in Figs 4.43 and 4.44.

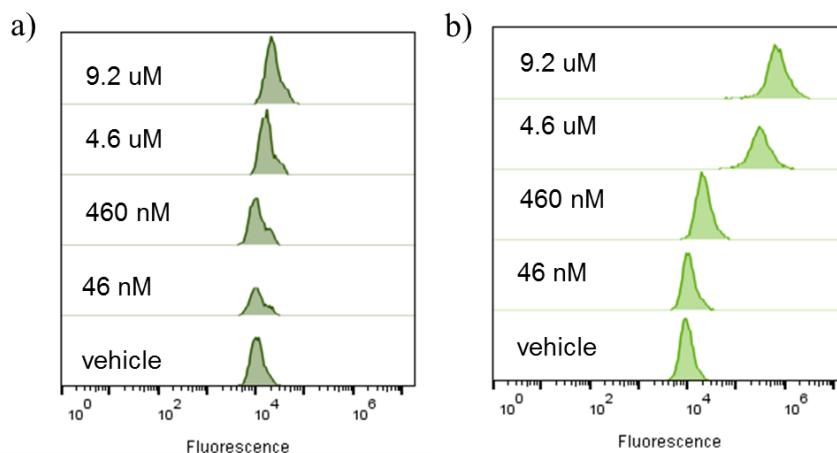


Figure 4.43 Representative histograms for cell uptake, showing concentration dependent uptake of FA-fl using a) complete media or b) serum-free media for HeLa cells. For a treatment of 9.2 μ M FA-fl there is a \sim 2-fold increase in fluorescence, whereas treatment in serum-free media yields a much larger increase in signal, about 75-fold increase. The drastic difference in fluorescence increase for serum-free media indicates that the bovine serum proteins may be altering the uptake mechanism of the material. This was evaluated in mechanistic uptake studies.

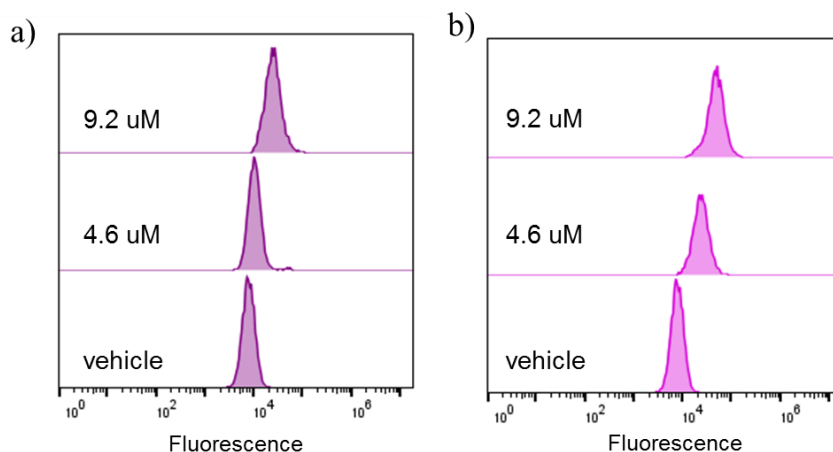


Figure 4.44 Representative histogram for cell uptake, showing concentration dependent uptake of formulations with HSA using a) complete media or b) serum-free media. For a treatment of 9.2 μ M with respect to fluorescein, a \sim 3-fold increase in fluorescence is observed, while treatment in serum-free media shows \sim 6-fold increase in fluorescence signal. The modest increases in fluorescence signal compared to FA-fl in serum-free media again alludes to the role of HSA and/or serum proteins in cell uptake.

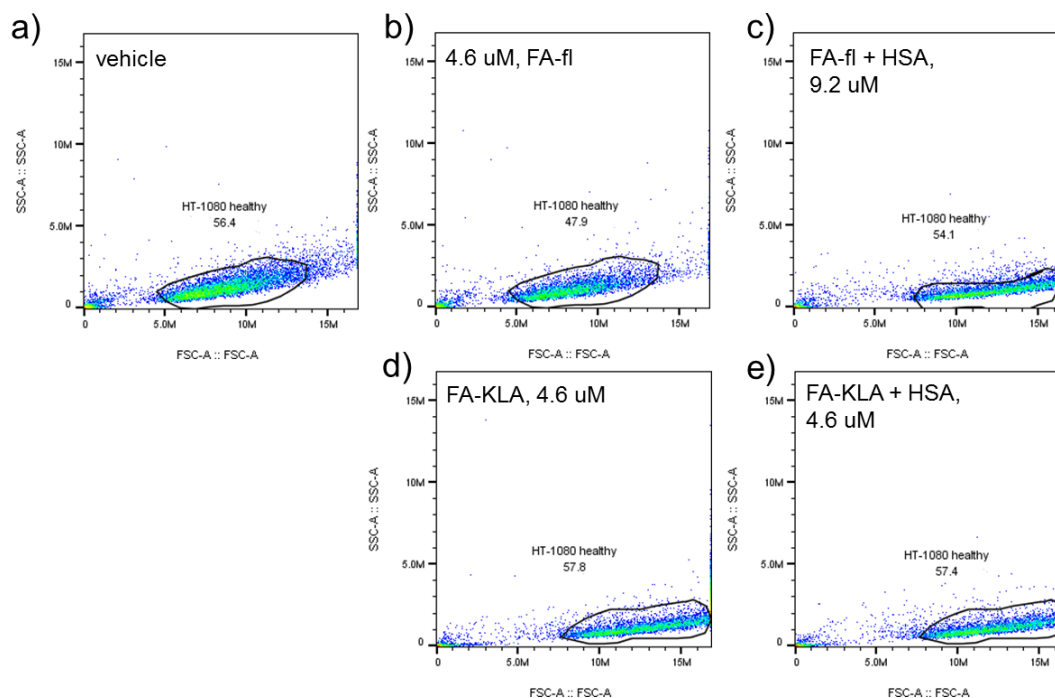


Figure 4.45 Dot plots showing forward scattering versus side scattering for representative experiments investigating mechanism of uptake of FA-fl, FA-fl + HSA, FA-KLA or FA-KLA + HSA materials in HT-1080 cells, and gating used for healthy cell populations. All experiments are done in complete media. Conditions for treatment are included in an inset in each plot and gated populations represent 47-57% of cell populations analyzed, indicating minimal effect of the treatment material on the cell morphology.

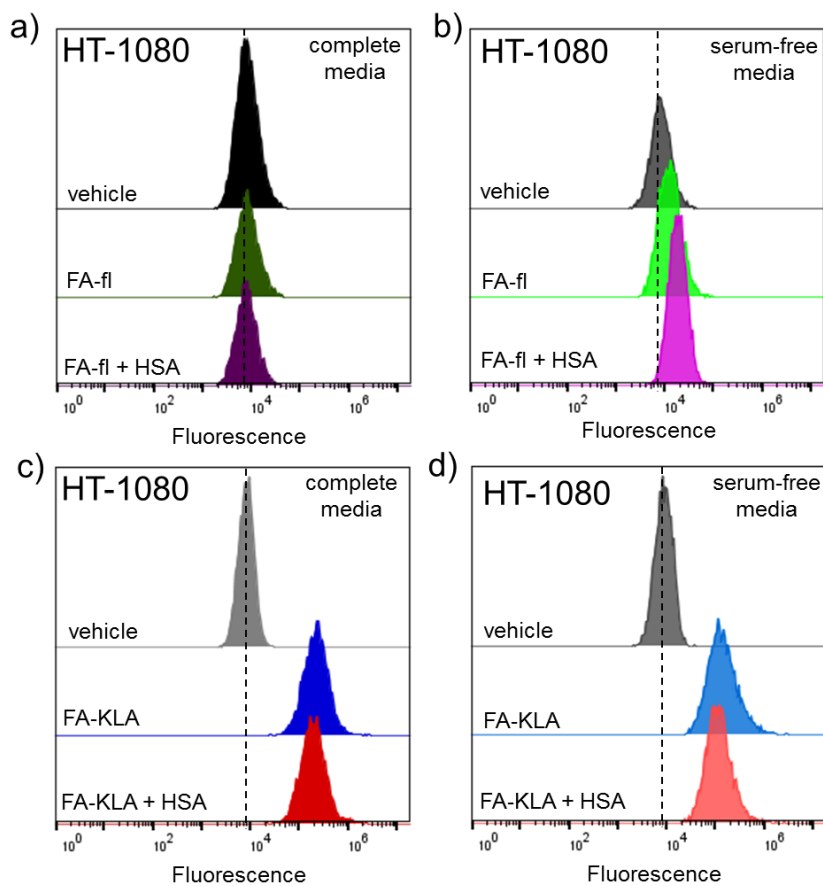


Figure 4.46 Representative histograms for cell uptake of FA-fl, FA-fl + HSA, FA-KLA or FA-KLA + HSA in HT-1080 cells. Treatments in complete and serum-free media were performed.

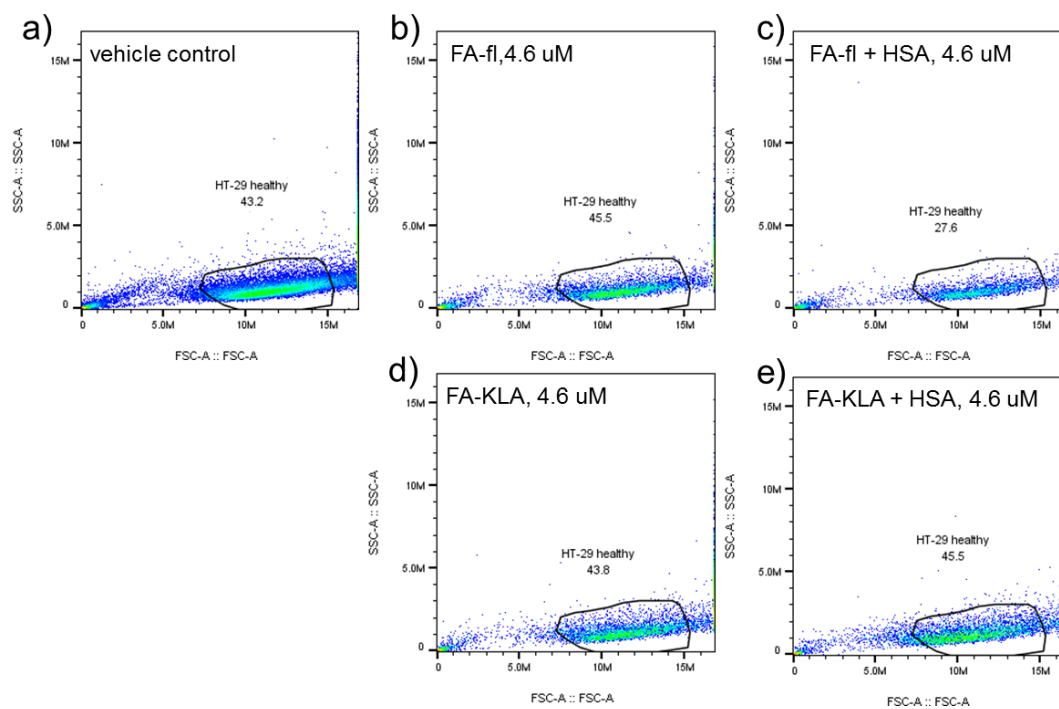


Figure 4.47 Dot plots showing forward scattering versus side scattering for representative experiments investigating mechanism of uptake of FA-fl, FA-fl + HSA, FA-KLA or FA-KLA + HSA materials in HT-29 cells, and gating used for healthy cell populations. All experiments are done in complete media. Conditions for treatment are included in an inset in each plot and gated populations represent 27-45% of cell populations analyzed.

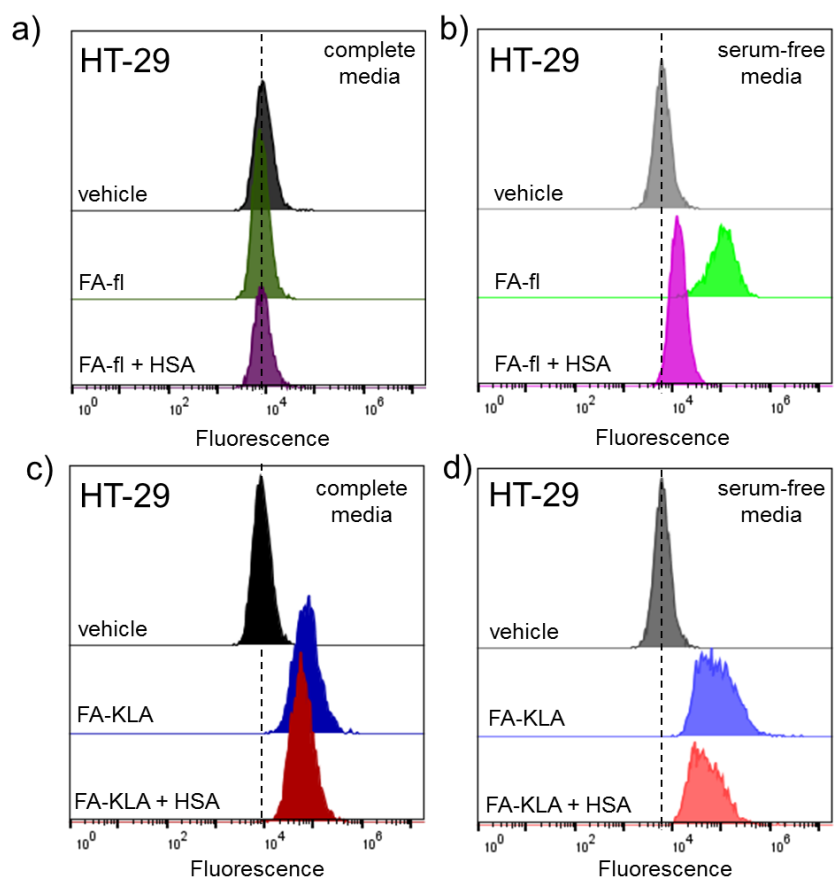


Figure 4.48 Representative histograms for cell uptake of FA-fl, FA-fl + HSA, FA-KLA or FA-KLA + HSA in HT-29 cells. Treatments in complete and serum-free media were performed.

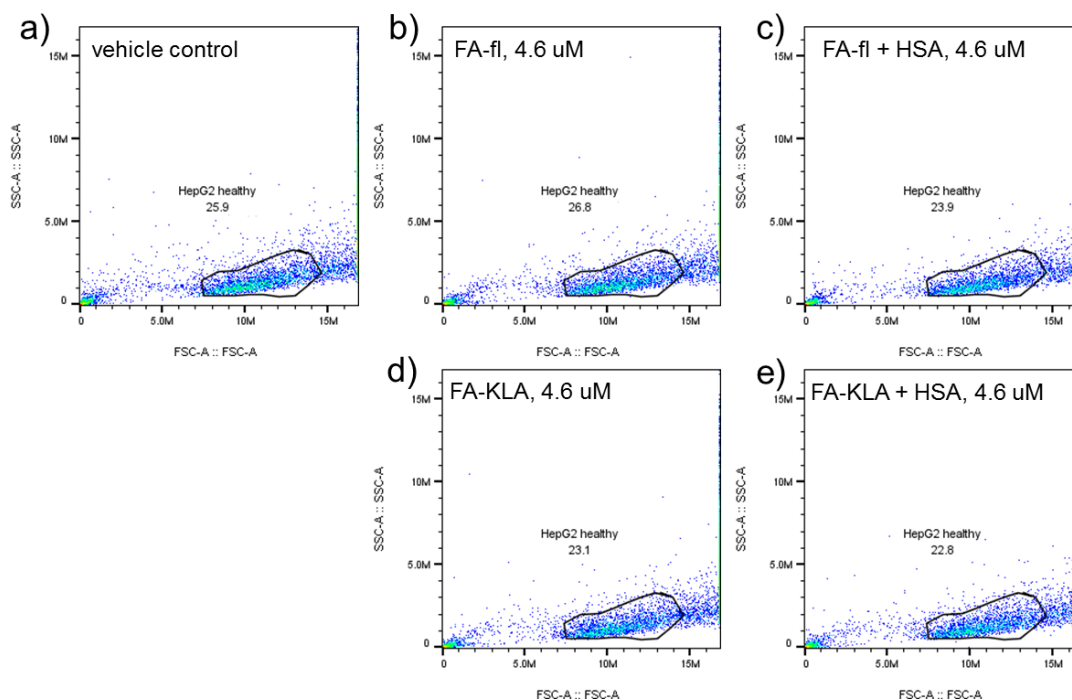


Figure 4.49 Dot plots showing forward scattering versus side scattering for representative experiments investigating mechanism of uptake of FA-fl, FA-fl + HSA, FA-KLA or FA-KLA + HSA materials in HepG2 cells, and gating used for healthy cell populations. All experiments are done in complete media. Conditions for treatment are included in an inset in each plot and gated populations represent 22-27% of cell populations analyzed.

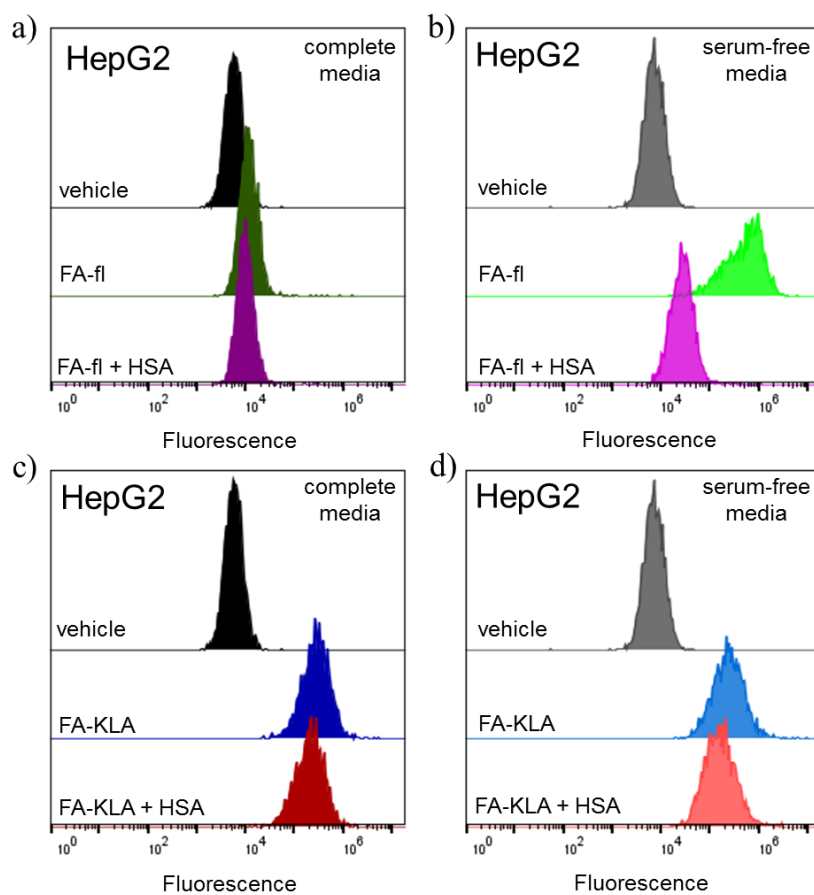


Figure 4.50 Representative histograms for cell uptake of FA-fl, FA-fl + HSA, FA-KLA or FA-KLA + HSA in HepG2 cells. Treatments in complete and serum-free media were performed.

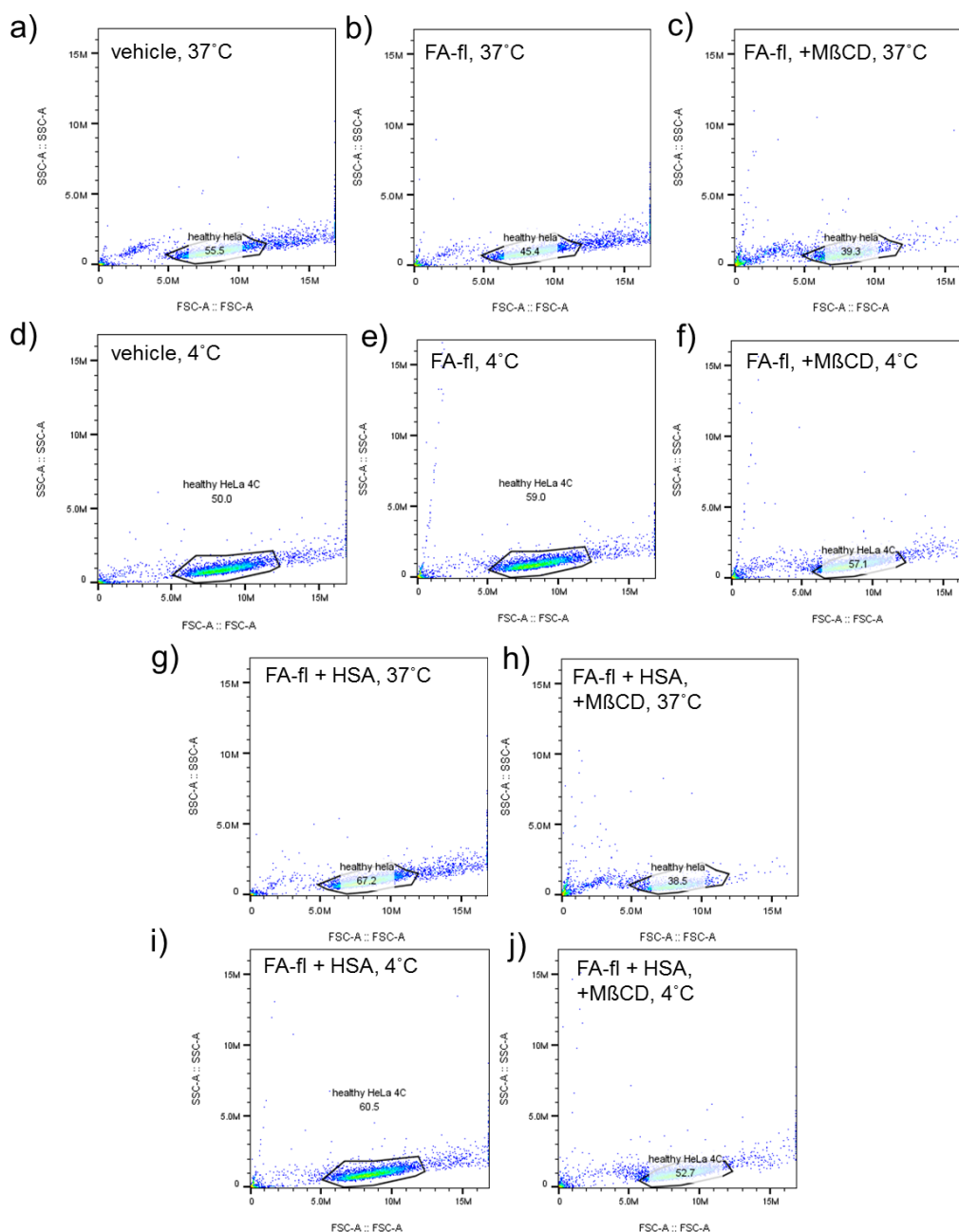


Figure 4.51 HeLa cells treated with FA-fl formulations in complete media. Dot plots showing forward scattering versus side scattering for representative experiments investigating mechanism of uptake of FA-fl or FA-fl + HSA materials in HeLa cells, and gating used for healthy cell populations, using complete media. Conditions for treatment are included in an inset in each plot. There appeared to be no change in populations of healthy cells when incubated at 37°C (a) or 4°C (d). gating from vehicle controls to experimental samples included 45-67% of population analyzed; a decrease in gated population was observed for treatment with MβCD at 37°C (c and h), with ~38% of population included in fluorescence analysis. This decrease in healthy cells is attributed to MβCD disturbing the cell membrane. Select histograms showing population shifts in fluorescence intensity is shown in Fig. 4.52.

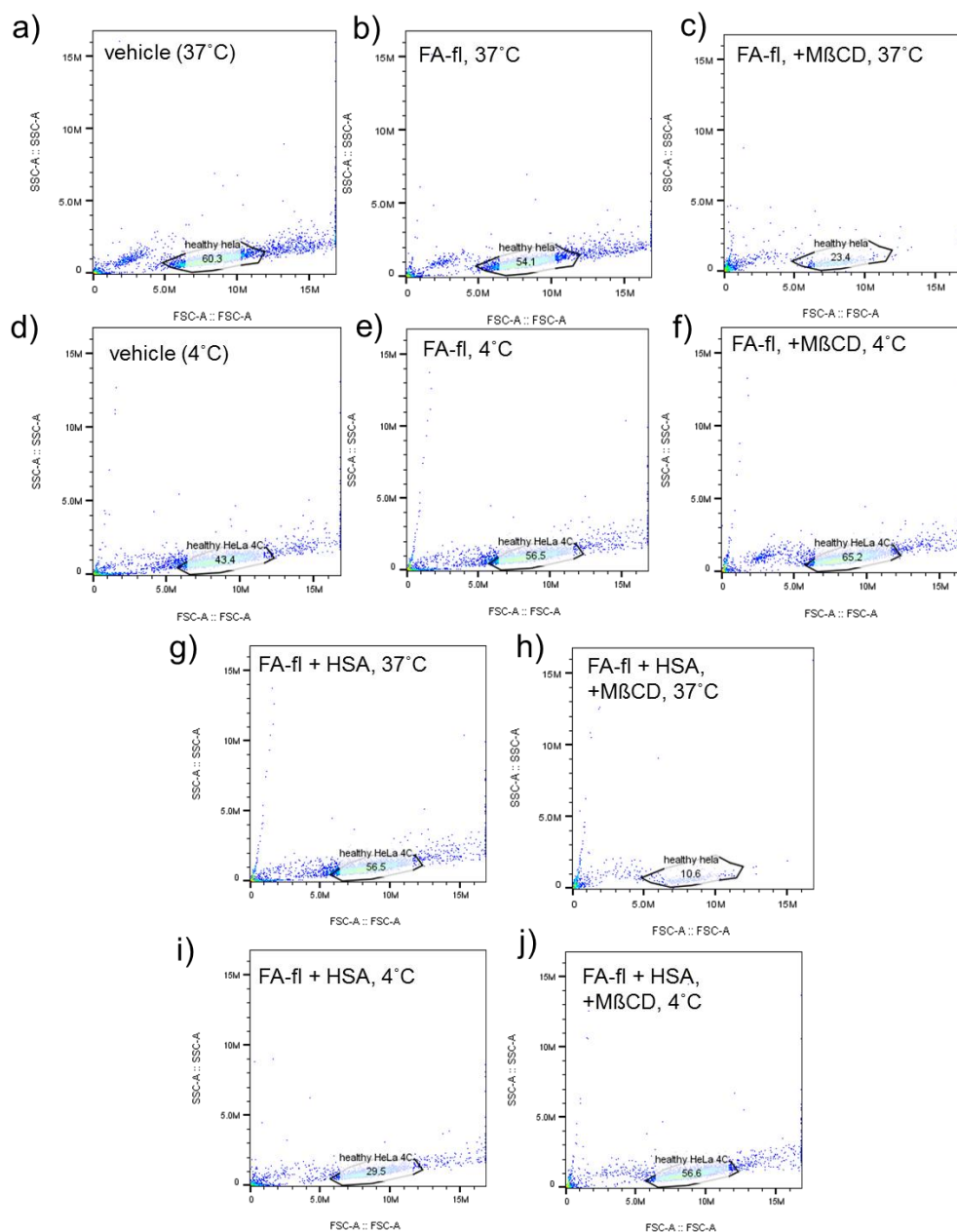


Figure 4.52 HeLa cells treated with FA-fl formulations in serum-free media. Dot plots showing forward scattering versus side scattering for representative experiments investigating mechanism of uptake, and gating used for healthy cell populations, using serum-free media. Again, there appeared to be no major change in populations of healthy cells when incubated at 37°C (a) or 4°C (d). Gating from vehicle controls to experimental samples included 43-65% of population analyzed; a decrease in gated population was observed for treatment with M β CD at 37°C (c and h), with ~23 or 10% of cell population included in fluorescence analysis. This decrease in healthy cells is attributed to M β CD disturbing the cell membrane. Incubation of FA-fl + HSA at 4°C also showed a decrease in gated cell population (plot i), 29% of population). Select histograms showing population shifts in fluorescence intensity is shown in Fig. 4.53.

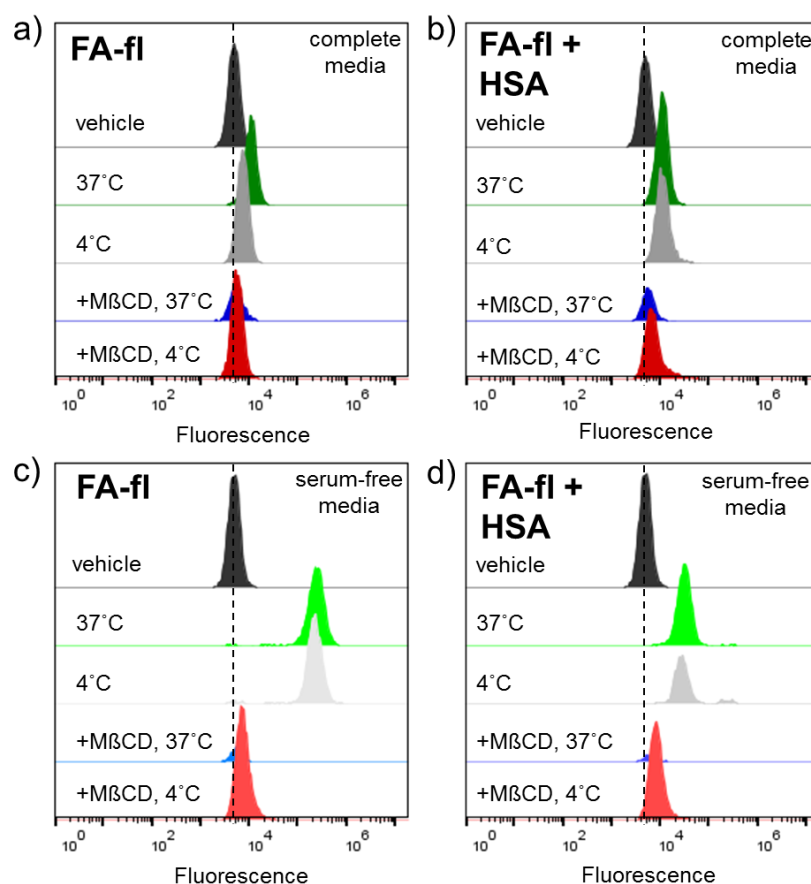


Figure 4.53 Representative histograms for mechanistic cell uptake studies on HeLa cells for FA-fl (a and c) and FA-fl + HSA (b and d) formulations under various conditions. The top two panels are treatments in complete media (a and b), while lighter colors (c and d) are treatments in serum-free media.

4.26 References

- (1) Liu, Z.; Chen, X. *Chem. Soc. Rev.* **2016**, 45 (5), 1432–1456.
- (2) Callmann, C. E.; Thompson, M. P.; LeGuyader, C. L. M.; Gianneschi, N. C.; Bertin, P. A. *Modified Cytotoxins and Their Therapeutic Use*. PCT/US2016/052829, 2016.
- (3) Nagaraja, T. N.; Croxen, R. L.; Panda, S.; Knight, R. A.; Keenan, K. A.; Brown, S. L.; Fenstermacher, J. D.; Ewing, J. R. *J. Neurosci. Methods* **2006**, 157 (2), 238–245.
- (4) Domínguez, A.; Fernández, A.; González, N.; Iglesias, E.; Montenegro, L. *J. Chem. Educ.* **1997**, 74 (10), 1227–1231.
- (5) Spinazzi, A.; Lorusso, V.; Pirovano, G.; Kirchin, M. *Acad. Radiol.* **1999**, 6 (5), 282–

291.

- (6) Muller, R. N.; Radüchel, B.; Laurent, S.; Platzek, J.; Piérart, C.; Mareski, P.; Vander Elst, L. *Eur. J. Inorg. Chem.* **1999**, 1999 (11), 1949–1955.
- (7) Multihance® [package insert].
- (8) Kratz, F. *J. Control. Release* **2008**, 132 (3), 171–183.
- (9) Purcell, W. T.; Ettinger, D. S. *Curr. Oncol. Rep.* **2003**, 5 (2), 114–125.
- (10) Abolmaali, S. S.; Tamaddon, A. M.; Dinarvand, R. *Cancer Chemother. Pharmacol.* **2013**, 71 (5), 1115–1130.
- (11) Venditto, V. J.; Simanek, E. E. *Mol. Pharm.* **2010**, 7 (2), 307–349.
- (12) Ellerby, H. M.; Arap, W.; Ellerby, L. M.; Kain, R.; Andrusiak, R.; Rio, G. D.; Krajewski, S.; Lombardo, C. R.; Rao, R.; Ruoslahti, E.; Bredesen, D. E.; Pasqualini, R. *Nat. Med.* **1999**, 5 (9), 1032–1038.
- (13) Chalovich, J. M.; Eisenberg, E. *Biophys. Chem.* **2005**, 257 (5), 2432–2437.
- (14) Singh, Y.; Palombo, M.; Sinko, P. J. *Curr Med Chem* **2008**, 15 (18), 1802–1826.
- (15) Blum, A. P.; Kammeyer, J. K.; Gianneschi, N. C. *Chem. Sci.* **2016**, 7 (2), 989–994.
- (16) Vercauteren, D.; Vandenbroucke, R. E.; Jones, A. T.; Rejman, J.; Demeester, J.; De Smedt, S. C.; Sanders, N. N.; Braeckmans, K. *Mol. Ther.* **2010**, 18 (3), 561–569.
- (17) Zidovetzki, R.; Levitan, I. *Biochim. Biophys. Acta - Biomembr.* **2007**, 1768 (6), 1311–1324.
- (18) Ashbrook, J. D.; Spector, A. A.; Santos, E. C.; Fletcher, J. E. *J. Biol. Chem.* **1975**, 250 (6), 2333–2338.
- (19) Callmann, C. E.; Barback, C. V.; Thompson, M. P.; Hall, D. J.; Mattrey, R. F.; Gianneschi, N. C. *Adv. Mater.* **2015**, 27 (31), 4611–4615.

Chapter 5

Conclusions and Perspectives

5.27 Conclusions on Polymeric Nanoparticle and Bioconjugate

MRI Contrast Agents for *In Vivo* Imaging

In this dissertation, two strategies were studied towards the goal of using macromolecular scaffolds as carriers of conventional small molecule MRI contrast agents. Using a graft-through approach to polymerize a novel gadolinium-based contrast agent monomer, polymer amphiphiles were synthesized, then formulated in to nanoparticles. These nanoassemblies were either spherical or fibrillar in phase. Using these MR-active materials, the biodistribution patterns were investigated using intraperitoneal injections followed by *in vivo* imaging and *ex vivo* elemental analysis. Our results demonstrated the importance of nanoparticle shape in enhancing retention of materials in the peritoneal space, and suggested differential clearance *via* the RES system. As an alternative to polymeric nanomaterials, we explored a second strategy employing human serum albumin-specific ligands conjugated to the gadolinium based contrast agent. By high-jacking albumin blood proteins we sought to enhance the circulation time of a small molecule contrast agent, and take advantage of the affiliation of albumin with different disease states.

The studies performed herein demonstrate proof-of-concept of strategies to enhance the circulation and distribution profiles of small molecule MRI contrast agents. Further, *in vivo* imaging experiments proved that these materials are useful in non-invasive imaging applications.

5.28 On-Going and Future Work

Despite the progress made in understanding polymer self-assembly towards interesting morphologies and developing nanomaterials towards *in vivo* imaging, the optimal nanoparticle system for all drug delivery applications has not been identified for any nanoparticle systems. Studies over the years in the Gianneschi group have capitalized on the MMP-responsive targeted nanoparticle systems, but sensitive imaging of clinically relevant disease models remains to be articulated.

The nanoparticle systems discussed in this thesis, particularly the gadolinium-containing spherical and fibrillar nanoparticles, represent crucial preliminary studies motivating on-going work in the lab. As described, intra-peritoneal injections were used in these studies, and represents an important treatment paradigm for malignancies of the peritoneal cavity. On-going work in the lab consist of formulating nanoparticles loaded with platinum-based drugs to specifically target ovarian cancer. Designing materials with high-aspect ratios and introducing them *via* the peritoneum are key design principles being developed in these projects.

Often times, the nanoparticles formulated with ROMP polymers results in spherical structures. A hallmark project pursued in the lab is working to understand how to formulate nanoparticles with diverse structures predictably, either through polymer design or micellization strategy. Colleagues are evaluating kinetic and thermodynamic effects of polynorbornene and other polymer architectures towards answering questions regarding the energetics of polymeric nanoparticle formation. The findings in this thesis, particularly that non-aromatic hydrophobic blocks are useful to formulating cylindrical nanoparticles, have been used in publication from the lab, and are considered in this project.¹

The albumin drug carrier project described in Chapter 4 has revealed fascinating fundamental science and applied clinical questions. A main contribution from this author is in designing and evaluating MRI contrast agents using this fatty acid platform technology. The initial results demonstrating enhanced blood circulation, especially compared to other clinical agents, is a good start in evaluating another class of blood-pool imaging agents. We know that albumin loaded with a therapeutic agent are effective at suppressing tumor growth, so on-going work in this project is identifying how and why the diagnostic agents accumulate (or not) in the intended tumor target. By taking advantage of the body's natural small molecule carrying system, e.g. abundant blood proteins like albumin, we hope to avoid any unintended immune response.

The amenability of the fatty acid conjugates means that any number of warheads may be attached. In Chapter 4, other cytotoxins and peptides were evaluated, and on-going collaborations extend to nucleic acid and gadolinium-free agents as fatty-acid conjugates. Fundamental science questions that may be addressed with this technology include evaluation of the targeting mechanism of the HSA-formulations. On-going collaborative work in this project is investigating cell receptors and endocytotic pathways responsible for internalization of fatty acid conjugates or albumin-carried conjugates. Using a CRISPR-Cas9 gene screen, key cell uptake pathways involving fatty acid transport and albumin specific uptake will be evaluated.

5.29 Perspective: The Future of Translatable Nanoparticle Drug Delivery Systems

The ultimate goals of the field of nanomedicine is to be able to more efficiently delivery cargo to a target, with minimal off-target or toxicity effects. The research and development

divisions at pharmaceutical industrial companies invest billions of dollars towards capturing the most effective new drug for market, yet the industry still suffers from low output, as well as challenges for more efficient and sustainable research programs. Early pipeline screens for efficacy and toxicity have been identified as a key area for improvement towards clinical approval.² As the field of polymeric nanoparticle drug delivery continues to expand and diversify, if clinical applicability is sought, focus needs to switch towards designing more robust materials, coupled with early pipeline identification of potentially successful drug candidates. As outlined in a meta-review by Chan *et. al.*, despite the vast resources contributed towards nanomedicine in the recent decades, there is still a disconnect between materials developed in the lab, and clinical approval.³ Furthermore, researchers continue to overstate the importance of the enhanced permeability and retention effect in human translatable nanosystems.⁴ Rather than developing highly complex and intricate nanoparticle systems, researchers should focus on more robust nanoparticle design and preparation, and better methods for pre-clinical evaluation.

With respect to nanoassembly design, the physicochemical parameters of size, shape and charge are the principal properties to consider and evaluate. It is challenging to examine all physicochemical properties in one study, and size, shape and charge of a material do not stand on isolated pedestals as the key contributing factors to nanoparticle success or failure. Topics not explored in this work, but of interest to the field include the force modulus, or stiffness of material, and how the material behaves in flow and under sheer forces.^{5,6}

With respect to laboratory evaluation of efficacy, 3D assays, co-culturing and organotypic tissue slicing may be more informative than monolayer *in vitro* experiments with regards to high through-put assays.⁷ Recent advances in organ-on-a-chip technologies present opportunities for informative, high-throughput studies.⁸ As discussed in the introduction, the translatability from animal model to humans is severely lacking. While organ-on-a-chip

technology is not yet capable of providing the same pharmacokinetic and pharmacodynamic information that a murine model might provide, we must critically think about the best way to evaluate materials for effectiveness and toxicity profiles. In our own work, we employ xenograft tumor models: immune-suppressed mice burdened with a human tumor mass. This is the standard for evaluation for drug delivery materials such as those studied in this dissertation, though the most obvious body system, the immune system, is absent. Evaluation of materials in healthy animals as well as humanized mice containing hallmarks of the human immune system alongside immunosuppressed xenograft models may aid in understanding off-target effects and toxicities of nanoparticle delivery systems.⁹ With the age of personalized medicine, decades of research in nanomedicine, and a pivot in focus towards better methods to evaluate potential efficacy of a drug early in development, the field stands ready for major advancements in disease treatment in the coming years.

5.30 References

- (1) Li, Y.; Huang, Y.; Wang, Z.; Carniato, F.; Xie, Y.; Patterson, J. P.; Thompson, M. P.; Andolina, C. M.; Ditri, T. B.; Millstone, J. E.; Figueroa, J. S.; Rinehart, J. D.; Scadeng, M.; Botta, M.; Gianneschi, N. C. *Small* **2016**, *12* (5), 668–677.
- (2) Paul, S. M.; Mytelka, D. S.; Dunwiddie, C. T.; Persinger, C. C.; Munos, B. H.; Lindborg, S. R.; Schacht, A. L. *Nat. Rev. Drug Discov.* **2010**, *9* (MARch).
- (3) Wilhelm, S.; Tavares, A. J.; Dai, Q.; Ohta, S.; Audet, J.; Dvorak, H. F.; Chan, W. C. W. *Nat. Rev. Mater.* **2016**, *1*, 1–12.
- (4) Nakamura, Y.; Mochida, A.; Choyke, P. L.; Kobayashi, H. *Bioconjug. Chem.* **2016**, *27* (10), 2225–2238.
- (5) Kamaly, N.; Xiao, Z.; Valencia, P. M.; Radovic-Moreno, A. F.; Farokhzad, O. C. *Chem. Soc. Rev.* **2012**, *41* (7), 2971–3010.
- (6) Geng, Y.; Dalhaimer, P.; Cai, S.; Tsai, R.; Tewari, M.; Minko, T.; Discher, D. E. *Nat. Nanotechnol.* **2007**, *2* (4), 249–255.
- (7) Goodman, T. T.; Ng, C. P.; Pun, S. H. *Bioconjug. Chem.* **2008**, *19* (10), 1951–1959.
- (8) Esch, E. W.; Bahinski, A.; Huh, D. *Nat. Rev. Drug Discov.* **2015**, *14* (4), 248–260.

- (9) Ito, R.; Takahashi, T.; Katano, I.; Ito, M. *Cell. Mol. Immunol.* **2012**, 9 (3), 208–214.